d:Collection

A THESIS
FOR THE DEGREE OF DOCTOR OF PHILOSOPHY

Development of Flexible Composite Film based Hybrid Energy Harvesters for Self-Powered Sensors

VENKATESWARAN VIVEKANANTHAN

Department of Mechatronics Engineering

GRADUATE SCHOOL

JEJU NATIONAL UNIVERSITY

February 2020

Development of Flexible Composite Film based Hybrid Energy Harvesters for Self-Powered Sensors

VENKATESWARAN VIVEKANANTHAN

(Supervised by Professor Kim Sang-Jae)

A thesis submitted in partial fulfillment of the requirement for the degree of
Doctor of Philosophy
2019.12.13

The thesis has been examined and approved.

....

Thesis Director,
Prof. Lee Gae Myoung

Professor, Department of Electrical Engineering
College of Engineering, Jeju National University

....

Thesis Committee Member,
Prof. Kang Chang Nam

Professor, Department of Mechanical Engineering
College of Engineering, Jeju National University

....
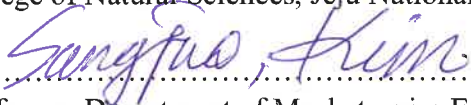
Thesis Committee Member,
Prof. Woo Seung Min

Assistant Professor, Department of Energy Engineering
College of Engineering, Jeju National University

....

Thesis Committee Member,
Prof. Lee Han Ju

Assistant Professor, Department of Physics
College of Natural Sciences, Jeju National University

....

Thesis Committee Member,
Prof. Kim Sang-Jae

Professor, Department of Mechatronics Engineering
College of Engineering, Jeju National University

December 2019

Department of Mechatronics Engineering
GRADUATE SCHOOL
JEJU NATIONAL UNIVERSITY
Republic of Korea
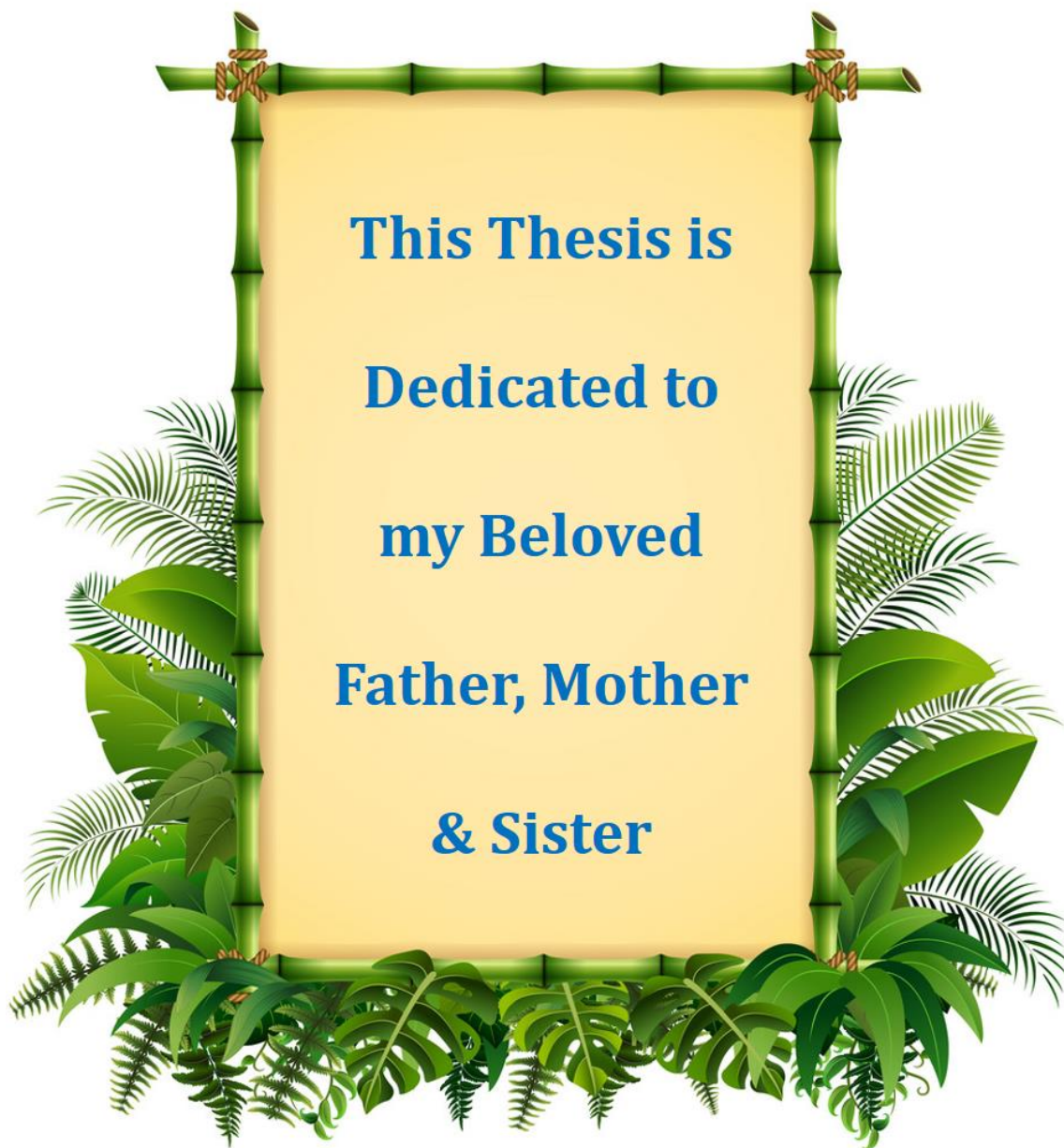
This Thesis is

Dedicated to

my Beloved

Father, Mother

& Sister

Acknowledgements

I would like to express my sincere gratitude to all who have supported, contributed to the completion of my doctoral thesis. I have crossed several obstacles and experienced various situations, toughest paths, failures and significant achievements during the entire period of my doctoral thesis. I am so grateful to all the people who have helped me to overcome the barriers with their constant encouragement.

My First and foremost sincere and deep gratitude to my respectful research advisor, **Prof. Sang Jae Kim**, Professor in Jeju National University, for giving me the opportunity to work in his laboratory and allow me to carry out my research work, providing invaluable suggestions, guidance and support throughout the entire research period. The suggestions provided by him through discussions and periodical lab meetings motivates me to work smartly and hardly. It was a great honor and privilege to work with him under his kind guidance and expecting the same in my future career as well. My heartfelt thanks to my co-research supervisor **Prof. Chang Nam Kang,** Jeju National University, for his scholarly advice, scholarship support and help during the whole research period. My sincere gratitude and I am very mech thankful to him for the academic support and encouragement during the research period.

I express my thanks to **Prof. Venkata Krishnan,** from Indian Institute of Technology Mandi and **Prof. Narendhar Chandrasekar**, from Sri Ramakrishna Engineering College, who have initiated my research career, providing valuable suggestions and showing me the right path and direction to extend my research work to the doctorate level.

I express my sincere gratitude to my friend, **Dr. Yuvasree Purusothaman** for whom I would like to dedicate my thesis as well. Many thanks to her for being a role model for me during my research period. I have learnt many things from you in research and the obstacle you have overcome during the research period and achieved a grant success motivates me during my tough times. I sincerely thank my beloved seniors **Dr. Nagamalleswara Rao Alluri** and **Dr. Arunkumar Chandrasekhar** for their help and guidance throughout my research period. The guidance I have received from you is invaluable and the way you both have treated me is like your own brother. My deepest gratitude to both of you forever in my life time.

My heartfelt gratitude to **Dr. Dharaneedharan Subramanian, Dr. Roshini Arivazhagan, Dr. Ganesh Kumar Veerasubramani and Dr. Sophia Selvarajan** for their support and encouragement. Many thanks to my beloved sisters and well-wishers **Mrs. Deepa Katti** and **Mrs. Poornima Maran** for their kind support and making me to feel like living with the family. I extend my thanks to the new sisters **Mrs. Sri Latha Alluri, Mrs. Juhi Garg and Mrs. Anjali Pandey** for their constant support all the time.

It's a significant challenge to stay away in another country leaving the family, friends, relatives and my own country. I am very happy to have friends who make a homely environment, lots of unforgettable moments and hardships. My sincere thanks to **Dr. Anil Kumar Khambampati, Mr. Konki Sravan Kumar, Mr. Vineet Singh and Mr. Sachin Kumar Gupta** for your invaluable support and encouragement.

I sincerely thanks to my colleagues **Dr. K. Karthikeyan, Dr. Parthiban Pazhamalai, Dr. Dipak Kumar Khatua, Dr. Natarajan Subramanian, Mr. Surjit**

Sahoo, **Mr. Gaurav Khandelwal, Mr. M J Raj Nirmal Prashanth, Ms. Sindhuja Manoharan, Mr. Vimal Kumar, Mr. K. S. Abishegapriyan, Mr. Dhanasekar, Mr. Swapnil Nardekar, Mr. Woo Joong Kim, Mr. Sugato Hajra, Ms. Manisha Sahu, Ms. Aparna Sajeev and Mr. Arun Prasath** for the timely help and support during my research activities. I extend my thanks to **Mr. Cho Inho, Mrs. Lee Hyeun Seok** and **Mr. Kim Chan** for their kind help in official document work and BK office works.

I extend my sincere gratitude to **Prof. Lee Byoung Gul** and **Prof. Kang Young Hoon** for their encouragement and support during the JISO activities and also with my academic activities. I extend my thanks and gratitude to all the members of the center for international affairs (**Ms. Kim Tae Young, Ms. Kang Yun Young and Ms. Oh Eun Yeong**), Library office (**Ms. Lee Jung Hyo**) and the members of graduate school office (**Ms. Ji Hyo Jung**) for their constant support and encouragement during the activities performed.

My heartful thanks to all the friends and former members of Jeju national university **Dr. MSP Sudhakaran, Mr. Gnanaselvan, Mr. Arun George, Ms. Deba Priya, Mr. Mohan Raj, Mr. Prem Kumar, Mrs. Priyanka Rajan, Mr. Jithin, Dr. Sunny kumar, Mr. Abdul Rahim, Mr. Vikram Pratap, Ms. Jayalakshmi, Mr. Rai Suresh, Ms. Shirjana, Mr. Roshan, Mr. Sunam Sharma, Ms. Saritha, Mr. Nilojan, Mr. Kugan, Mr. Pavithiran, Mr. Thatchanesh kanth and Mr. Hasitha Karunaratne** for their constant support, encouragement and fun filled activities.

Thesis Overview

Design of Hybrid energy Harvesters for Self-Powered Sensors

Contents

CHAPTER I

INTRODUCTION

CHAPTER II

Materials, Methods and Measurement Techniques

CHAPTER - III

Biocompatible collagen-nanofibrils: An approach for sustainable energy harvesting and battery-free humidity sensor applications

CHAPTER IV

4.1 A flexible, planar energy harvesting device for scavenging road side waste mechanical energy *via* synergistic piezoelectric response of $K_{0.5}Na_{0.5}NbO_3$-$BaTiO_3$/PVDF composite films

4.2 Zero-Power Consuming Intruder Identification System by Enhanced Piezoelectricity of $K_{0.5}Na_{0.5}NbO_3$ using Substitutional Doping of BTO NPs

4.3 A Flexible Piezoelectric Composite Nanogenerator Based on Doping Enhanced Lead-Free Nanoparticles

CHAPTER V

A Highly Reliable, Impervious and Sustainable Triboelectric Nanogenerator as a Zero-power Consuming Active Pressure Sensor

CHAPTER VI

Substantial Improvement on Electrical Energy Harvesting by Chemically Modified/Sandpaper-based Surface Modification in Micro-scale for Hybrid Nanogenerators

CHAPTER VII

7.1 A Sliding mode Contact Electrification based Triboelectric-Electromagnetic Hybrid Generator for Small-Scale Biomechanical Energy Harvesting

7.3 Fe_2O_3 Magnetic Particles derived Triboelectric-Electromagnetic Hybrid Generator for Zero-Power Consuming Seismic Detection

CHAPTER VIII

Summary and Future Prospective

Nomenclature

PENG	Piezoelectric nanogenerator
LED	Light emitting diode
PVDF	Polyvinylidene fluoride
XRD	X-Ray diffraction
XPS	X-Ray photoelectron spectroscopy
FT-IR	Fourier transform infrared spectroscopy
FE-SEM	Field emission scanning electron microscope
PDMS	Polydimethyl siloxane
EDS	Energy dispersive x-ray spectroscopy
H-NG	Hybrid nanogenerator
DI	De-ionized
EMG	Electromagnetic generator
TENG	Triboelectric nanogenerator
CPNG	Composite piezoelectric nanogenerator
CF	Composite films
LCD	Liquid crystal display
SSR	Solid state reaction

List of Tables

List of Figures

behavior of a commercial capacitor 0.22 μF (c) Load resistance and power density analysis and (d) stability test for a period of 2000 s 10 N.

humidity sensing response showing the voltage drop upon addition of different % RH(c) change in voltage response at positive and negative sides of voltage peaks and it shows a linear operating behavior.

sectional FE-SEM image of pure PVDF film and the thickness is ≈119 μm. The inset shows estimated PVDF molecular chains in aligned manner shows electroactive β-phase. **(d)**Cross-sectional FE-SEM image of PVDF/KNN-xBTO CF ($x = 0.02$) and the thickness is ≈121 μm. The inset shows estimated PVDF molecular chains in aligned manner along with the KNN-xBTO nanoparticles.

device when pressed inside the water tub. (f) Humidity test of WR-SE-TENG device under various percentages of relative humidity ranging from 10 %, 42%, 68%, 80% and 99% RH and the device shows stable output in the entire period.

the side view and top opened view showing the particles inside.

under various percentages of relative humidity (10-90 % RH).

초 록

비용 효율적인 비전통적 에너지 원을 사용하여 소형 전자 기기, 휴대용 및 착용 가능한 전자 기기에 전원을 공급하기 위한 지속 가능한 전원을 개발하는 것은 빠르게 성장하는 전자 분야에서 여전히 중요한 과제이다. 전자 산업의 발전으로 전자 기기의 크기가 줄어들어, 필요한 전력 또한 줄어들었다. 전자 디스플레이, 생의학 및 이식 가능한 장치와 같이 다양한 간단한 기계장치에는 마이크로와트에서 밀리와트 범위의 전력이 필요하다. 기존 전자 기기는 배터리를 사용하여 전원을 공급하기 때문에 빈번한 교체가 필요하여 사용자의 불편뿐만 아니라 환경오염도 야기한다. 배터리로 인한 단점을 극복하기 위한 안정적인 에너지 수확 기술은 환경에서 사용 가능한 에너지를 수확 할 수 있다. 환경에서 이용할 수 있는 매우 풍부한 에너지원은 인체 운동, 진동 및 차량 운동에서 생성 될 수 있는 기계적 에너지이다. 이러한 기계적 에너지는 정전기 유도 [Triboelectric nanogenerators (TENG)], 전자기 유도 [EMG] 및 압전 효과 [Piezoelectric nanogenerator (PENG)]를 사용하는 나노 발전기를 사용하여 유용한 전기 에너지로 변환 될 수 있다. 개별

TENG, PENG 및 EMG 로 제작 된 나노발전기는 전기 출력 성능으로 인해 다양한 응용 분야에 크게 사용할 수 없다.

이 논문은 이러한 문제를 극복하기 위해 단일 장치 구조에서 TENG-PENG 구성 요소와 단일 하이브리드 장치의 TENG-EMG 구성 요소로 구성된 하이브리드 에너지 수확기를 소개한다. 하이브리드 에너지 수확기는 향상된 전력 밀도로 전압 및 전류 측면에서 높은 전기 출력을 생성한다. 압전 복합 필름으로 만든 TENG-PENG 결합 하이브리드 장치는 장치에 기계적 힘을 가하는 유사한 메커니즘을 사용하여 마찰 전기 구성 요소와 압전 구성 요소를 동시에 활성화한다. 메커니즘에서, 장치에 가해지는 힘은 쌍극자가 단일 방향으로 배향하여 압전 전위를 생성하도록 유도하고, 다른 한편으로 복합 필름 상에 발생된 표면 전하는 마찰 전기 효과를 발생시킨다. 결합된 전기 출력은 개별 TENG 및 PENG 구성 요소와 비교할 때보다 더 높다. 복합 필름은 칼륨 나트륨 니오 베이트 ($K_{0.5}Na_{0.5}NbO_3$)와 같은 압전 나노 입자 및 폴리 디메틸 실록산 (PDMS) 및 폴리 비닐 리덴 플루오 라이드 (PVDF)와 같은 중합체를 갖는 이중 시스템 ($K_{0.5}Na_{0.5}NbO_3$- $BaTiO_3$) 나노 입자로 제조된다. 이를 위해 바이오 폴리머 계 압전 재료인 콜라겐

또한 전기 성능이 연구되었다. 마찬가지로 TENG-EMG 하이브리드 발전기도

정전기 효과 및 전자기 유도 효과를 모두 발휘하였으며 자석이 자성입자로

사용되어 제작되었고 전기 출력 성능이 연구되었다. 또한 동일한 기계적 운동으로

두 구성 요소가 모두 작동되었으며, 결합된 성능은 높았다. 제조된 장치는 차량 및

인체 운동에서 발생하는 폐 기계 에너지 소거, 전력 소비가 적은 침입자 식별 시스템,

수면 모니터링 시스템, 습도 센서 및 지진 감지와 같은 다양한 응용 분야에

사용되었다. 따라서 하이브리드 에너지 수확기는 미래의 전자, 센서 및 사물 인터넷

분야에서 매우 안정적이고 깨끗한 전원으로 발전할 것이다.

Abstract

Developing a sustainable power source for powering small electronic devices, portable and wearable electronics using a cost-effective unconventional energy source remains a significant challenge in the rapidly growing electronic field. The advancement in electronics industry makes the electronic gadgets shrinking in size, which eventually makes its power requirement less. Various gadgets require power in the range of microwatts to mill watts such as electronic displays, biomedical and implantable devices. The existing electronics gadgets use batteries for powering them, which creates inconvenience to environment due to pollution as well as for the users because it requires frequent replacement. To overcome the drawbacks faced by batteries, a reliable energy harvesting technology can harvest the energy which is available in the environment. The highly abundant energy source available in the environment is the mechanical energy that can be produced from human body motions, vibrations and vehicle motions. This mechanical energy can be converted into useful electrical energy by the use of nanogenerators utilizing electrostatic induction [Triboelectric nanogenerators (TENG)], electromagnetic induction [electromagnetic generators (EMG)] and piezoelectric effects [Piezoelectric nanogenerator (PENG)]. The nanogenerator made of individual TENG, PENG, and EMG is not highly capable in using for a wide variety of applications due to the electrical output performance.

To overcome the problems, this thesis introduces a hybrid energy harvester that is made of TENG-PENG components in a single device structure and TENG-EMG components as a single hybrid device. The hybrid energy harvester generates high

electrical output in terms of both voltage and current with improved power density. The TENG-PENG combined hybrid device made of piezoelectric composite film uses similar mechanism of applying mechanical force on the device, which activates both triboelectric and piezoelectric components simultaneously. In mechanism, the force applied on the device induces the dipoles to orient in a single direction to generate the piezoelectric potential, and on the other hand the surface charges developed on the composite film generate triboelectric effect. The combined electrical output is higher when compared to the individual TENG and PENG components. The composite film is made of piezoelectric nanoparticles such as potassium sodium niobate ($K_{0.5}Na_{0.5}NbO_3$) and its dual systems ($K_{0.5}Na_{0.5}NbO_3$-$BaTiO_3$) nanoparticles with the polymers such as polydimethylsiloxane (PDMS) and polyvinylidene fluoride (PVDF). To this, a biopolymer-based piezoelectric material; collagen is also studied with its electrical performance. Similarly, the TENG-EMG hybrid generator also works on both electrostatic effect, and electromagnetic induction effect have also been fabricated using magnet as well as magnetic particles and studied its electrical output performances. Here also, both the components were activated upon the same mechanical motion, and the combined performance is high. The fabricated device had been used for various applications such as scavenging waste mechanical energy from vehicle and human body motion, zero power consuming intruder identification system, sleep monitoring system, humidity sensor, and seismic detection. Hence, the hybrid energy harvester paves way as a highly reliable and clean power source in future in the field of electronics, sensors, and internet of things.

CHAPTER I

INTRODUCTION

1.1 Background

The rapid urbanization and industrial growth all over the world have become a potential threat to the global pollution and become one of the major causes for global warming and energy crises. The consumption of fossil fuels such as natural gas, coal, and petroleum have also raised concerns about global warming and environmental pollution. So, the search for clean and renewable energy has becoming a challenging task towards the sustainable development of the society and wellbeing of the humans and environments.
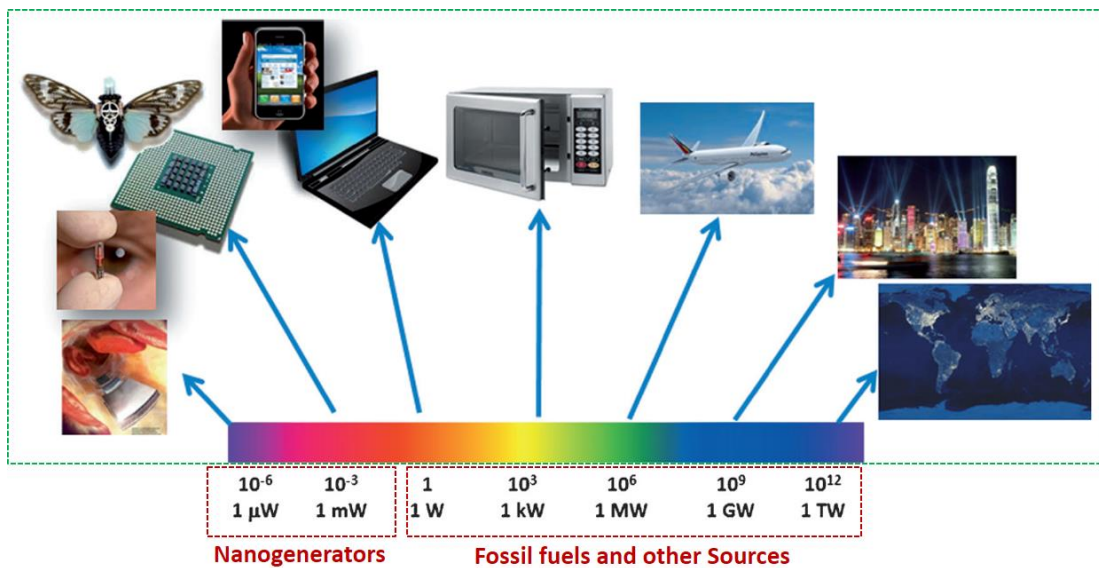
Figure 1.1 Global power requirement and the components powered by various sources and the proposed nanogenerators and the power requirement for self-powered systems.

The majority of energy that we consume today had been generated from non-renewable sources such as thermal power plants that operate on coal, diesel power plants operating with the help of oil. These natural resources are limited in supply, and it will take thousands of years to regenerate. The usage of fossil fuels such as coal and oil in the generation of electricity creates huge pollution to environment thereby it leads to the reduction of life span to humans. To overcome this issue an alternative energy harvesting approach had been introduced across the globe to protect mankind as well as to overcome the increasing energy crisis. The modern-day technology uses mech of electronic devices and there is a rapid growth in the field of mobile electronics and it is used for a wide variety of applications ranging from communication sector, health care sectors, and environmental monitoring which is schematically shown in Figure 1. These devices require power in the range of few milli watts to watts and are powered using batteries. The batteries have several drawbacks such as the batteries having a limited life span, short charging/discharging cyclic stability, heavy and risk overheating effect needs proper replacement. So, there is a high requirement to replace the batteries having more drawbacks and creating various threats to the environment. In order to have a sustainable power source, research is focusing towards the development of a battery-free or self-powered system which can harvest energy and utilize for itself. The present thesis shows the systematic approach of fabricating various types of energy harvesters composed of triboelectric effect, piezoelectric effect and electromagnetic effect and the developed energy harvesters are utilized successfully for battery-free or self-powered sensors and systems.

1.2 Necessity of this research

The present energy sources are generally obtained from various conventional and non-conventional energy sources such as thermal power, hydro power, natural gas, nuclear power solar and wind power. These power plants require high investment and capital costs and also requires periodical maintenance and higher maintenance costs. Similarly, thermal power plants are the main reasons for air and environmental pollution, as well as nuclear power plants are big threat to the human society due to its radiations. As per the law of conservation of energy, energy can neither be created nor destroyed but can be converted from one form to another. In such case, the most abundant energy sources are mechanical energy. There are a various source of mechanical energy ranging from wind, water wave, vibration, machinery in industry, human walking motion and vehicle motions. A survey by international traffic forum says that the average vehicles run per day in South Korea is more than 22,000, which that covers over 300,000 kms a day[3]. Then consider the waste mechanical energy generated through vehicle motions globally.
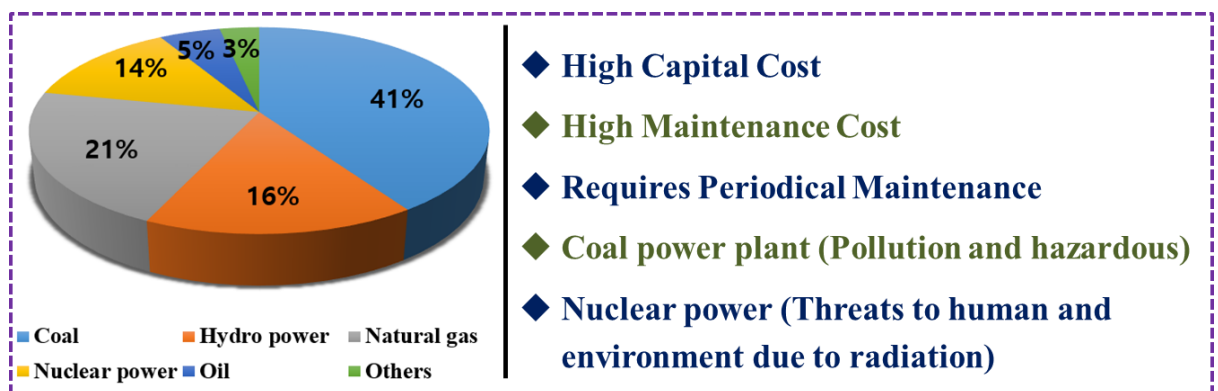
Figure 1.2 An overview of current energy sources and their drawbacks

In macroscopic view the global vehicle motions and wind can be a potential source of energy which can be used for the generation of cleaner and greener power sources for powering low power consumer electronics and can able to develop a sustainable future. Over the past decade, new kind of non-conventional energy sources are introduced and properly reported by different ways such as piezoelectric effect[7], triboelectric effect[8-10], pyroelectric effect[11] and thermoelectric effects[12].
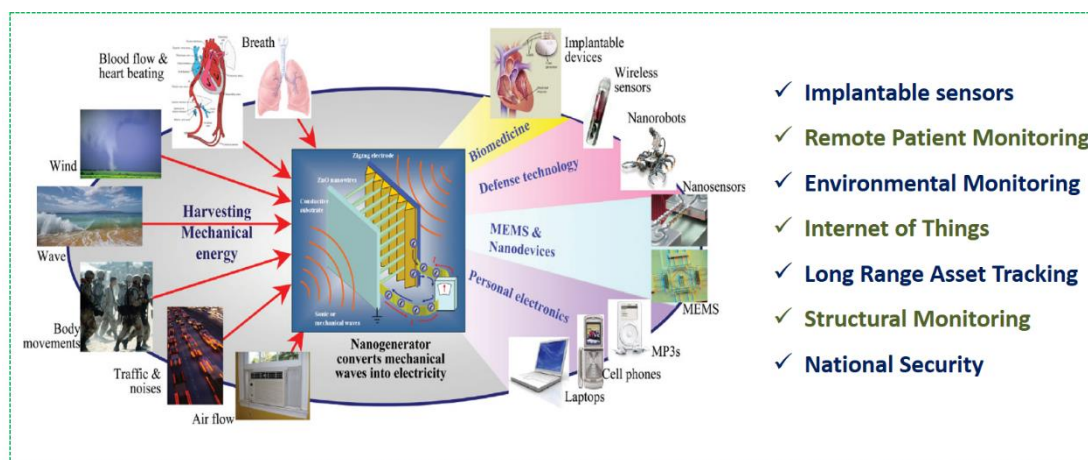
Figure 1.3 Harvesting mechanical energy from ambient sources and utilizing for various self-powered applications

1.3 Types of mechanical energy harvesters

1.3.1 Triboelectric nanogenerators

A triboelectric nanogenerator (TENG) is a type of energy harvester which can convert any type of external mechanical motion into clean electricity with contact electrification and electrostatic induction effects. The TENG device uses a positive triboelectric layer and negative triboelectric layer placed opposite to each other under various operating modes such as vertical contact separation mode, linear sliding mode, single electrode mode and free-standing mode. At either case of the operating modes, there will be a friction between two triboelectric layers, leading to the generation of electric potential by means of flow of electrons through an external load resistance. A

4

typical TENG device is schematically shown in Figure 1.3a with its digital photographic image.

1.3.2 Piezoelectric Nanogenerators

A piezoelectric nanogenerator (PENG) is a type of energy harvesting device capable of converting external kinetic energy into an useful electrical energy. The PENG device uses different kinds of piezoelectric materials such as ceramic based (barium titanate, potassium sodium niobite, bismuth titanate), polymer based (polyvinylidene fluoride) and bio-polymer based materials (collagen, chitin, dentin). A typical schematic and construction of a PENG device is shown in Figure 1.3b. The piezoelectric energy harvesting technology is one of the potential breakthroughs for the miniaturization and leading towards the development of various MEMS based systems. This type of energy harvester is highly reliable and been utilized for various battery-free sensors and self-powered applications.
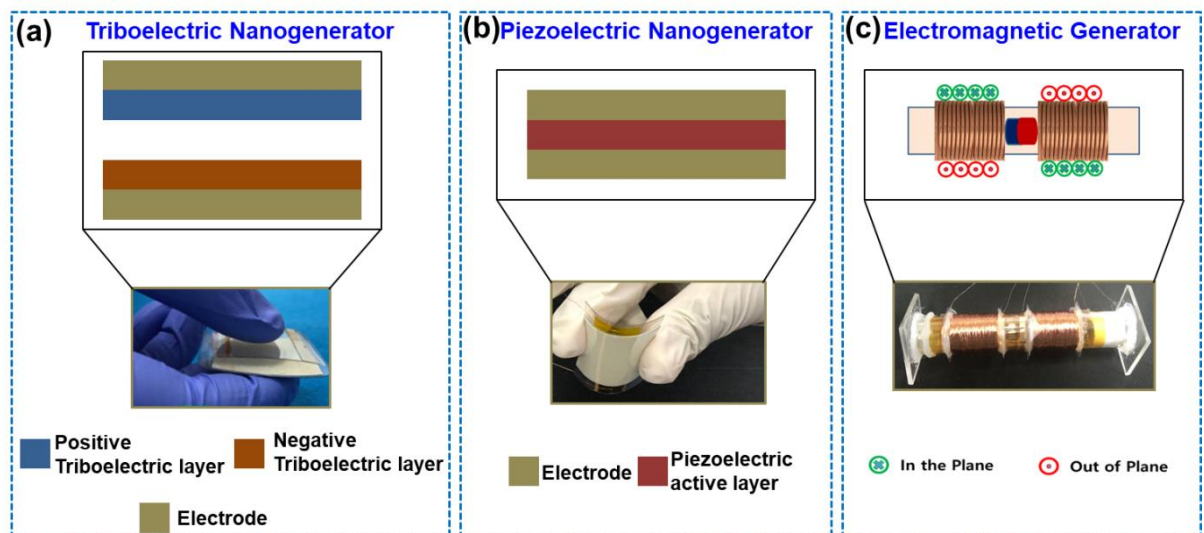
Figure 1.4 Types of mechanical energy harvesters (a) TENG (b) PENG (c) EMG

1.3.3 Electromagnetic generator

Electromagnetic generators (EMGs) are conventional energy harvesters traditionally used in all the energy harvesting systems. This energy harvesters worked on the principle of faraday's law of electromagnetic induction. The law states that whenever a current carrying conductor is placed in a magnetic field, an emf is induced in it. The induced emf is equal to the rate of change of flux linked in tit. The EMG device can operate in two mode, one is via a rotating mode and the other is through vertical motion of magnets into the coil. Based on these two operating modes, different kind of devices were designed and operated for various applications. There are few parameters to be considered for designing an EMG device and the parameters such as dimension of the magnetic material used and the coil parameters such as length of the coil, area of the coil, diameter of the coil and number of turns used for the design of device. The best performance EMG device are made through magnets made with rare earth material based permanent magnets specially made with the neodymium iron boron (NdFeB) magnets, which can produce strongest magnetic field. The schematic of the EMG device is shown in Figure 1.4c.

1.4 Need for hybrid generator

The performances of individual mechanical energy harvesters are not sufficient to power up various applications and powering up electronic components. So, there is a requirement for high output power source for powering up electronic components as well as a promising power source. There is an enormous research to improve the electrical output of energy harvester by changing material, doping of materials and enhancing the functional property of materials. Then researchers started to focus

제주대학교 중앙도서관
JEJU NATIONAL UNIVERSITY LIBRARY

towards hybridizing (combining two or more energy harvesters in a single package) the energy harvesters. There are reports on hybridizing the mechanical energy harvesters with solar cell, pyroelectric generator and thermoelectric generators. But their operating modes vary with each other leading to the usage of these devices for a wide variety of applications. So, researchers started focusing towards hybridizing the mechanical energy harvesters itself respected to their working mode, thereby TENG-PENG hybrid, TENG-EMG hybrid, TENG-PENG-EMG hybrid. Here TENG acts as a voltage source and the EMG or PENG acts as a stable current source. This approach enhances the output performance of the device leading to the increase in output power density to watt per meter square. Figure 1.4a shows the TENG-PENG hybrid device and Figure 1.4b shows the TENG-EMG hybrid device investigated in the present thesis.
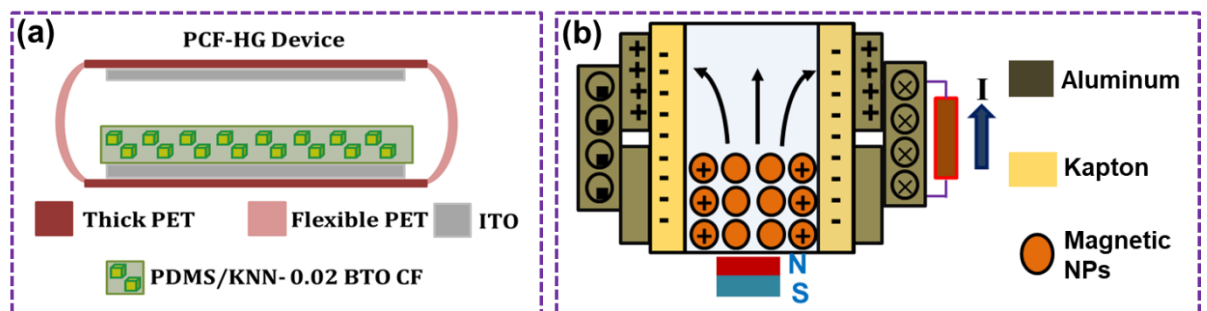
Figure 1.5 Hybrid generators (a) TENG-PENG (b) TENG-EMG

1.5 Self-powered sensors/systems

The self-powered systems generally composed of an energy harvesting device performs an application of active or passive sensing such as chemical, humidity, speed, pressure, force and powering up electronic devices using the nanogenerator device. The device can power the sensor or electronic devices or can perform the same function of a sensor actively with the energy harvester itself. The present thesis shows various self-powered sensors using the TENG, PENG and Hybrid devices ranges from self-

powered humidity sensor, sleep monitoring system, proximity sensor, pressure sensing and accelerometers. By the successful optimization of various parameters of the self-powered sensors, the device can be commercialized and been used for future electronics, sensor for environment and health care applications.
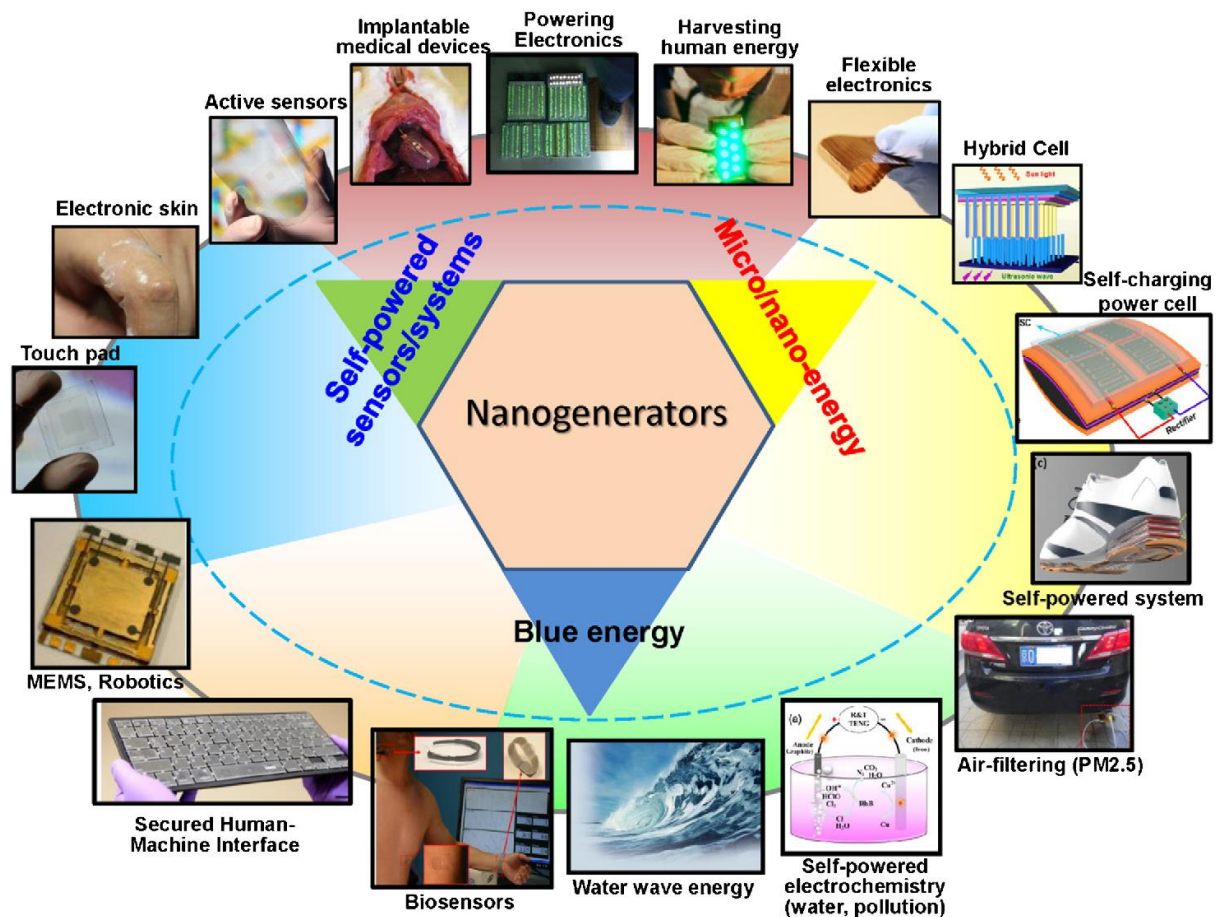
Figure 1.6 Nanogenerators for energy harvesting and self-powered sensors

1.6 Objective and scope of this thesis

The objective starts from the energy crisis and usage of natural resources and fossil fuels for the generation of electricity. By the usage of fossil fuels, they possess a great threat to the environment and the human society. The fossil fuels consumed at present will take thousands of years to recover it. Hence, focusing towards a non-conventional energy sources is highly required. The conventional energy sources require high investment for establishing the facilities, requires periodical maintenance and cost of maintenance is also high. So the thesis starts with the literature review on mechanical energy harvesters such as TENG, PENG and hybrid systems with good output performance. By the successful development of these mechanical energy harvesters with good electrical performance, the thesis shows the potential to use them as a power source alternative to battery. This thesis also shows that the energy harvesters are used as self-powered or zero-power consuming sensors. In this regard, bio-polymer material collagen was investigated for its energy harvesting performance and a dual perovskite solid system, $(1-x)$ $K_{0.5}Na_{0.5}NbO_3$- x $BaTiO_3$ designated as [KNN-BTO], where $x = 0$, 0.02, 0.04, 0.06 and 0.08 was developed and studied its piezoelectric performance. Further to improve the output of the device a hybrid generator made of TENG-PENG and TENG-EMG components was designed and the devices were used for scavenging waste mechanical energy, humidity sensor, intruder identification system, sleep monitoring system and seismic detection.

제주대학교 중앙도서관
JEJU NATIONAL UNIVERSITY LIBRARY
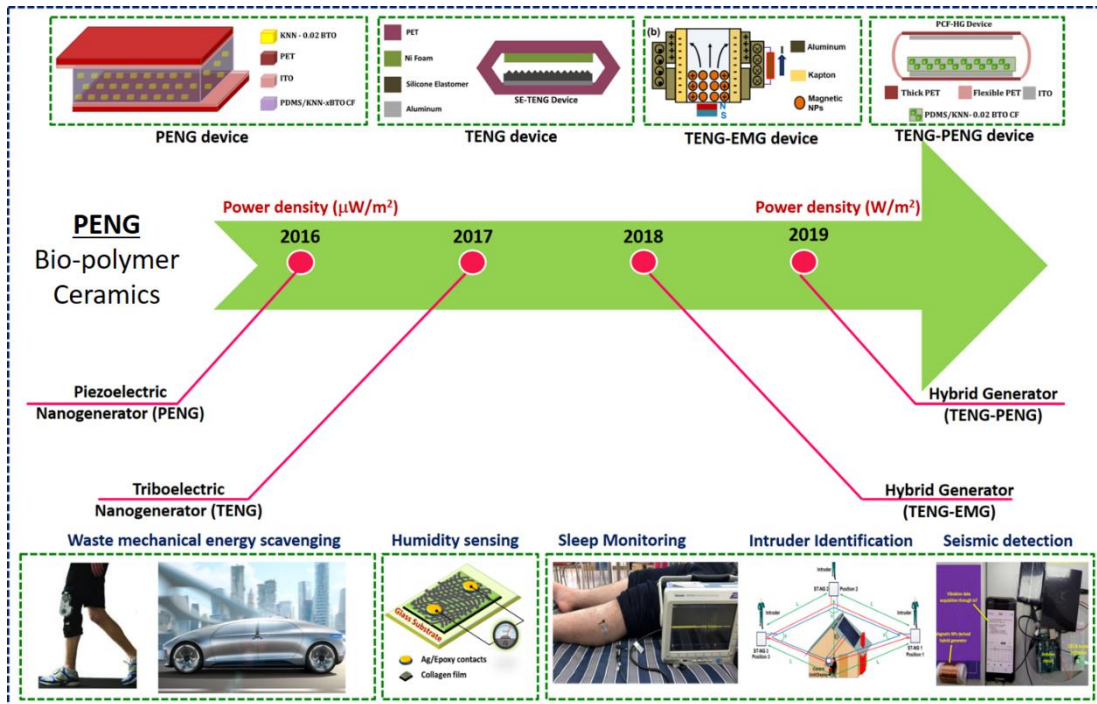
Figure 1.7 Overview, objective and scope of this thesis

➢ To prepare a highly crystalline $K_{0.5}Na_{0.5}NbO_3$, $BaTiO_3$ and KNN-BTO material for using a cost-effective solid-state reaction technique.

➢ The synthesized material is then blended with polydimethylsiloxane (PDMS) and polyvinylidine fluoride (PVDF) to make as a composite film (CF). The composite film is then attached with electrodes on either side to make it as a PNG device.

➢ The crystallinity, phase purity and morphology are analyzed using X-ray diffraction (XRD), Raman spectroscopy, X-ray photoelectron spectroscopy (XPS) and field emission scanning electron microscopy (FE-SEM) analysis.

➢ PNG devices were fabricated with various configurations such s Al/CF/AL, ITO/CF/Al, ITO/CF/ITO and used for scavenging mechanical energy and also used as a self-powered sensor.

➢ Next, TENG device was fabricated with Nickel (Ni) electrode as positive triboelectric layer and silicone elastomer as negative triboelectric layer, housed inside a PET layers with an air gap of 1 cm.

제주대학교 중앙도서관
JEJU NATIONAL UNIVERSITY LIBRARY

- The device is then packed with a polymeric pouch to protect the layers from humidity and moisture. The humidity reduces the electrical output performance of the nanogenerator device.

- The device is tested for its humidity resistance capability and used as a self-powered pressure sensor.

- After the individual TENG and PENG device fabrication, a TENG-PENG hybrid device is fabricated by using PDMS/KNN-BTO composite film as negative layer and ITO as positive layer with the air gap of 1 cm.

- The device is then studied for its energy harvesting mechanism and been used for powering up low power electronic devices such as charging a commercial capacitor, wrist watch, hygrometer and a set of 60 green LEDs.

- Then a TENG-EMG hybrid device was fabricated with Kapton and paper as triboelectric layers in which the paper slides over Kapton generating triboelectric potential. The magnet slides along with the paper inside the tube which is wound by copper coil activates the EMG component. The device is used for scavenging bio-mechanical energy by human walking, running and bending motions.

- In a similar fashion, for the first time a TENG-EMG hybrid device was fabricated with magnetic nanoparticles (Fe_2O_3), in which the particle slides on the Kapton sheet placed inside the device creating the TENG output and also the magnetic particles move inside the copper coil activating the EMG component.

- This device is then used for zero-power consuming seismic detection, and energy harvesting from vibrations.

1.7   References

1.   Service, R. F., Nanogenerators Tap Waste Energy To Power Ultrasmall Electronics. *Science* **2010,** *328* (5976), 304-305.

2.   Yao, C.; Hernandez, A.; Yu, Y.; Cai, Z.; Wang, X., Triboelectric nanogenerators and power-boards from cellulose nanofibrils and recycled materials. *Nano Energy* **2016,** *30*, 103-108.

3.   Mao, Y.; Geng, D.; Liang, E.; Wang, X., Single-electrode triboelectric nanogenerator for scavenging friction energy from rolling tires. *Nano Energy* **2015,** *15*, 227-234.

4.   ITF, *Road Safety Annual Report 2016*. OECD Publishing.

5.   이춘식; 김광호; 최항철, Experiences on wind energy utilization in Korea. International seminar on environment and integrated rural energy systems.

6.   Wang, S.; Niu, S.; Yang, J.; Lin, L.; Wang, Z. L., Quantitative Measurements of Vibration Amplitude Using a Contact-Mode Freestanding Triboelectric Nanogenerator. *ACS Nano* **2014,** *8* (12), 12004-12013.

7.   Ding, R.; Liu, H.; Zhang, X.; Xiao, J.; Kishor, R.; Sun, H.; Zhu, B.; Chen, G.; Gao, F.; Feng, X.; Chen, J.; Chen, X.; Sun, X.; Zheng, Y., Flexible Piezoelectric Nanocomposite Generators Based on Formamidinium Lead Halide Perovskite Nanoparticles. *Advanced Functional Materials* **2016,** *26* (42), 7708-7716.

8.   Chandrasekhar, A.; Alluri, N. R.; Vivekananthan, V.; Purusothaman, Y.; Kim, S.-J., A sustainable freestanding biomechanical energy harvesting smart backpack as a portable-wearable power source. *Journal of Materials Chemistry C* **2017,** *5* (6), 1488-1493.

9.   Wang, S.; Lin, L.; Wang, Z. L., Triboelectric nanogenerators as self-powered active sensors. *Nano Energy* **2015,** *11*, 436-462.

10.   Zhang, Q.; Liang, Q.; Liao, Q.; Yi, F.; Zheng, X.; Ma, M.; Gao, F.; Zhang, Y., Service Behavior of Multifunctional Triboelectric Nanogenerators. *Advanced Materials* **2017,** *29* (17), 1606703-n/a.

11.   Wang, Z.; Yu, R.; Pan, C.; Li, Z.; Yang, J.; Yi, F.; Wang, Z. L., Light-induced pyroelectric effect as an effective approach for ultrafast ultraviolet nanosensing. *Nature Communications* **2015,** *6*, 8401.

12.   Yang, Y.; Guo, W.; Pradel, K. C.; Zhu, G.; Zhou, Y.; Zhang, Y.; Hu, Y.; Lin, L.; Wang, Z. L., Pyroelectric Nanogenerators for Harvesting Thermoelectric Energy. *Nano Letters* **2012,** *12* (6), 2833-2838.

CHAPTER II

Materials, Methods and Measurement Techniques

This chapter shows a detailed overview of chemicals and materials used for the synthesis of materials and also for the fabrication of energy harvesting devices such as triboelectric, piezoelectric and hybrid nanogenerators. A cost-effective solid state reaction technique is employed for the synthesis of piezoelectric materials. Further, the chapter also explains about the characterization techniques used in this research work such as FE-SEM, EDS, XRD, Raman spectroscopy, FT-IR spectroscopy, XPS, ferroelectric tester (P-E loop analysis), and electrometer.

2.1 Chemical details

The reagents and chemicals used for the synthesis of highly pure nanomaterials reported in this thesis are listed in below T**able 2.1**. All the chemicals used for the experiments are of laboratory grade and used without any further purifications.

Table 2.1 List of chemical used for the experiments

Reagents	Molecular Formula	Purity	Details
Potassium cabonate	K_2CO_3	99.5%	Dae-Jung Chemical, Korea
Sodium carbonate	Na_2CO_3	99%	Dae-Jung Chemical, Korea
Niobium pentoxide	Nb_2O_5	99.9%,	Dae-Jung Chemical, Korea
Sodium hydroxide	NaOH	-	-
Polydimethylsiloxane	$(C6H6OSi)n$	-	Dow Corning Corporation
ITO/PET	-	-	-
Al foil	-	-	-
Kapton film	-	-	-
Ethanol	CH3CH2OH	99.9%	Dae-Jung Chemical, Korea
Acetone	C3H6O	99.8%	Dae-Jung Chemical, Korea

Copper leads	Cu	-	Nilaco Corporation, Japan
Alumina crucible	Al$_2$O$_3$		
Silver paste	Ag	-	Dupont, 4922N
Polyvinylidene difluoride	-(C2H2F2)n-		Alfa Aesar
Antistatic tape	-	-	-
Flexible PET sheet	-	-	-

The apparatus used to synthesis the nanomaterials and fabricate the piezoelectric nanogenerator, triboelectric nanogenerator, electromagnetic generator and hybrid generators are listed in below **table 2.2**.

Table 2.2 List of apparatus used in this work

Apparatus	Model	Supplier
Oven	OF-02-GW	JIEO Tech
Magnetic stirrer and hot plate	MS300HS	M TOPS
Muffle furnace	CRF-M15	Ceber
Spin coater	SPIN 1200	Midas Syste,
Tubular furnace	-	Korea Furnace Development Co.Ltd
Bath sonicator	SONIC VCX 500 model	-

	(20 kHz, 500 W)	
Centrifuge	Gyrozen 580 MG	Gyrozen
Multimeter	73303	Yokogawa
Thermal evaporator	JEE-4X	JEOL

2.2 Synthesis methodology

The present thesis involves synthesis of materials for the development of nanogenerator devices. Solid state reaction and sonochemical method are predominantly used here.

2.2.1 Solid state reaction (SSR)

The solid state reaction is the most widely used synthesis methods for the preparation of polycrystalline solids. This method involves a high temperature reaction ranging between 1000 °C to 1500 °C. This synthesis technique does not involve any solvent and can be used to react with solid materials. This technique is highly used for synthesizing polycrystalline materials and can also be used for the preparation of organic materials also. The reaction involves various processes such as nucleation and diffusion to obtain the final product. In the present work synthesis of KNN, BTO and KNN-BTO materials were synthesized by this SSR method.

2.2.2 Sonochemical method

Sonochemical synthesis is the process which utilizes the principles of sonochemistry to make molecules undergo a chemical reaction with the application of powerful ultrasound radiation (20 kHz–10 MHz). Sonochemistry generates hot spots that can achieve very high temperatures (5000–25.000 K), pressures of more than 1000 atmospheres, and rates of heating and cooling that can exceed 10^{11} K/s. High

17

intensity ultrasound produces chemical and physical effects that can be used for the production or modification of a wide range of nanostructured materials. In the present thesis, sonochemical method is involved in the synthesis of PVDF films and PVDF/KNN-BTO composite films.

2.3 Measurement techniques and specifications

The synthesized material undergoes characterization for the phase formation, morphology and its functional groups. The detailed characterization instruments and their specifications are given below.

2.3.1 Field emission scanning electron microscope (FE-SEM)

FE-SEM is used to visualize the very small topographical details of the material or its surface. The visualization can be done with the beam of electrons with high electric field focusing on the materials. As a result, secondary electrons are emitted and it is detected by a detector, which is then transformed into an image. The synthesized materials and composite films in this research work were analyzed using a FE-SEM TESCAN MIRA 3 with an accelerated maximum voltage of 30 kV. Before the measurement of non-conducting samples, a platinum coating has to be done to avoid charging of samples due to accumulation of electrons.

2.3.2 Energy dispersive x-ray spectroscopy

This technique is used along with the FE-SEM, in which an EDAX detector detects the scattered electron and analyzed its chemical composition by a mapping process showing various elements in the synthesized material. The EDAX used is Bruker Nano.

2.3.3 X-ray diffraction (XRD)

This technique is used for determining the atomic and molecular structure of the crystal in which the crystalline structures causes the beam of incident x-rays to diffract into

many specific diffractions. The instrument used in this thesis work is XRD, Rigaku with Cu-Kα radiation (λ = 1.5406 Å) 2θ range from 20° to 80°operated Room temperature having an applied power supply of 40 kV and 40 mA.

2.3.4 Raman spectroscopy

Raman spectroscopic technique is a vibrational spectroscopic analysis technique, in which the analysis is based on the inelastic scattering of the monochromatic light. This technique analyses the chemical structure, molecular vibration, phase and intrinsic stress/strain of the material. The Raman analysis were carried out in the range of 100-1000 cm-1 with an excitation wave length of 514 nm using a high throughput micro Raman spectroscopy, Horiba, LabRam HR evaluation.

2.3.5 X-ray photoelectron spectroscopy (XPS)

XPS is a surface analysis technique providing valuable and quantitative chemical information. It is also called as electron spectroscopy for chemical analysis. It is useful to analyze the oxidation state, electronic structure and elemental composition in a material. This study uses an instrument XPS (XPS, ESCA-2000, VG Microtech Ltd.) at a high-flux X-ray source at 1486.6 eV (Al anode) with an applied source of 14 kV.

2.3.6 Fourier transform infrared spectroscopy (FT-IR)

This spectroscopy reveals about the functional groups and vibrational bending and stretching of the material. The carbonyl and amide groups present in the collagen film was confirmed using Fourier transform infrared spectroscopy in ATR mode. The present thesis uses FT-IR in the range of 400 to 4000 cm^{-1} using FT-IR, Thermo Scientific Nicolet- 6700.

2.3.7 Ferroelectric hysteresis tester (P-E loop analysis)

The measurements such as remnant polarization, saturation polarization, coercive field, leakage current and driving voltage are analyzed by a PE-loop hysteresis measurement. The behavior of the obtained P-E loop describes the ferroelectric polarization of the materials possessing the ferroelectric, resistance or capacitance. The piezoelectric materials used in this thesis are analyzed using a ferroelectric tester, Radiant technologies with fast hysteresis frequency rating of 250 KHz at +/-10 V built-in to the system.

2.3.8 Transmission electron microscopy (TEM)

TEM is a technique that uses an electron beam to image a nanoparticle sample, providing much higher resolution than is possible with light-based imaging techniques. **TEM** is the preferred method to directly measure nanoparticle size, grain size, size distribution, and morphology. The instrument used for the present thesis is TEM, JEM-2011, JEOL for analyzing the morphology and structure of iron oxide nanoparticles.

2.4 Device fabrication techniques

The present thesis involves fabrication of various energy harvesting devices such as PNG, TENG and EMG. Along with the energy harvesting devices, self-powered sensors were also fabricated based on the materials used for the fabrication of energy harvesters. The device fabrication process differs according to the type of the device.

2.4.1 Piezoelectric nanogenerator (PNG)

The mechanical energy harvesting capability of the synthesized piezoelectric nanomaterial can be determined by configuring it as a piezoelectric nanogenerator. The synthesized piezoelectric nanomaterials such as KNN, BTO and KNN-BTO are mixed

제주대학교 중앙도서관
JEJU NATIONAL UNIVERSITY LIBRARY

with the polymers such as polydimethylsiloxane (PDMS) and polyvinylidine fluoride (PVDF) to make it as a piezoelectric composite film. The composite film is then attached with electrodes on either side to make it as an energy harvesting device. Copper wires are then attached on the electrodes for making electrical connections. The device is then packed with polymers such as PDMS, Kapton or PET for mechanical protection.

2.4.2 Triboelectric nanogenerator (TENG)

The two triboelectric layers can be used for scavenging frictional energy by the arrangement of contact separation, sliding, free standing and single electrode mode of triboelectric nanogenerators. The layers are housed into a proper housing and by applying mechanical energy to the device, leading to the generation of electrical output. The works demonstrated in the present thesis has the TENG device works on contact-separation mode and sliding modes.

2.4.3 Electromagnetic generator (EMG)

The electromagnetic generator is the oldest electric generator made by following the Faraday's law of electromagnetic induction principle. The core of the device is a plastic tube wound with copper coils on the outer side and the inner wall of the tube is attached with Kapton film coated with gold. A magnet is placed inside the tube with the sliding of magnet over Kapton activates the TENG components and the same siding mode inside the coil activates the TEMG components. The EMG reported in the present thesis is a hybrid generator composed of TENG and EMG components.

2.4.4 Hybrid generator

Hybrid generator is a type of energy harvester which combines two or more energy harvesters in a single unit. There are more reposts on combining triboelectric,

21

piezoelectric, electromagnetic, pyroelectric, thermoelectric and photovoltaic effects to make as a hybrid generator device. The present thesis has a part demonstrating the hybrid energy harvesters made of TENG-PENG combinations and TENG-EMG combinations.

2.5 Electrical characterizations

The energy harvesting devices highly requires electrical measurements for analyzing its energy harvesting performances. The electrical analysis such as voltage, current, power, power density, energy stored in capacitor are highly required for predicting the efficiency of energy harvesting devices.

2.5.1 Electrical output measurements

The electrical output of the device made in the thesis was measured by applying a suitable mechanical force on the device. The mechanical force is applied with the help of a linear motor (LinMot-HF01-37) operated with variable acceleration which is controlled with LabVIEW software. The instruments used for recording the electrical output are Electrometer (Keithley 6514), picoammeter (Keithley 6485), nanovoltmeter (Keithley 2184) and low noise current pre-amplifier (Stanford SR 570).

2.5.2 Semiconductor analyzer

The I-V characteristics of the sensor developed using collagen material were analyzed using a frequency variable CV-IV system (Agilent-B1500A). The measurement was carried out with the voltage window of ± 10 V with the varying percentages of relative humidity.

2.6 Calculation of electrical parameters

The electrical parameters used for determining the performance of the energy harvester and sensor are discussed here with the corresponding equations[1-5].

2.6.1 Power density

The power density of the TENG, PENG and hybrid devices was calculated using the following equation:

$$P_A = \frac{V^2}{R \times A}$$

where R is the load resistance across the NG, A is the surface area and V is the electrical output voltage obtained.

2.6.2 Spontaneous polarization

The electromechanical response of the PNG device was analyzed using the spontaneous polarization (P_s), obtained.

The following equation was used for determining the P_s

$$d_{33} = 2Q_{eff}.\varepsilon_0.\varepsilon_r.P_s$$

where Q_{eff} is the effective electrostriction coefficient, piezoelectric coefficient (d_{33}), ε_0 is the permittivity of free space and ε_r is the relative permittivity.

2.6.4 EMG output

The electrical output voltage and current from the EMG component could be calculated using the Faraday's law as follows

$$V_{EMG} = -N\frac{d\Phi_B}{dt}$$

$$I_{EMG} = \frac{V_{OC}}{R}$$

Where Φ_B the magnetic flux in each coil, N is the number of turns and B is the magnetic field.

2.6.5 TENG output

The voltage and current output of TENG was measured using an electrometer, which can be expressed via equations as follows

$$V_{TENG} = \frac{\sigma S}{C}$$

$$I_{TENG} = S\frac{dQ_{SC}}{dt}$$

Where C is the capacitance between the electrodes, S is the contact area, σ is the surface charge density of the iron oxide particle.

2.7 References

1.   Vivekananthan, V.; Alluri, N. R.; Chandrasekhar, A.; Purusothaman, Y.; Gupta, A.; Kim, S.-J., Zero-power consuming intruder identification system by enhanced piezoelectricity of K0.5Na0.5NbO3 using substitutional doping of BTO NPs. *Journal of Materials Chemistry C* **2019**.

2.   Kim, D.; Jin, I. K.; Choi, Y.-K., Ferromagnetic nanoparticle-embedded hybrid nanogenerator for harvesting omnidirectional vibration energy. *Nanoscale* **2018,** *10* (26), 12276-12283.

3.   Seol, M.-L.; Jeon, S.-B.; Han, J.-W.; Choi, Y.-K., Ferrofluid-based triboelectric-electromagnetic hybrid generator for sensitive and sustainable vibration energy harvesting. *Nano Energy* **2017,** *31*, 233-238.

4.   Whiter, R. A.; Narayan, V.; Kar-Narayan, S., A Scalable Nanogenerator Based on Self-Poled Piezoelectric Polymer Nanowires with High Energy Conversion Efficiency. *Advanced Energy Materials* **2014,** *4* (18), 1400519.

5.   Furukawa, T.; Seo, N., Electrostriction as the Origin of Piezoelectricity in Ferroelectric Polymers. *Japanese Journal of Applied Physics* **1990,** *29* (Part 1, No. 4), 675-680.

CHAPTER III

Biocompatible collagen-nanofibrils: An approach for sustainable energy harvesting and battery-free humidity sensor applications

Highlights

➢ A piezoelectric collagen-nanofibrils (PCNF) biopolymer deposited on a cotton fabric has been developed for the first time.

➢ The material can act as an energy harvester using the piezoelectric effect and generates a maximum electrical output of 45 V/250 nA upon 5 N

➢ Three different type of fabrics were chosen with different thickness and checked for energy harvesting performance.

➢ The humidity sensor exhibits a linear I-V and I-T response with an excellent sensitivity of 0.1287 μA/ % RH and a correlation coefficient of 0.99554.

Graphical Outline
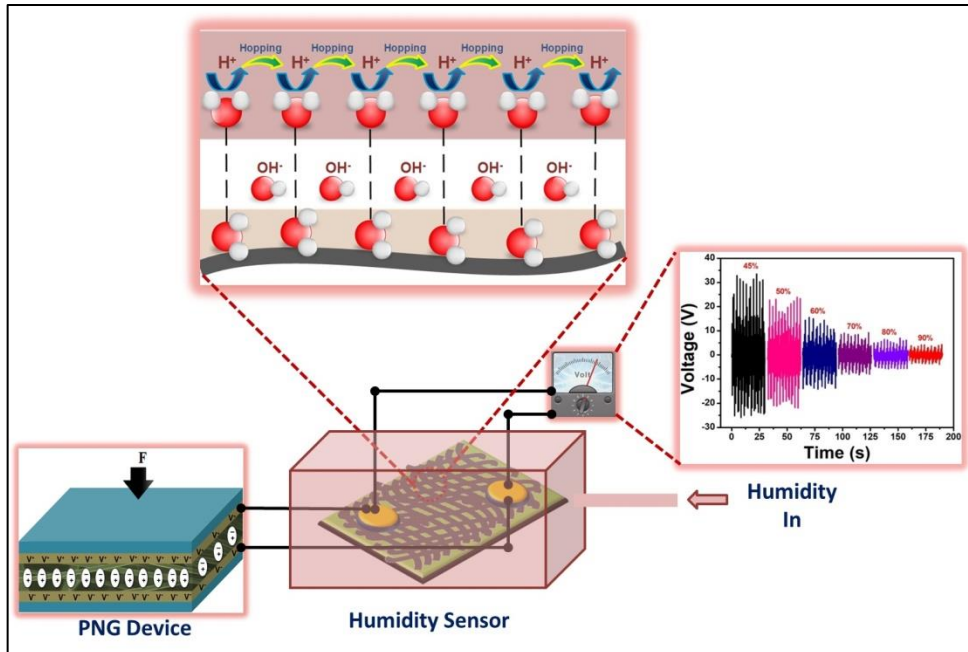
3.1 Introduction

Developing a sustainable, eco-friendly and bio-compatible material in the field of sensors and energy harvesting is still a major challenge. Many researchers have developed several organic and inorganic materials in this field[1-2], but they are limited due to its toxicity, bio-degradability and environmental issues. Nowadays fabricating a piezoelectric nanogenerator for self-powered systems is multiplying for a wide variety of applications ranging from sensors to electronics and medical to environmental[3-5]. Till date, many reports are available on fabricating a piezoelectric nanogenerator (PNG) by a wide range of materials such as zinc oxide (ZnO)[6], barium titanate (BaTiO$_3$)[7], polyvinylidene fluoride (PVDF)[8] and its copolymers[9], lead managanese niobium titanate (PMN-PT)[10], lead zirconate titanate (PZT)[11], potassium sodium niobate (KNN)[12], and zinc stannate (ZnSnO$_3$)[13]. However, to provide an eco-friendly self-powered system is still a challenge because during in vivo conditions a very low toxicity even can harm the life of a human. To overcome these issues, researchers focus towards greener materials such as multifunctional biopolymers[14-15]. Bio-polymers are polymeric biomolecules which can beextracted from the living organisms. They are abundant in all kinds of plants, animals, human body and even in the cells of many living organisms[16]. These biopolymers are biologically degradable as their molecular compositions are oxygen and nitrogen since they can be degraded naturally by different biological processes. Because of its high bio-degradability[17-19] and bio-compatibility[20], many researchers were attracted towards investigating biopolymers for various applications ranging from drug delivery systems[21], tissue engineering[22], wound healing[23], medical implants[24-25], biosensors[26-27], and energy harvesting[28]. Recently bio-polymers such as cellulose[29], collagen[30], gelatin[14], and

chitosan[31] have attracted many scientists due to its compatibility with the environment and human life. Among the various other bio-polymers collagen has attracted interests among the researchers globally due to its chemical and physical properties such as extensibility, high tensile strength, swelling, solubility in water, contraction on heating, high affinity with water and its piezoelectric coefficient (8 pC/N)[32-33]. Very recently many collagen-based products are approved by the U.S food and drug administration (FDA) for commercial as well as clinical use. The collagen used here is deposited on cotton fibers in which the collagen gets adsorbed on the fibers. By having a fibrous substrate the device has a wide variety of advantages such as highly flexible, cost-effective and less brittle in nature. These types of fabric based substrates were successively utilized for sensors[34] and supercapacitors[35].

On the other hand, a vast demand arises for humidity sensors (HS) with excellent sensitivity, selectivity, cost-effective and high feasibility towards its usage in day to day life. These sensors are mandatory in applications with the controlled humid environment such as clean rooms, smelting furnaces, medical air pipelines, and engine test beds. Humidity sensor holds a market revenue breakdown of 4.2% (a report by Frost & Sullivan market research 2015) which is higher than many other sensors. Till now the existing humidity sensors are developed based on various detection techniques such as contact electrification[36], electrochemical-based[37], photoluminescence based[38], field effect transistor (FET)[39] based as well as self-powered[40] using semiconductor materials[41]. Many reports on humidity sensors were available with metal oxides (ceramic based[42], perovskite-based[43], organic/inorganic hybrid based[44-45]) and polymer (cellulose acetate butyrate (CAB)[46], poly(methyl methacrylate) (PMMA)[47], polyethylene terephthalate (PET)[48], polyphthalamide (PPA)[49]) based, but these are not

eco-friendly and biocompatible. In order to overcome these issues and to make it as a sustainable sensor, a biopolymer material is highly required.

3.2 Experimental section

3.2.1 Fabrication of BP-NG device

Herein, a simple fabrication method is adopted by utilizing a commercially available collagen deposited cotton fabric (MATRIX, collagen velvet, Germany) with three different thicknesses ranging 372 μm, 500 μm and 1.2mm which acts as a piezoelectric material (3 cm × 3 cm). Further, the collagen-cotton fabric was freeze dried and Al foil (thickness ≈ 10 μm) was attached to both the sides of collagen sheet, and external connections are made by the attachment of copper wire on the Al foil using silver paste. Finally, polypropylene (PP) film (thickness of ≈125 μm) was used to laminate the device which intends as a protecting layer of the device from external factors such as mechanical stress, dust and humidity.

3.2.2 Fabrication of collagen-based humidity sensor

The collagen film (3 cm × 3 cm) is attached on to a clean glass slide, and two silver electrodes were attached to the collagen film. Diagonal contacts were made using a silver paste, and electrical connections were made using copper wires. An epoxy layer was coated on the electrodes to avoid the interaction between silver and water vapors (humidity)

3.2.3 Measurement systems

The crystalline structure of polypeptide chains present in collagen was characterized by X-ray diffractometer (XRD, Rigaku) with Cu-Kα radiation ($\lambda = 1.5406$ Å) with a 2θ range from 5 ° to 35 °, operating under room temperature with an applied power of 40 kV and 40 mA. The carbonyl and amide groups present in the collagen film was

confirmed using Fourier transform infrared spectroscopy in ATR mode (FT-IR, Thermo Scientific Nicolet- 6700). The surface morphology of the three different thickness collagen films was analyzed using a field emission scanning electron microscope (FE-SEM, JSM-6700F, JEOL, Japan). The elemental composition of the material was identified using X-ray photoelectron spectroscopy (XPS, ESCA-2000, VG Microtech Ltd.) at a high-flux X-ray source at 1486.6 eV (Al anode) with an applied source of 14 kV. Finally, the electrical outputs of BP-NG were measured using an electrometer (Keithley 6514) and a picoammeter (Keithley 6485).The I-V measurements were performed using semiconductor device parameter analyzer (Agilent-B1500A) with the help of a home-made humidity chamber.

3.3 Results and discussions

3.3.1 Structural and morphological analysis of CPNG device

The present manuscript describes the fabrication of a self-powered piezoelectric bio polymer humidity sensor (SP-PB-HS) for the first time. Here, the thickness (372 μm, 500 μm and 1.2 mm) and morphology of collagen-nanofibrils (CNF) deposited on cotton cloth were evaluated based on its piezoelectric potential. The CNF deposited on a cotton fabric acts as an energy harvester as well as a sensor. I-V technique was employed to study the sensing behavior of collagen film towards a different percentage of relative humidity (% RH) at a fixed bias voltage. Further to demonstrate its self-powered sensing capability a parallel electrical connection is established between the sensor device and collagen piezoelectric nanogenerator (CPNG) device. The PNG device was made by attaching two Aluminum (Al) electrodes on the top and bottom side of the collagen film (3 cm × 3 cm) and laminated using a polypropylene (PP) film, which is explained briefly in supporting information.

31

The generated piezoelectric potential from the CPNG is used to drive the CNF based HS. The experiments and results show that bio-polymer based sensors and energy harvesting devices are capable materials which pave the way for future in the field of self-powered sensors, implantable devices, and other medical applications.
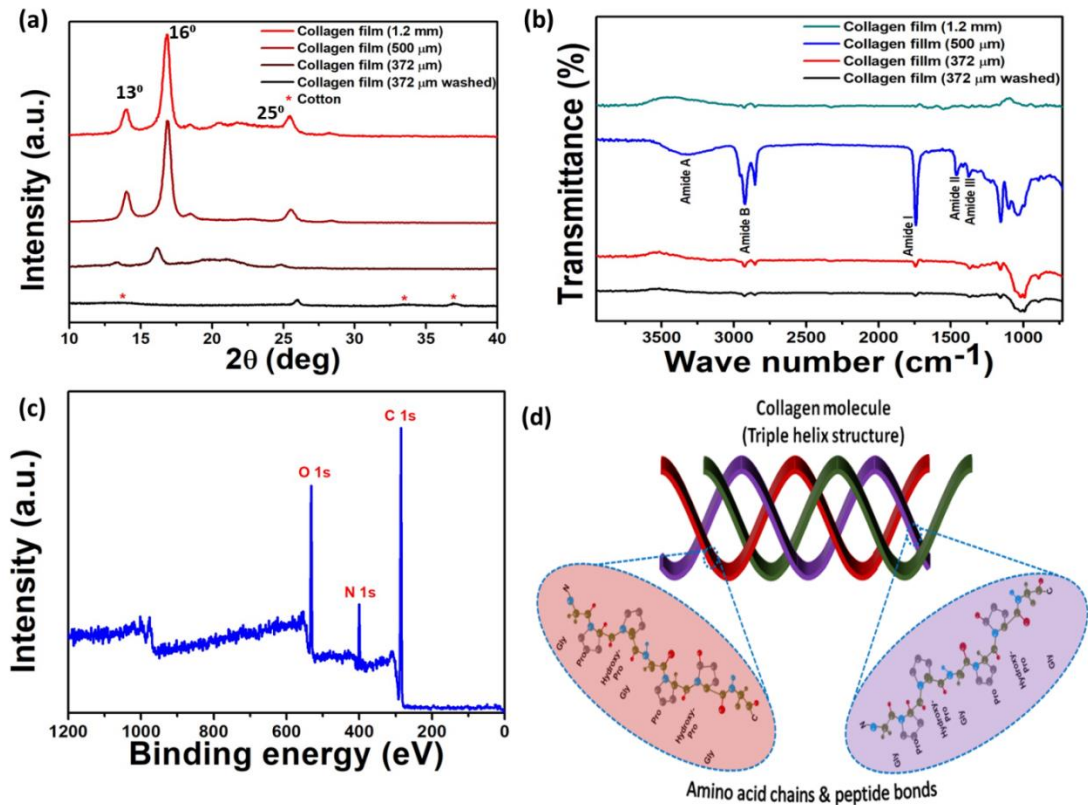
Figure 3.1 Structural analysis of collagen-cotton film. (a) XRD analysis of different thickness collagen film confirms the presence of collagen with respect to the different cotton fiber (b) FT-IR spectroscopy analysis showing the presence of various functional groups in the collagen-cotton film (c) XPS spectroscopy showing the elemental analysis of collagen (d) Tri-peptide chain of collagen nano-fibrils showing various amino acid sequences.

Figure 3.1a shows the XRD pattern of the three different thickness collagen films along with a washed film, in which the CNF content was removed from the fabric by washing it several times with deionized water. The peak rising at 13 ° at 2θ denotes

the lateral intermolecular packing of CNF. The sharp peak at 16 ° corresponds to pure crystalline collagen.[50] The deconvoluted peak at 25 ° corresponds to the triple helix structure of CNF. The triple helix structure of CNF consists of a different sequence of unusual amino acids (glycine, proline and hydroxyproline) and its compositions as shown in Figure3.1d, whereas the polypeptide chains of amino acid were confirmed by Raman spectroscopy as shown in Figure 3.1b. The presence of carbonyl group was confirmed by the rise in 1661 cm^{-1} which is due to the stretching of Amide I group ((C = O) Gly-X-Y tripeptide sequence). A vibrational band arises at 1278 cm^{-1} is due to the deformation in its in-plane structure describing to amide III band (C − N). The polar triple helix structure would be identified from the band which ascribes to C − N stretching mode. Additional bands such as 1090 cm^{-1} (glutamic acid), 948 cm^{-1} (Proline), 864 cm^{-1} (hydroxyproline) shows weak scattering due to its saturated side chainrings. There are few Raman inactive sights which could be confirmed by FT-IR spectroscopy as shown in Figure 3.1b. The amide II band in the CNF was examined from the peak arises at 1466 cm^{-1}. Similarly, the bands rising at 3348 cm^{-1} (Amide A) and 3010 cm^{-1} (Amide B) correspond to N − H stretching and C − H stretching respectively. Hence, all the peaks from Raman and FT-IR spectroscopy directly correspond to the presence of triple helix structure in the CNF along with its tripeptide sequence (Gly-Pro-Y and Gly-X-Hyp). The X-ray photoelectron spectroscopy analysis was performed to characterize the elemental composition of the CNF as shown in Figure 3.1c. The samples contain signals for the elements O1s, N1s and C1s. These elements constitute chemically along with hydrogen to form collagen. The spectra obey Guass-Lorentz repartition as they contain the expanded peaks. At 284 eV a single bond is formed between two carbon atoms (C - C) which correspond to the peak C1s.

33

The peak of N1s corresponds to C = N and N – H bond at 399.8 eV and 398.6 eV correspondingly.
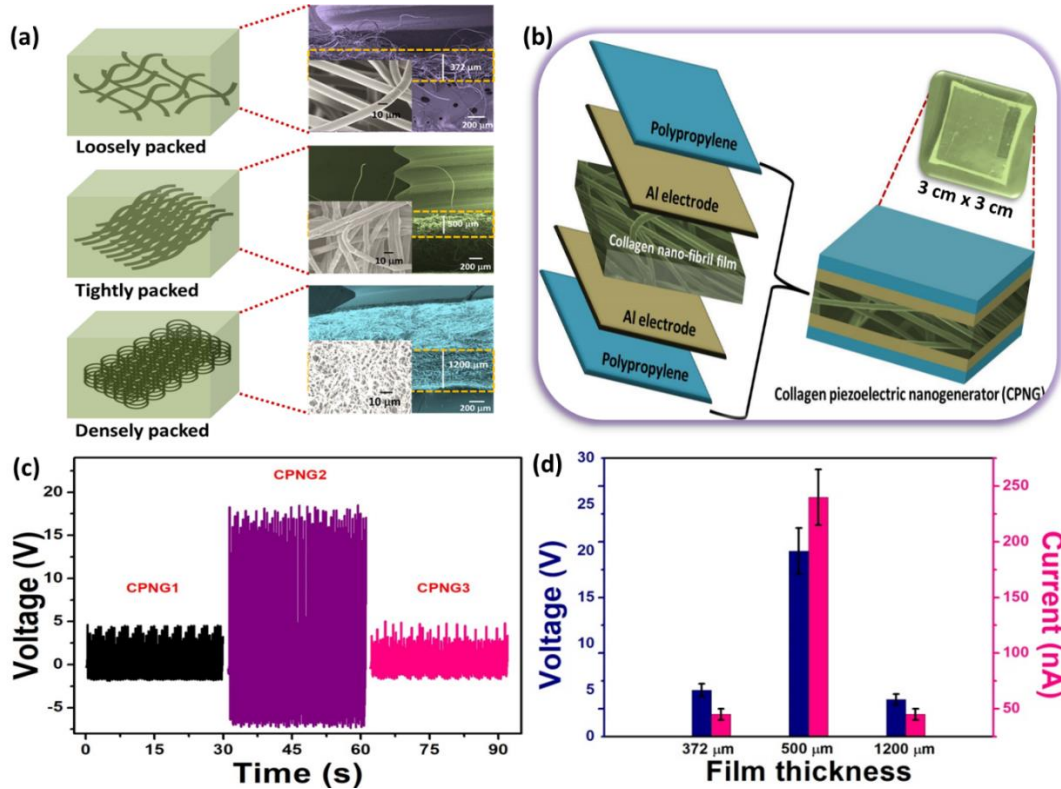
Figure 3.2 Surface morphology of CNF and electrical response of CPNG. (a) The schematic shows the different packing structure of CNF deposited cotton fabric and its corresponding surface morphology analyzed by FE-SEM (200 μm) and the inset at a scale of (10 μm) (b) Layer by layer schematic arrangement of CPNG device (c) Voltage response of CPNG devices under a mechanical force of 5 N and (d) Cumulative voltage and current response of CPNG devices with an error of 10% with different thickness (372 μm, 500 μm and 1.2 mm).

Figure 3.2a shows the surface morphology and thickness of the CNF deposited cotton fabric had been confirmed by field emission scanning electron microscopy. The CNF deposited fabric exhibits loosely, tightly and densely packed nanofibrils for 372 μm, 500 μm and 1.2 mm. Figure 3.2b shows the schematic of PNG devices fabricated by using the collagen films as the active material with the device dimension of 3 cm × 3 cm. Al foil was used as an electrode which was attached on either side of the films.

Initially, the obtained $V_{OC\ (p-p)}$ and $I_{SC\ (p-p)}$ of 372 μm thick collagen PNG device (CPNG1) was ≈ 8 V and ≈ 50 nA under a constant mechanical force of 5 N with the help of a linear motor as shown in Figure 3.2c. Further, the other two devices, such as 500 μm (CPNG2) and 1.2 mm (CPNG3) were fabricated and resulted in an electrical response under the same mechanical force as shown in figure 3.2c and d.

The electrical output reaches a maximum of V_{OC}≈ 30V and I_{SC}≈ 250 nA for CPNG2. The CPNG3 device shows a lower output compared to CPNG2 (the comparison in V_{OC} and I_{SC} is shown in figure 3.2d.This output behavior clearly indicates that the increase in thickness of the cotton fabric leads to improper deposition of CNF, which directly affects the piezoelectric response. Also the less electrical output in CPNG1 and CPNG3 is due to the improper distribution of collagen nano-fibrils into the cotton fabric. This type of non-uniformity can cause poor orientation of the electrical dipoles and weak inductive charges. As a result of this a small number of dipoles orient on the film which is not in a proper direction which leads to a weak piezoelectric response of the CPNG1 and CPNG3 device. The electrical response from the CPNG2 device was validated by performing a switching polarity test. The generated electrical output from the device is confirmed by the observed phase shift by forward and reverse connections. This confirms the output is not from any external sources and it is purely from the device.
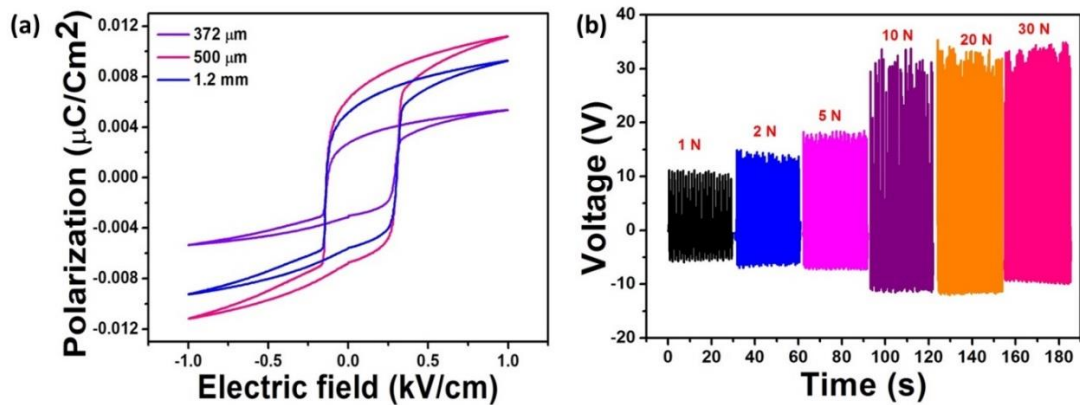
Figure 3.3 Hysteresis measurement and force analysis. (a)Hysteresis measurement of different thickness CNF deposited cotton fabric at room temperature with an operating frequency of 200 ms. (b) Force analysis of CPNG device and its corresponding voltage response upon different compressive force ranging 1 N, 2 N, 5 N, 10 N, 20 N and 30 N.

Whenever a compressive force acts on the top surface of the CPNG1 in a perpendicular direction, the dipoles orient in an aligned manner leading towards the potential difference between the electrodes. Hence, the electron flow starts from the top electrode to the bottom electrode through an external circuit (ii) When the compressive force gets removed from the device, the direction of the electric dipoles changes and the electron flow from bottom to top electrodes (iii) The 500 μm collagen film shows a maximum saturated polarization of $\approx$ 0.0112 μC/cm^2 (at 1 kV/cm), whereas the other films show less polarization as shown in Figure 3.3a. The electrical response of CPNG device upon different compressive force (1, 2, 5, 10, 20 and 30 N) is shown in Figure 3.3b. The magnitude of the output response varies with an increase in mechanical force, which is observed from 1 N to 10 N. With further increase in the load the electrical response get stabilized. This shows that the CPNG has a good electrical output response at 10 N load and the same load is preferred for further studies.

3.3.2 Capacitors charging-discharging, Load resistance analysis and stability test of CPNG device

Figure 3.4a shows the charging behaviour of various commercial capacitors (47 nF, 0.22 µF, and 47 µF) using the CPNG device electrical output and the calculated energy stored $E = \frac{1}{2}CV^2$, where C is the capacitance) for a period of 200 s. When the capacitor rating increases from 47 nF to 47 µF the amount of energy stored in the capacitor decreases from 18 µJ to 1 µJ respectively. The charging and discharging behaviour of the 0.22 µF capacitor with multiple cycles are shown in figure 3.4b.Instantaneous power density calculation, load resistance analysis, charging/discharging and energy storage analysis of commercial capacitors and stability test of CPNG was performedin order to identify the impedance matching and proper usage of CPNG device towards real-time applications. The instantaneous area power density ($P_A = (V^2/(R \times A))$) is maximum $\approx$ 1.6 mW/m^2 at a load resistance of 1 GΩ suggesting that this is the optimum load matching resistance (R) for real-time applications as shown in figure 3.4c. The steadiness of the CPNG device was measured for a period of $\approx$ 2000 s, which suggests that the device has a continuous and stable electrical response over the period of $\approx$ 2000 seconds which is shown in figure 3.4d.This suggests that the device is suitable for utilizing towards any real-time applications and monitoring.
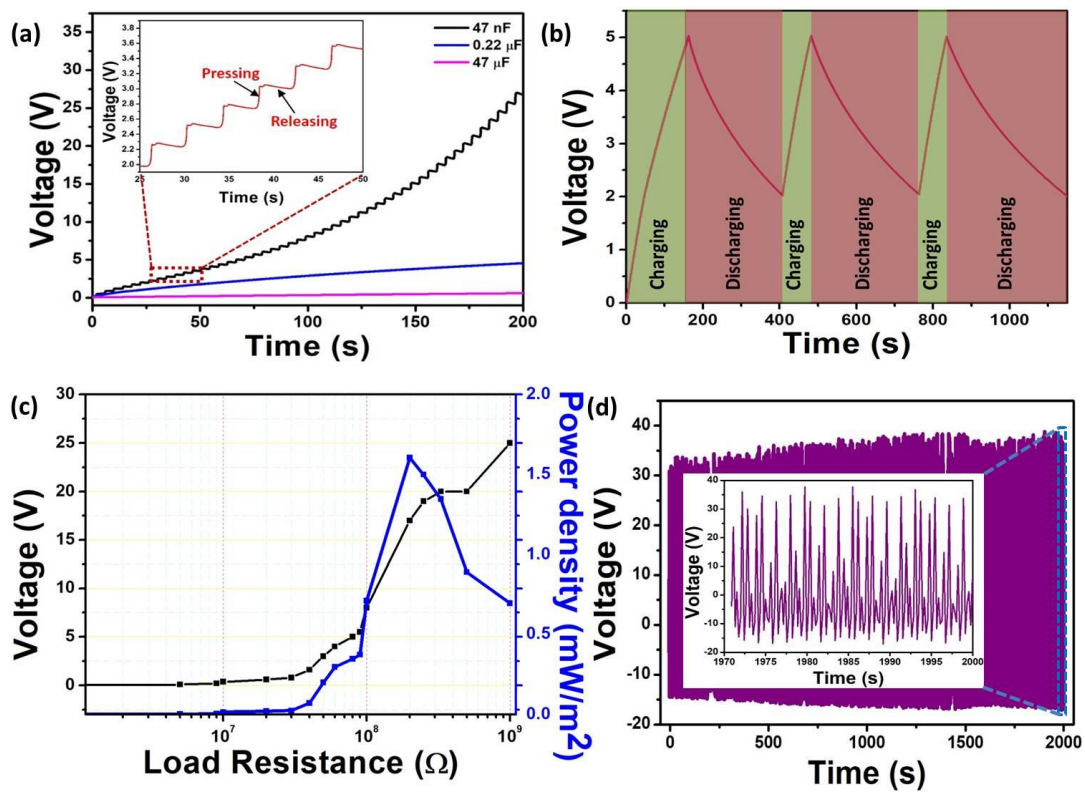
Figure 3.4: Electrical Analysis of CPNG devcice (a) commercial capacitors such as 47 nF, 0.22 µF and 47 µF shows a charging behavior for 200 seconds. (b) Charging and discharging behavior of a commercial capacitor 0.22 µF (c) Load resistance and power density analysis and (d) stability test for a period of 2000 s at 10 N.

3.3.3 I-V characteristics of Collagen film under humidity conditions

After analyzing the structural and piezoelectric property of the CNF, the affinity of CNF towards water molecule has been considered and the HS analysis is performed. The schematic of HS is shown in Figure 3.5a and the sensing experiments were performed in a homemade humidity chamber which is shown in Figure 3.5b. Initially, I-V response of the SP-PB-HS was measured without any humidity (the in-room humidity was 45 % RH). The sensor response shows an ohmic behavior (resistor) with 2.34 µA current at a bias voltage of ± 10 V. Further with the increase in humidity (50 % to 90%) the current response remarkably increases from 2.34 µA to 10.44 µA as shown in figure 3.5c.

38
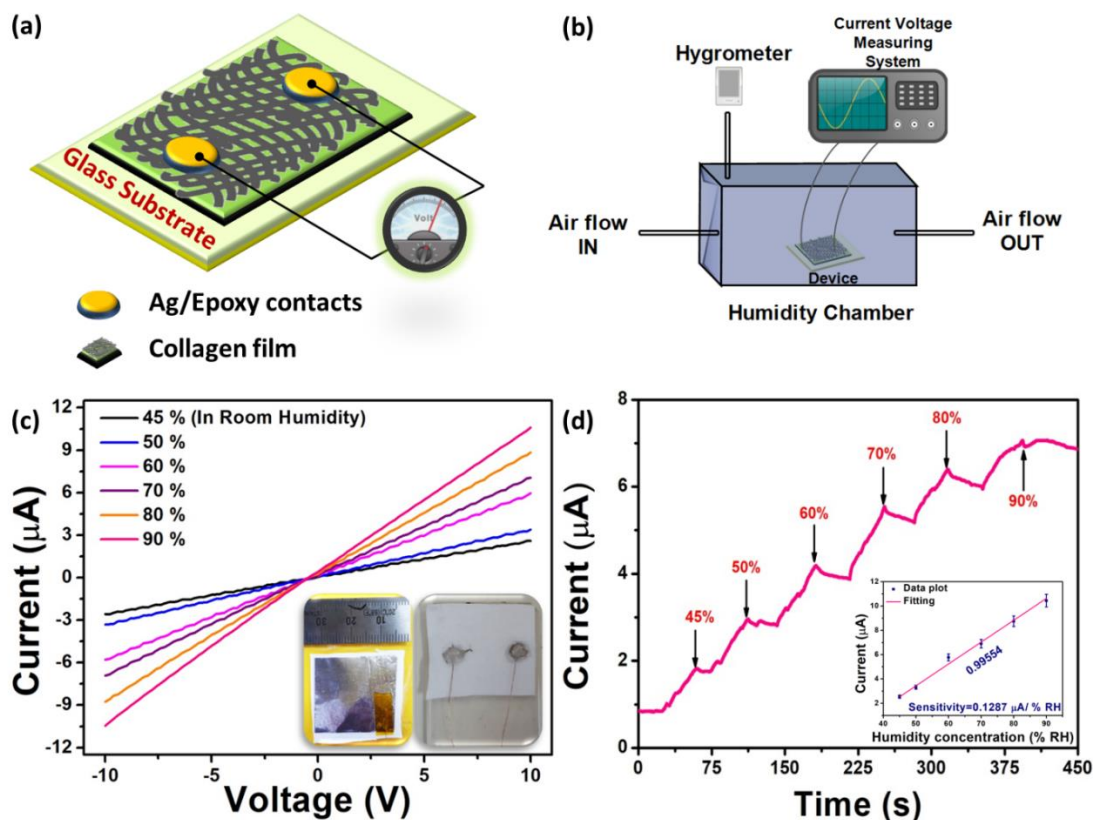
Figure 3.5 current-voltage characteristics of SP-BP-HS. (a) layer by layer schematic response of as fabricated humidity sensor (HS) (b) homemade humidity chamber for measuring the relative humidity (c) I-V response analysis of the HS with respect to different percentages of relative humidity (% RH) at a bias voltage of ± 10 V and the inset shows the digital image of device and its dimension (3 cm x 3 cm) the fabricated BP-HS device (d) current vs time (I-T) response of HS with respect to different % RH (inset shows the calibration plot with a linear behavior at ±5 % error bar and having a correlation co-efficient of 0.99554 with a sensitivity of 0.1287 µA/ % RH and resolution of 0.119 µA/ % RH).

The inset in figure 3.5c shows the as fabricated humidity sensor device. In order to estimate the sensitivity of the SP-BP-HS, the current vs time analysis (I-T analysis) was performed from in-room humidity up to maximum humidity i.e., from 45 % RH to 90 % RH at an applied bias voltage of 10 V. A linear current response was observed with increase in the % RH range (50 % to 90 % RH) as shown in figure 3.5d. The calibration plot is shown in the inset of figure 3.5d indicates the linearity between the

current and % of RH with a correlation coefficient and sensitivity in the range of 0.99554 and 0.1287 μA/ % RH. The sensitivity or resolution is a key factor for any kind of sensor, which is calculated to be 0.119 μA/ % RH as shown in Figure 3.6a and b. The same experiments were repeated for another device and showed an excellent repeatability with 5% error. From the correlation coefficient and sensitivity, it is suggested that the sensor has a linear response concerning the increase in humidity.

3.3.4 Detailed Humidity sensing mechanism

The detailed sensing mechanism is explained graphically in Figure 3.7a. The mechanism of humidity sensing is a water adsorption process in which water vapor gets chemisorbed on the surface of the collagen film or replacement of oxygen by the incoming water molecules, and so, the oxygen vacancies in the collagen film acts as an active sites to endorse the dissociation of adsorbed water molecules[51]. (i) Under low % RH a little amount of water molecules gets adsorbed on the surface to form a first chemisorbed layer ($H_2O \rightarrow H^+ + OH^-$). This leads towards a formation of an irregular layer on the surface of collagen film which hinders the free movement of H_2O molecules, and so the protons act as a conductive carrier with high energy requirement which causes the V_{OC} output to be higher at low % RH.
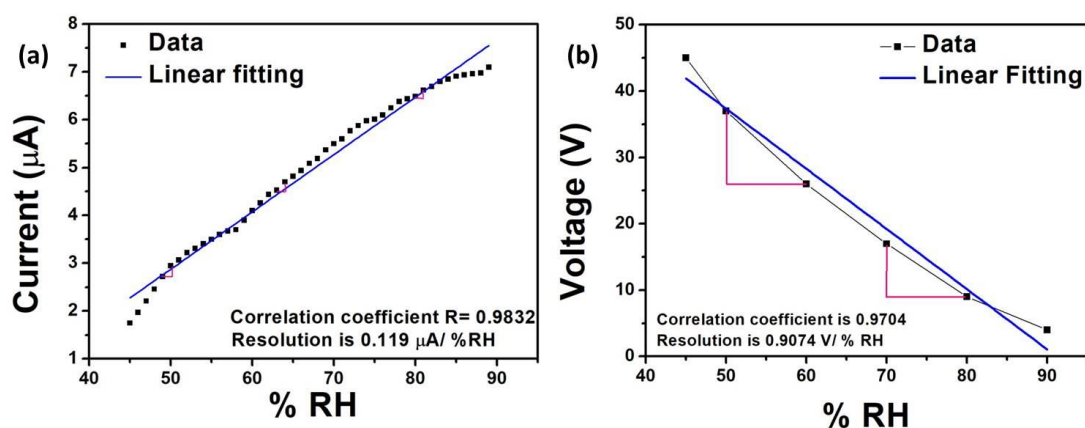
Figure 3.6: (a) The resolution of (SP-PB)-HS evaluated using the I-T analysis. The obtained resolution or sensitivity is 0.119 μA/ % RH (b) The estimated resolution of (SP-PB)-HS under constant mechanical force with respect to humidity is 0.907 V/ % RH.

As the % RH increases with the continuous flow of water vapor forms a multilayer water adsorption. Under this high % RH condition, the electric field from the CPNG1 starts to ionize the water molecules and induces to form hydronium (H_3O^+) ions as a charge carrier. Due to the high amount of water molecules accumulated a strong electrostatic field was created between the first chemisorbed layer and the incoming water molecules. (ii) Upon continuous hydration, a second physisorbed layer is formed which produces protons ($H_2O + H_2O \rightarrow H_3O^+ + OH^-$) and hopping of these protons between adjacent hydrogen ion sites in the other water molecules as per the grotthuss mechanism. Due to this physisorption process and continuous flow of water molecules through varying the humidity rate (RH%), the resistance of the HS is reduced gradually and the V_{OC} gets reduces with increase in water molecule adsorption.
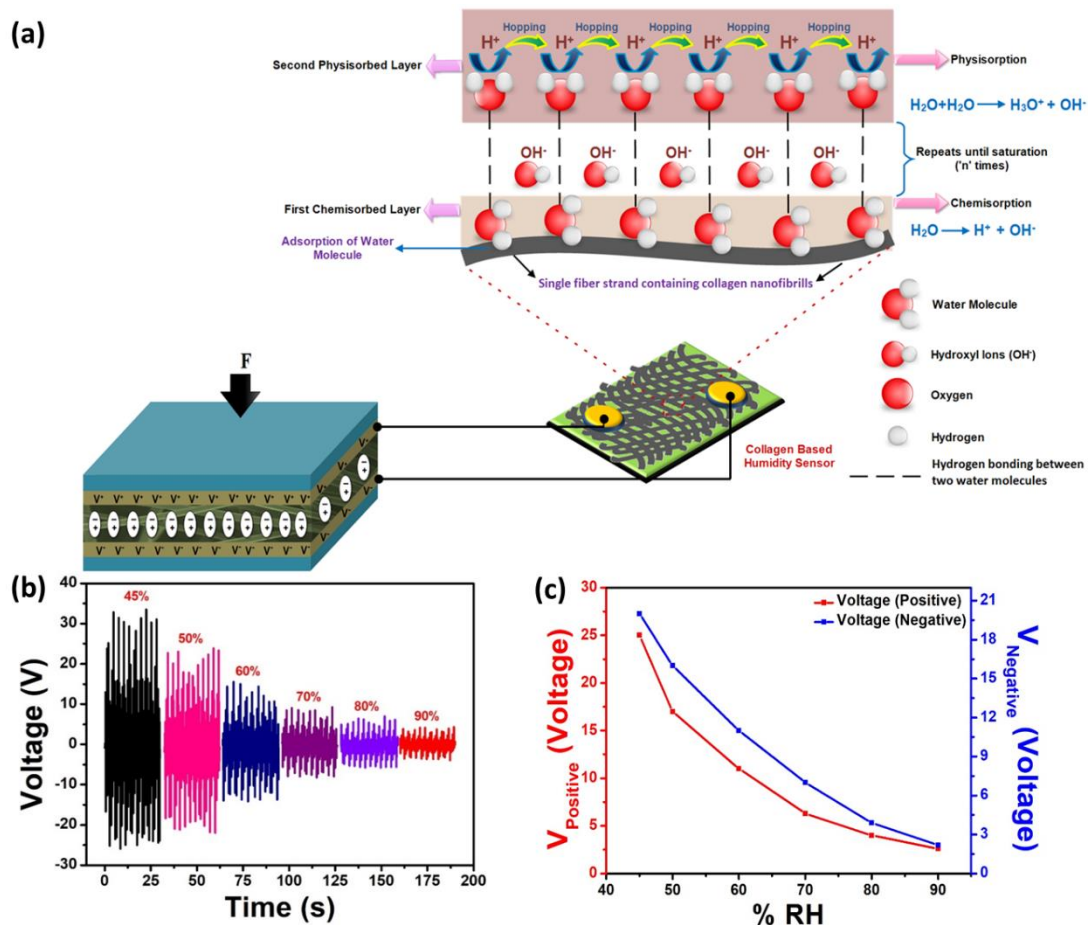
Figure 3.7 Self-powered HS mechanism. (a) A detailed humidity sensing mechanism of the SP-BP-HS device (b) self-powered humidity sensing response showing the voltage drop upon addition of different % RH(c) change in voltage response at positive and negative sides of voltage peaks and it shows a linear operating behavior.

To claim the sensing response from I-V measurement and its dual functionality potential as a SP-BP-HS, the CPNG1 device and HS (metal-semiconductor-metal) was connected in parallel. The CPNG1 device is fixed in the linear motor (force ≈ 10 N), and the output of the energy harvester is fed as input to the SP-BP-HS as shown in figure. 3.7a, where its electrical response is measured with the help of Keithley 6514 electrometer. Here, the $V_{OC \ (p-p)}$ response decreases from 45 V to 4 V with an increase in the % RH indicating that the resistance gets lowered across the humidity sensor which is shown in Figure 3.7b. When the sensor exposes towards humidity, the

resistance of the sensor gets reduced linearly. To avoid short circuit due to the presence of water vapor, the Ag electrodes were covered by an epoxy resin which is non-conductive. By plotting the positive and negative peak voltage, a linear behavior is observed from 50 % to 90 % RH as shown in Figure 3.7c. This clearly shows that the humidity sensor works actively from 50% to 90% RH ranges. These results confirms that the SP-BP-HS is a promising candidate for the detection of humidity and the biopolymer devices opens up a way towards greener environment.

3.4 Conclusion

In summary, a cost-effective self-powered, eco-friendly and bio-compatible, SP-BP-HS was developed for the first time. The CNF deposited cotton fabric with 500 μm thickness (CPNG2) demonstrates an upright structural and piezoelectric property. Also the multifunctional device exhibits a good electrical response at a maximum of $V_{OC} \approx 50$ V and $I_{SC} \approx 250$ nA. The load resistance analysis, switching polarity tests, poling effect, stability test and charging-discharging of commercial capacitors were successfully performed. As a dual functionality device, the SP-PB-HS exhibits a linear I-V response and I-T response with an exquisite sensitivity of 0.1287 μA/ % RH, resolution of 0.119 μA/ % RH and a correlation coefficient of 0.99554 with better detection capability in the range of 50 % to 90 % RH. The above results imply that biopolymer-based materials has the possibility to use in the smart health care systems, implantable devices, and e-skin based sensors and devices.

3.5 References

1.   Guo, W.; Wang, S.; Yu, X.; Qiu, J.; Li, J.; Tang, W.; Li, Z.; Mou, X.; Liu, H.; Wang, Z., Construction of a 3D rGO-collagen Hybrid Scaffold for Enhancement of the Neural Differentiation of Mesenchymal Stem Cells. *Nanoscale* **2016,** *8* (4), 1897-1904.

2.   Dahiya, A. S.; Morini, F.; Boubenia, S.; Nadaud, K.; Alquier, D.; Poulin-Vittrant, G., Organic/Inorganic Hybrid Stretchable Piezoelectric Nanogenerators for Self-Powered Wearable Electronics. *Advanced Materials Technologies* **2018,** *3* (2), 1700249.

3.   Zheng, Q.; Zhang, H.; Shi, B.; Xue, X.; Liu, Z.; Jin, Y.; Ma, Y.; Zou, Y.; Wang, X.; An, Z.; Tang, W.; Zhang, W.; Yang, F.; Liu, Y.; Lang, X.; Xu, Z.; Li, Z.; Wang, Z. L., In Vivo Self-Powered Wireless Cardiac Monitoring via Implantable Triboelectric Nanogenerator. *ACS Nano* **2016,** *10* (7), 6510-6518.

4.   Li, Z.; Chen, J.; Yang, J.; Su, Y.; Fan, X.; Wu, Y.; Yu, C.; Wang, Z. L., [Small Beta]-Cyclodextrin Enhanced Triboelectrification for Self-powered Phenol Detection and Electrochemical Degradation. *Energy & Environmental Science* **2015,** *8* (3), 887-896.

5.   Lee, M.; Bae, J.; Lee, J.; Lee, C.-S.; Hong, S.; Wang, Z. L., Self-powered Environmental Sensor System Driven by Nanogenerators. *Energy & Environmental Science* **2011,** *4* (9), 3359-3363.

6.   Wang, Z. L.; Song, J., Piezoelectric Nanogenerators Based on Zinc Oxide Nanowire Arrays. *Science* **2006,** *312* (5771), 242-246.

7.   Alluri, N. R.; Chandrasekhar, A.; Vivekananthan, V.; Purusothaman, Y.; Selvarajan, S.; Jeong, J. H.; Kim, S.-J., Scavenging Biomechanical Energy Using High-Performance, Flexible BaTiO3 Nanocube/PDMS Composite Films. *ACS Sustainable Chemistry & Engineering* **2017,** 5, 4730-4738.

8.   Karan, S. K.; Bera, R.; Paria, S.; Das, A. K.; Maiti, S.; Maitra, A.; Khatua, B. B., An Approach to Design Highly Durable Piezoelectric Nanogenerator Based on Self-Poled PVDF/AlO-rGO Flexible Nanocomposite with High Power Density and Energy Conversion Efficiency. *Advanced Energy Materials* **2016,** *6* (20), 1601016-n/a.

9.   Persano, L.; Dagdeviren, C.; Su, Y.; Zhang, Y.; Girardo, S.; Pisignano, D.; Huang, Y.; Rogers, J. A., High Performance Piezoelectric Devices Based on Aligned Arrays of Nanofibers of Poly(vinylidenefluoride-co-trifluoroethylene). *Nature Communications* **2013,** *4*, 1633.

10.   Xu, S.; Poirier, G.; Yao, N., PMN-PT Nanowires with a Very High Piezoelectric Constant. *Nano Letters* **2012,** *12* (5), 2238-2242.

11.   Park, K.-I.; Son, J. H.; Hwang, G.-T.; Jeong, C. K.; Ryu, J.; Koo, M.; Choi, I.; Lee, S. H.; Byun, M.; Wang, Z. L.; Lee, K. J., Highly-Efficient, Flexible Piezoelectric PZT Thin Film Nanogenerator on Plastic Substrates. *Advanced Materials* **2014,** *26* (16), 2514-2520.

12.   Vivekananthan, V.; Alluri, N. R.; Purusothaman, Y.; Chandrasekhar, A.; Kim, S.-J., A Flexible, Planar Energy Harvesting Device for Scavenging Road Side Waste Mechanical Energy via the Synergistic Piezoelectric Response of $K_{0.5}Na_{0.5}NbO_3$-$BaTiO_3$/PVDF Composite Films. *Nanoscale* **2017,** *9* (39), 15122-15130.

13.   Lee, K. Y.; Kim, D.; Lee, J.-H.; Kim, T. Y.; Gupta, M. K.; Kim, S.-W., Hybrid Nanocomposites: Unidirectional High-Power Generation via Stress-Induced Dipole Alignment from ZnSnO₃ Nanocubes/Polymer Hybrid Piezoelectric Nanogenerator (Adv. Funct. Mater. 1/2014). *Advanced Functional Materials* **2014,** *24* (1), 1-1.

14.   Ghosh, S. K.; Adhikary, P.; Jana, S.; Biswas, A.; Sencadas, V.; Gupta, S. D.; Tudu, B.; Mandal, D., Electrospun Gelatin Nanofiber based Self-powered Bio-e-skin for Health Care Monitoring. *Nano Energy* **2017,** *36* (Supplement C), 166-175.

15.   Alluri, N. R.; Selvarajan, S.; Chandrasekhar, A.; Saravanakumar, B.; Jeong, J. H.; Kim, S.-J., Piezoelectric BaTiO3/Alginate Spherical Composite Beads for Energy Harvesting and Self-powered Wearable Flexion Sensor. *Composites Science and Technology* **2017,** *142*, 65-78.

16.   Mohammadinejad, R.; Karimi, S.; Iravani, S.; Varma, R. S., Plant-derived Nanostructures: Types and Applications. *Green Chemistry* **2016,** *18* (1), 20-52.

17.   Gao, X.; Huang, L.; Wang, B.; Xu, D.; Zhong, J.; Hu, Z.; Zhang, L.; Zhou, J., Natural Materials Assembled, Biodegradable, and Transparent Paper-Based Electret Nanogenerator. *ACS Applied Materials & Interfaces* **2016,** *8* (51), 35587-35592.

18.   Kim, K. N.; Chun, J.; Chae, S. A.; Ahn, C. W.; Kim, I. W.; Kim, S.-W.; Wang, Z. L.; Baik, J. M., Silk Fibroin-based Biodegradable Piezoelectric Composite Nanogenerators Ssing Lead-free Ferroelectric Nanoparticles. *Nano Energy* **2015,** *14* (Supplement C), 87-94.

19.   Pan, R.; Xuan, W.; Chen, J.; Dong, S.; Jin, H.; Wang, X.; Li, H.; Luo, J., Fully Biodegradable Triboelectric Nanogenerators based on Electrospun Polylactic acid and Nanostructured Gelatin Films. *Nano Energy* **2018,** *45*, 193-202.

20.   Zhao, C.; Zhang, J.; Wang, Z. L.; Ren, K., A Poly(l-Lactic Acid) Polymer-Based Thermally Stable Cantilever for Vibration Energy Harvesting Applications. *Advanced Sustainable Systems* **2017,** *1* (9), 1700068-n/a.

21.   Song, P.; Kuang, S.; Panwar, N.; Yang, G.; Tng, D. J. H.; Tjin, S. C.; Ng, W. J.; Majid, M. B. A.; Zhu, G.; Yong, K.-T.; Wang, Z. L., A Self-Powered Implantable Drug-Delivery System Using Biokinetic Energy. *Advanced Materials* **2017,** *29* (11), 1605668-n/a.

22.   Hubbell, J. A., Biomaterials in Tissue Engineering. *Bio/Technology* **1995,** *13*, 565.

23.   Smith, A. M.; Moxon, S.; Morris, G. A., 13 - Biopolymers as Wound Healing Materials A2 - Ågren, Magnus S. In *Wound Healing Biomaterials*, Woodhead Publishing: 2016; pp 261-287.

24.   Zheng, Q.; Shi, B.; Li, Z.; Wang, Z. L., Recent Progress on Piezoelectric and Triboelectric Energy Harvesters in Biomedical Systems. *Advanced Science* **2017,** *4* (7), 1700029-n/a.

25.   Zheng, Q.; Zou, Y.; Zhang, Y.; Liu, Z.; Shi, B.; Wang, X.; Jin, Y.; Ouyang, H.; Li, Z.; Wang, Z. L., Biodegradable Triboelectric Nanogenerator as a Life-time Designed Implantable Power Source. *Science Advances* **2016,** *2* (3), e1501478.

26.   Selvarajan, S.; Alluri, N. R.; Chandrasekhar, A.; Kim, S.-J., Direct Detection of Cysteine Using Functionalized BaTiO3 Nanoparticles Film based Self-powered Biosensor. *Biosensors and Bioelectronics* **2017,** *91*, 203-210.

27.   Chen, C.-H.; Lee, P.-W.; Tsao, Y.-H.; Lin, Z.-H., Utilization of Self-powered Electrochemical Systems: Metallic Nanoparticle Synthesis and Lactate Detection. *Nano Energy* **2017,** *42*, 241-248.

28.   Ghosh, S. K.; Mandal, D., Sustainable Energy Generation from Piezoelectric Biomaterial for Noninvasive Physiological Signal Monitoring. *ACS Sustainable Chemistry & Engineering* **2017,** *5* (10), 8836-8843.

29.   Chandrasekhar, A.; Alluri, N. R.; Saravanakumar, B.; Selvarajan, S.; Kim, S.-J., A Microcrystalline Cellulose Ingrained Polydimethylsiloxane Triboelectric Nanogenerator as a Self-powered Locomotion Detector. *Journal of Materials Chemistry C* **2017,** *5* (7), 1810-1815.

30.   Denning, D.; Kilpatrick, J. I.; Fukada, E.; Zhang, N.; Habelitz, S.; Fertala, A.; Gilchrist, M. D.; Zhang, Y.; Tofail, S. A. M.; Rodriguez, B. J., Piezoelectric Tensor of Collagen Fibrils Determined at the Nanoscale. *ACS Biomaterials Science & Engineering* **2017,** *3* (6), 929-935.

31.   Wang, H.; Qian, J.; Ding, F., Recent Advances in Engineered Chitosan-based Nanogels for Biomedical Applications. *Journal of Materials Chemistry B* **2017,** *5* (34), 6986-7007.

32.   Eiichi, F.; Iwao, Y., Piezoelectric Effects in Collagen. *Japanese Journal of Applied Physics* **1964,** *3* (2), 117.

33.   Denning, D.; Paukshto, M. V.; Habelitz, S.; Rodriguez, B. J., Piezoelectric Properties of Aligned Collagen Membranes. *Journal of Biomedical Materials Research Part B: Applied Biomaterials* **2014,** *102* (2), 284-292.

34.   Lee, J.; Kwon, H.; Seo, J.; Shin, S.; Koo, J. H.; Pang, C.; Son, S.; Kim, J. H.; Jang, Y. H.; Kim, D. E.; Lee, T., Conductive Fiber-Based Ultrasensitive Textile Pressure Sensor for Wearable Electronics. *Advanced Materials* **2015,** *27* (15), 2433-2439.

35. Jost, K.; Stenger, D.; Perez, C. R.; McDonough, J. K.; Lian, K.; Gogotsi, Y.; Dion, G., Knitted and Screen Printed Carbon-Fiber Supercapacitors for Applications in Wearable Electronics. *Energy & Environmental Science* **2013,** *6* (9), 2698-2705.

36. Chang, T.-H.; Peng, Y.-W.; Chen, C.-H.; Chang, T.-W.; Wu, J.-M.; Hwang, J.-C.; Gan, J.-Y.; Lin, Z.-H., Protein-based Contact Electrification and its Uses for Mechanical Energy Harvesting and Humidity Detecting. *Nano Energy* **2016,** *21*, 238-246.

37. Erande, M. B.; Pawar, M. S.; Late, D. J., Humidity Sensing and Photodetection Behavior of Electrochemically Exfoliated Atomically Thin-Layered Black Phosphorus Nanosheets. *ACS Applied Materials & Interfaces* **2016,** *8* (18), 11548-11556.

38. Lu, T.; Song, H.; Dong, X.; Hu, J.; Lv, Y., A Highly Selective and Fast-response Photoluminescence Humidity Sensor based on F-decorated NH_2-MIL-53(Al) nanorods. *Journal of Materials Chemistry C* **2017,** *5* (36), 9465-9471.

39. Kuang, Q.; Lao, C.; Wang, Z. L.; Xie, Z.; Zheng, L., High-Sensitivity Humidity Sensor Based on a Single SnO2 Nanowire. *Journal of the American Chemical Society* **2007,** *129* (19), 6070-6071.

40. Chang, T.-W.; Wang, C.-W.; Chen, C.-H.; Li, Y.-C.; Hsu, C.-L.; Chang, H.-T.; Lin, Z.-H., Controlled Synthesis of Se-supported Au/Pd Nanoparticles with Photo-assisted Electrocatalytic Activity and their Application in Self-powered Sensing Systems. *Nano Energy* **2016,** *22*, 564-571.

41. Yu, B.; Fu, Y.; Wang, P.; Zhao, Y.; Xing, L.; Xue, X., Enhanced Piezo-Humidity Sensing of a Cd-ZnO Nanowire Nanogenerator as a Self-powered/Active Gas Sensor by Coupling the Piezoelectric Screening Effect and Dopant Displacement Mechanism. *Physical Chemistry Chemical Physics* **2015,** *17* (16), 10856-10860.

42.   Zhang, H. F.; Li, J.; Shao, G. Q.; Gao, Z. S.; Liu, J. H.; Girish, H. N., The Humidity Sensitivity and Mechanism of Strontium-Hexaferrite Ceramics. *Sensor Letters* **2017,** *15* (3), 236-241.

43.   Zhao, J.; Liu, Y.; Li, X.; Lu, G.; You, L.; Liang, X.; Liu, F.; Zhang, T.; Du, Y., Highly Sensitive Humidity Sensor based on High Surface Area Mesoporous LaFeO$_3$ Prepared by a Nanocasting Route. *Sensors and Actuators B: Chemical* **2013,** *181* (Supplement C), 802-809.

44.   Zang, W.; Li, P.; Fu, Y.; Xing, L.; Xue, X., Hydrothermal synthesis of Co-ZnO Nanowire Array and its Application as Piezo-driven Self-powered Humidity Sensor with High Sensitivity and Repeatability. *RSC Advances* **2015,** *5* (102), 84343-84349.

45.   Gao, Y.; Jing, P.; Yan, N.; Hilbers, M.; Zhang, H.; Rothenberg, G.; Tanase, S., Dual-mode Humidity Detection Using a Lanthanide-based Metal-Organic Framework: Towards Multifunctional Humidity Sensors. *Chemical Communications* **2017,** *53* (32), 4465-4468.

46.   Xu, W.; Huang, W.-B.; Huang, X.-G.; Yu, C.-y., A Simple Fiber-Optic Humidity Sensor based on Extrinsic Fabry–Perot Cavity Constructed by Cellulose Acetate Butyrate Film. *Optical Fiber Technology* **2013,** *19* (6, Part A), 583-586.

47.   Zhang, W.; Webb, D. J., Humidity Responsivity of Poly(methyl methacrylate)-based Optical Fiber Bragg Grating Sensors. *Opt. Lett.* **2014,** *39* (10), 3026-3029.

48.   Reddy, A. S. G.; Narakathu, B. B.; Atashbar, M. Z.; Rebros, M.; Rebrosova, E.; Bazuin, B. J.; Joyce, M. K.; Fleming, P. D.; Pekarovicova, A., Printed Capacitive Based Humidity Sensors on Flexible Substrates. *Sensor Letters* **2011,** *9* (2), 869-871.

49.   Zhang, W.; Webb, D. J.; Peng, G. D., Investigation Into Time Response of Polymer Fiber Bragg Grating Based Humidity Sensors. *J. Lightwave Technol.* **2012,** *30* (8), 1090-1096.

50.   Ghosh, S. K.; Mandal, D., High-performance Bio-piezoelectric Nanogenerator Made with Fish Scale. *Applied Physics Letters* **2016,** *109* (10), 103701.

51.   Singh, H.; Tomer, V. K.; Jena, N.; Bala, I.; Sharma, N.; Nepak, D.; De Sarkar, A.; Kailasam, K.; Pal, S. K., A Porous, Crystalline Truxene-based Covalent Organic Framework and its Application in Humidity Sensing. *Journal of Materials Chemistry A* **2017,** *5* (41), 21820-21827.

CHAPTER IV

4.1 A flexible, planar energy harvesting device for scavenging road side waste mechanical energy *via* synergistic piezoelectric response of $K_{0.5}Na_{0.5}NbO_3$-$BaTiO_3$/PVDF composite films

Highlights

➢ Flexible, planar composite piezoelectric nanogenerators (C-PNGs) were developed to harness waste mechanical energy using the cost-effective composite films (CFs) prepared by probe-sonication technique

➢ CFs were made up of highly crystalline, randomly oriented lead free piezoelectric nanoparticles $(1-x)K_{0.5}Na_{0.5}NbO_3$-$xBaTiO_3$ where x=0.02, 0.04, 0.06, 0.08 [designated as KNN-xBTO], were impregnated in polyvinylidene fluoride (PVDF) matrix

➢ KNN piezoelectric properties were tuned by the substitution of BTO nanoparticles without altering its orthorhombic phase

➢ C-PNG device (x≈0.02) generates maximum open circuit voltage ≈160 V and the instantaneous area power density is ≈14 mW/m^2 upon low mechanical force ≈0.4 N

➢ Further, experimentally demonstrated C-PNG device output is sufficient to drive commercial blue light emitting diodes. C-PNG device was placed on road side and test the maximum energy generation, stability under real time harsh environments such as vehicle motions and human walking motions.

Graphical Outline
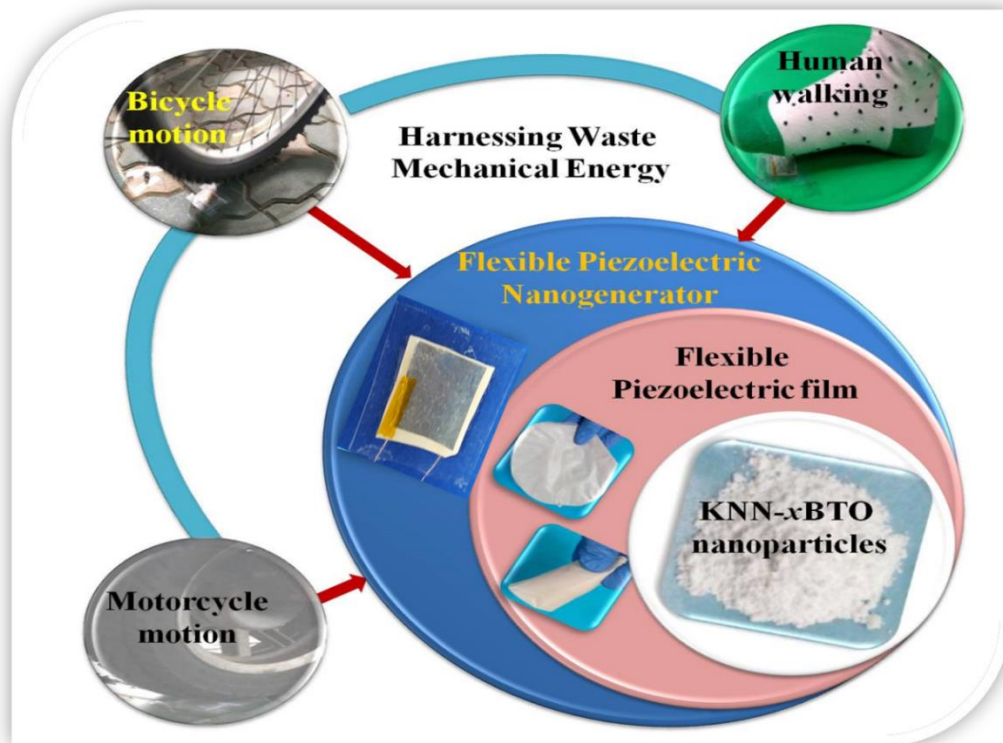
4.1.1 Introduction

Harnessing waste mechanical energy (WME) into useful electrical energy by nano-sized material possesses an innovative direction to explore the cost-effective unconventional energy harvesting systems (UC-EHS)[1]. The WME sources are human body movements[2], vehicular motions[3, 4] natural wind flow[5] and various mechanical vibrations of machines in industry[6], etc. Globally, lots of mechanical energy is going to be wasted in our day-to-day life. For example, the average vehicles run per day in South Korea is greater than 22,000, which covers greater than 300,000 kms (as per the report of International Transport Forum (ITF), 2016)[3]. Similarly, the wind power capacity in South Korea is 835 MW with the annual wind speed of 4-4.5 m/s. Further, it is expected to be increased to 2.5GW in the near future. In macroscopic view i.e. worldwide lots of vehicle/machinery motions and human body movements are generating surplus amount of mechanical energy. But there is no proper technology to utilize this type of WME. Recently, few cost-effective UC-EHS are implemented to harness this mechanical energy and generates clean and pollution free electrical energy. Other than these, the development of UC-EHS intends to address the various concerns related to global warming, CO_2 emissions and other environmental issues. The traditional EHSs using wind, solar, biomass, geo thermal and hydrogen energy requires high capital cost and requires periodical maintenance. Over the past decade, new kind of UC-EHSs introduced and thoroughly reported in various ways using piezoelectric effect[7], triboelectric effect[8-10], pyroelectric effect[11] and thermoelectric effects[12]. Among them, piezoelectric nanogenerators (PNG) using piezoelectric effect of nanostructures emerging as a promising approach, which can convert various external kinetic energy sources into electrical energy[13]. Moreover, piezoelectric

제주대학교 중앙도서관
JEJU NATIONAL UNIVERSITY LIBRARY

materials have much significance and advantageous than triboelectric[8-10], pyroelectric[11] and thermoelectric effect[12]. They are highly stable in nature with very less leakage current. Also it cannot be affected by any external interference, which makes it to work more stable over a long period of time. Many researchers shows great interest and reported the possible ways to utilize the human body movements (such as eye blinking[14], walking[15], stretching muscles[16], and hand fingers motion[17]), structural and mechanical vibrations of buildings/bridges, Wind/water flow motions and sound energies. The generated electrical energy from PNGs are sufficient, that are possible to power up various low power consumer electronic devices and also capable to drive various micro/nano sensors such as glucose[18], pH[19], fluid velocity[20], flexion[21], pressure[22, 23], accelerometer[24], strain[25] and UV photodetectors[26] respectively.

Till date, Many piezoelectric nanomaterials (ZnO[27, 28], BaTiO$_3$ (designated as BTO),[29] Pb(ZrTi)O$_3$ (designated as PZT),[30] KNaNbO$_3$ (designated as KNN)[31], GaN[32]), polymers (polyvinylidene fluoride (PVDF) and its copolymers) and composites (PVDF/BTO, polydimethylsiloxane (PDMS)/PZT, PVDF/ZnO) were tested for enhancing the output power, stability and portability/flexibility of PNGs. PNGs energy conversion efficiency depends on the selection and tuning of piezoelectric coefficient of nanomaterials[33], which in turn depends on synthesis procedure, crystallographic orientation of lattice, substitution of foreign elements into parent lattice. Recently, composite technology based films and its composite piezoelectric nanogenerators (C-PNGs) attracts great attention due to its advantages like increasing flexibility, reducing leakage current, higher output power, cost-effective, eco-friendly nature, biodegradability and easy fabrication of PNG devices[34]. In recent times, Inorganic pervoskite nanomaterials such as PZT, BTO, and KNN were used as filler materials in

55

polymer matrix with optimized weight ratio based PNGs that generates medium range output power (nW/m^2 to $\mu W/m^2$)[35-37] with good flexibility. Here, BTO has less piezoelectric coefficient (d_{33}) than PZT. But, PZT nanomaterials face a global restriction due to its toxicity and pollution issues. In contrast, KNN has medium d_{33} and possible to improve by the substitution of suitable foreign elements into KNN material. Till date, limited number of KNN based PNG reports were published with normal output power[38, 39]. It is highly desirable to enhance the output power in the range of mW/m^2 or W/m^2 for KNN based PNGs.

In this work, high crystalline $[(1-x)\,(K_{0.5}\,Na_{0.5})\,NbO_3 - xBaTiO_3$ ($x = 0.02$, 0.04, 0.06, and 0.08) pervoskite nanomaterial (designated as KNN-xBTO ($x = 0.02$, 0.04, 0.06, and 0.08)), piezoelectric PVDF film and composite films were used to investigate the energy harvesting performance. Here, PVDF matrix is used as a host matrix to immobilize the KNN-xBTO nanoparticles and to form as PVDF/KNN-xBTO composite film (CF). Predefined CFs (3 cm × 3 cm) were electrically polarized (10 kV) by attaching two aluminum (Al) foil electrodes on top/bottom of the CF. Various types of PNGs were fabricated such as PVDF, PVDF/KNN, PVDF/KNN-xBTO ($x=$ 0.02, 0.04, 0.06 and 0.08) to understand effect of BTO substitution into KNN parent lattice and in PVDF matrix. Among them, C-PNG ($x= 0.02$) generates higher electrical output voltage (160 V) and current (400 nA), when the mechanical force (0.4 N) acts on it. Next, C-PNG device ($x= 0.02$) was tested for scavenging WME, which is obtained from bicycle, motorcycle and human walking motions. The results and its experimental demonstration suggest that C-PNG device is a potential candidate for harnessing WME from our day-to-day life activates and the generated energy from C-PNG is pollution free, cost-effective and low maintenance.

4.1.2 Experimental details

4.1.2.1 Synthesis of $(1-x)$ $(K_{0.5}$ $Na_{0.5})$ NbO_3- xBaTiO$_3$ nanoparticles

Commercial Powders of potassium carbonate (K_2CO_3, 99.99%), sodium carbonate (Na_2CO_3, 99.5%), niobium pentoxide (Nb_2O_5, 99.9%), barium carbonate ($BaCO_3$, 99.95%) and titanium dioxide (TiO_2, 98%) were used as precursors to prepare stoichiometric $(1-x)$KNN-xBTO (x =0.02,0.04,0.06 and 0.08) nanoparticles by solid state reaction method (designated as SSR method). The detailed synthesis protocol was schematically demonstrated in results and discussion part. The weighted raw materials were homogenously mixed in ethanol medium by hand grinding (30 min.) in mortar and pestle. The homogenous mixture is then placed in alumina boat and fired at a temperature of 1200 °C/ 2 h with a heating rate of 5 °C/min. As-prepared final product is then washed with hot DI water to remove the by-products formed during the reaction and dried at 60 °C overnight to obtain a white colored product Further, secondary heat treatment i.e. 1100 °C for 2 h used to improve the densifying nature and crystallinity of $(1-x)$KNN-xBTO nanoparticles.

4.1.2.2 Composite film (CF) and piezoelectric nanogenerator (PNG) Fabrication

An amount of 1g of PVDF (Sigma-Aldrich) was dissolved in 10 ml of N'N'-dimethylformamide and undergoes sonication to obtain a homogeneous transparent solution using a probe sonicator for 60 min. Next, 20 wt % of $(1-x)$ $(K_{0.5}$ $Na_{0.5})$ NbO_3-xBaTiO$_3$ (x= 0.02, 0.04, 0.06 and 0.08) nanoparticles were added to the above prepared PVDF solution and sonicated for 1 h using a probe sonicator respectively. The final solution was poured into a glass Petri dish and dried in a hot air oven at 70 °C overnight which is schematically discussed in results and discussion part. The dried film is then peeled off from the petri dish and altered it to the required dimensions (3 cm × 3 cm)

of a composite PNG (C-PNG). C-PNG made up of direct attachment of low cost based aluminum (Al) foil electrodes (thickness ≈ 10 µm) on top/bottom of the predefined CF and external connections were obtained by the attachment of copper (Cu) wires on both sides of Al/CF/Al using silver paste. Finally, PDMS matrix used as a packaging layer to C-PNG device, for protecting from the external typical conditions such as humidity, temperature and high mechanical pressure. The C-PNG devices were poled at 10 kV for 24 h before carrying out with the electrical measurements in room temperature.

4.1.2.3 Measurement System

The phase formation of $(1-x)$KNN-xBTO (x =0.02,0.04,0.06 and 0.08) nanoparticles were characterized by an X-ray diffractometer (XRD, Rigaku) with Cu-Kα radiation (λ = 1.5406 Å) 2θ range from 20° to 80°operated Room temperature having an applied power supply of 40 kV and 40 mA. Raman spectra for all samples were recorded from 150 cm^{-1} to 1000 cm^{-1} with the laser excitation source of 514 nm using a single stage high throughput micro Raman spectroscopy (LabRAM HR Evaluation, Japan). The morphological characterization of KNN-xBTO nanoparticles and CFs were analyzed by a field emission scanning electron microscope (FE-SEM, JEOL JSM 6700F, Japan). The electrical measurements such as open circuit voltage (V_{OC}) and short circuit current (I_{SC}) of C-PNGs were recorded by a nanovoltmeter (Keithley 2182A) and a picoammeter (Keithley 6485), respectively.

4.1.3 Results and Discussion

The C-PNG device structure schematically shown in Figure 4.1.1a, which consists of five layers such as active piezoelectric layer (PVDF/$(1-x)$KNN-xBTO), top/bottom aluminum foil electrodes (thickness ≈16 µm) and top/bottom PDMS packaging layers, respectively. The inset shows digital photograph of as-fabricated C-

58

PNG device. Before the fabrication of C-PNG, piezoelectric crystalline phase, surface morphological analysis of various (1-x)KNN-xBTO (x =0.02, 0.04, 0.06 and 0.08) nanoparticles and PVDF/(1-x)KNN-xBTO (x =0.02, 0.04, 0.06 and 0.08) CFs were evaluated by XRD, Raman and FE-SEM techniques. High temperature solid state reaction technique was used to synthesize KNN-xBTO nanoparticles as shown in Figure 4.1.1b and the detailed explanation was given in the experimental section. Figure 4.1.1c shows XRD patterns of pure KNN, modified KNN i.e. 0.98 KNN-0.02 BTO and composite film. All the patterns show the splitting nature at 45˚ peak position and the corresponding planes are (040), (004) confirms the existence of orthorhombic crystalline phase. Impurity peaks or additional peaks related to the byproducts of raw materials were not observed for all patterns and well matched with the inorganic crystal structure database (ICSD) i.e. card number: 01-073-6542. The calculated lattice parameters, space group and number for pure KNN are (a = 7.8360, b= 7.9380 and c = 7.9000), Pm-m2 and 25. The orthorhombic phase of perovskite KNN lattice[40] were not changed, when the substitution of BTO content (x) value reached to 0.02, indicates the perfect diffusion of BTO content in to parent lattice. In contrast, x = 0.04, the peak splitting nature at 45° is start to converge and becomes single broad peak with less intensity clearly indicates the conversion of orthorhombic phase of KNN to tetragonal. Further, atomic vibrations of all samples were analyzed by the Raman patterns as shown in Figure 4.1.1d. The orthorhombic phase of KNN lattice have six major active modes positioned at $\nu6$ (200 cm^{-1}), $\nu5$ (267 cm^{-1}), $\nu2$ (568 cm^{-1}), $\nu1$ (621 cm^{-1}), $\nu3$ (649 cm^{-1}) and $\nu1+ \nu5$ (869 cm^{-1}), respectively. These modes are directly related to the external/internal vibrations of cations/ NbO$_6$ polyhedron in KNN lattice[41]. Similar

제주대학교 중앙도서관
JEJU NATIONAL UNIVERSITY LIBRARY

peak patterns were observed for 0.98KNN-0.02BTO nanoparticles and PVDF/0.98KNN-0.02BTO CF as shown in Figure 4.1.1d.
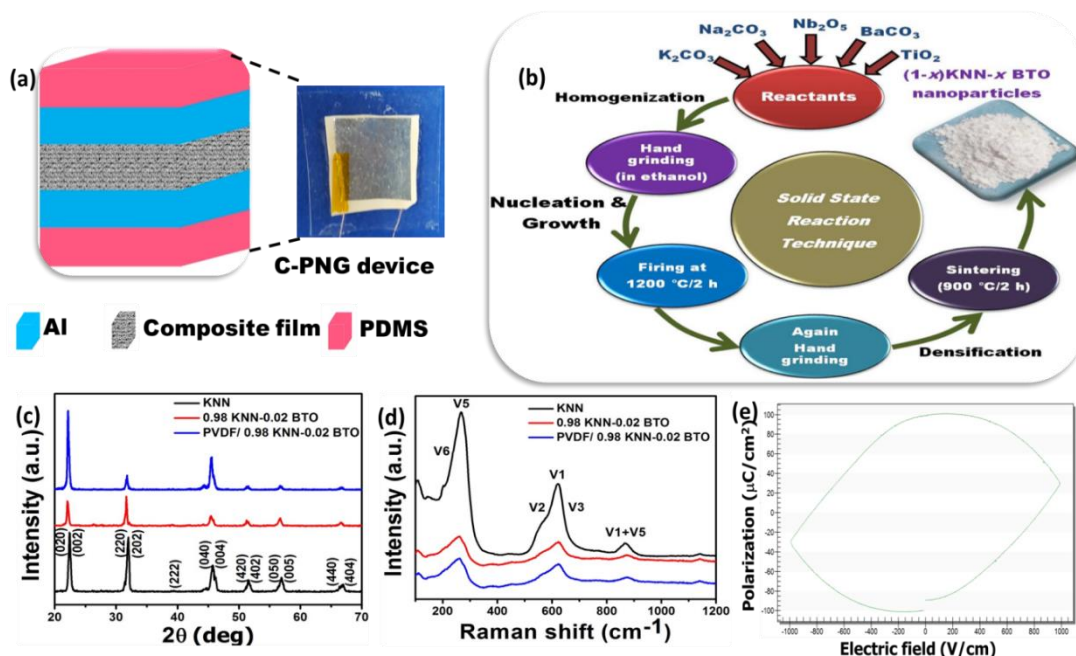
Figure 4.1.1 C-PNG Device layers, synthesisprotocol/structural analysis of KNN-*x*BTO nanoparticles. (a) Schematic of C-PNG device structure shows five device layers such as piezoelectric active layer, top/bottom Al electrodes, and top/bottom PDMS packaging layers. Inset shows the digital image of as-fabricated C-PNG device **(b)** Schematic for the synthesis of KNN-*x*BTO nanoparticles using high temperature solid state reaction technique **(c, d)** X-ray diffraction and Raman spectroscopy analysis of KNN, 0.98KNN-0.02BTO and PVDF/0.98KNN-0.02BTO CF confirms the orthorhombic crystalline phase.

The XRD and Raman patterns were clearly confirming that, $x = 0.02$ (i.e. BTO content) is the optimized doping ratio to KNN lattice without change of orthorhombic phase (higher piezoelectric property). The hysteresis loop measurements of KNN were analyzed and the obtained maximum polarization is 98 $\mu C/cm^2$ at 200 V/cm as shown in Figure 4.1.1e. Pure PVDF and composite film fabrication was schematically given in Figure 4.1.2 (a, b). Surface morphology of as-prepared nanoparticles and thickness of CFs were analyzed by field emission scanning electron microscopy as shown in Figure 4.1.2. Highly crystalline KNN nanocubes were observed at 1 µm scale (figure

S3a) and shape of these nanocubes were distorted and changed to random oriented nanoparticles with good crystalline nature when BTO nanoparticles ($x = 0.02$) were substituted in to KNN lattice (Inset of Figure 4.1.2b). The shapes of nanocubes were distorted heavily, while increasing the doping concentration of BTO from 0.02. The digital photograph of transparent PVDF film were shown in Figure 4.1.2a and the corresponding top surface morphology shown in inset Figure 4.1.2a. Fixed weight percentage of KNN and 0.98KNN-0.02BTO nanoparticles were homogeneously distributed in PVDF matrix using ultrasonication process and the corresponding surface morphology of CFs were shown in Figure 4.1.2b (right inset). The digital photograph of PVDF/0.98KNN-0.02BTO CF and its flexibility were shown in Figure 4.1.2b.
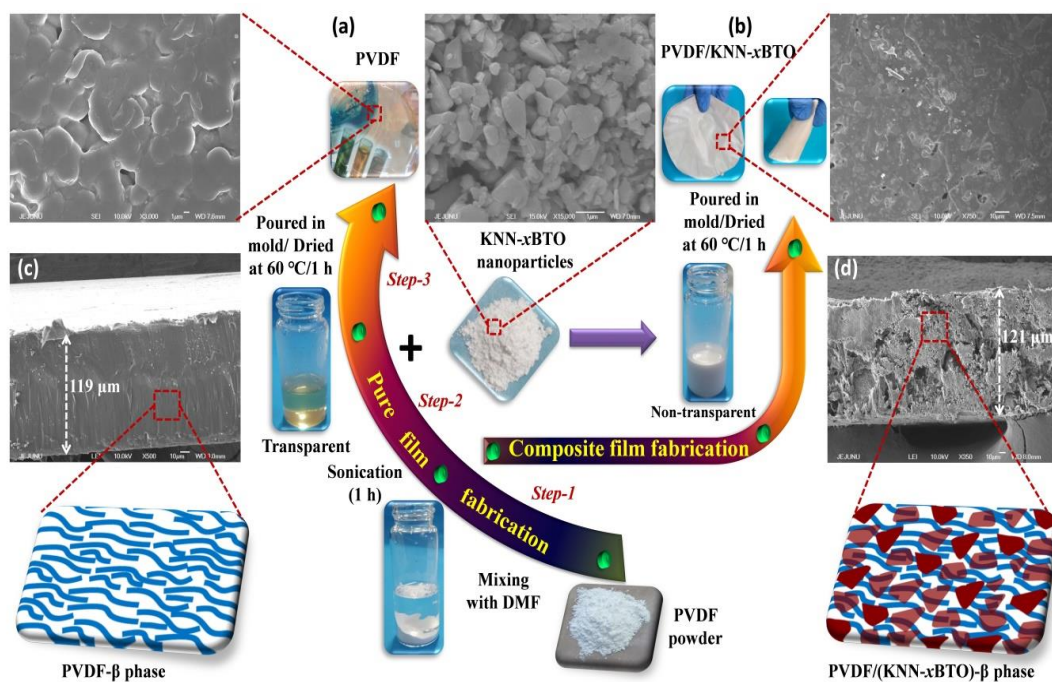
Figure 4.1.2- Fabrication procedure of PVDF and PVDF/KNN-*x*BTO CF: (a) Step by step procedure for fabricating PVDF film with electroactive β-phase and the inset shows the top surface morphology of PVDF. **(b)** Fabrication process of PVDF/KNN-*x*BTO CF ($x = 0.02$) and the inset shows the corresponding surface morphology, well distribution of KNN-*x*BTO nanoparticles in PVDF matrix. **(c)** Cross-sectional FE-SEM image of pure PVDF film and the thickness is ≈119 μm. The inset shows

estimated PVDF molecular chains in aligned manner shows electroactive β-phase. **(d)** Cross-sectional FE-SEM image of PVDF/ KNN-xBTO CF ($x = 0.02$) and the thickness is ≈121 μm. The inset shows estimated PVDF molecular chains in aligned manner along with the KNN-xBTO nanoparticles.

Further, thickness of PVDF, PVDF/0.98KNN-0.02BTO films were analyzed by cross-sectional FE-SEM images as shown in Figure 4.1.2 (c, d). PVDF/0.98KNN-0.02BTO CF thickness is 121 μm is higher than pure PVDF film thickness ≈119 μm. All films were prepared under same conditions such as fixed mold, PVDF transparent solution and sonication process conditions. Here, the variable parameter is amount of fillers substituted in PVDF solution; this is the reason for increment of thickness for CFs. The piezoelectric potential distribution in C-PNG and dependency of BTO doping concentrations in KNN lattice *via* fixed PVDF solution was evaluated.

Initially, the generated $V_{OC(p-p)}$ and $I_{SC(p-p)}$ of poled PVDF/KNN CF based PNG device (designated as C-PNG1) are ≈100 V and ≈190 nA, which is observed by applying constant periodic mechanical force (0.4 N) in perpendicular manner as shown in Figure 4.1.3c. Further, various poled CFs based PNG devices such PVDF/0.98KNN-0.02BTO (C-PNG2), PVDF/0.96KNN-0.04BTO (C-PNG3), PVDF/0.94KNN-0.06BTO (C-PNG4) and PVDF/0.92KNN-0.08BTO (C-PNG5) was fabricated and observed the generated $V_{OC(p-p)}$ and $I_{SC(p-p)}$ with an application of same input mechanical force as shown in Figure 4.1.3(a, b). The output electrical response increased and reached to the maximum value (V_{OC} ≈170 V, I_{SC} ≈350 nA) for C-PNG2 device as compared to the response of C-PNG1 as shown in Figure 4.1.3 (a, b). Other devices (C-PNG3 to C-PNG5) have less electrical response as compared to the C-PNG2 device. It indicates that the increment of BTO doping concentration (x >0.02) in KNN lattice modulating the orientation of electrical dipoles towards direction of

lower piezoelectric response. It depends on crystalline phase formation of KNN-BTO

nanoparticles and interfacial interaction between the distributions of nanoparticles into

PVDF matrix. XRD analysis confirms that, x>0.02 shown the possibility of phase

conversion form orthorhombic to tetragonal phase for KNN-BTO nanoparticles. This

phase conversion may possible to reduce the piezoelectric coefficient of KNN-BTO

nanoparticles[42, 43]. Moreover, there is another possibility i.e. phase mismatch between

the generated electric dipoles in KNN-BTO nanoparticles to the existed electric dipoles

of piezoelectric PVDF matrix. In order to confirm this, pure PVDF film (without KNN-

BTO nanoparticles) based PNG device (designated C-PNG0) was fabricated and

observed the electrical response by applying the same mechanical force as shown in

Figure 4.1.3 (a, b). It generates low electrical output as compared to all other C-PNG

devices. This output may be due to the electroactive β-phase of PVDF matrix, which

is confirm by the XRD peak at 2θ ≈ 20.13°. C-PNG3, C-PNG4 and C-PNG5 have

higher output as compared to C-PNG0 device confirm that, there is no phase mismatch

of electrical dipoles between nanoparticles and PVDF matrix as shown in the figure

4.1.3c. So that the low electrical response of C-PNG3, C-PNG4 and C-PNG5 as

compared to C-PNG2 device due to lower piezoelectric response of KNN-BTO

nanoparticles and not by the PVDF matrix. Theoretically, the V_{OC} and I_{SC} of C-PNG

can be evaluated by the following equations:[20, 33, 44]

$$V_{oc} = (d_{33}/\varepsilon_0 K)\sigma Y t \qquad (4.1.1)$$

$$I_{sc} = d_{33} A \sigma Y \qquad (4.1.2)$$

Where t, A, Y, K, d_{33} and σ are thickness and area of C-PNG, Young's modulus,

dielectric constant, and piezoelectric coefficient of CF, and perpendicular strain acting

on C-PNG device. The working mechanism of C-PNG device and its electric dipole

orientation with respect to force and no force condition is shown in Figure 4.1.3d. When a compressive force acts perpendicular manner to the top surface of C-PNG device, resulting an orientation of electric dipoles in aligned manner creates the potential difference across the top/bottom electrodes. Here, the electrons are moving from the top Al electrode to bottom electrode via external circuit as shown in Figure 4.1.3d (ii). Next, when a compressive force is released from C-PNG device, the electric dipoles changes its direction and electron flow will be from the bottom Al electrode to top Al electrode as shown in Figure 4.1.3d (iii). Under no force condition, the existed electric dipoles in CF will undergo in relax mode, correspondingly there is no generation of piezoelectric potential across two electrode as shown in Figure 4.1.3d (i)
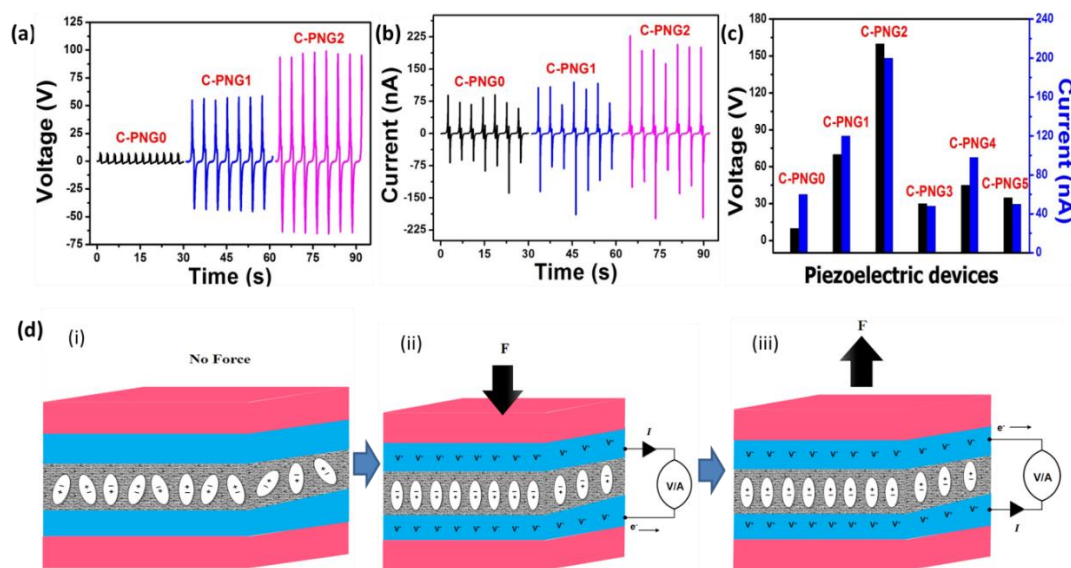
Figure 4.1.3- Electrical responses of C-PNG devices and its working mechanism: **(a, b)** Output voltage and current response of C-PNG0, C-PNG1 and C-PNG2 devices upon mechanical force ≈0.4 N. **(c)** Comparison of electrical responses of six C-PNG devices, among them C-PNG2 shows high electrical output response **(d)** Working mechanism of C-PNG device: **(i)** Zero electrical output generated during no force condition **(ii)** When force acts on C-PNG device, the dipoles aligned in one direction and the piezoelectric charge carriers starts flowing from top electrode to the bottom electrode through an external load **(iii)** When the force is removed from C-PNG device, the piezoelectric potential disappears and accumulated charge carriers flow back in opposite direction with an observed electrical signal.

The validation of electrical output response of C-PNG was performed by the switching polarity test as shown in Figure 4.1.4a. The phase shifts was observed for the output signals of C-PNG device during forward and reverse connections, confirms that the generated electrical output is coming from the C-PNG device and not by any other external sources as shown in Figure 4.1.4a. Before electrical poling, the C-PNG device generates an electrical response of 100 V, (200 nA) by the input mechanical force (N). Next, the C-PNG devices were electrically poled at various electric fields such as 8 kV and 10 kV for 24 h, in order to improve the piezoelectric polarization of C-PNG device as shown in Figure 4.1.4b.
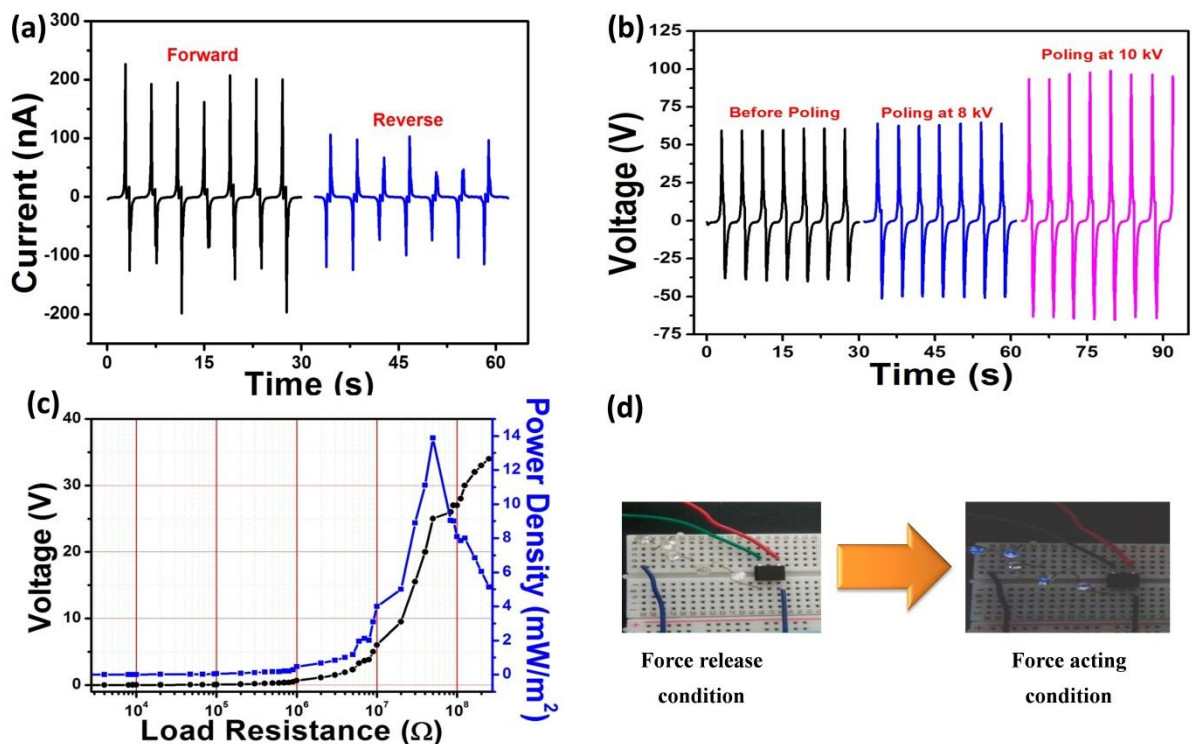
Figure 4.1.4 (a) Switching polarity test of C-PNG2 upon constant mechanical force. **(b)** Electrical poling (0 kV, 8 kV and 10 kV for 24 h) dependent output voltage of C-PNG2 upon constant mechanical force. **(c)** Load resistance analysis of C-PNG2 upon constant mechanical force and its generated instantaneous area power density ≈14 mW/m^2 at 100 MΩ. (d) Demonstration of powering up five blue LEDs using the C-PNG2 device output shows the capability of self-powered behavior.

The electric field at 8 kV for 24 h has no improvement in electrical response of C-PNG device upon same mechanical force, which clearly suggests that the applied electric filed is not sufficient to trigger the orientation of existed electric dipoles. In contrast, the electrical response of C-PNG device poled at 10 kV/24 h was improved (160 V, 400 nA) considerably upon same mechanical force[31] as shown Figure 4b. This is due to the orientation of all electric dipoles in one particular direction creates the permanent polarization in C-PNG device.

Further, load resistance analysis, instantaneous power density, calculation, powering up commercial light emitting diodes (LEDs), charge/discharge and energy storage analysis of commercial capacitors and stability test of C-PNG device was performed to identify the proper impedance matching and reliability of C-PNG for practical applications. Figure 4.1.4c shows the load resistance analysis (100 Ω to 1 GΩ) and its generated voltage (V), area power density (P_A) form C-PNG device upon the constant mechanical force $\approx$0.4 N. Here, the instantaneous area ($A \approx$3 cm $\times$ 3 cm) power density ($P_A = (V^2/(RxA))$)[24] is maximum $\approx$14 mW/m^2 at load resistance of 100 MΩ suggest the optimized load matching resistance (R) for commercial applications. Figure 4.1.4d shows the practical real time demonstration of powering up five blue commercial LEDs such as ON/OFF using the generated C-PNG device output upon constant pressing/releasing the mechanical force $\approx$0.4 N. Figure 4.1.5a shows the charging commercial capacitors (47 nF, 0.22 and 2.2 μF) using the C-PNG device output over a period of time $\approx$200 seconds. The amount of stored in voltage value in capacitor decreased from 30 V to 2 V, when the load capacitor value increases from 47 nF to 2.2 μF, respectively. The inset figure 4.1.5a shows the way of charging the capacitor during force ON and OFF on C-PNG device. Figure 4.1.5b shows the

66

charging and discharging behavior in 0.22 µF capacitor with multiple cycles. The calculated stored energy in 47 nF capacitor is 0.22 J, when a constant mechanical force (0.4 N) act on C-PNG device. This value decreased from 0.22 J to 0.025 J, 0.01J, when increasing the load capacitor value from 47 nF to 0.22 µF, 2.2 µF as shown in Figu4.1.5c. The endurance capability of C-PNG device was measured over a period of time ≈2000 seconds as shown in Figure 4.1.5d. There is no change in the electrical response of C-PNG device over a period of time suggest that the C-PNG device has good stability and a potential candidate for real time monitoring applications.
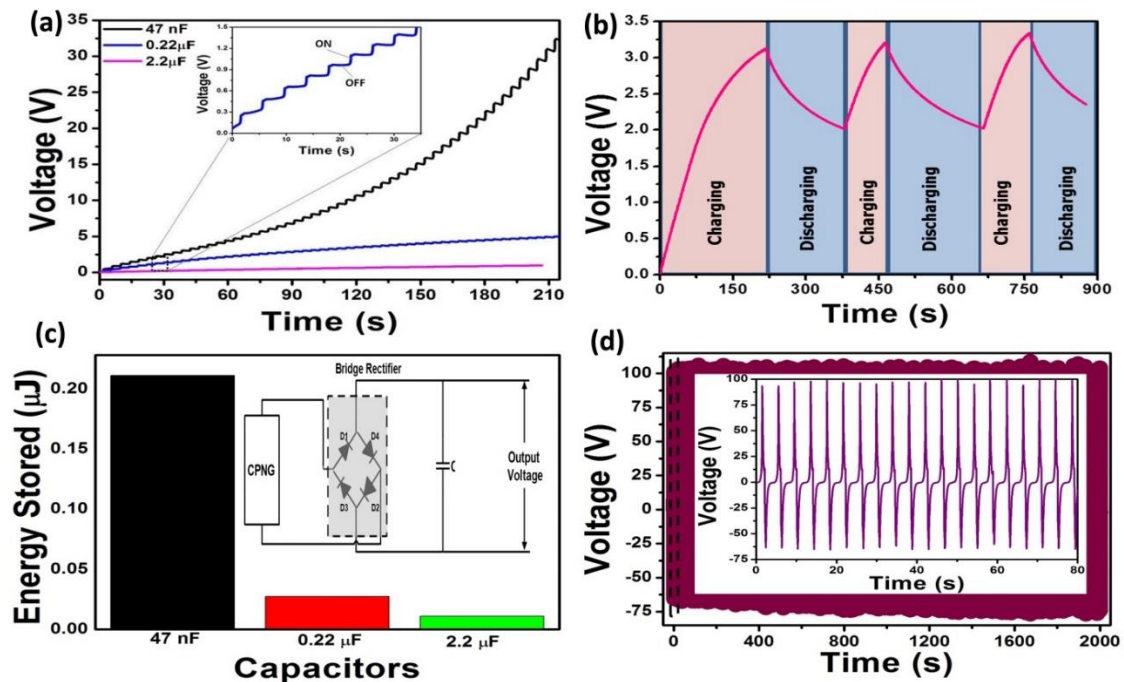
Figure 4.1.5 Charge/discharge analysis of commercial capacitor using C-PNG2 output and its stability test: (a) Charging various commercial capacitors such as 47 nF, 0.22 µF and 2.2 µF over a period of time ≈200 seconds using C-PNG2 output. The inset shows magnified part of charging peak behavior of 2.2 µF, when the force ON/OFF conditions on C-PNG2. **(b)** Charging and discharging cycles of capacitor ≈0.22 µF **(c)** The bar graph shows the stored energy in capacitors, when 0.4 N force act on C-PNG2. **(d)** Stability test of C-PNG2 device over a period of 2000 s, which constantly generates a peak-to-peak voltage of 160 V.

Now a days, harnessing WME such as human body movements, vehicle motions, ocean waves and wind motions using UC-EHS approach gained a great attention due to various advantages like no consumption of fossil fuels, eco-friendly, zero carbon emission and partially possible to reduce world energy crisis. The C-PNG device results and its planar device structure suggest that C-PNG is a potential candidate to utilize the waste mechanical energy on road/streets such as motorcycle, bicycle and human leg motions. Figure 4.1.6a shows the electrical output voltage response of C-PNG device under various conditions. The maximum generated peak-to-peak voltage of C-PNG device is ≈16 V upon the motorcycle forward/backward motions. Similarly, maximum generated peak-to-peak voltage of C-PNG device is 12 V and 9 V, when bicycle and human leg forward/backward motions acting on it. Figure 4.1.6b shows the digital photographs were taken during the time of harnessing waste mechanical energy and the images depicts that forward/backward motions of motorcycle, bicycle and leg motions on C-PNG device. The real time stability of C-PNG2 was evaluated using four different motorcycles having different weight and engine power. Here, the motorcycles are passing on C-PNG2 device in circular manner with different time intervals. The C-PNG2 device generates stable outputs with all types of motorcycle motions in periodic manner over a period of 500 seconds as shown in Figure 4.1.6c. The observed peak-to-peak output voltage lies between the +5 V to -10 V or vice versa. In present case, the observed electrical output from C-PNG device is non-symmetric and have little fluctuations, this may be due to the fluctuations of vehicle/leg periodic motions, speed, weight and its frequency[45, 46]. However, the C-PNG devices generates considerable output voltage during vehicle/leg motions, which is sufficient to power up/drive the low power consumed electronic devices. The

composite film and its fabrication process is cost-effective, low processing time, simple and the corresponding C-PNG device results suggest that, potential candidate to harvest the waste mechanical energy without using any storage components and additional circuits. In future this type of devices and its energy will be useful to power up road side sensors[47], speed tachometers[48] and light indicators present in the highway roads[49].
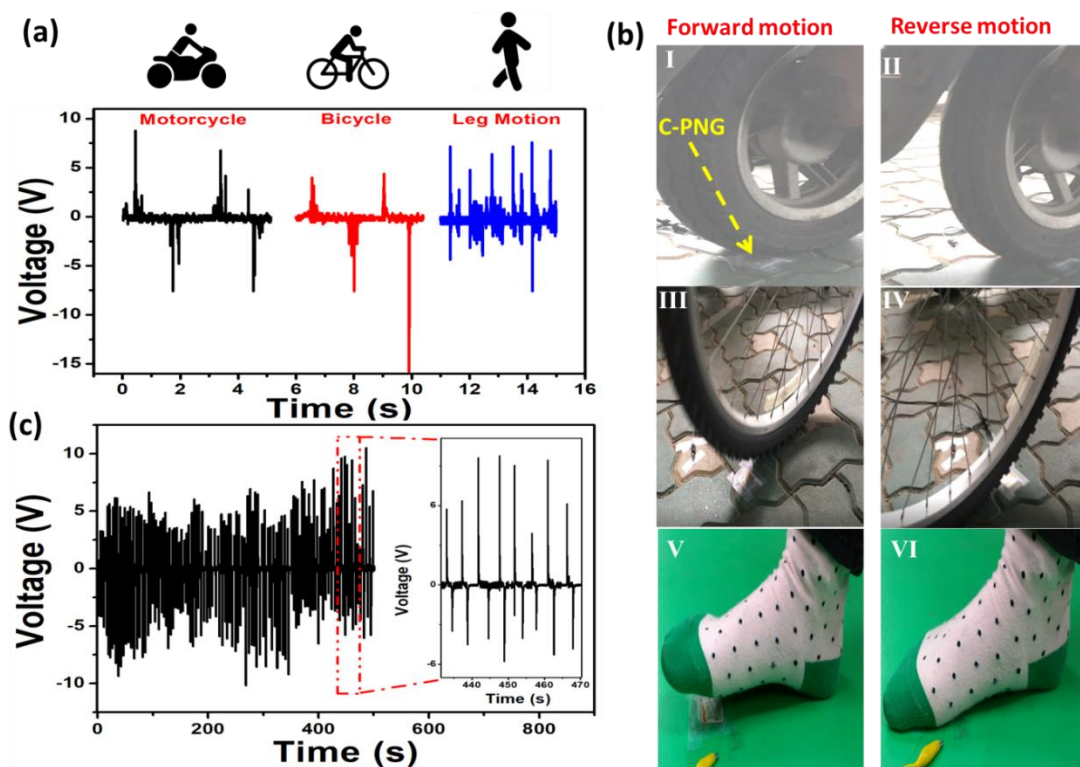
Figure 4.1.6 Real time utilization of WME (vehicles motion and human walking) using C-PNG2 device: **(a)** Output voltage response of C-PNG2 located on road, when the motorcycle, bicycle and human walking act on it. **(b)** Digital photographs of forward/reverse conditions of motorcycle, bicycle and human walking on C-PNG2. The photographs were taken during the time of experimental demonstration. **(c)** Real-time stability test of C-PNG2 device under motorcycle motions over a period of 500 seconds.

4.1.4 Conclusion

In summary, we have successfully developed a cost-effective, efficient and highly flexible PVDF/KNN-xBTO composite film ($x \approx 0.02$) using simple ultrasonication process followed by solution casting technique. The substitution of BTO nanoparticles into KNN lattice up to ($x \approx 0.02$) will lead to improve piezoelectric property and no change in the orthorhombic phase of KNN lattice. If $x > 0.02$, there is a possibility of change in KNN crystalline phase from orthorhombic phase to tetragonal phase lead to decrease the piezoelectric performance of KNN-xBTO. Among all the devices, the C-PNG device ($x \approx 0.02$) generates maximum electrical output response $V_{OC} \approx 160$ V and $I_{SC} \approx 400$ nA up on constant low mechanical force 0.4 N, respectively. The electrical responses of various concentrations of BTO nanoparticles into KNN lattice/PVDF composite films, electrical poling effect (8 kV and 10 kV for 24 h), switching polarity test of C-PNG device, load resistance/capacitor analysis, instantaneous area power density and energy storage analysis in commercial capacitors was evaluated and analyzed successfully. Real-time utilization of C-PNG device output to power up five commercial blue LEDs was demonstrated. Moreover, the C-PNG device has good stability and highly sensitive to the various types of mechanical motions on road/streets. Next, C-PNG device generates maximum peak-to-peak output voltage ≈ 16 V, during the motorcycle forward/backward motions on it. All the results suggest that, the C-PNG device output is high, comparable to many published reports and the generated output possible to use/power up road side sensors, speed tachometers and light indicators present in the highway roads.

4.1.5 References

1.   Service, R. F., Nanogenerators Tap Waste Energy To Power Ultrasmall Electronics. *Science* **2010,** *328* (5976), 304-305.

2.   Yao, C.; Hernandez, A.; Yu, Y.; Cai, Z.; Wang, X., Triboelectric nanogenerators and power-boards from cellulose nanofibrils and recycled materials. *Nano Energy* **2016,** *30*, 103-108.

3.   Mao, Y.; Geng, D.; Liang, E.; Wang, X., Single-electrode triboelectric nanogenerator for scavenging friction energy from rolling tires. *Nano Energy* **2015,** *15*, 227-234.

4.   ITF, *Road Safety Annual Report 2016*. OECD Publishing.

5.   이춘식; 김광호; 최항철, Experiences on wind energy utilization in Korea. International seminar on environment and integrated rural energy systems.

6.   Wang, S.; Niu, S.; Yang, J.; Lin, L.; Wang, Z. L., Quantitative Measurements of Vibration Amplitude Using a Contact-Mode Freestanding Triboelectric Nanogenerator. *ACS Nano* **2014,** *8* (12), 12004-12013.

7.   Ding, R.; Liu, H.; Zhang, X.; Xiao, J.; Kishor, R.; Sun, H.; Zhu, B.; Chen, G.; Gao, F.; Feng, X.; Chen, J.; Chen, X.; Sun, X.; Zheng, Y., Flexible Piezoelectric Nanocomposite Generators Based on Formamidinium Lead Halide Perovskite Nanoparticles. *Advanced Functional Materials* **2016,** *26* (42), 7708-7716.

8.   Chandrasekhar, A.; Alluri, N. R.; Vivekananthan, V.; Purusothaman, Y.; Kim, S.-J., A sustainable freestanding biomechanical energy harvesting smart backpack as a portable-wearable power source. *Journal of Materials Chemistry C* **2017,** *5* (6), 1488-1493.

9.   Wang, S.; Lin, L.; Wang, Z. L., Triboelectric nanogenerators as self-powered active sensors. *Nano Energy* **2015,** *11*, 436-462.

10.   Zhang, Q.; Liang, Q.; Liao, Q.; Yi, F.; Zheng, X.; Ma, M.; Gao, F.; Zhang, Y., Service Behavior of Multifunctional Triboelectric Nanogenerators. *Advanced Materials* **2017,** *29* (17), 1606703-n/a.

11.   Wang, Z.; Yu, R.; Pan, C.; Li, Z.; Yang, J.; Yi, F.; Wang, Z. L., Light-induced pyroelectric effect as an effective approach for ultrafast ultraviolet nanosensing. *Nature Communications* **2015,** *6*, 8401.

12.   Yang, Y.; Guo, W.; Pradel, K. C.; Zhu, G.; Zhou, Y.; Zhang, Y.; Hu, Y.; Lin, L.; Wang, Z. L., Pyroelectric Nanogenerators for Harvesting Thermoelectric Energy. *Nano Letters* **2012,** *12* (6), 2833-2838.

13.   Wang, Z. L.; Song, J., Piezoelectric Nanogenerators Based on Zinc Oxide Nanowire Arrays. *Science* **2006,** *312* (5771), 242-246.

14.   Lee, S.; Bae, S.-H.; Lin, L.; Yang, Y.; Park, C.; Kim, S.-W.; Cha, S. N.; Kim, H.; Park, Y. J.; Wang, Z. L., Super-Flexible Nanogenerator for Energy Harvesting from Gentle Wind and as an Active Deformation Sensor. *Advanced Functional Materials* **2013,** *23* (19), 2445-2449.

15.   Wang, J.; Li, S.; Yi, F.; Zi, Y.; Lin, J.; Wang, X.; Xu, Y.; Wang, Z. L., Sustainably powering wearable electronics solely by biomechanical energy. *Nature Communications* **2016,** *7*, 12744.

16.   Yang, R.; Qin, Y.; Li, C.; Zhu, G.; Wang, Z. L., Converting Biomechanical Energy into Electricity by a Muscle-Movement-Driven Nanogenerator. *Nano Letters* **2009,** *9* (3), 1201-1205.

17. Ghosh, S. K.; Adhikary, P.; Jana, S.; Biswas, A.; Sencadas, V.; Gupta, S. D.; Tudu, B.; Mandal, D., Electrospun gelatin nanofiber based self-powered bio-e-skin for health care monitoring. *Nano Energy* **2017,** *36*, 166-175.

18. Selvarajan, S.; Alluri, N. R.; Chandrasekhar, A.; Kim, S.-J., BaTiO3 nanoparticles as biomaterial film for self-powered glucose sensor application. *Sensors and Actuators B: Chemical* **2016,** *234*, 395-403.

19. Saravanakumar, B.; Soyoon, S.; Kim, S.-J., Self-Powered pH Sensor Based on a Flexible Organic–Inorganic Hybrid Composite Nanogenerator. *ACS Applied Materials & Interfaces* **2014,** *6* (16), 13716-13723.

20. Alluri, N. R.; Saravanakumar, B.; Kim, S.-J., Flexible, Hybrid Piezoelectric Film (BaTi(1–x)ZrxO3)/PVDF Nanogenerator as a Self-Powered Fluid Velocity Sensor. *ACS Applied Materials & Interfaces* **2015,** *7* (18), 9831-9840.

21. Alluri, N. R.; Selvarajan, S.; Chandrasekhar, A.; Saravanakumar, B.; Jeong, J. H.; Kim, S.-J., Piezoelectric BaTiO3/alginate spherical composite beads for energy harvesting and self-powered wearable flexion sensor. *Composites Science and Technology* **2017,** *142*, 65-78.

22. Chen, X.; Shao, J.; An, N.; Li, X.; Tian, H.; Xu, C.; Ding, Y., Self-powered flexible pressure sensors with vertically well-aligned piezoelectric nanowire arrays for monitoring vital signs. *Journal of Materials Chemistry C* **2015,** *3* (45), 11806-11814.

23. Ma, M.; Zhang, Z.; Liao, Q.; Yi, F.; Han, L.; Zhang, G.; Liu, S.; Liao, X.; Zhang, Y., Self-powered artificial electronic skin for high-resolution pressure sensing. *Nano Energy* **2017,** *32*, 389-396.

24.   Alluri, N. R.; Chandrasekhar, A.; Jeong, J. H.; Kim, S.-J., Enhanced electroactive [small beta]-phase of the sonication-process-derived PVDF-activated carbon composite film for efficient energy conversion and a battery-free acceleration sensor. *Journal of Materials Chemistry C* **2017**.

25.   Zhang, Y.; Yang, Y.; Gu, Y.; Yan, X.; Liao, Q.; Li, P.; Zhang, Z.; Wang, Z., Performance and service behavior in 1-D nanostructured energy conversion devices. *Nano Energy* **2015,** *14*, 30-48.

26.   Duan, L.; He, F.; Tian, Y.; Sun, B.; Fan, J.; Yu, X.; Ni, L.; Zhang, Y.; Chen, Y.; Zhang, W., Fabrication of Self-Powered Fast-Response Ultraviolet Photodetectors Based on Graphene/ZnO:Al Nanorod-Array-Film Structure with Stable Schottky Barrier. *ACS Applied Materials & Interfaces* **2017,** *9* (9), 8161-8168.

27.   Stassi, S.; Cauda, V.; Ottone, C.; Chiodoni, A.; Pirri, C. F.; Canavese, G., Flexible piezoelectric energy nanogenerator based on ZnO nanotubes hosted in a polycarbonate membrane. *Nano Energy* **2015,** *13*, 474-481.

28.   Zhang, Y.; Yan, X.; Yang, Y.; Huang, Y.; Liao, Q.; Qi, J., Scanning Probe Study on the Piezotronic Effect in ZnO Nanomaterials and Nanodevices. *Advanced Materials* **2012,** *24* (34), 4647-4655.

29.   Park, K.-I.; Lee, M.; Liu, Y.; Moon, S.; Hwang, G.-T.; Zhu, G.; Kim, J. E.; Kim, S. O.; Kim, D. K.; Wang, Z. L.; Lee, K. J., Flexible Nanocomposite Generator Made of BaTiO3 Nanoparticles and Graphitic Carbons. *Advanced Materials* **2012,** *24* (22), 2999-3004.

30.   Park, K.-I.; Son, J. H.; Hwang, G.-T.; Jeong, C. K.; Ryu, J.; Koo, M.; Choi, I.; Lee, S. H.; Byun, M.; Wang, Z. L.; Lee, K. J., Highly-Efficient, Flexible Piezoelectric PZT Thin Film Nanogenerator on Plastic Substrates. *Advanced Materials* **2014,** *26* (16), 2514-2520.

31.   Gupta, M. K.; Kim, S.-W.; Kumar, B., Flexible High-Performance Lead-Free Na0.47K0.47Li0.06NbO3 Microcube-Structure-Based Piezoelectric Energy Harvester. *ACS Applied Materials & Interfaces* **2016,** *8* (3), 1766-1773.

32.   Jamond, N.; Chretien, P.; Gatilova, L.; Galopin, E.; Travers, L.; Harmand, J.-C.; Glas, F.; Houze, F.; Gogneau, N., Energy harvesting efficiency in GaN nanowire-based nanogenerators: the critical influence of the Schottky nanocontact. *Nanoscale* **2017,** *9* (13), 4610-4619.

33.   Whiter, R. A.; Narayan, V.; Kar-Narayan, S., A Scalable Nanogenerator Based on Self-Poled Piezoelectric Polymer Nanowires with High Energy Conversion Efficiency. *Advanced Energy Materials* **2014,** *4* (18), 1400519-n/a.

34.   Shin, S.-H.; Kim, Y.-H.; Lee, M. H.; Jung, J.-Y.; Nah, J., Hemispherically Aggregated BaTiO3 Nanoparticle Composite Thin Film for High-Performance Flexible Piezoelectric Nanogenerator. *ACS Nano* **2014,** *8* (3), 2766-2773.

35.   Chen, X.; Xu, S.; Yao, N.; Shi, Y., 1.6 V Nanogenerator for Mechanical Energy Harvesting Using PZT Nanofibers. *Nano Letters* **2010,** *10* (6), 2133-2137.

36.   Park, K.-I.; Xu, S.; Liu, Y.; Hwang, G.-T.; Kang, S.-J. L.; Wang, Z. L.; Lee, K. J., Piezoelectric BaTiO3 Thin Film Nanogenerator on Plastic Substrates. *Nano Letters* **2010,** *10* (12), 4939-4943.

37.   Kang, M.-G.; Oh, S.-M.; Jung, W.-S.; Gyu Moon, H.; Baek, S.-H.; Nahm, S.; Yoon, S.-J.; Kang, C.-Y., Enhanced piezoelectric properties of vertically aligned single-crystalline NKN nano-rod arrays. *Scientific Reports* **2015,** *5*, 10151.

38.   Ge, H.; Hou, Y.; Zhu, M.; Wang, H.; Yan, H., Facile synthesis and high d33 of single-crystalline KNbO3 nanocubes. *Chemical Communications* **2008,** (41), 5137-5139.

39.   Zhang, Y.; Li, L.; Shen, B.; Zhai, J., Effect of orthorhombic-tetragonal phase transition on structure and piezoelectric properties of KNN-based lead-free ceramics. *Dalton Transactions* **2015,** *44* (17), 7797-7802.

40.   Wang, X.; Wu, J.; Xiao, D.; Zhu, J.; Cheng, X.; Zheng, T.; Zhang, B.; Lou, X.; Wang, X., Giant Piezoelectricity in Potassium–Sodium Niobate Lead-Free Ceramics. *Journal of the American Chemical Society* **2014,** *136* (7), 2905-2910.

41.   Purusothaman, Y.; Alluri, N. R.; Chandrasekhar, A.; Kim, S.-J., Harnessing low frequency-based energy using a K0.5Na0.5NbO3 (KNN) pigmented piezoelectric paint system. *Journal of Materials Chemistry C* **2017,** *5* (22), 5501-5508.

42.   Yamada, H.; Matsuoka, T.; Kozuka, H.; Yamazaki, M.; Ohbayashi, K.; Ida, T., Crystal structure and phase transition behavior in (K1−xNax)NbO3-based lead-free piezoelectric ceramic over a wide range of temperatures. *Journal of Applied Physics* **2016,** *120* (21), 214102.

43.   Liang, W.; Wu, W.; Xiao, D.; Zhu, J., Effect of the Addition of CaZrO3 and LiNbO3 on the Phase Transitions and Piezoelectric Properties of K0.5Na0.5NbO3 Lead-Free Ceramics. *Journal of the American Ceramic Society* **2011,** *94* (12), 4317-4322.

44.   Zhang, G.; Liao, Q.; Ma, M.; Zhang, Z.; Si, H.; Liu, S.; Zheng, X.; Ding, Y.; Zhang, Y., A rationally designed output current measurement procedure and comprehensive understanding of the output characteristics for piezoelectric nanogenerators. *Nano Energy* **2016,** *30*, 180-186.

45.   Yang, W.; Chen, J.; Zhu, G.; Yang, J.; Bai, P.; Su, Y.; Jing, Q.; Cao, X.; Wang, Z. L., Harvesting Energy from the Natural Vibration of Human Walking. *ACS Nano* **2013,** *7* (12), 11317-11324.

46.   Lee, K. Y.; Kim, D.; Lee, J.-H.; Kim, T. Y.; Gupta, M. K.; Kim, S.-W., Unidirectional High-Power Generation via Stress-Induced Dipole Alignment from ZnSnO3 Nanocubes/Polymer Hybrid Piezoelectric Nanogenerator. *Advanced Functional Materials* **2014,** *24* (1), 37-43.

47.   Taghvaeeyan, S.; Rajamani, R., Portable Roadside Sensors for Vehicle Counting, Classification, and Speed Measurement. *Trans. Intell. Transport. Sys.* **2014,** *15* (1), 73-83.

48.   Wilcox, G.; Mason, J. L., A Temperature Stabilized Tachometer for the Fuel Efficient Automobile. *IEEE Transactions on Consumer Electronics* **1980,** *CE-26* (3), 664-669.

49.   Boys, J.; Green, A. In *Intelligent road-studs-lighting the paths of the future*, IPENZ Annual Conference 1996, Proceedings of: Engineering, providing the foundations for society; Volume 2; Papers presented in the technical programme of the IPENZ Annual Conference held in Dunedin, February 9-13, 1996, Institution of Professional Engineers New Zealand: 1996; p 169.

4.2 Zero-Power Consuming Intruder Identification System by Enhanced Piezoelectricity of $K_{0.5}Na_{0.5}NbO_3$ using Substitutional Doping of BTO NPs

Highlights

> ➤ A zero-power consumed or self-powered intruder system (SPIS) was reported for the first time using the flexible piezoelectric composite film nanogenerator (FPCF-NG) made-up of polydimethylsiloxane (PDMS) and solid state reaction (SSR) based dual perovskite system i.e. $(1-x)K_{0.5}Na_{0.5}NbO_3$- xBaTiO$_3$ (adopted as KNN- xBTO, $x \approx 0$, 0.02, 0.04, 0.06 and 0.08).

> ➤ The tetragonal phase of BTO random nanoparticles (NPs) were doped into the orthorhombic phase of KNN nanocubes (NCs) without altering structural properties, enhancing the piezoelectric properties of parent material.

> ➤ The FPCF-NG device shows excellent flexibility, stability as well as generates a maximum voltage, area power density of 180 V, ≈ 35 mW/m^2 by applying load 4 N.

> ➤ The electrical responses of FPCF-NG were evaluated under various conditions such as weight ratio analysis of the composite films (CFs), electrical poling, switching polarity test, force analysis, capacitor charging, and liquid crystal display (LCD)/ light emitting diodes (LED) lit up.

> ➤ Further, three FPCF-NGs were used to demonstrate a real-time application of SPIS, which can produce a warning alarm/LED glow and display a message in a computer screen upon any intrusion on the device.

Graphical Outline
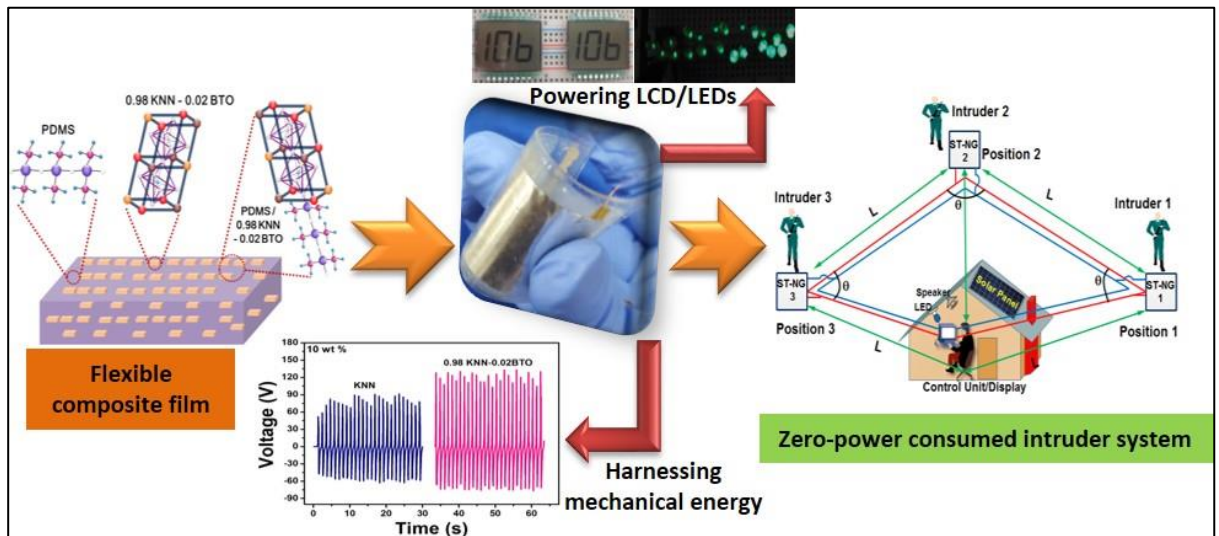
4.2.1 Introduction

Rapid growth in global population impulse to forge the smart societies with the green energy solutions, cost-effective, and long-life efficient security systems. High accuracy, zero power consumed security system are highly desirable to protect the people and their belongings against the burglars/intruders[1]. Recently, UNODC (United Nations Office on Drugs and Crime) reported the rise of burglaries is vast day-by-day[2]. Also, the existing security systems with the PIR sensor and the alarming unit can be identified easily by the intruders. Generally, the usage of burglar alarm starts from residential, commercial to industrial, and military. The survey by statista reveals that approximately 8.4 million and 31 million units of alarms were installed for consumer safety in Europe/North America. It is expected to increase further to 10.6 million and 36 million in the year 2020. Also, 23 % of people in Australia are also using the burglar alarms for their safety purposes[3]. The significant aspect of the alarming system (intruder identification, proximity) is uninterrupted service and accuracy. However, the existed alarming technology (sensor and other components) has a drawback in providing the continuous service due to the utilization of limited life complex battery for powering the alarming system[4].

Moreover, these batteries certain drawbacks large packaging size, power consumption, high cost, and risk of environmental pollution. Mostly passive infrared sensors (PIR sensors, power consumption≈5 to 20 V, 65 mA) will play a pivotal role to identify the intruders (humans or animals) and triggering (sending a signal) the control units (Arduino power consumption≈7-12 V, 50 mA) to pass the alert message to the user[5]. It demonstrates that the whole alarming system will work only when the

80

external power supply is available. Therefore, it is highly necessary and desirable to develop an active alarming system which should not use battery source and proving continuous service all-over the time, good accuracy in intruder identification/position[6, 7]. This could be possible by replacing the PIR sensor with the active sensor (i.e., Nanogenerator) made of $K_{0.5}Na_{0.5}NbO_3$[8-10] based material and external battery with renewable energy source[11].

The advancements on piezoelectric nanogenerators (PNG) as a self-powered sensor[12] (Air pressure sensor[13], photodetectors[14], flexion sensor[15], glucose sensors[16], strain sensor[17] and pressure sensors[18]) were reported extensively over the last decade using various approaches. These are (i) type of materials i.e. inorganic[19], polymer[20], composites[21] (ii) tailored device design types i.e. planar thin film[22], composite thick film[23], wire/fibre[24], stretchable e-skins[25] (iii) controlled growth of various nanostructure morphologies (nanowires[26, 27], nanocubes[28], nanospheres[29], and nanorods[30]) of active piezoelectric materials, (iv) performance improvements by suitable foreign elements doping's into parent lattice respectively[31, 32]. The studies mentioned above were demonstrated that PNG could replace the PIR sensor in alarming system[33].

To demonstrate that a high-performance ferroelectric/piezoelectric nanomaterial was selected to fabricate the flexible piezoelectric composite film nanogenerators (FPCF-NGs). Highly crystalline, lead free perovskite $(1-x)$ $K_{0.5}N_{0.5}NbO_3$- xBaTiO₃ (designated as KNN-xBTO, $x \approx 0.02$, 0.04, 0.06, 0.08) nanoparticles were synthesized by the high temperature solid state reaction (SSR) technique. Further multiple flexible composite films (KNN- xBTO/ Polydimethylsiloxane (PDMS)) were fabricated by the cost-effective, eco-friendly

81

spin coating process. The colloidal solution containing PDMS/KNN- xBTO was spin coated onto an ITO/PET film and cured at 70 °C. PDMS was used for the immobilisation of KNN- xBTO NPs to form composite films. An aluminum foil was attached to the top surface of the as-fabricated composite film serves as a top electrode. A similar protocol has been followed to fabricate the other devices with concentrations of BTO dopants (x values). From that, it was identified that FCPF-PNG ($x\approx0.02$) produces a high piezoelectric output of 180 V/ 1.1 µA upon a perpendicular force of 4 N. Further, a real-time self-triggered intruder identification/object position estimation was demonstrated using the as-fabricated three FCPF-PNG ($x\approx0.02$) devices installed on the top surface of the floor. Next, a primary approach was established to convert the self-triggered[34] intruder system into self-powered intruder system by the utilisation of as-fabricated FCPF-PNGs (works as a sensor) and a commercial solar cell (works as a power source unit). The proposed approach is highly useful in deep forests to find the animal trafficking and also human trafficking in remote border areas between two countries. It can pave the way for a self-powered SMART (Scalable Measures for Automated Recognition Technologies) surveillance technologies[35].

4.2.2 Experimental details

4.2.2.1 Synthesis of KNN and 0.98 KNN- 0.02 BTO nanoparticles

Commercially available powders of potassium carbonate (K_2CO_3, daejung chemicals, 99.99%), sodium carbonate (Na_2CO_3, daejung chemicals, 99.5%), niobium pentoxide (Nb_2O_5, daejung chemicals, 99.9%), titanium dioxide (TiO_2, daejung chemicals, 98%) and barium carbonate ($BaCO_3$, daejung chemicals, 99.95%) were the precursors to formulate stoichiometric KNN and a 0.98 KNN-0.02 BTO NPs by a SSR

method. Pure KNN NPs were synthesised with a firing temperature at 850 °C for 10 h, whereas in the case of a binary solid solution such as 0.98 KNN-0.02 BTO NPs were processed at 1200 °C (Heating rate ≈5 °C min^{-1}) for 2 h. The obtained products (KNN, 0.98 KNN-0.02 BTO) were ground thoroughly over 30 min and centrifuged using hot deionised water (DI) to separate the particles from the big clusters. After that, the wet power poured into a glass Petri dish and dried overnight at 60 °C to get a smooth white powder. Further, the obtained products were heat-treated at 1100 °C for 2 h for better densification and high purity single crystalline phase.

4.2.2.2 Fabrication of PDMS/0.98KNN-0.02BTO piezoelectric composite film (CF) and a nanogenerator

Polydimethylsiloxane (PDMS) monomer and cross-linker were mixed (10:1) for 20 min, under magnetic stirring to obtain a homogeneous solution. To that 5 wt %, 10 wt %, 15 wt % and 20 wt % of 0.98 KNN-0.02BTO NPs were added individually and stirred further for 20 min. The final solution is then degassed to remove the presence of small air bubbles and spin coated on an indium tin oxide/polyethylene terephthalate (ITO/PET) substrate (3.5 cm × 3.5 cm) at 500 RPM for 20 seconds and cured at 70 °C for 1 h. Next, the FPCF-NG device was made b,y attaching aluminium foil (Al) (3 cm × 3 cm) electrodes (Thickness ≈10 μm) on top of the composite layer. The electrical connections were made by attaching copper (Cu) wire Al/CF/ITO/PET using a fine layer of silver (Ag) paste. At last, a thin layer of PDMS film is used as a protecting layer. The devices were electrically poled at 5 kV (22.7 MV/m)/ 24 h before carrying out the electrical output analysis.

4.2.2.3 Measurement system

The phase realisation of the KNN and 0.98 KNN-0.02 BTO NPs were analysed using a powder X-ray diffractometer (XRD, Rigaku, Japan). The X-Ray source wavelength of λ = 1.5406 Å with Cu-Kα radiation working under room temperature with a useful electrical input of 40 kV and 40 mA. The Raman spectrum analysis for all weight ratios of NPs was recorded high quantity micro-Raman spectrometer (LabRAM, Japan) under an excitation source of 514 nm. The surface, thickness and cross-section morphological characterisation of KNN and 0.98 KNN- 0.02 BTO NPs and CFs were analyzed by a field emission scanning electron microscope (FE-SEM, TESCAN, MIRA). Hysteresis measurements were performed using RADIANT technologies precision LC II 10 kV-SC ferroelectric tester. Electrical measurements of FPCF-PNGs were recorded using an electrometer (Keithley-6514) and a picoammeter (Keithley-6485).

4.2.3 Results and discussion

The KNN, (1- x) KNN- xBTO NPs (where x =0.02, 0.04, 0.06, 0.08) were prepared by a cost-effective SSR method and its phase purity was evaluated by X-ray diffractometer/Raman spectroscopy as shown in Figure 4.2.1(a-c). The XRD peak pattern of KNN and 0.02 BTO doped KNN NPs shows an orthorhombic crystalline phase (Reference pattern ICSD No: 01-073-6542) without any peaks of raw materials/by-products and shows a peak splitting at 45° corresponds to the plane of (040)/(004) as shown in Figure 4.2.1a. The evaluated space group/number for the as-prepared pure KNN NPs are pm-m2/25, and the lattice parameters are a≈0.7968 nm, b≈0.802 nm, c≈0.7966, and the corresponding unit cell volume is 0.5090 nm^3

respectively. The KNN lattice parameters/volume values got substantially decreased by the substitutional doping of multiple concentrations of BTO NPs into parent lattice, and the corresponding values were shown in supporting information. At the same time, the huge variation observed in the lattice strain (L)/crystalline size (C) of pure KNN and doped solid solutions ($x \approx 0.02$, 0.04, 0.06, 0.08), and the corresponding results were depicted in Figure 4.2.1b. Here, 0.02 doped solid solution shows higher $C \approx 68$ nm and $L \approx 0.052$ than the pure KNN values (44 nm, 0.02). XRD spectra of KNN-0.02BTO binary solid solution depicts that the exact diffusion of BTO into the parent lattice, which is observed from the unchanged orthorhombic phase present in the parent KNN lattice. If the $x > 0.02$, the C values decrease gradually with increasing the concentrations (0.04, 0.06, and 0.08), but whereas in the case of lattice strain values suddenly dropped and reached to pure KNN value. The convergence of peak split arises at 45° when the dopant BTO concentration (x) increases from 0.02 to 0.04, 0.06, and 0.08, respectively. This demonstrates that the deviation of the orthorhombic phase of KNN to tetragonal crystalline structure corresponds to the lower ferroelectric/piezoelectric polarisation behaviour as shown in Figure 4.2.1b. Further, the Raman spectroscopic studies were performed for all the compositions and the results are shown in Figure 4.2.1c (and supporting Figure S1b). The KNN lattice have six vibration modes actively situated at ν1 (622 cm^{-1}), ν2 (568 cm^{-1}), ν3 (649 cm^{-1}), ν5 (266 cm^{-1}), ν6 (200 cm^{-1}) and ν1+ ν5 (869 cm^{-1}), respectively. The internal/external vibration of cations, i.e., in the NbO_6 polyhedron in the KNN lattice was directly related to the above-discussed vibration modes. From the XRD and Raman spectroscopy, it was confirmed clearly that $x = 0.02$ BTO was the adjusted count for the doping content into the KNN framework without affecting the orthorhombic phase

which has higher piezoelectric property. The P-E loop analyses (applied electric field frequency 200 ms) were performed using the as-prepared KNN and 0.98 KNN- 0.02 BTO pellets as shown in Figure 4.2.1d.
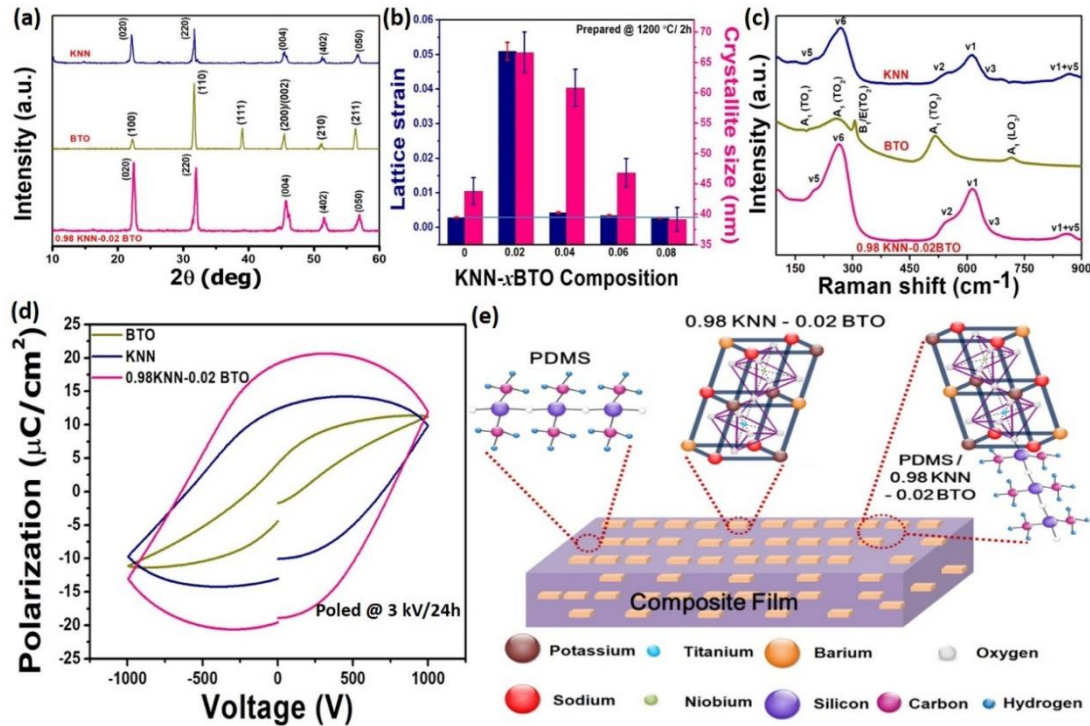
Figure 4.2.1 - Structural analysis and functional characterization of synthesized NPs. (a) XRD spectra KNN, BTO and 0.98 KNN- 0.02BTO NPs (b) Calculated lattice strain and crystalline size of all NPs synthesized by SSR (c, d) Raman spectra and P-E loop measurement of KNN, BTO and 0.98 KNN- 0.02BTO NPs (d) Molecular structure of PDMS, 0.98 KNN- 0.02 BTO and PDMS/0.98KNN- 0.02 BTO.

Here, the as-prepared pellets having a diameter/thickness of 0.9 cm/1.5 mm and fired at 1100°C for 4 h to densify, remove the traces of polyvinyl alcohol (PVA). 0.98 KNN- 0.02 BTO composition shows a soft ferroelectric behaviour with a polarisation of 20 µC/cm^2 at 1000 V, whereas the KNN composition shows an intense polarisation of 10 µC/cm^2 at 1000 V as shown in Figure 4.2.1d. Figure 4.2.1e shows the schematic of as-prepared CF made by the substitution of the 0.98KNN-0.02BTO NPs into the transparent PDMS matrix. The insets show the chemical bond formation

of the PDMS matrix, unit cell configuration of the 0.98KNN-0.02BTO NPs and the interaction of PDMS and 0.98KNN-0.02BTO NPs *via* an oxygen atom. Figure 4.2.3 demonstrates the cost-effective fabrication of the composite film *via* solution casting technique (SCT) and its piezoelectric nanogenerator. It majorly consists of three key steps: (1) synthesis of NPs and its composite solution using suitable polymer matrix, (2) Spin coating process of the composite solution on flexible ITO/PET and thermal treatment at 70 °C, and (3) development of the flexible FPCF-NG. The step-1 represents the SSR method for the synthesis of white coloured 0.98KNN-0.02BTO NPs shown as a digital photograph. The fixed weight ratio of as-prepared NPs was poured into a transparent PDMS solution and mixed thoroughly until to get a whitish coloured composite solution. Step-2 indicates that the fixed amount of composite solution spin coated (500 RPM@20 seconds) on to a flexible ITO/PET substrate (3.5 cm x 3.5 cm) followed by the thermal treatment at 70 °C for 1 h for obtaining the flexible composite film. The flexibility of CFs are shown in digital photographs (Figure 4.2.3).
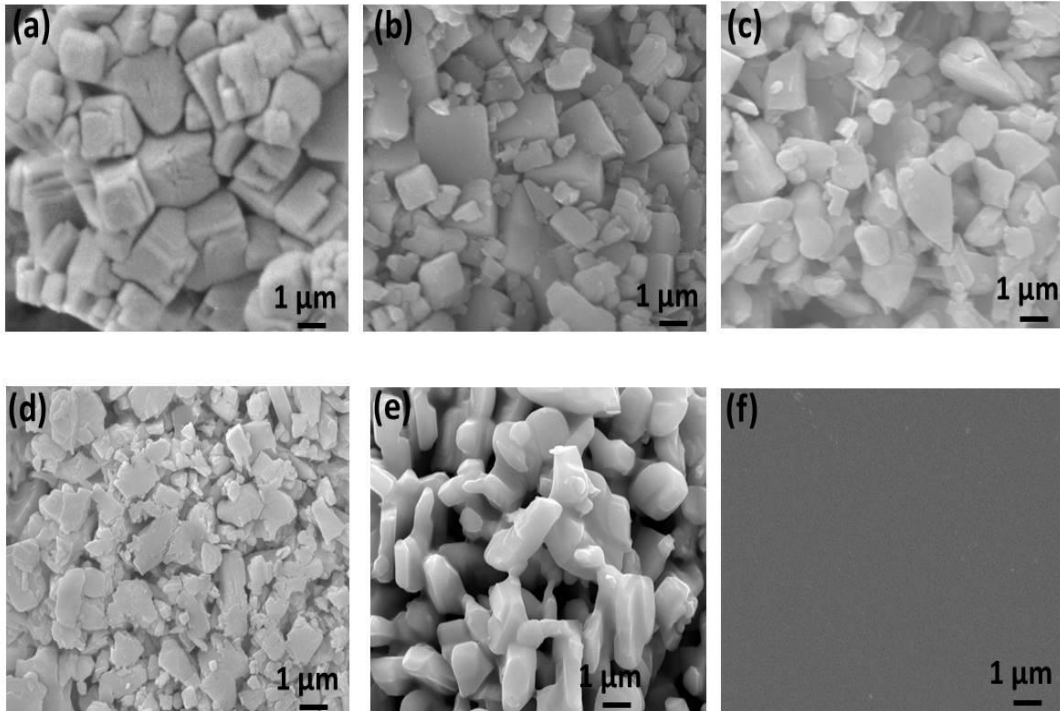
Figure 4.2.2 (a-e) FE-SEM morphology analysis of KNN and (1-*x*) KNN- *x* BTO Nanoparticles (f) FE-SEM surface morphology of plain PDMS film

Before the fabrication of FPCF-NG, the surface morphology of the as-prepared NPs, CFs and thickness analysis of CFs were evaluated using the FE-SEM characterisation. Figure 4.2.3a shows the randomly oriented, high distorted shapes of NPs at 10 μm scale. The magnified image at 100 nm (Figure 4.2.3a) depicts that the randomly oriented NPs (BTO doped KNN) were generated from the distorted shapes of parent KNN nanocubes at 1 μm scale as shown in Figure 4.2.2a. Similar kind of morphology of NPs was observed, when increasing the BTO dopant concentration from 0.02 to 0.04, 0.06 and 0.08 as shown in Figure 4.2.2 (b-e). Figure 4.2.3b shows the cross-sectional images of as-prepared CF demonstrates that the CF has a thickness of 220 μm. The surface analysis (1 μm) of CF reflects the distribution of the randomly oriented piezoelectric NPs into the PDMS matrix as shown in Figure 4.2.3c. On the

other side, the pure PDMS surface shows the smooth surface at 1 μm demonstrated in Figure 4.2.2f. Step-3 schematic demonstrates the development of FPCF-NG by the sandwich process of the four layers such as ITO/PET film, CF, electrode and packing PDMS layer as shown in Figure 4.2.3e. The cross-sectional FE-SEM of FPCF-NG device demonstrates that there is no evidence of air gap in between the layers of the FCPF-PNG device.

The FPCF-NG device was examined to harness the waste mechanical energy into useful electrical energy. Here, as-fabricated poled (5 kV (22.7 MV/m) /12 h) FPCF-NG device (0.98KNN-0.02BTO/PDMS) electrical responses were analysed under various conditions such as weight ratio of 0.98KNN-0.02BTO NPs (0, 5, 10, 15, and 20 wt%) in PDMS matrix, various doping concentrations of CF (PDMS/KNN-xBTO NPs, x=0, 0.02, 0.04, 0.06 and 0.08), electric poling (poling/without poling), switching polarity test, force dependent analysis (1, 2, 4, 5, and 6 N), and stability analysis under constant force. Figure 4.2.4a and b shows the comparison of the electrical responses (open circuit voltage (V_{OC}), short circuit current (I_{SC})) of the KNN/PDMS and 0.98KNN-0.02BTO NPs/PDMS based FPCF-NG devices (10 wt % of NPs) under constant mechanical force (4 N) and its working mechanism shown schematically. Here, the doped CF based FPCF-NG device shows better response (180 V/ 1.1 μA) than the pure NPs based CF based FPCF-NG (130 V/ 0.5 μA) demonstrates that the doping of BTO NPs to KNN parent lattice increases the electrical polarization (observed by the P-E loop analysis), which in turn improves the generated piezoelectric charge carriers across the surface of the film under force condition.

89
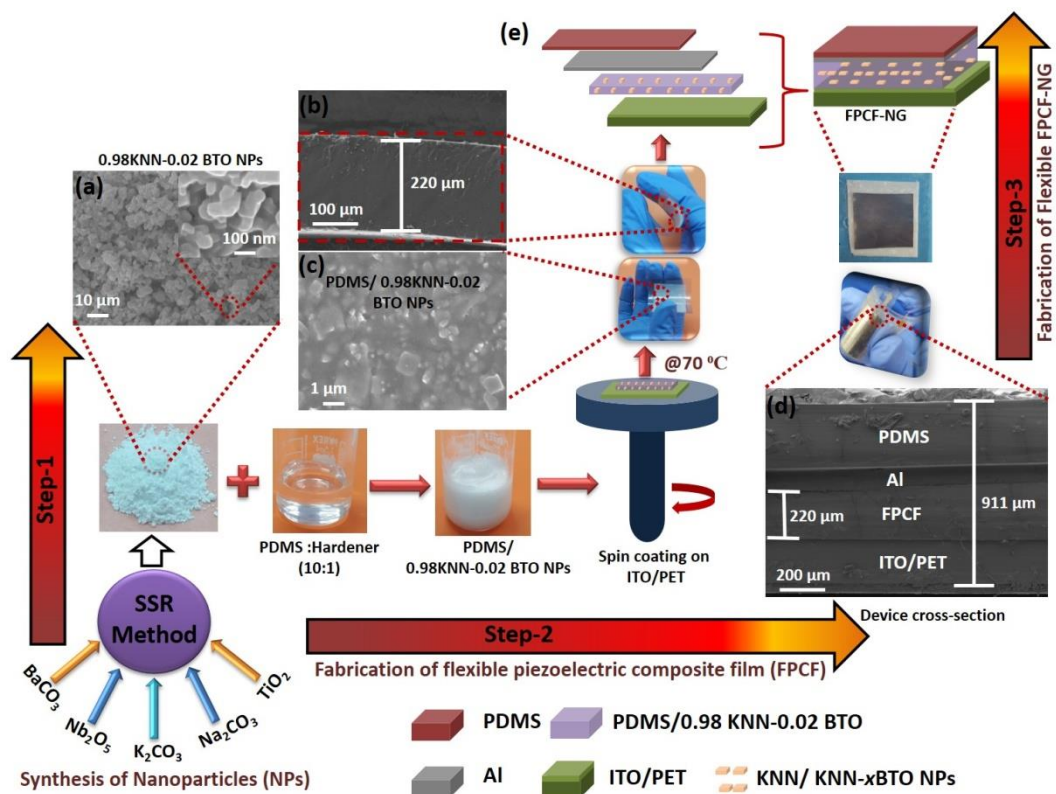
Figure 4.2.3 – Schematically shown the Synthesis procedure for KNN and KNN-xBTO nanoparticles and fabrication of flexible composite films. (a) FE-SEM image of as-synthesized 0.98KNN- 0.02BTO NPs at a scale of 10 μm and the inset shows the magnified image of random NPs at 100 nm. (b, c) Cross-sectional FE-SEM image shows the thickness of the composite film (at 100 μm scale) and surface morphology of uniformly dispersed NPs into the a PDMS matrix. (d) Cross-section FE-SEM image of FPCF-NG device shows no air gap present between active layers confirms the output is not from any other sources. (e) Schematic of FPCF-NG and its device layers. The digital photograph shows as-fabricated FPCF-NG and its flexibility.

Here, 10 wt% of NPs to the CF was optimized for better performance, which is analysed by performing the weight ratio analysis (0, 5, 10, 15 and 20 wt% of 0.98KNN-0.02BTO NPs) of FPCF-NG devices and the corresponding electrical response results under constant force 4 N was shown in Figure 4.2.4. Beyond 10 wt% of NPs in PDMS based FPCF-NG devices generates lower electrical output under constant force (Figure 4.2.4d) due to the agglomeration of NPs, distribution of applied mechanical force on each NPs is not uniform due to the uneven surfaces of the CF.

Next, the unpoled FPCF-NG generates peak-to-peak electrical output (70 V, 0.3 μA) upon 4 N load as shown in Figure 4.2.4c. This output is less compared to the poled FPCF-NG device response demonstrates that the electrical poling will align the maximum number of electric dipoles in one alignment results better performance when applied a force on it (Figure 4.2.4c and d). The efficient binary solid solution, a composite film for NG analysis was optimised not only by the structural, functional characterisations and also by the energy harvesting analysis. Here, the PDMS/KNN-xBTO NPs CFs (x = 0, 0.02, 0.04, 0.06 and 0.08) based NGs were prepared and investigated the energy harvesting performance under constant force. The PDMS/KNN based NG has generated the electrical output of (130 V, 0.5 μA), is increased to (180 V, 1.1 μA) when the BTO concentration (x =0.02) doped to KNN parent lattice, i.e. PDMS/KNN-0.02BTO NPs based NG. If x>0.02, the NG electrical output decreased gradually to (70 V, 0.3 μA) for x=0.04, (60 V, 0.2 μA) for x =0.06 and (55 V, 0.15 μA) for x= 0.08 demonstrate that the optimized BTO concentration is 0.02 to improve the piezoelectric performance KNN. The working mechanism of the FCPF-PNG device contains three key steps such as no force condition (but electrically poled), the perpendicular force applied/removed conditions. During no force but poled condition of the FPCF-NG, the cumulative electric dipole momentum is not zero, but the existed charge carriers are not transferred to the electrodes. When the force applied on the FPCF-NG device, all the electric dipoles orient in one direction results in the opposite charge carriers on the surface of the CF, which is collected by the attached electrodes (electron flow from top to bottom). Exactly opposite phenomena will arise, when the applied force removed on the FPCF-NG device. The V_{OC} and I_{SC} of the FPCF-NG device depend on the piezoelectric coefficient (d_{33}) of the CF can be evaluated as

follows:

$$V_{oc} = (d_{33}/\varepsilon_0 K)\sigma Y t \qquad (4.2.1)$$

Where K, Y, σ and t are dielectric constant, Young's modulus, strain and the thickness of CF, A is the area of FPCF-NG device.

$$I = \dot{q} = \frac{dq}{dt}$$

$$I = \dot{q} = d_{33} AY\dot{\varepsilon} \qquad (4.2.2)$$

Where I is the generated current, $\dot{q}$ is the generated charge rate, d_{33} is the piezoelectric voltage constant, Y is the young's modulus, $\dot{\varepsilon}$ is the applied strain rate and A is the cross-sectional area[36, 37]. The justification of the electrical output analysed from the switching polarity test of the FPCF-NG as shown in Figure 4.2.4e. The forward/reverse connections of FPCF-NG demonstrate an exact phase shift which confirms that the generated output is true, not from any external sources. Next, the FPCF-NG output as a function of force (1, 2, 4, 5, and 6 N) generated from the linear motor was evaluated and the corresponding results were shown in Figure 4.2.4f. The FPCF-NG output increased, gradually from 1 N to up to 4 N and then the decreased when the applied force increased from 4 N. It demonstrates that the optimized force is 4 N for generating the maximum electrical response from the proposed FPCF-NG device.
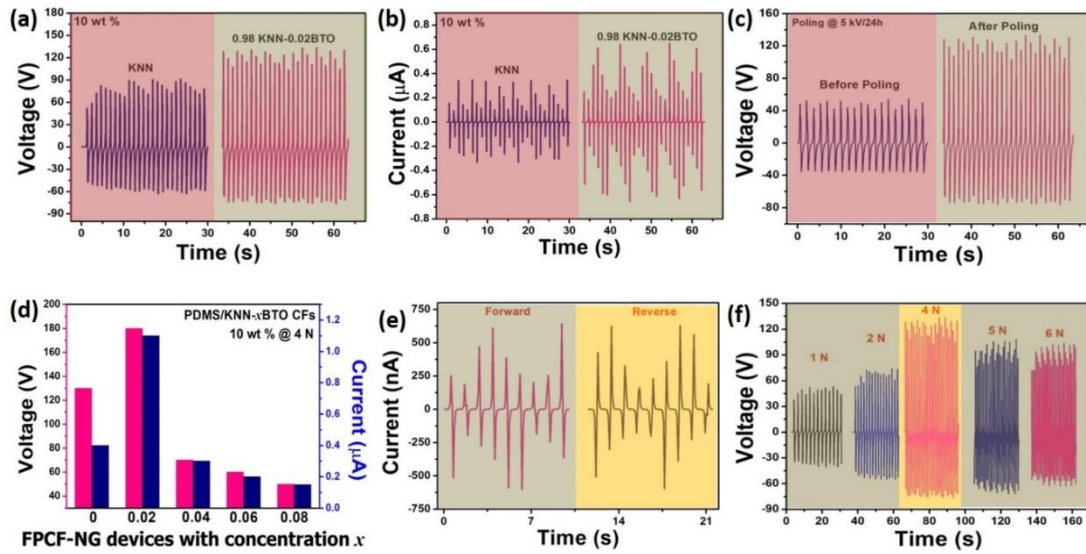
Figure 4.2.4 – Electrical response analysis of FPCF-NG as a function of various forces. (a, b) Voltage and current responses of KNN, 0.98KNN-0.02BTO composite device (10 wt % NPs) upon 4 N force. (c) Electrical poling dependent response of FPCF-NG device (10 wt% of NPs, x=0.02) upon constant mechanical force (4 N). (d) Cumulative output comparison of all FPCF-NGs (x=0.02) upon 4 N force. (e) Switching polarity test of FPCF-NG device (x=0.02) upon 4N force (f) Force dependent electrical response of FPCF-NG device (x=0.02).

Further load resistance analysis, instantaneous power density calculations, commercial capacitor charging/discharging, stability tests and light emitting diodes (LED)/liquid crystal display (LCD) lit up were performed. Figure 4.2.5a shows the load resistance and instantaneous area power density (P_A) investigation of the FPCF-NG device (applied force = 4 N) in the range from 100 Ω to 1 GΩ. Here, the size of the active region is of ≈3 cm × 3 cm, the power density ($P_A = (V^2/(R \times A))$)[38] is maximum ≈35 mW/m^2 at a load resistance of 10 MΩ suggest the adjusted load equivalent resistance (R) for future applications. At a constant force of 4 N, the capacitor rated at 47 nF stores maximum energy of 47.1 μJ. Further with the increase in capacitor rating from 47 nF to 0.22 μF and then to 2.2 μF the corresponding stored energies decreases to 3.97 μJ and 1.1 μJ respectively. The inset Figure 4.2.5b demonstrates the charging /

discharging sequences of a commercial 0.22 µF capacitor upon manifold periods. Figure S6b displays the charging of different commercial capacitors (47 nF, 0.22 µF and 2.2 µF) for a period of 200 s. Figure 4.2.5c shows the stability analysis of the FPCF-NG device where the device does not show any variation in the output over a period of 2000 s. Then the real-time application of the device was initiated by displaying two commercial LCDs and lighting up 20 green LEDs as shown in Figure 4.2.5d.
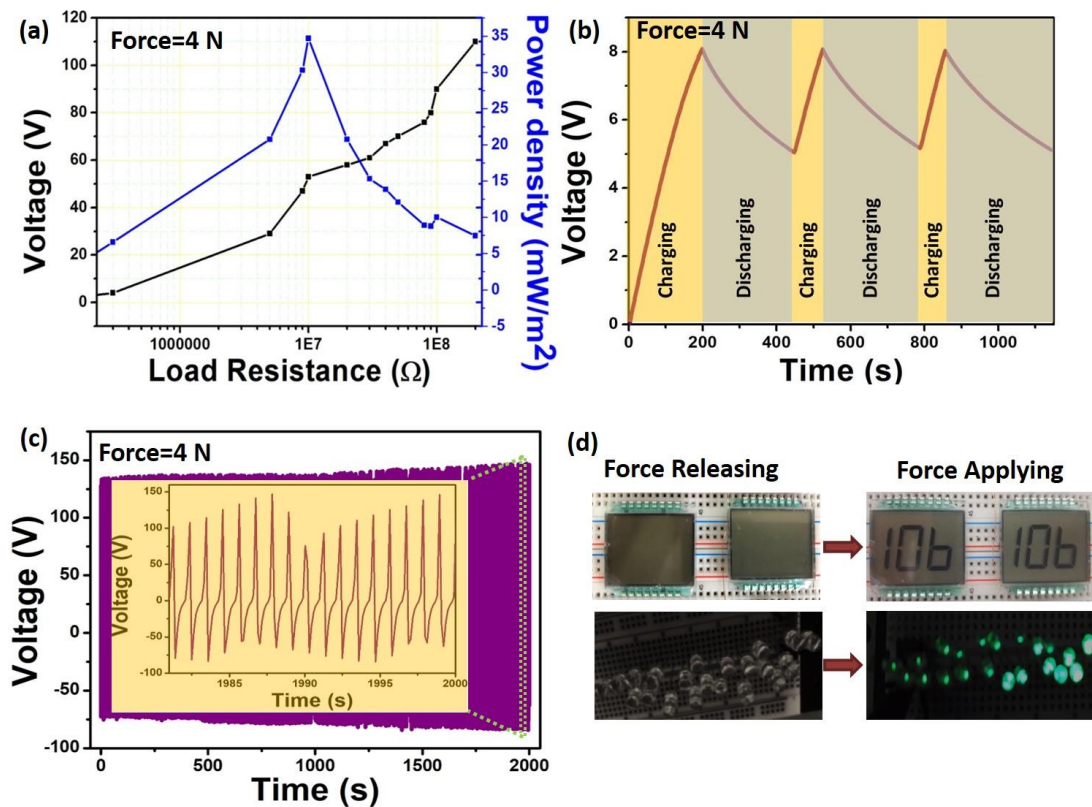
Figure 4.2.5- (a) Load resistance analysis of FPCF-NG (x=0.02) upon 4 N force showing the maximum power density of 35 mW/m² at 10 MΩ. (b) The cyclic response of charging/discharging analysis of commercially purchased (0.22 µF) capacitor upon constant force ON/OFF. (c) Stability test of FPCF-PNG (x=0.02) shows the stable voltage signal for the 2000 s. (d) LCD display/20 LEDs (green) powering by the electrical output of FPCF-PNG device at 4 N force ON/OFF conditions.

Further, a real-time self-triggered/self-powered intruder system (STIS/SPIS) was demonstrated successfully using three FCPF-NGs and programmable controlling unit (Arduino with LED/Buzzer). The development of STIS/SPIS or SMART surveillance system is highly necessary due to the broad utilisation in residential, industry, animal tracking in the forest (or remote areas), and military sectors. Figure 4.2.6a represents the protocol of STIS, i.e. replacement of PIR sensor in conventional burglar alarm system (CBAS) by the as-fabricated FPCF-NGs and SPIS, i.e. replacement of PIR sensor/external battery by FPCF-NGs/solar cell. Uninterrupted service, low cost installation cost, quick response (buzzer sound or LED glow) with respect to any intruder (animal/human/vehicle), position classification/identification, eco-friendly nature, complete replacement of limited life external battery unit are the advantages of the proposed STIS/SPISs than the existed CBAS technology. Figure 4.2.6b shows the proposed schematic to demonstrate the STIS/SPIS consists of continuous monitoring/data recording unit (along with Buzzer and LED) installed inside the home along with solar panel, three FPCF-NGs (as self-triggered NGs, ST-NG) located at distinct positions (P1, P2 and P3) having certain lengths (L)/angles (θ) from control unit and the intruders. Figure 4.2.6c demonstrates the experimental test site to demonstrate STIS/SPIS, the top left inset shows the intruders passing on FPCF-NGs in a random manner and monitoring unit located at the centre, the bottom right inset shows Arduino with LED/Buzzer, LED ON/OFF conditions with respect to intruders, driving Arduino board with the commercial solar panel. Here the position/angles of FPCF-NGs located 300 cm, 250 cm and 83^0, 166^0 from the control unit. FPCF-NG1 sends a triggering signal (shown in Figure 4.2.6e, IT-1 peaks) to the Arduino unit correspondingly both the buzzer/LED is ON over certain period of time,

95

when a first intruder (IT-1) is entering into our test-site through the P1 side and passing over P1 (as shown in left inset figure 4.2.6c) as demonstrated in real time experimental Video@S1. Also, the display unit shows the IT-1 position with location 1 as shown on the right side of Figure 4.2.6d (i).

Similarly, FPCF-NG 2, 3 sends a triggering signal (shown in Figure 4.2.6e, IT-2, IT-3 peaks) individually when an intruders passing over the positions P2, P3 and the corresponding display unit messages were shown in Figure 4.2.6d (ii, iii). Also tested the proposed STIS activity, when an intruders entering all the sides of home or controlling unit through the sides of P1, P2 and P3, the installed FPCF-NG1, 2, and 3 devices were actively sends a triggering signals (shown in Figure 4.2.6e, IT-1, 2, 3 peaks) to Arduino unit correspondingly both the buzzer/LED is ON alerting the near surrounding people and also displayed the intruders locations on the display unit. Here, the asymmetry in triggering signals was observed from the FPCF-NGs (1, 2, and 3) is purely due to the intruder's physical characteristics such as leg movement, frequency, the weight of the body and location of the foot on the FPCF-NGs. Further, the STIS protocol was extended to the SPIS using the commercial solar cell unit to drive the Arduino board unit (i.e., controlling unit). It demonstrates that the battery-driven-CBAS possible to transform into zero-power consumed SPIS using the as-fabricated FPCF-NGs and the renewable energy sources. The proposed devices, the approach can pave the way to develop the self-powered SMART (Scalable Measures for Automated Recognition Technologies) surveillance technologies to be used in areas such as un-manned remote borders of countries, forest locations to protect from wild animals and

also in the house to alert people from burglars at any time.
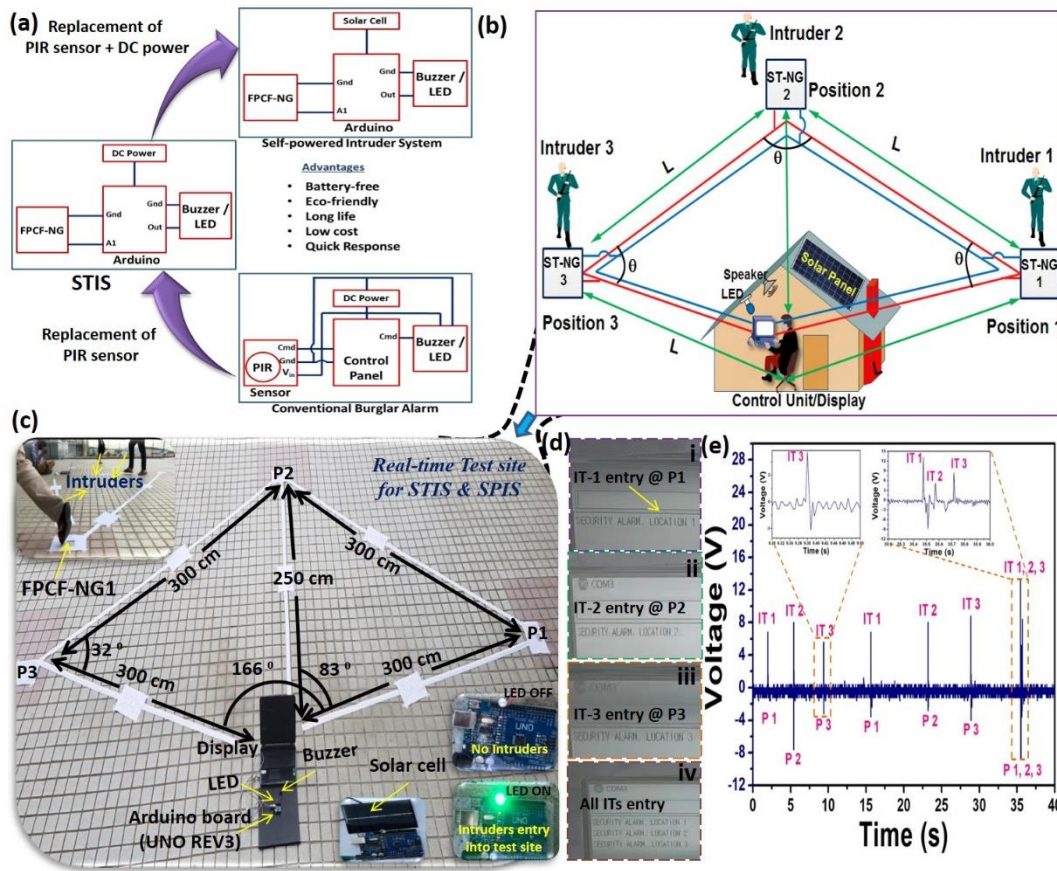
Figure 4.2.6 – a Real-time demonstration of the STIS/SPIS using the multiple FPCF-NGs and solar cell. (a) Schematic approach for a conventional burglar alarm to STIS/SPIS and its advantages. (b) An estimated schematic sight to demonstrate the STIS/SPIS and the establishment of individual components such as FPCF-NGs (or ST-NGs), control unit/display, solar cell, LEDs and Buzzer components. (c) Real-time test site of STIS/SPIS and measurement lengths and position angles from the control unit. The insets show the used components (Arduino board with LED OFF/ON conditions, solar cell and others) and the intruders passing from the device (d) Alert messages/classification of the position of intruders from the display unit when individual intruders are entering the test site, all intruders at a time. (e) Triggering voltage response from the FPCF-NGs when intruders are passing from the devices and its position information.

4.2.4 Conclusion

High remnant polarisation was found for KNN-xBTO NPs with $x \approx 0.02$ than the other dopant concentrations ($x \approx 0$, 0.02, 0.04, 0.06 and 0.08) were synthesized by a cost-effective SSR technique. The eco-friendly spin coating process was used to fabricate the flexible CFs made-up of KNN-0.02BTO NPs, and PDMS matrix and tested these CFs to harness the mechanical energy. The FPCF-NG output was tested under various conditions weight ratio of NPs, force dependent studies, electrical poling conditions, switching polarity test, load resistance analysis, charging/discharging commercial capacitors, stability test (over a period of 2000 s), and powering LEDs/LED devices. The proposed FPCF-NG device produces a high output (180 V, 0.9μA) and the generated instantaneous power density is 35 mW/m^2 at 10 MΩ load resistance upon a force of 4 N. Finally, multiple FPCF-NGs were used to demonstrate the real-time application of STIS/SPIS for the identification of intruders and their position tracking were reported with the help of the Arduino-circuit board. The devices respond to the interaction with the intruders will send a triggering signal (voltage) to the Arduino which eventually drives the buzzer, signal indicators, and displays a message on the computer screen successfully. These results suggest that FPCF-PNG device has a respectable output performance and can be potentially used as a self-triggering system for the detection of any intrusions, unauthorised entry into a building or a specific area. Further, the combined use of FPCF-NGs, solar cell and Arduino-circuit board were demonstrated the SPIS (Zero power consumed) to monitor the unmanned remote borders of countries, forest locations to protect from wild animals and also in the house to alert people from burglars at any time.

4.2.5 References

1.   Ranapurwala, S. I.; Berg, M. T.; Casteel, C., Reporting Crime Victimizations to the Police and the Incidence of Future Victimizations: A Longitudinal Study. *PLOS ONE* **2016,** *11* (7), e0160072.

2.   Persons, G. R. o. T. i., United Nations Office on Drugs and Crime. **Vienna 2016**.

3.   Installed Base of Monitored Alarm Systems in Europe and North America in 2015 and 2020 (in millions). *Techmology and Telecommuncations* **Statista 2015**.

4.   Suresh, S.; Bhavya, J.; Sakshi, S.; Varun, K.; Debarshi, G. In *Home Monitoring and Security system*, 2016 International Conference on ICT in Business Industry & Government (ICTBIG), 18-19 Nov. 2016; 2016; pp 1-5.

5.   Suresh, S.; Anusha, H. N. S.; Rajath, T.; Soundarya, P.; Vudatha, S. V. P. In *Automatic lighting and Control System For Classroom*, 2016 International Conference on ICT in Business Industry & Government (ICTBIG), 18-19 Nov. 2016; 2016; pp 1-

6.   Bai, P.; Zhu, G.; Jing, Q.; Wu, Y.; Yang, J.; Chen, J.; Ma, J.; Zhang, G.; Wang, Z. L., Transparent and flexible barcode based on sliding electrification for self-powered identification systems. *Nano Energy* **2015,** *12*, 278-286.

7.   Chandrasekhar, A.; Alluri, N. R.; Saravanakumar, B.; Selvarajan, S.; Kim, S.-J., A microcrystalline cellulose ingrained polydimethylsiloxane triboelectric nanogenerator as a self-powered locomotion detector. *Journal of Materials Chemistry C* **2017,** *5* (7), 1810-1815.

8.   Han, H.-S.; Koruza, J.; Patterson, E. A.; Schultheiß, J.; Erdem, E.; Jo, W.; Lee, J.-S.; Rödel, J., Hardening behavior and highly enhanced mechanical quality factor in (K0.5Na0.5)NbO3–based ceramics. *Journal of the European Ceramic Society* **2017,** *37* (5), 2083-2089.

9.   Kaftelen, H.; Kanar, D. E.; Repp, S.; Weber, S.; Erdem, E., Investigation of Mn-doped sodium-potassium niobate ((K,Na)NbO3) ceramics by EPR and impedance spectroscopic methods. *Ferroelectrics* **2016,** *494* (1), 11-18.

10.   Purusothaman, Y.; Alluri, N. R.; Chandrasekhar, A.; Kim, S.-J., Harnessing low frequency-based energy using a K0.5Na0.5NbO3 (KNN) pigmented piezoelectric paint system. *Journal of Materials Chemistry C* **2017**.

11.   Zhu, G.; Yang, W. Q.; Zhang, T.; Jing, Q.; Chen, J.; Zhou, Y. S.; Bai, P.; Wang, Z. L., Self-Powered, Ultrasensitive, Flexible Tactile Sensors Based on Contact Electrification. *Nano Letters* **2014,** *14* (6), 3208-3213.

12.   Wang, Z. L.; Song, J., Piezoelectric Nanogenerators Based on Zinc Oxide Nanowire Arrays. *Science* **2006,** *312* (5771), 242-246.

13.   Alluri, N. R.; Chandrasekhar, A.; Kim, S.-J., Exalted Electric Output via Piezoelectric–Triboelectric Coupling/Sustainable Butterfly Wing Structure Type Multiunit Hybrid Nanogenerator. *ACS Sustainable Chemistry & Engineering* **2018,** *6* (2), 1919-1933.

14.   Purusothaman, Y.; Alluri, N. R.; Chandrasekhar, A.; Vivekananthan, V.; Kim, S.-J., Direct In Situ Hybridized Interfacial Quantification to Stimulate Highly Flexile Self-Powered Photodetector. *The Journal of Physical Chemistry C* **2018,** *122* (23), 12177-12184.

15.   Alluri, N. R.; Selvarajan, S.; Chandrasekhar, A.; Saravanakumar, B.; Jeong, J. H.; Kim, S.-J., Piezoelectric BaTiO3/alginate spherical composite beads for energy harvesting and self-powered wearable flexion sensor. *Composites Science and Technology* **2017,** *142*, 65-78.

16.   Slaughter, G.; Kulkarni, T., Highly Selective and Sensitive Self-Powered Glucose Sensor Based on Capacitor Circuit. *Scientific Reports* **2017,** *7* (1), 1471.

17.   Liu, Y.; Hu, Y.; Zhao, J.; Wu, G.; Tao, X.; Chen, W., Self-Powered Piezoionic Strain Sensor toward the Monitoring of Human Activities. *Small* **2016,** *12* (36), 5074-5080.

18.   Qian, J.; Kim, D.-S.; Lee, D.-W., On-vehicle triboelectric nanogenerator enabled self-powered sensor for tire pressure monitoring. *Nano Energy* **2018,** *49*, 126-136.

19.   Dahiya, A. S.; Morini, F.; Boubenia, S.; Nadaud, K.; Alquier, D.; Poulin-Vittrant, G., Organic/Inorganic Hybrid Stretchable Piezoelectric Nanogenerators for Self-Powered Wearable Electronics. *Advanced Materials Technologies* **2018,** *3* (2), 1700249.

20.   Wang, A. C.; Wu, C.; Pisignano, D.; Wang, Z. L.; Persano, L., Polymer nanogenerators: Opportunities and challenges for large-scale applications. *Journal of Applied Polymer Science* **2018,** *135* (24), 45674.

21.   Zhang, C.; Fan, Y.; Li, H.; Li, Y.; Zhang, L.; Cao, S.; Kuang, S.; Zhao, Y.; Chen, A.; Zhu, G.; Wang, Z. L., Fully Rollable Lead-Free Poly(vinylidene fluoride)-Niobate-Based Nanogenerator with Ultra-Flexible Nano-Network Electrodes. *ACS Nano* **2018,** *12* (5), 4803-4811.

22.   Park, D. Y.; Joe, D. J.; Kim, D. H.; Park, H.; Han, J. H.; Jeong, C. K.; Park, H.; Park, J. G.; Joung, B.; Lee, K. J., Self-Powered Real-Time Arterial Pulse Monitoring Using Ultrathin Epidermal Piezoelectric Sensors. *Advanced Materials* **2017,** *29* (37), 1702308.

23.   Vivekananthan, V.; Alluri, N. R.; Purusothaman, Y.; Chandrasekhar, A.; Kim, S.-J., A flexible, planar energy harvesting device for scavenging road side waste mechanical energy via the synergistic piezoelectric response of K0.5Na0.5NbO3-BaTiO3/PVDF composite films. *Nanoscale* **2017,** *9* (39), 15122-15130.

24.   Purusothaman, Y.; Alluri, N. R.; Chandrasekhar, A.; Vivekananthan, V.; Kim, S. J., Regulation of Charge Carrier Dynamics in ZnO Microarchitecture-Based UV/Visible Photodetector via Photonic-Strain Induced Effects. *Small* **2018,** *14* (11), 1703044.

25.   Ghosh, S. K.; Adhikary, P.; Jana, S.; Biswas, A.; Sencadas, V.; Gupta, S. D.; Tudu, B.; Mandal, D., Electrospun gelatin nanofiber based self-powered bio-e-skin for health care monitoring. *Nano Energy* **2017,** *36*, 166-175.

26.   Xu, S.; Hansen, B. J.; Wang, Z. L., Piezoelectric-nanowire-enabled power source for driving wireless microelectronics. *Nature Communications* **2010,** *1*, 93.

27.   Vivekananthan, V.; Alluri, N. R.; Purusothaman, Y.; Chandrasekhar, A.; Selvarajan, S.; Kim, S.-J., Biocompatible Collagen Nanofibrils: An Approach for Sustainable Energy Harvesting and Battery-Free Humidity Sensor Applications. *ACS Applied Materials & Interfaces* **2018,** *10* (22), 18650-18656.

28.   Lee, K. Y.; Kim, D.; Lee, J.-H.; Kim, T. Y.; Gupta, M. K.; Kim, S.-W., Unidirectional High-Power Generation via Stress-Induced Dipole Alignment from ZnSnO3 Nanocubes/Polymer Hybrid Piezoelectric Nanogenerator. *Advanced Functional Materials* **2014,** *24* (1), 37-43.

29.   Chun, J.; Lee, K. Y.; Kang, C.-Y.; Kim, M. W.; Kim, S.-W.; Baik, J. M., Embossed Hollow Hemisphere-Based Piezoelectric Nanogenerator and Highly Responsive Pressure Sensor. *Advanced Functional Materials* **2014,** *24* (14), 2038-2043.

30.   Qiu, Y.; Zhang, H.; Hu, L.; Yang, D.; Wang, L.; Wang, B.; Ji, J.; Liu, G.; Liu, X.; Lin, J.; Li, F.; Han, S., Flexible piezoelectric nanogenerators based on ZnO nanorods grown on common paper substrates. *Nanoscale* **2012,** *4* (20), 6568-6573.

31.   Zhang, Y.; Liu, C.; Liu, J.; Xiong, J.; Liu, J.; Zhang, K.; Liu, Y.; Peng, M.; Yu, A.; Zhang, A.; Zhang, Y.; Wang, Z.; Zhai, J.; Wang, Z. L., Lattice Strain Induced Remarkable Enhancement in Piezoelectric Performance of ZnO-Based Flexible Nanogenerators. *ACS Appl Mater Interfaces* **2016,** *8* (2), 1381-7.

32.   Liu, C.; Yu, A.; Peng, M.; Song, M.; Liu, W.; Zhang, Y.; Zhai, J., Improvement in the Piezoelectric Performance of a ZnO Nanogenerator by a Combination of Chemical Doping and Interfacial Modification. *The Journal of Physical Chemistry C* **2016,** *120* (13), 6971-6977.

33.   Bai, P.; Zhu, G.; Jing, Q.; Yang, J.; Chen, J.; Su, Y.; Ma, J.; Zhang, G.; Wang, Z. L., Membrane-Based Self-Powered Triboelectric Sensors for Pressure Change Detection and Its Uses in Security Surveillance and Healthcare Monitoring. *Advanced Functional Materials* **2014,** *24* (37), 5807-5813.

34.   Jie, Y.; Zhu, H.; Cao, X.; Zhang, Y.; Wang, N.; Zhang, L.; Wang, Z. L., One-Piece Triboelectric Nanosensor for Self-Triggered Alarm System and Latent Fingerprint Detection. *ACS Nano* **2016,** *10* (11), 10366-10372.

35.   Fan, X.; Chen, J.; Yang, J.; Bai, P.; Li, Z.; Wang, Z. L., Ultrathin, Rollable, Paper-Based Triboelectric Nanogenerator for Acoustic Energy Harvesting and Self-Powered Sound Recording. *ACS Nano* **2015,** *9* (4), 4236-4243.

36.   Bowen, C. R.; Taylor, J.; LeBoulbar, E.; Zabek, D.; Chauhan, A.; Vaish, R., Pyroelectric materials and devices for energy harvesting applications. *Energy & Environmental Science* **2014,** *7* (12), 3836-3856.

37.   Chang, C.; Tran, V. H.; Wang, J.; Fuh, Y.-K.; Lin, L., Direct-Write Piezoelectric Polymeric Nanogenerator with High Energy Conversion Efficiency. *Nano Letters* **2010,** *10* (2), 726-731.

38.   Alluri, N. R.; Chandrasekhar, A.; Jeong, J. H.; Kim, S.-J., Enhanced electroactive [small beta]-phase of the sonication-process-derived PVDF-activated carbon composite film for efficient energy conversion and a battery-free acceleration sensor. *Journal of Materials Chemistry C* **2017**.

4.3 A Flexible Piezoelectric Composite Nanogenerator Based on Doping Enhanced Lead-Free Nanoparticles

Highlights

➤ Lead-free (1-x) KNN-xBTO nanoparticles were prepared by solid state reaction method

➤ The composite films were made by mixing the nanoparticles into Polydimethylsiloxane

➤ Composite film made of 10 wt% nanoparticles generates the maximum electrical output

➤ The nanogenerator device is used as an active sensor for sleep monitoring system

Graphical Outline
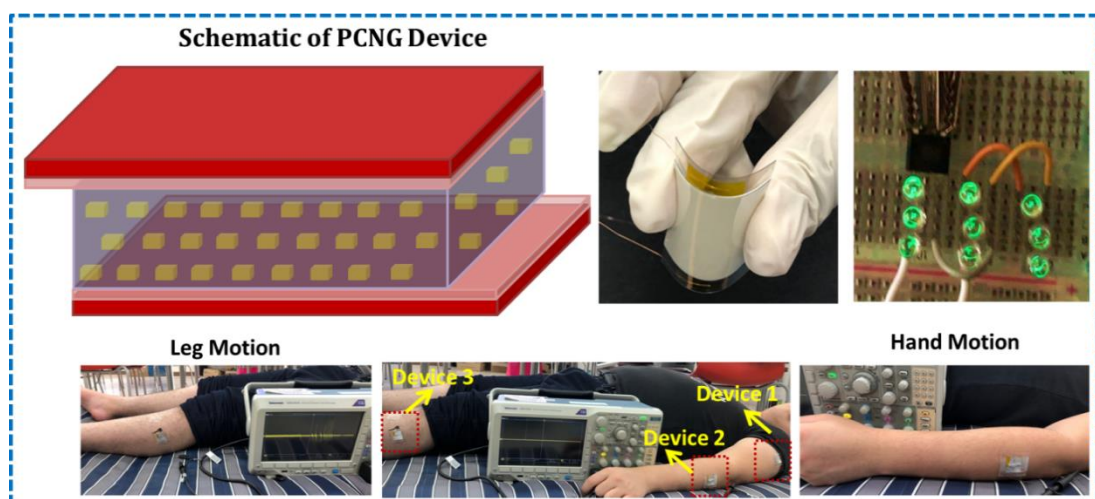
4.3.1 Introduction

Exploration of various non-conventional energy sources and utilizing it in the day-to-day life is one of the most promising challenges. There are various kinds of non-conventional energy sources available in various forms[1]. Among them harvesting electrical energy from ambient mechanical energy is one of the popular approach which can be used as a power source for low power electronic devices. For harvesting mechanical energy, nanogenerators such as triboelectric[2-3], piezoelectric[4], thermoelectric[5] and pyroelectric[6] are utilized. Among that, piezoelectric nanogenerators have various advantages such as high durability and mechanical stability[7]. The promising thing is proper selection of piezoelectric materials for the high electrical output[8]. Materials with perovskite structures such as PMN-PT[9], PZT[10] have high piezoelectric coefficients but lead based materials have several hazardous effect to environment as well as humans[11-12]. So researchers focussing towards lead-free materials with high piezoelectric properties[13].

On the other hand $KNaNbO_3$ (KNN) is a promising lead-free piezoelectric material having the piezoelectric property similar to PZT. But pure KNN have relatively less piezoelectric coefficient which results in less electrical output[14]. There are reports which show the enhancement of piezoelectric property of KNN with proper doping. In this work, a perovskite piezoelectric material $BaTiO_3$ (BTO) is doped into the KNN material without affecting the orthorhombic phase of the KNN i.e. (1-x) KNN-x BTO (x = 0.02, 0.04, 0.06 and 0.08). This enhances the piezoelectric property of the KNN material. The electrical output of the KNN-x BTO (x = 0.02) (58 V/ 450 nA) is higher than the pure KNN (40 V/ 280 nA). Further, the PCNG was used to

demonstrate as an active sensor for sleep monitoring of patients, kids and elder persons.

4.3.2 Experimental details

4.3.2.1 Synthesis of (1-*x*) KNN-*x* BTO NPs and nanogenerator device fabrication

(1-*x*) KNN-*x* BTO NPs (x = 0.02, 0.04, 0.06 and 0.08) were synthesised by SSR method by mixing an equal stoichiometry of commercial potassium carbonate (K_2CO_3), Sodium carbonate (Na_2CO_3), barium carbonate ($BaCO_3$), titanium dioxide (TiO_2) and niobium pentoxide (Nb_2O_5). The reactants were mixed homogeneously using a mortar and pestle and fired at 1200 °C for 2 h at an increasing temperature rate of 5 °C per min. The prepared final product is then washed carefully in DI water to remove the by-products. The synthesis schematic is provided in Figure S1.

PDMS monomer and cross-linker (10:1) were mixed by stirring for 15 min in a magnetic stirrer, to that 10 wt % of (1-*x*) KNN-*x* BTO NPs (x = 0.02, 0.04, 0.06 and 0.08) were added and stirred for 20 min. The solution is then spin coated on to an ITO coated PET (ITO-PET) substrate (3 × 3 cm) and dried for 1 h at 70 °C in a hot air oven. Followed by this the composite film is then covered by attaching a top electrode using an ITO-PET substrate. Then Cu wires were attached on either electrodes using a KAPTON film. The device is then hot pressed over night for the tight adhesion and packaging to form a PCNG. The devices are electrically poled at 5 kV for 12 h before carrying out the electrical analysis. The device schematic and digital photograph of device is shown in Figure 1a.

4.3.3 Results and discussion

Figure 4.3.1a (i-ii) shows the morphology of the synthesized (1-*x*) KNN-*x* BTO NPs (*x* = 0.02, 0.04, 0.06 and 0.08) NPs, the thickness of the CF using FE-SEM and the digital photograph of the PCNG device is shown in Figure 4.3.1a (iii). The nanoparticles exhibit a cubic morphology and the composite film has a thickness of around 150 μm. The structural analysis such as XRD and Raman for the synthesized (1-*x*) KNN-*x* BTO NPs were shown in Figure 4.3.1b and c. The XRD pattern shows the peak splitting at (004) and (402) planes in both the pure KNN and 0.98 KNN- 0.02 BTO, which confirms the orthorhombic phase (exhibits better piezoelectric property). When the *x* value increases from 0.02 the peak at 45° converges and converts to a sole peak. This observation visibly indicates the transformation of phase from orthorhombic to tetragonal.
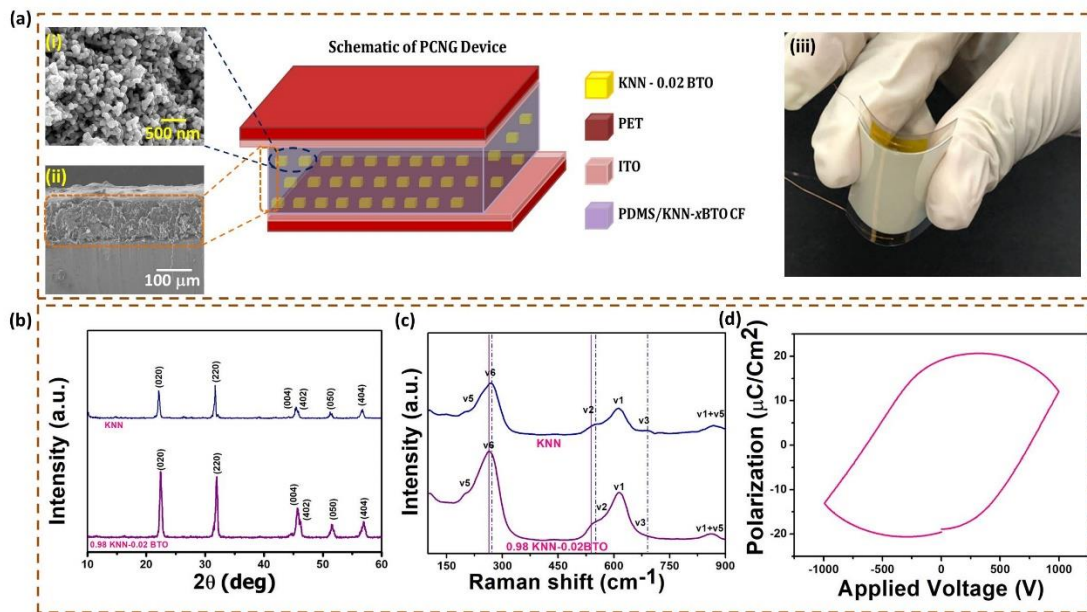
Figure 4.3.1 structural analysis (a) schematic of the PCNG device (i) morphology of the synthesized nanoparticle (*x* = 0.02) (ii) thickness of the composite film with a scale bar of 100 μm (iii) digital photograph of PCNG device. (b) XRD analysis (c) Raman analysis (d) P-E loop measurement of KNN-0.02 BTO

The XRD patterns are matched exactly with the ICSD card number 01-073-6542. The Raman analysis shows the atomic vibrations of the NPs with the orthorhombic phase of six active modes placed at 869 cm^{-1}, 649 cm^{-1}, 621 cm^{-1}, 568 cm^{-1}, 267 cm^{-1} and 200 cm^{-1}. When the x value increases there is a slight peak shift and the intensity of the peak varies. The P-E loop measurement was done for the KNN-0.02 BTO shown in Figure 4.3.1d and a maximum polarization of 20 μC/cm^2 was obtained under an applied voltage of 1000 V.

The working mechanism of the PCNG is shown in Figure 4.3.2a. When a perpendicular force acts on the device, the electric dipoles align in a single direction leads to the creation of potential difference across both the electrodes. This causes the current to flow from top to bottom electrode through an outer circuit as shown in Figure 4.3.2a (i). When the force gets released, the electric dipoles reverses and makes the current to flow from the bottom to top electrode as shown in figure 4.3.2a (ii). In order to orient the maximum dipoles in a single direction, the PCNG device should be poled electrically. Here, the device gets poled at an applied electric potential of 5 kV for 12 h. The electrical output enhances after the poling has done which is shown in Figure 4.3.2b. To identify the maximum output with respect to force using the linear motor, the electrical output was measured with different force (2 N, 4 N, 6 N, 8 N, 10 N and 12 N). The generated electrical output is maximum at 10 N (58 V peak to peak), with the further increase in the force to 12 N the electrical output drops to 35 V. This clearly shows that the device gets depolarized with large force as shown in Figure 4.3.2c. The further analysis has been performed at a force of 10 N. Figure 4.3.2d and e shows the electrical output of KNN, KNN- 0.02 BTO and BTO NPs, in which the KNN- 0.02 BTO NPs shows the maximum electrical output of 58 V/ 450 nA. Figure 4f shows the

weight ratio analysis of KNN- 0.02 BTO NPs in which the 10 wt % composite film generates the maximum electrical output (58 V/ 450 nA). The doped PCNG device (PCNG 2 (KNN- 0.02 BTO)) shows the maximum electrical output compared to pure KNN (PCNG 1) device generating an electrical output of 40 V/ 280 nA and the other doped devices such as KNN- 0.04 BTO (PCNG 3), KNN- 0.06 BTO (PCNG 4), KNN- 0.08 BTO (PCNG 5) as shown in Figure 4.3.2g. The device has a maximum power density of 3.25 mW/m^2 at 10 MΩ load resistance.
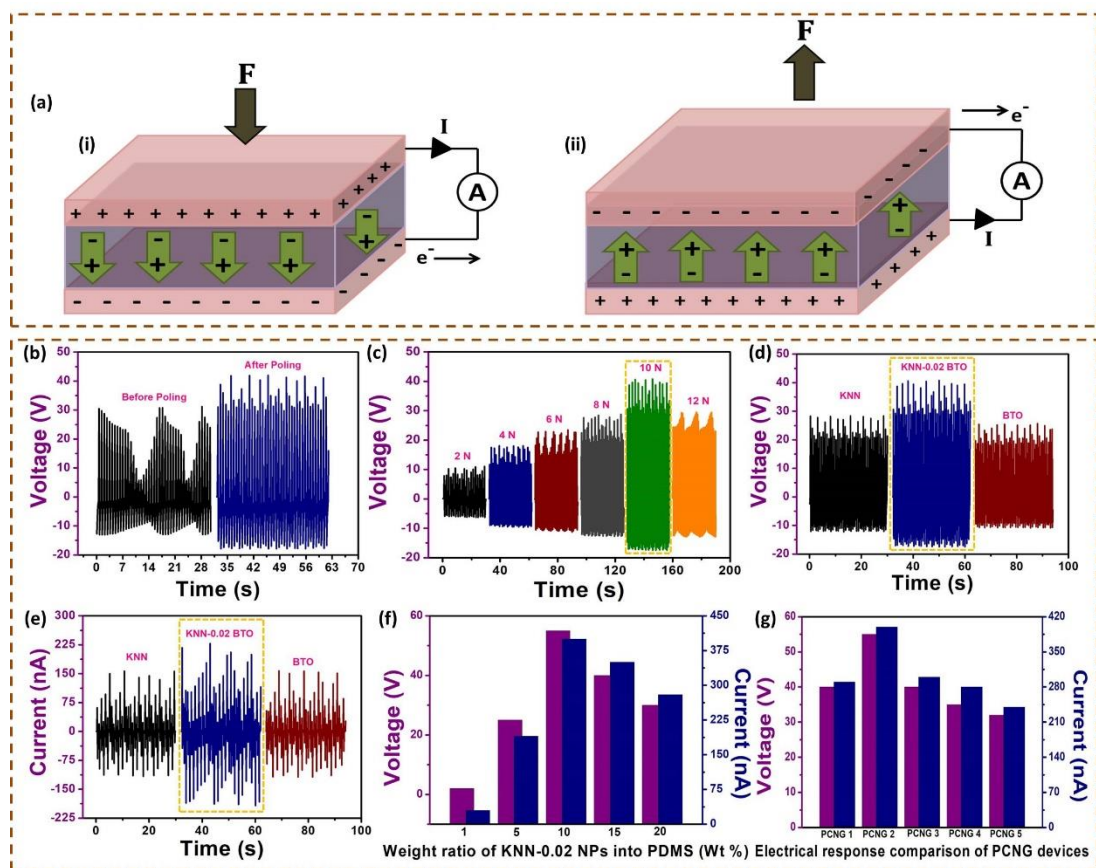
Figure 4.3.2- (a) Working mechanism of the PCNG device (b) electrical output before and after poling (c) force analysis of PCNG (d-e) voltage and current output of the PCNG (f) weight ratio analysis of the KNN-0.02 NPs into PDMS (g) electrical response comparison of PCNG devices.

To demonstrate the capability of the PCNG in the real-time applications, capacitors (47 nF, 0.22 µF and 1 µF) were charged by the PCNG device for a duration of 150 seconds. The energy stored in terms of voltage decreases from 24 V to 2 V when the capacitance value increases from 47 nF to 2.2 µF which is shown in Figure 4.3.3a and the inset shows the charging method during force applied and releasing. To prove the durability of the PCNG device a stability test was performed for a period of 1000 seconds each day for seven consecutive days as shown in Figure 4.3.3b. The PCNG device works actively without any change in the electrical output. Figure 4.3.3c shows the LED lit up using PCNG device where 9 green LEDs were lit up in a parallel connection mode. The PCNG device is then tested as an active sensor for self-powered sleep monitoring system. The PCNG device is placed in various positions in the hand and leg to monitor the person's movement during the sleeping condition. The schematic of self-powered sleep monitoring system is shown in Figure 4.3.3e. Figure 4.3.3d and f shows the electrical response of the leg and hand motion during the person's movement at sleep. From this result we can confirm that the PCNG is an active candidate in sensing the body movement which in turn can make a path to smart health care monitoring system.
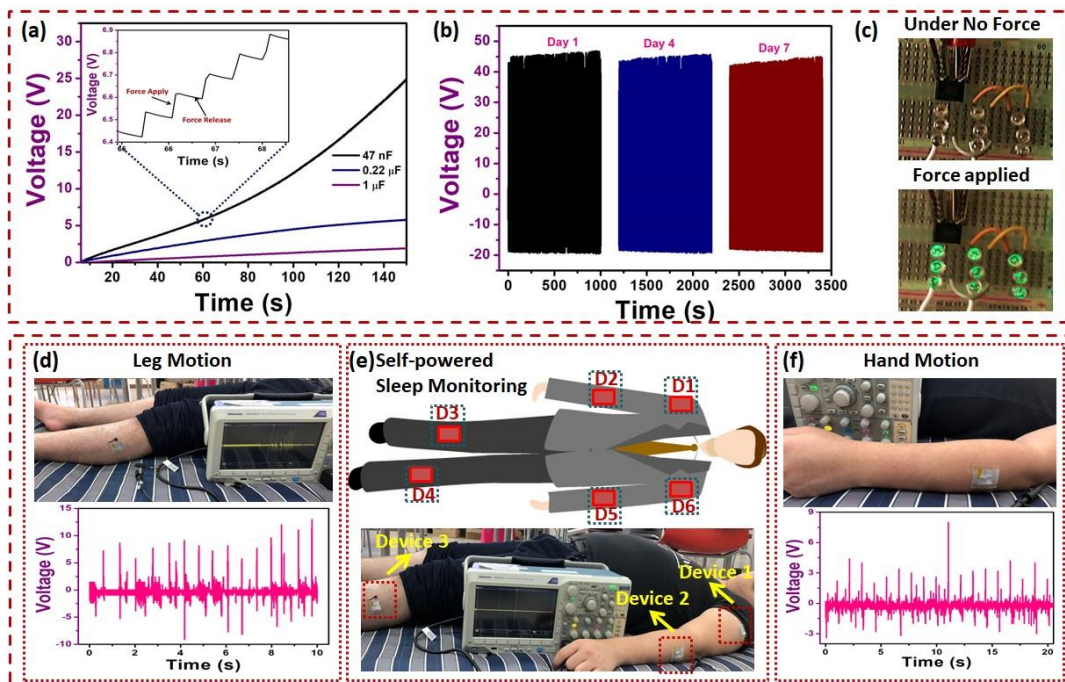
Figure 4.3.3- (a) Capacitor charging analysis (b) Stability test for a period of 7 days (c) LED lit up (d) real-time sleep monitoring system with leg motion (e) schematic and device position of self-powered sleep monitoring (f) real-time sleep monitoring system with hand motion.

4.3.4 Conclusion

In summary, a lead-free flexible piezoelectric composite nanogenerator was fabricated using (1-x) KNN-x BTO NPs (x = 0.02, 0.04, 0.06 and 0.08) NPs. Successful doping of BTO into the KNN lattice without affecting its orthorhombic phase has been achieved using SSR method. The PCNG device made of x = 0.02 generates a maximum electrical output of 58 V and 450 nA compared to the other doping materials and pure KNN. Further weight ratio analysis, capacitor charging, force analysis and LED lit up had been performed successfully. Finally, the PCNG device is used for the sleep monitoring system for the patients, kids and elders. Also, this type of system can be used for the diagnosis of sleeping disorders and other neurological disorders. Hence, these findings make a strategy to achieve a mobile health monitoring in the modern health care management fields.

4.3.5 References

1.   Jeyaraman, A. R.; Balasingam, S. K.; Lee, C.; Lee, H.; Balakrishnan, B.; Manickam, S.; Yi, M.; Kim, H.-J.; Sivalingam Nallathambi, K.; Jun, Y.; Kuzhandaivel, H., Enhanced solar to electrical energy conversion of titania nanoparticles and nanotubes-based combined photoanodes for dye-sensitized solar cells. *Materials Letters* **2019,** *243*, 180-182.

2.   Wang, S.; Lin, L.; Wang, Z. L., Triboelectric nanogenerators as self-powered active sensors. *Nano Energy* **2015,** *11*, 436-462.

3.   Chandrasekhar, A.; Khandelwal, G.; Alluri, N. R.; Vivekananthan, V.; Kim, S.-J., Battery-Free Electronic Smart Toys: A Step toward the Commercialization of Sustainable Triboelectric Nanogenerators. *ACS Sustainable Chemistry & Engineering* **2018,** *6* (5), 6110-6116.

4.   Wang, Z. L.; Song, J., Piezoelectric Nanogenerators Based on Zinc Oxide Nanowire Arrays. *Science* **2006,** *312* (5771), 242-246.

5.   Yang, Y.; Guo, W.; Pradel, K. C.; Zhu, G.; Zhou, Y.; Zhang, Y.; Hu, Y.; Lin, L.; Wang, Z. L., Pyroelectric Nanogenerators for Harvesting Thermoelectric Energy. *Nano Letters* **2012,** *12* (6), 2833-2838.

6.   Wang, Z.; Yu, R.; Pan, C.; Li, Z.; Yang, J.; Yi, F.; Wang, Z. L., Light-induced pyroelectric effect as an effective approach for ultrafast ultraviolet nanosensing. *Nature Communications* **2015,** *6*, 8401.

7.   Vivekananthan, V.; Alluri, N. R.; Purusothaman, Y.; Chandrasekhar, A.; Kim, S.-J., A flexible, planar energy harvesting device for scavenging road side waste mechanical energy via the synergistic piezoelectric response of K0.5Na0.5NbO3-BaTiO3/PVDF composite films. *Nanoscale* **2017,** *9* (39), 15122-15130.

8.	Alluri, N. R.; Chandrasekhar, A.; Kim, S.-J., Exalted Electric Output via Piezoelectric–Triboelectric Coupling/Sustainable Butterfly Wing Structure Type Multiunit Hybrid Nanogenerator. *ACS Sustainable Chemistry & Engineering* **2018,** *6* (2), 1919-1933.

9.	Ran Han, K.; Wung Jeong, J.; Kim, C.-S.; Kwon, Y.-S., Low-temperature fabrication of 0.65 PMN–0.35 PT by a mixed oxide method. *Materials Letters* **2006,** *60* (29), 3596-3600.

10.	Ohno, T.; Fukumitsu, K.; Honda, T.; Sakamoto, A.; Tanaka, S.; Hirai, S.; Matsuda, T.; Sakamoto, N.; Suzuki, H., Piezoelectric properties of a near strain-free lead zirconate titanate thin films deposited on a Si substrate. *Materials Letters* **2018**.

11.	Jeong, C. K.; Park, K. I.; Ryu, J.; Hwang, G. T.; Lee, K. J., Large-Area and Flexible Lead-Free Nanocomposite Generator Using Alkaline Niobate Particles and Metal Nanorod Filler. *Advanced Functional Materials* **2014,** *24* (18), 2620-2629.

12.	Balasingam, S. K.; Kang, M. G.; Jun, Y., Metal substrate based electrodes for flexible dye-sensitized solar cells: fabrication methods, progress and challenges. *Chemical Communications* **2013,** *49* (98), 11457-11475.

13.	Vivekananthan, V.; Alluri, N. R.; Purusothaman, Y.; Chandrasekhar, A.; Selvarajan, S.; Kim, S.-J., Biocompatible Collagen Nanofibrils: An Approach for Sustainable Energy Harvesting and Battery-Free Humidity Sensor Applications. *ACS Applied Materials & Interfaces* **2018,** *10* (22), 18650-18656.

14.	Wu, M.; Zheng, T.; Zheng, H.; Li, J.; Wang, W.; Zhu, M.; Li, F.; Yue, G.; Gu, Y.; Wu, J., High-performance piezoelectric-energy-harvester and self-powered mechanosensing using lead-free potassium–sodium niobate flexible piezoelectric composites. *Journal of Materials Chemistry A* **2018,** *6* (34), 16439-16449.

CHAPTER V

A Highly Reliable, Impervious and Sustainable Triboelectric Nanogenerator as a Zero-power Consuming Active Pressure Sensor

Highlights

> The present manuscript overcomes the humidity issues by the introduction of an impervious TENG concept, where we restrict the effect of humidity which is the main reason for affecting the device performance.

> The device is extremely light weight and generates a maximum power density ~17 mW/m^2. Also, it is highly reliable and stable for a long period.

> The electrical output of TENG device was tested under various percentages of relative humidity from 10% R-H to 99% R-H.

> Under both humid and dry conditions, the electrical output is stable without any interruptions.

> Further, the device was used to demonstrate a real-time application of scavenging bio-mechanical energy and also been used for zero power consuming/ self-powered pressure sensing applications.

Graphical Outline

WR-SE-TENG device

Bio-mechanical Energy Scavenging

Water Proof , Humidity Resistant

Zero-Power Consuming Sensor
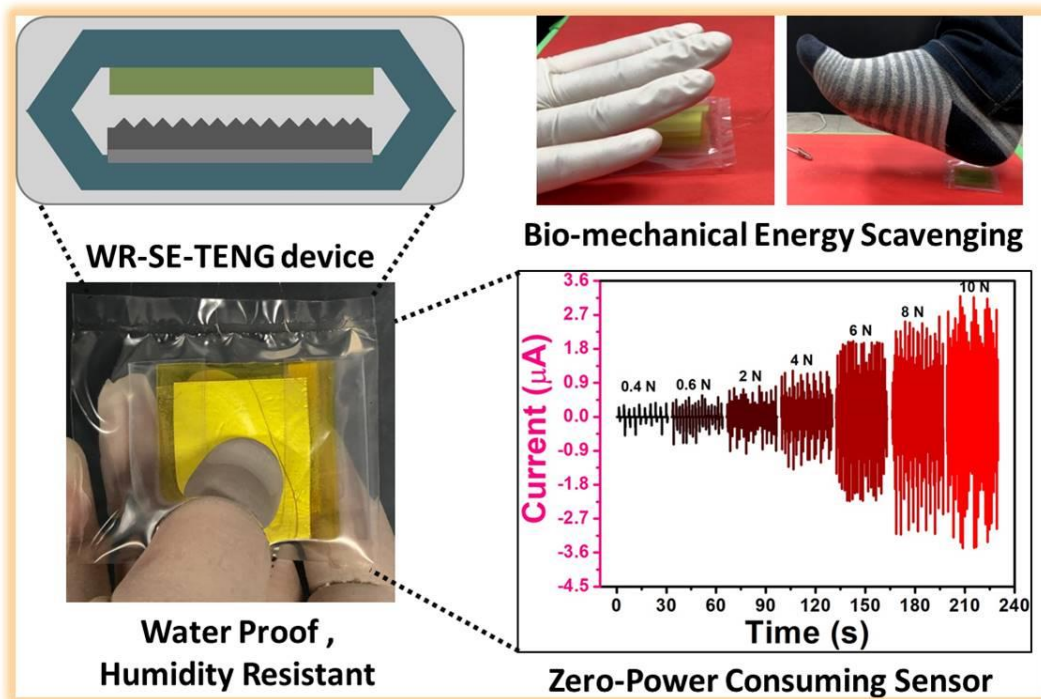
5.1 Introduction

Energy harvesting technologies are recently been the trending topic which has the potential to bring solutions to the global energy crisis. In the recent years harvesting energy from sustainable energy sources such as wind[1], water wave[2-3], bio-mechanical[4-5] and vibrational[6-7] sources gained immense attention due to its simpler energy conversion ability. Among these sources, energy harvesting from mechanical motions have expanded due to the abundant mechanical energy in our day-to-day life. Triboelectric nanogenerators (TENGs) are considered to be the promising candidate for harvesting mechanical energy from various sources such as tidal[3], ocean wave[8-9], human motions[10], and strain[11]. Because of their simple design, cost-effective fabrication, highly reliable output performance and durability many researchers are working towards its commercialization[4]. The first ever TENG has been reported by Z.L. Wang's group in 2012 for harvesting mechanical energy[12] and been utilized for small scale energy harvesting. Now, TENGs have been improved further with technological advancements and used form energy harvesting to various applications in self-powered sensors[13-15]. In addition, many researchers are working to improve the output performance of the TENG by modifying the device structure, improving the surface contact area and other doping process. In general, TENG work on two major effects called triboelectrification and electrostatic induction. When two dissimilar triboelectric materials come into contact with each other either in vertical contact and separation or lateral sliding motion, a surface charge develops on the layers and drives the electrons to flow through an external load with the production of a potential drop[16]. This shows that proper selection of active layers is the major paradigm in designing a high performance TENG device.

118

Next, to design the high performance TENG device two key factors needs to be considered (i) the surface charge generation increases with increase in applied pressure (ii) surface charge increases with increase in contact points according to Volta-Helmholtz hypothesis[17]. The most suitable route to multiply the contact point is to create surface roughness on the active layers. There are a lots of techniques carried out to create surface roughness such as photolithography, reactive ion etching, inductively coupled plasma etching, thermal imprint lithography[18-20]. But these techniques involve high cost, careful operation, and time consuming[21]. Similarly, there is a major drawback that TENGs have been facing is, it's stability under moist and humid environmental conditions[22]. There are many strong evidences proved that the output performance of the TENGs have been reduced drastically with respect to humidity which eventually blocks its way towards the full-fledged commercialization on day – to-day usage[23-25]. Recently, TENGs have been designed as humidity resistant by developing its active layers by adopting super hydrophobic techniques[26]. But still, the selection of materials, cost and time consuming process makes this as a complicated process.

To overcome the above process, the present manuscript reports a water-resistant silicone elastomer based triboelectric nanogenerator (WR-SE-TENG) which is impervious in nature. The device was configured with metal-dielectric configuration using nickel (Ni) foam and micro roughness created silicone elastomer film as active triboelectric layers. The silicone elastomer film was made via an easy and cost-effective soft lithography technique using a commercial micro roughness sand paper. The Ni foam in general having a porous networked structure contributes to high surface roughness was used directly as a positive triboelectric layer. Ni foam having a porous

nature could not damage the roughness on the silicone elastomer layer during the contact and separation process, making the output to be stable for a prolonged duration. The device was laminated using a polyethylene sheet with the help of a pouch laminator inside a glove box. The packing resists the water and humidity which is responsible for affecting the performance of the TENG. The output performance of the silicone elastomer (SE-TENG) device with different positive layers such as Aluminum (Al), Copper (Cu), and Nickel (Ni) foam have also been compared. Among them SE-TENG made of Ni foam as positive layer generates a maximum voltage and current of ~370 V/ 6.1 μA with a maximum area power density of ~17 mW/m^2 at 1GΩ load resistance. The stability of SE-TENG was analyzed for 2000 s and the stability of WR-SE-TENG was analyzed under various percentages of relative humidity ranging from 10 % RH to 99 % RH. This approach proves that the device has been protected from humidity as well as stable in its output performance without decreasing its efficiency. The device was used successfully for charging commercial capacitors, glowing light emitting diodes (LEDs) and powering up electronic wrist watches. Further, the WR-SE-TENG device was used for scavenging bio-mechanical energy from human motions such as finger tapping, palm tapping and foot tapping and LED glowing under bio-mechanical motions. The above experiments and tests prove that the WR-SE-TENG device is a promising sensor device to work under harsh and humid weather conditions.

5.2 Experimental section

5.2.1 Fabrication of silicone elastomer film by soft lithography technique

The negative triboelectric material was made by replicating the micro rough pattern on the sand paper through the soft lithography technique. The dielectric layer was made by mixing an equal volume ratio of 1:1 (Ecoflex silicone 00-30) liquid silicone in a beaker followed by pouring it on to a sand paper. The liquid silicone poured sand paper is then kept in 30 °C and allow it to cure for 6 h. After curing, the silicone film was peeled off slowly from the sand paper to obtain the roughness created silicone film.

5.2.2 Fabrication of water-resistant SE-TENG device

Next, to fabricate the TENG device, two PET films with the dimensions of 4×4 cm^2 were used as the supporting frames in the contact and separation device. Aluminum (Al) foils with an area of 3×3 cm^2 were attached on the bottom PET film through center, followed by attaching the copper (Cu) wires using silver paste. Then, the silicone film was cut in to the dimension of 3×3 cm^2 and attached on the Al foil. To fabricate the positive layer, nickel (Ni) foam was selected and attached in to the top PET sheet using a double sided tape and Cu electrodes were attached in the similar fashion. Further two more TENG devices were fabricated using Al and Cu as positive electrodes for the comparison and performance analysis of TENG device. Further, the device is covered with polyethylene and sealed completely using a pouch laminator to make a WP-TENG.

제주대학교 중앙도서관
JEJU NATIONAL UNIVERSITY LIBRARY
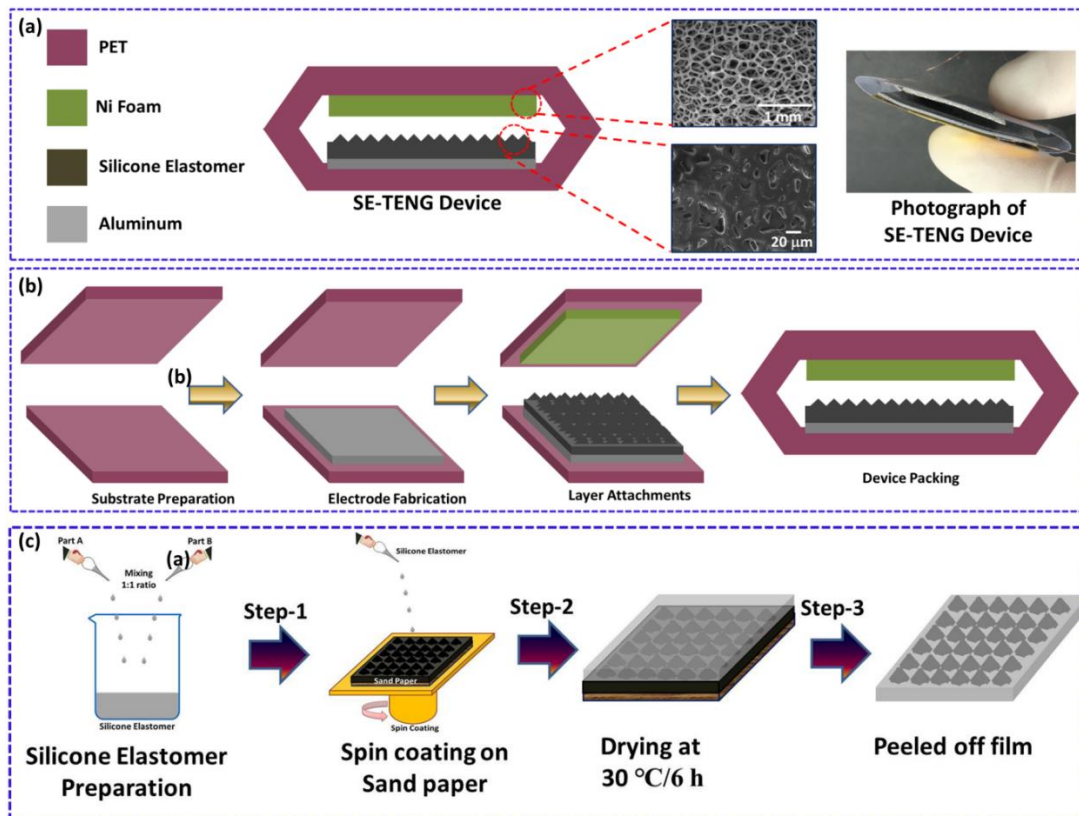
Figure 5.1- SE-TENG device schematic and fabrication. (a) Layer-by-layer Schematic of SE-TENG device and the inset show the FE-SEM morphology of porous Ni foam and roughness created silicone elastomer film with the photograph of device. (b) Step by step schematic showing the SE-TENG device fabrication with every working layer used in the device. (c) Step-by-step fabrication of silicone elastomer film from liquid silicone via soft lithography technique using micro roughness sand paper.

5.2.3 Characterization and electrical measurement

The surface morphology of the Ni foam and micro roughness silicone films were characterized using a field emission scanning electron microscope (FE-SEM, TESCAN, MIRA 3). The electrical output analysis such as voltage and current were measured using an electrometer (Keithley 6514 Instruments Inc., USA) and SR 570 low noise current amplifier (Stanford research Systems, USA). The external force for measuring the electrical output was applied using a linear motor (LinMot, Inc.,

Switzerland). A software platform using LabVIEW was built for real-time data acquisition and electrical analysis. A grounded home-made faraday cage was set up for electrical measurements.

5.3 Results and discussions
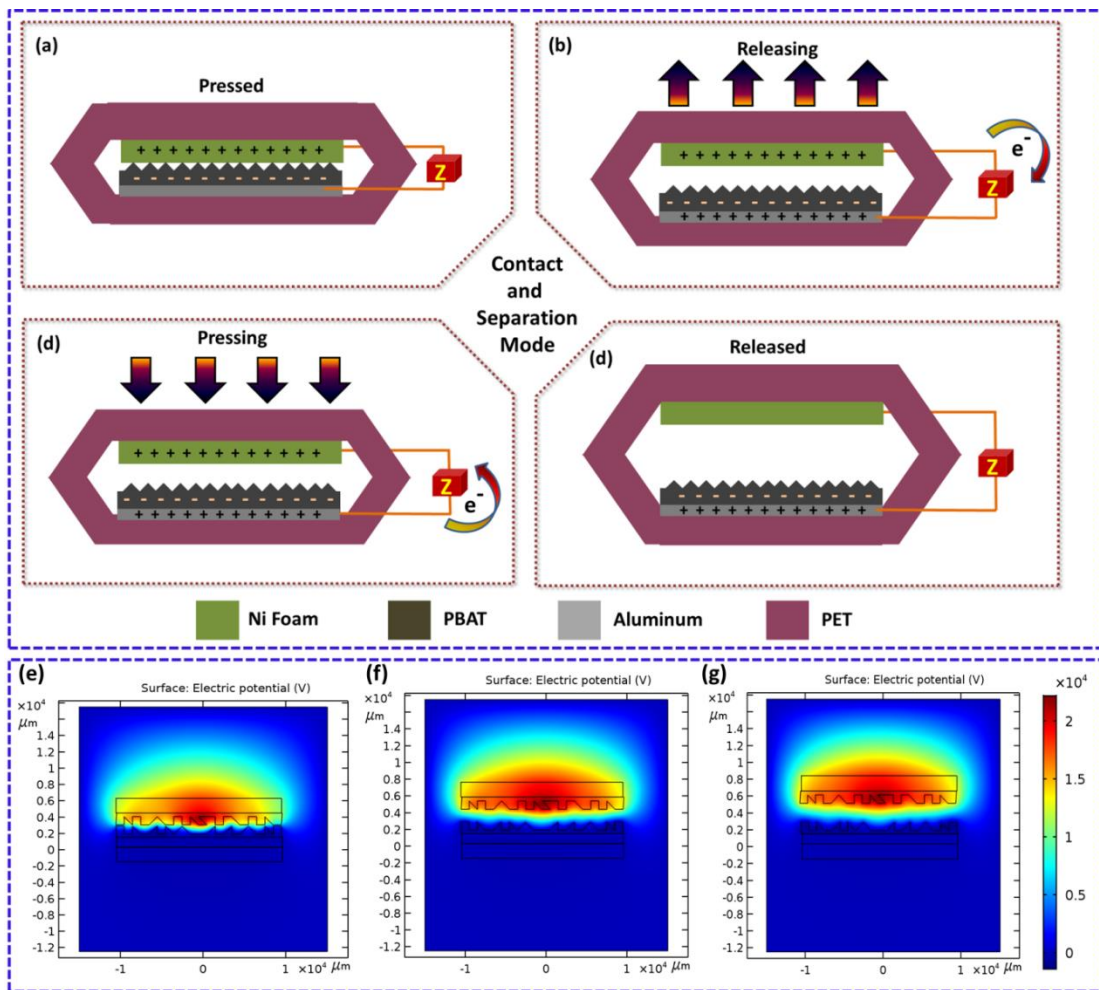
Figure 5.2- Working mechanism of SE-TENG. (a-d) Contact and separation mode working mechanism of SE-TENG device with pressing and releasing motion and the respective electron flow directions. (e-g) Potential distribution of SE-TENG at various separation distances using COMSOL software.

Figure 5.1a shows the layer by layer schematic of the SE-TENG device and its digital photographic image. The triboelectric layers are made of nickel foam and roughness created PDMS film. The FE-SEM image shows the structure of Ni foam and the micro roughness created via soft lithography technique. Figure 5.1b shows the step by step fabrication of SE-TENG device. The device fabrication starts with the preparation of supporting substrates for the contact and separation based TENG followed by placing electrodes on either side. The electrodes itself acts as positive triboelectric layers, whereas the negative triboelectric layer was fabricated via a soft lithography technique. By using this technique, the micro structured roughness was transferred to the silicone elastomer film from sand paper. The detailed fabrication process is explained in the experimental section. Figure 5.1c represents the schematic chart of preparation of silicone elastomer film via a cost-effective soft lithography technique. Silicone elastomer part A and part B are mixed equally in a 1:1 ratio in a beaker. The solution is then poured drop wise on a sand paper and spread evenly through spin coating technique. The silicone elastomer coated sand paper is then dried at 30 °C for 6h. After drying, the film is peeled off from the sand paper and utilized as an active layer in the SE-TENG. The detailed film preparation process is explained in the experimental section. . The working mechanism of SE-TENG is depicted in Figure 5.2a- d, which is because of the triboelectric and electrostatic effects. At the initial condition, the top electrode is in contact with the bottom dielectric layer with no flow of electrons in the electrodes. Due to the mechanical motion applied on the device, the layers separate from each other leading towards the occurrence of charge difference across the electrodes. This phenomenon induces the electrons to move from top electrode to bottom electrode through the external circuit. This action is responsible

124

for the first half cycle of the electrical output signal (alternating current (AC)). With the further actuating motion on to the device, the layers again moves close to each other induces the electrons to flow in the reverse direction, leads to the generation of second half cycle. The potential distribution of the device is theoretically analyzed by a simple finite element simulation using COMSOL multiphysics software. The figure 5.2e-g shows the surface potential distribution from contact state until the maximum release state.
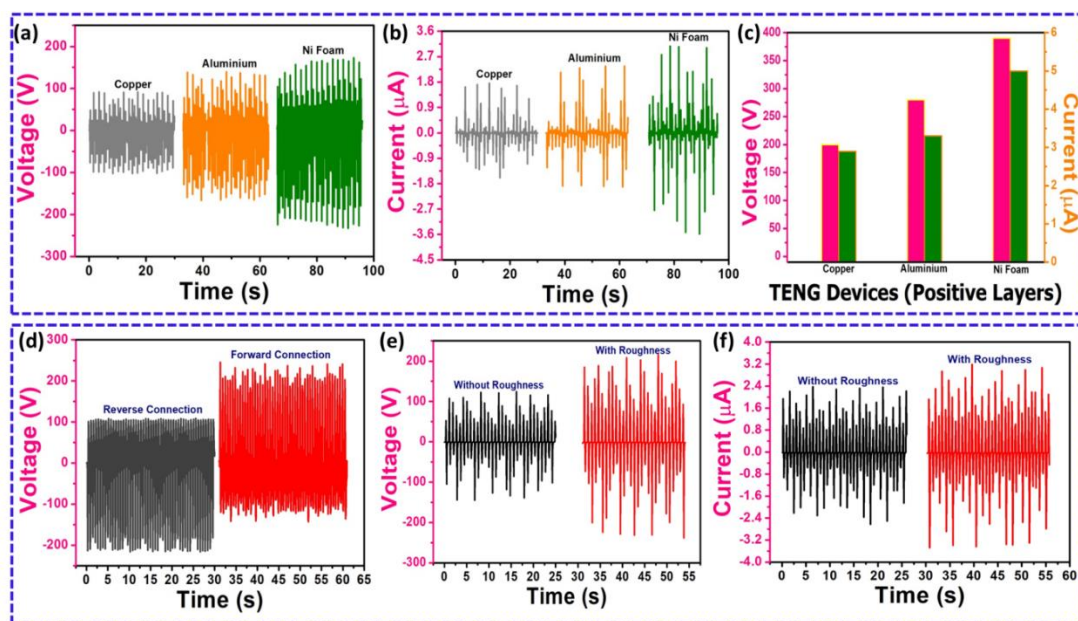
Figure 5.3- Electrical output analysis of SE-TENG device. (a-c) Voltage and current output comparison of SE-TENG device showing the maximum electrical output with Ni foam as positive triboelectric material. (d) Voltage signal showing the polarity test of SE-TENG with forward and reverse connection characteristics (e and f) Electrical output performance comparison of silicone elastomer film with roughness and without surface roughness.

The electrical output analysis was performed for the TENG devices made of Al, Cu and Ni foam as positive electrodes and silicone elastomer remained as the negative triboelectric layer. Figure 5.3a-c shows the electrical output comparison of

TENG devices made of Al, Cu and Ni foam positive electrodes. The output is higher in case of the TENG device made of Ni Foam. As we know that the roughness in the triboelectric layers plays a major role in the enhancement of electrical output. In the similar way, Ni foam which has a porous in nature having a good surface roughness as well as a positive triboelectric property which proved to be the exact material for contact electrification. On the other hand, the Al and Cu films do not have any surface roughness or porosity on its surface. The draw back with a plain positive side and a micro roughness negative layer would lead to the damage of roughness after few actuations. But in the case of Ni foam and roughness created negative layer, leads to the enhancement in contact area as well as the triboelectric charge generation. The porous layer in the positive side under contact and separation working mode would not damage the roughness present in the negative side, which makes the output to be stable for a prolonged period of time. The maximum electrical output obtained from the SE-TENG with Ni electrode generates ~370 V/ 6.1 µA. But the SE-TENG made of Cu and Al as positive layer generates a maximum electrical output of ~180 V/ 2.5 µA and ~ 270 V/ 3.6 µA respectively as shown in Figure 5.3a and b. Figure 5.3c shows the performance of electrical output and its difference with respect to positive layers. The further analysis and the applications were made by using the Ni foam SE-TENG device, due to its high electrical output performance. To confirm the electrical output, which is purely from the triboelectric effect, a switching polarity test was carried out by switching the polarity of the TENG device during its measurement. The device shows an exact 180 ° phase shift in its generated electrical output signal. This clearly confirms that the electrical output is purely from the SE-TENG device which is shown in Figure 5.3d. To prove the contribution of surface roughness and its role in enhancing the

electrical performance, the electrical measurement was carried out with two SE-TENG devices; one made of roughness created elastomer film and the other with plain film. The electrical output clearly made evidence that the SE-TENG made of surface roughness created elastomer film shows higher output than the plain elastomer film as shown in Figure 5.3e and f.
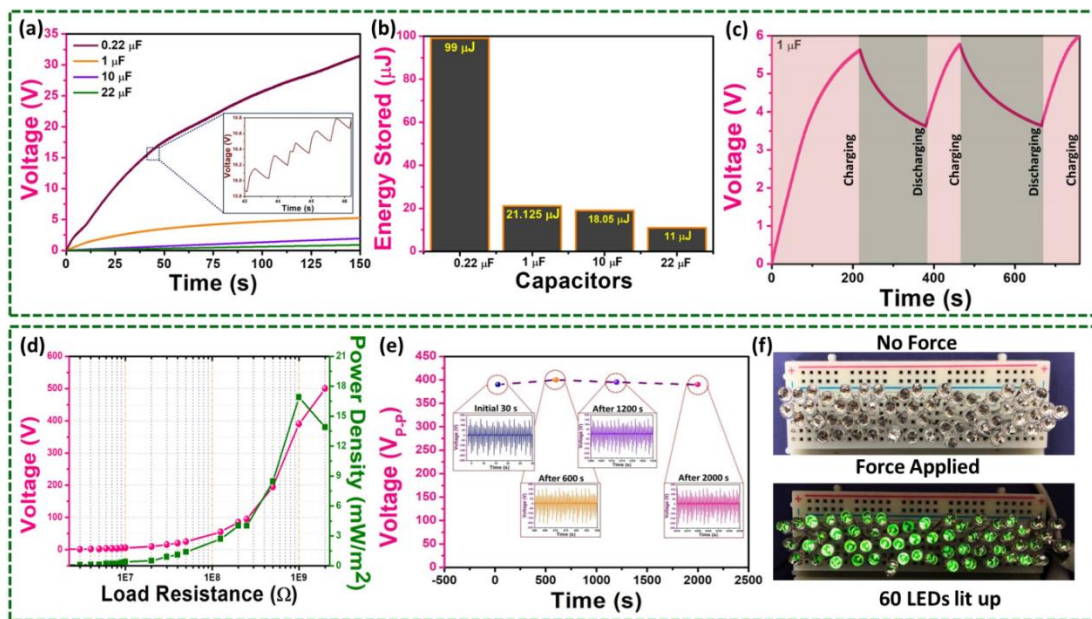
Figure 5.4- real time output analysis and durability test for SE-TENG device. (a) Commercial capacitor charging characteristics with various capacitors such as 0.22 μF, 1 μF, 10 μF and 22 μF for a period of 150 s. (b) Energy storage analysis of the capacitors charged using SE-TENG device (c) Charging and discharging cyclic characteristics of 1 μF capacitor. (d) Impedance matching analysis and instantaneous area power density of SE-TENG device upon various resistance values; the device shows the maximum area power density of ~ 17 mW/m^2 at 1 GΩ load resistance. (e) Stability analysis of SE-TENG showing its stable power delivering nature for the period of 2000s. Inset shows the output peak pattern with the interval of 600s. (f) 60 green LEDs glowing using SE-TENG upon applying the force by pressing and releasing the device.

To validate the electrical output of the SE-TENG device, various confirmatory tests has been performed, such as charging commercial capacitors, glowing LEDs, and

powering up a digital wrist watch. Figure 5.4a shows the charging characteristics of various rating commercial capacitors like 0.22 µF, 1 µF, 10 µF and 22 µF for a period of 150 s. The inset in Figure 4a shows the charging pattern during the device contact and separation with respect to external motion using linear motor. Figure S2 shows the circuit diagram which was used for performing the capacitor charging. The capacitor with least rating 0.22 µF charges quickly to 31 V in 150 s storing a maximum energy of 99 µJ. Similarly, the capacitor with highest rating stores a maximum energy of 11 µJ which was charged to 0.9 V in 150 s. The other two capacitors 1 µF and 10 µF charged to 5 V and 2 V with the maximum energy storage of 125 µJ and 18.05 µJ respectively as shown in Figure 5.4b. Figure 4c shows the charging and discharging cycle of 10 µF commercial capacitor under the mechanical force of 10 N. The capacitor stores 5 V in 150 s and the force is removed. This in turn makes the capacitor to discharge the stored potential till 3.5 V. The cycle is repeated for two more times to show the cyclic stability of commercial capacitor charging and discharging. The SE-TENG device shows the maximum area power density of ~17 mW/m^2 at 1GΩ load resistance as shown in Figure 5.4d. This indicates that 1 GΩ resistance was the exact load matching resistance for SE-TENG device and can be used further for focusing in the real-time applications. To show the durability of the SE-TENG device, a stability test was carried out for the period of 2000s as shown in Figure 5.4e.
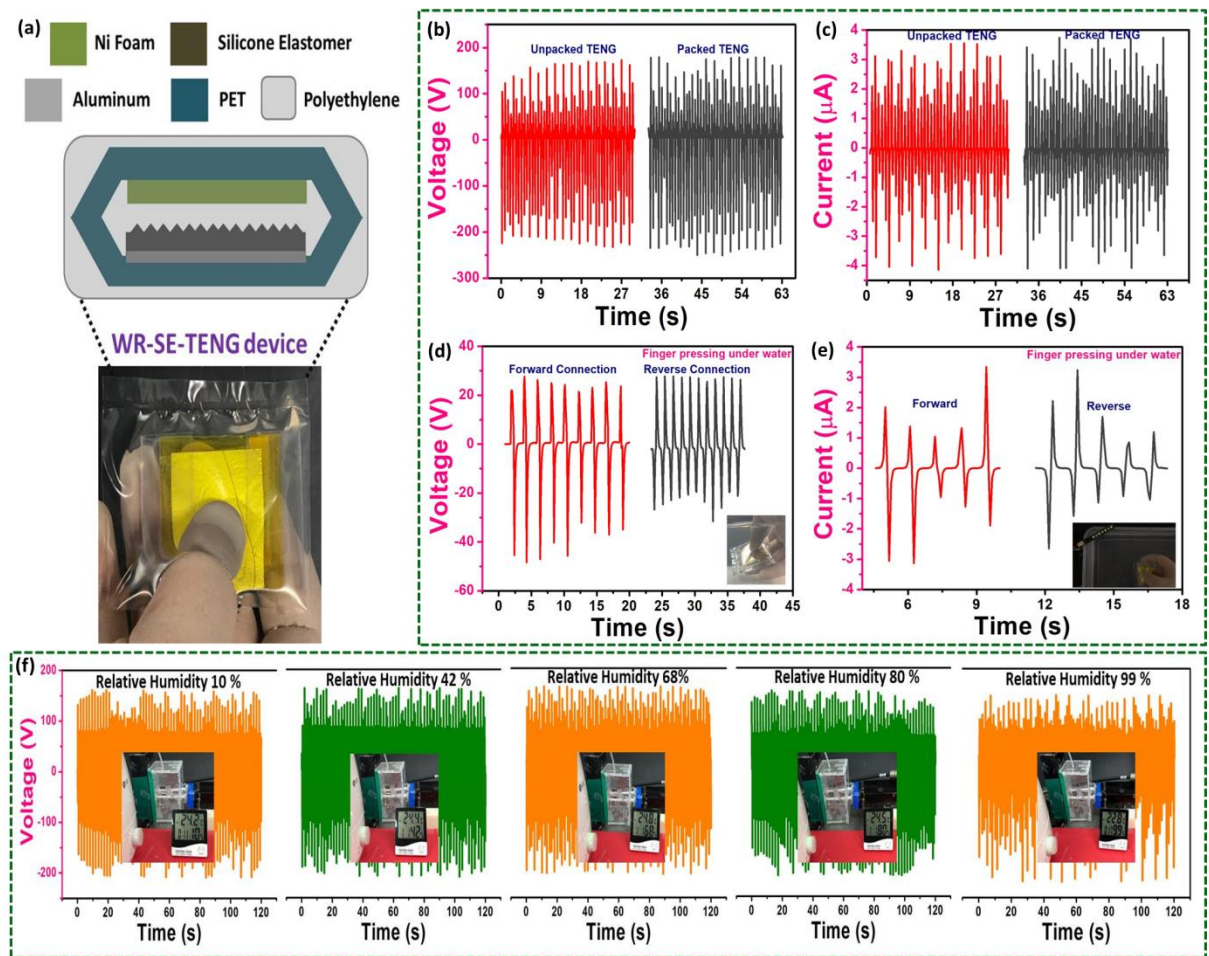
Figure 5.5- Water-resistant SE-TENG device fabrications and its electrical performance. (a) Layer-by-layer schematic diagram of WR-SE-TENG device and the digital photograph shows the device packed with polyethylene and placed inside water. (b and c) Voltage and current behavior of packed and unpacked SE-TENG device (d and e) Voltage and current behavior and polarity configurations of WR-SE-TENG device when pressed inside the water tub. (f) Humidity test of WR-SE-TENG device under various percentages of relative humidity ranging from 10 %, 42%, 68%, 80% and 99% RH and the device shows stable output in the entire period.

This shows that the device can work for a long period of time with a stable electrical output. Further the SE-TENG is used to glow 60 green LEDs in series connection as shown in Figure 5.4f. These tests validate that the SE-TENG is a promising candidate for powering low power electronic devices. In the recent past TENGs have been facing a drawback with its performance under the influence of

129

humidity. The stability and performance of the TENG would reduce due to the change in humidity. This is due to the interaction of moisture with the triboelectric layers leads to the reduction in surface charge generation. To overcome this issue, the SE-TENG has been packed completely with a polyethylene pouch and sealed using a pouch laminator. The packing does not allow the humidity, air or water droplets into the layers of the device. The schematic and digital photograph of the water resistance SE-TENG is shown in Figure 5.5a.. The electrical output performance of the packed and unpacked SE-TENG is shown in Figure 5.5b and c. The device shows similar output performance with respect to packing in case of both voltage and current proving that the performance has not reduced due to packing. Figure 5.5d and e shows the electrical output of water resistance SE-TENG by finger pressing under water. The output shows the exact phase shift in signal after being packed and actuated inside the water tub. The inset in Figure 5.5d shows the device immersed inside the water and inset in Figure 5.5e shows the LED glowing by pressing the device by placing in water. Further, the water resistance SE-TENG was tested under various percentages of relative humidity (% RH) as shown in Figure 5.5f. The device works stable from the humidity level at 10 % RH to 99 % RH. This also confirms that the device is packed perfectly and the influence of humidity does not affect the performance of the SE-TENG device. This proves that the packed TENG devices can be used in harsh weather and environmental conditions.
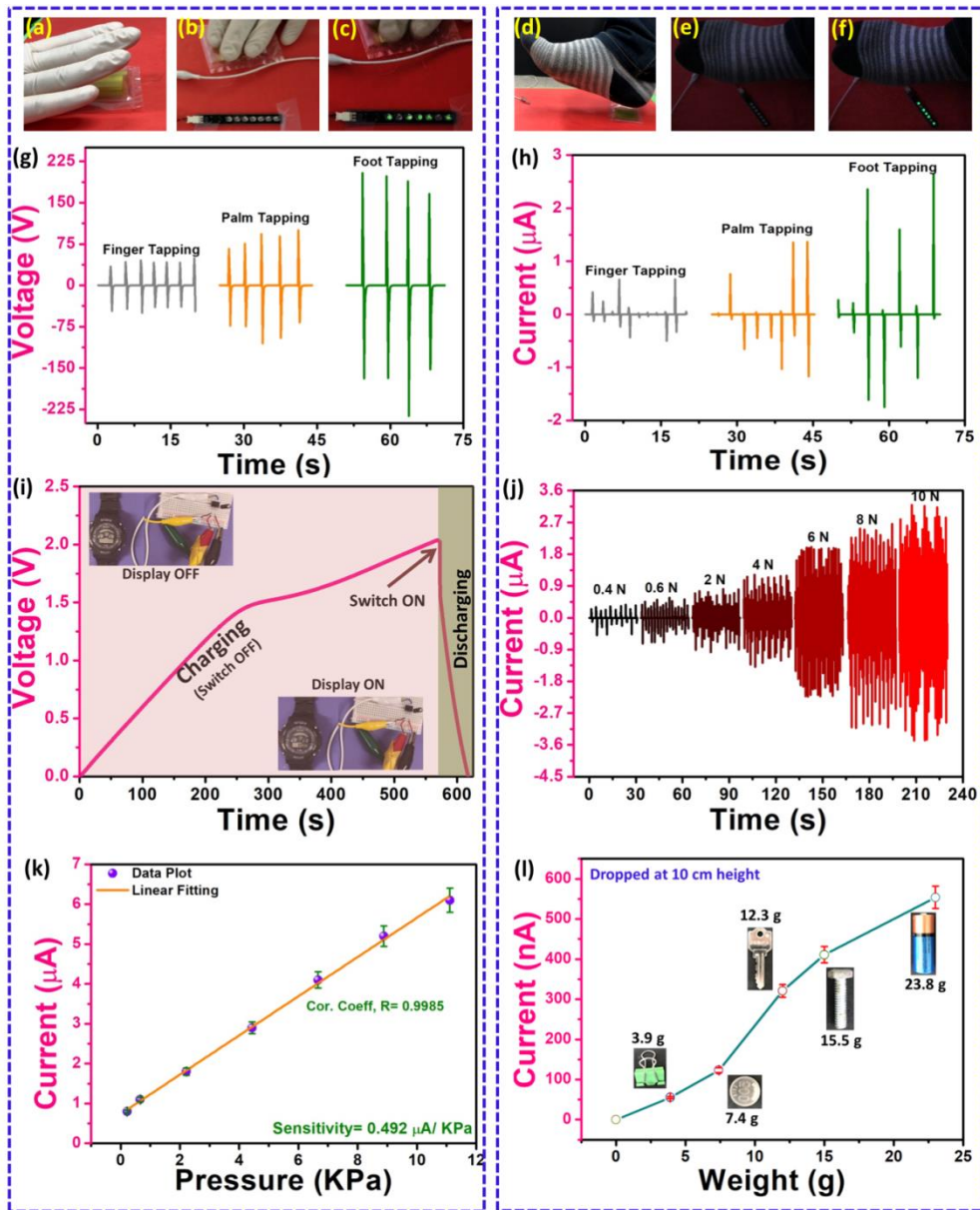
Figure 5.6- Bio-mechanical energy harvesting and zero power consuming pressure sensor applications. (a and h) digital photographs of WR-SE-TENG device under hand and foot tapping motions and LED glowing under human motions. (i) Powering up an electronic wrist watch with the help of 22 µF capacitor (j) Force analysis of WR-SE-TENG device upon various force from 0.4 N to 10 N and its current output profile. (k) self-powered/zero power consuming pressure sensor with difference pressure level and the linear behavior of its current value showing a correlation coefficient of 0.9985 and a better sensitivity of 0.492 µA/KPa. (l) Real-time response of different light weight items (paper clip, coin, key, bolt and battery) dropped on the device and its corresponding electrical output response.

After undergoing various confirmatory tests and performance analysis experiments using the SE-TENG and water-resistant SE-TENG, the device has been used for demonstrating few real-time applications which is mandatory for any kind of energy harvesters. Figure 5.6a-f shows the capability of SE-TENG for scavenging bio-mechanical energy from human hand and leg motions. The water resistant SE-TENG device was attached on the floor using a scotch tape to avoid unwanted movements and the LEDs were glow under human hand and leg motions. The biomechanical energy scavenging has been demonstrated by analyzing the electrical signal by applying the force by palm and leg tapping. The voltage and current are maximum during leg tapping and it is due to the weight and large pressure acting on the device, leads to the generation of higher electrical output as shown in Figure 5.6g and h. This demonstration makes a clear evidence of utilizing the SE-TENG as a bio mechanical energy harvester to harness the biomechanical motions in our day to day life. Similarly, a digital wrist watch was powered using the water-resistant SE-TENG by using a commercial 22 μF capacitor as shown in Figure 5.6i. In addition to that the water-resistant SE-TENG was demonstrated as a zero-power consuming pressure sensor. The device was placed on the flat surface and applied different ranges of force initially and recorded its current profile. The current profile increases with increase in the applied force as shown in Figure 5.6j. The sensing characteristics were studied with the relationship between the changes in pressure with respect to the increase in current. The sensor shows a linear response upon the increase in pressure with a sensitivity of 0.492 μA/ KPa and the correlation coefficient of 0.9985 as shown in Figure 5.6k. Figure 5.6l shows the electric output response of the active pressure sensing TENG device with its ability to detect the pressure of different weight objects fall from a

height of 10 cm. This shows the ability of device to detect the pressure in low ratings. From the results and studies made, it is clear that the water resistant TENG can effectively be used as a self-powered force sensor in harsh and humid environments such as in water tanks, water pipes and infusion pumps.

5.4 Conclusions

In summary, a highly reliable impervious SE-TENG has been fabricated successfully using a roughness created silicone elastomer and Ni foam as active layers. Cost-effective soft lithography technique had been introduced for creating the micro-roughness on the silicone elastomer film. With the similar configuration two other TENG devices made of Al-SE and Cu-SE has been fabricated and the electrical output was analyzed. Among the three devices, SE-TENG made of Ni foam had shown higher electrical output ~370 V/ 6.1 μA with a maximum area power density of ~17 mW/m^2 at 1GΩ load resistance. The device performance at real-time had been demonstrated by charging commercial capacitors, glowing LEDs and powering a digital watch. The durability of the device was analyzed by performing a stability test for a period of 2000s. To make the device to work actively in the harsh and humid environmental conditions, the device was fabricated as a water-resistant SE-TENG by packing it with polyethylene films and laminated tightly and demonstrated its water-resistant capability by actuating it inside water tub. The electrical output comparison with respect to packed and unpacked SE-TENG device has been analyzed and performed a humidity test of actuating the device under various percentages of relative humidity (10 % RH to 99 % RH). The test shows that the performance of the TENG device was not affected due to humidity as well as the packing gives a stable protection to the SE-

TENG device from humidity. Finally, the device was used to harness the bio mechanical energy from day-to-day human motions such as finer, hand and foot tapping. Also, the device was demonstrated for a potential real-time application of self-powered/ zero power consuming pressure sensor showing a good sensitivity of 0.492 µA/ KPa and the correlation coefficient of 0.9985. The above experiments and demonstrations prove that SE-TENG is a promising candidate to be used for measuring the variable pressures in harsh environments such as fluid pressure, gas pressure and water level indications.

5.5 References

1.   Zhang, L.; Zhang, B.; Chen, J.; Jin, L.; Deng, W.; Tang, J.; Zhang, H.; Pan, H.; Zhu, M.; Yang, W.; Wang, Z. L., Lawn Structured Triboelectric Nanogenerators for Scavenging Sweeping Wind Energy on Rooftops. *Adv Mater* **2016,** *28* (8), 1650-6.

2.   Lei, R.; Zhai, H.; Nie, J.; Zhong, W.; Bai, Y.; Liang, X.; Xu, L.; Jiang, T.; Chen, X.; Wang, Z. L., Butterfly-Inspired Triboelectric Nanogenerators with Spring-Assisted Linkage Structure for Water Wave Energy Harvesting. *Advanced Materials Technologies* **2019,** *4* (3), 1800514.

3.   Lai, Y.-C.; Hsiao, Y.-C.; Wu, H.-M.; Wang, Z. L., Waterproof Fabric-Based Multifunctional Triboelectric Nanogenerator for Universally Harvesting Energy from Raindrops, Wind, and Human Motions and as Self-Powered Sensors. *Advanced Science* **2019,** *6* (5), 1801883.

4.   Chandrasekhar, A.; Alluri, N. R.; Vivekananthan, V.; Park, J. H.; Kim, S.-J., Sustainable Biomechanical Energy Scavenger toward Self-Reliant Kids' Interactive Battery-Free Smart Puzzle. *ACS Sustainable Chemistry & Engineering* **2017,** *5* (8), 7310-7316.

5.   Chen, X.; Miao, L.; Guo, H.; Chen, H.; Song, Y.; Su, Z.; Zhang, H., Waterproof and stretchable triboelectric nanogenerator for biomechanical energy harvesting and self-powered sensing. *Applied Physics Letters* **2018,** *112* (20), 203902.

6.   Seol, M.-L.; Jeon, S.-B.; Han, J.-W.; Choi, Y.-K., Ferrofluid-based triboelectric-electromagnetic hybrid generator for sensitive and sustainable vibration energy harvesting. *Nano Energy* **2017,** *31*, 233-238.

7.   Chen, J.; Zhu, G.; Yang, W.; Jing, Q.; Bai, P.; Yang, Y.; Hou, T.-C.; Wang, Z. L., Harmonic-Resonator-Based Triboelectric Nanogenerator as a Sustainable Power Source and a Self-Powered Active Vibration Sensor. *Advanced Materials* **2013,** *25* (42), 6094-6099.

8.   Liu, G.; Guo, H.; Xu, S.; Hu, C.; Wang, Z. L., Oblate Spheroidal Triboelectric Nanogenerator for All-Weather Blue Energy Harvesting. *Advanced Energy Materials* *0* (0), 1900801.

9.   Wang, H.; Zhu, Q.; Ding, Z.; Li, Z.; Zheng, H.; Fu, J.; Diao, C.; Zhang, X.; Tian, J.; Zi, Y., A fully-packaged ship-shaped hybrid nanogenerator for blue energy harvesting toward seawater self-desalination and self-powered positioning. *Nano Energy* **2019,** *57*, 616-624.

10.   Vivekananthan, V.; Chandrasekhar, A.; Alluri, N. R.; Purusothaman, Y.; Joong Kim, W.; Kang, C.-N.; Kim, S.-J., A flexible piezoelectric composite nanogenerator based on doping enhanced lead-free nanoparticles. *Materials Letters* **2019,** *249*, 73-76.

11.   Purusothaman, Y.; Alluri, N. R.; Chandrasekhar, A.; Vivekananthan, V.; Kim, S. J., Regulation of Charge Carrier Dynamics in ZnO Microarchitecture-Based UV/Visible Photodetector via Photonic-Strain Induced Effects. *Small* **2018,** *14* (11), 1703044.

12.   Fan, F.-R.; Tian, Z.-Q.; Lin Wang, Z., Flexible triboelectric generator. *Nano Energy* **2012,** *1* (2), 328-334.

13.   Fan, F.-R.; Lin, L.; Zhu, G.; Wu, W.; Zhang, R.; Wang, Z. L., Transparent Triboelectric Nanogenerators and Self-Powered Pressure Sensors Based on Micropatterned Plastic Films. *Nano Letters* **2012,** *12* (6), 3109-3114.

14.   Vivekananthan, V.; Alluri, N. R.; Purusothaman, Y.; Chandrasekhar, A.; Selvarajan, S.; Kim, S.-J., Biocompatible Collagen Nanofibrils: An Approach for Sustainable Energy Harvesting and Battery-Free Humidity Sensor Applications. *ACS Applied Materials & Interfaces* **2018,** *10* (22), 18650-18656.

15.   Guo, H.; Chen, J.; Tian, L.; Leng, Q.; Xi, Y.; Hu, C., Airflow-Induced Triboelectric Nanogenerator as a Self-Powered Sensor for Detecting Humidity and Airflow Rate. *ACS Applied Materials & Interfaces* **2014,** *6* (19), 17184-17189.

16.   Chang, T.-H.; Peng, Y.-W.; Chen, C.-H.; Chang, T.-W.; Wu, J.-M.; Hwang, J.-C.; Gan, J.-Y.; Lin, Z.-H., Protein-based contact electrification and its uses for mechanical energy harvesting and humidity detecting. *Nano Energy* **2016,** *21*, 238-246.

17.   Harper, W. R., *Contact and frictional electrification*. Laplacian Press: Morgan Hill, Calif., 1998.

18.   Zhang, X.-S.; Han, M.-D.; Wang, R.-X.; Zhu, F.-Y.; Li, Z.-H.; Wang, W.; Zhang, H.-X., Frequency-Multiplication High-Output Triboelectric Nanogenerator for Sustainably Powering Biomedical Microsystems. *Nano Letters* **2013,** *13* (3), 1168-1172.

19.   Zhang, X.-S.; Han, M.-D.; Wang, R.-X.; Meng, B.; Zhu, F.-Y.; Sun, X.-M.; Hu, W.; Wang, W.; Li, Z.-H.; Zhang, H.-X., High-performance triboelectric nanogenerator with enhanced energy density based on single-step fluorocarbon plasma treatment. *Nano Energy* **2014,** *4*, 123-131.

20.   Zhu, Y.; Yang, B.; Liu, J.; Wang, X.; Wang, L.; Chen, X.; Yang, C., A flexible and biocompatible triboelectric nanogenerator with tunable internal resistance for powering wearable devices. *Scientific Reports* **2016,** *6*, 22233.

21.   Dudem, B.; Huynh, N. D.; Kim, W.; Kim, D. H.; Hwang, H. J.; Choi, D.; Yu, J. S., Nanopillar-array architectured PDMS-based triboelectric nanogenerator integrated with a windmill model for effective wind energy harvesting. *Nano Energy* **2017,** *42*, 269-281.

22.   Zhu, G.; Lin, Z.-H.; Jing, Q.; Bai, P.; Pan, C.; Yang, Y.; Zhou, Y.; Wang, Z. L., Toward Large-Scale Energy Harvesting by a Nanoparticle-Enhanced Triboelectric Nanogenerator. *Nano Letters* **2013,** *13* (2), 847-853.

23.   Nguyen, V.; Yang, R., Effect of humidity and pressure on the triboelectric nanogenerator. *Nano Energy* **2013,** *2* (5), 604-608.

24.   Chandrasekhar, A.; Vivekananthan, V.; Khandelwal, G.; Kim, S. J., A fully packed water-proof, humidity resistant triboelectric nanogenerator for transmitting Morse code. *Nano Energy* **2019,** *60*, 850-856.

25.   Chandrasekhar, A.; Khandelwal, G.; Alluri, N. R.; Vivekananthan, V.; Kim, S.-J., Battery-Free Electronic Smart Toys: A Step toward the Commercialization of Sustainable Triboelectric Nanogenerators. *ACS Sustainable Chemistry & Engineering* **2018,** *6* (5), 6110-6116.

26.   Zhao, K.; Wang, Z. L.; Yang, Y., Self-Powered Wireless Smart Sensor Node Enabled by an Ultrastable, Highly Efficient, and Superhydrophobic-Surface-Based Triboelectric Nanogenerator. *ACS Nano* **2016,** *10* (9), 9044-52.

CHAPTER VI

Substantial Improvement on Electrical Energy Harvesting by Chemically Modified/Sandpaper-based Surface Modification in Micro-scale for Hybrid Nanogenerators

Highlights

➢ A hybrid nanogenerator working with both triboelectric and piezoelectric mechanisms simultaneously.

➢ Composite film is made up of piezoelectric $(1\text{-}x)$ $K_{0.5}Na_{0.5}NbO_3$- x $BaTiO_3$ nanoparticles and Polydimethylsiloxane.

➢ Surface micro structures were created on composite films by chemically modified petri dish and sand paper.

➢ Electrical responses were analyzed and compared between flat and roughness created films.

Graphical Outline
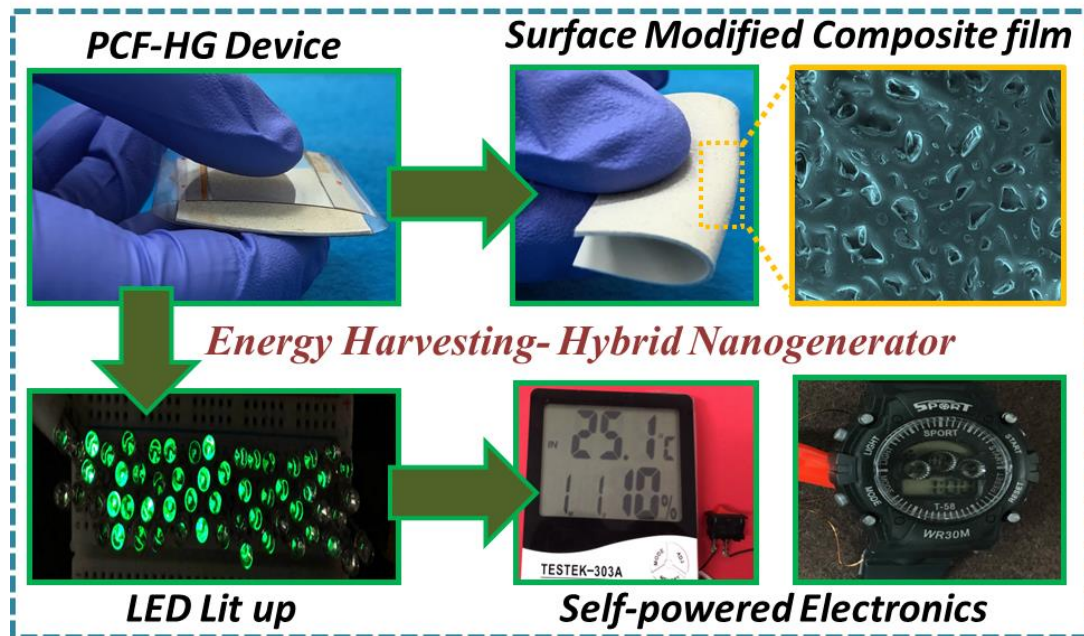
6.1 Introduction

Development of an eco-friendly and sustainable power source for powering low power electronic device is still a major challenge. The power sources are highly important for micro sensors(1), portable electronics(2) and bio-medical field(3) and implantable devices(4). As a most abundant source, mechanical energy from mechanical movements in day-to-day life acts as a promising power source for powering these devices. The mechanical motions can be generated form bio-mechanical motions(5) such as human body motions(6), ambient vibrations(7), fluid flow(8) and acoustic waves(9). The emerging of piezoelectric nanogenerators (PENG)(10, 11) for generating electric potential which is based on applying mechanical energy creates a huge positive impact in developing a portable power source. Recently, triboelectric nanogenerators (TENG)(12) create a pathway of harvesting mechanical energy efficiently in a cheaper cost with simple design on the basis of triboelectrification and electrostatic effects(13, 14). The power generated from TENGs is in sub-milli watt to few watts at low operating frequency, which opens its path towards the commercialization of TENGs for powering low power electronic devices(15). These advantages in TENGs make researchers significantly to prefer TENG over PENGs. There have been many reports on TENGs for powering a wide variety of low power electronic devices and TENG as active self-powered sensors(16). The energy harvesting source ranges from human body movements(17), wind(18), ocean(19), vibration(20) and strain(21, 22) with various applications in day-to-day life and activities(23).

Many researchers focus on hybridizing the TENGs with other energy

harvesting sources such as solar cell(24), electromagnetic generators (EMG)(25, 26) and PENGs(27, 28) to expand its application and commercialization. When comparing the hybridization with EMG and solar cell, TENG-PENG hybrid is more feasible as they share almost similar mechanism in converting mechanical energy into electrical energy. Both these TENG and PENG can respond to various mechanical energy sources such as bending, compression and vibrations(29, 30). Therefore, these two energy harvesting components can be combined together as a single energy harvester with boosted electrical output performances. Few reports are suggesting that these two energy harvesting components can be combined to form a single energy harvesting unit with integrated output performances. The only challenge in making the integrated hybrid energy harvester is the function of material and its surface which can contribute to both TENG and PENG electrical output generation. One other thing is the development of triboelectric output enhances with the increase in surface roughness(31). As surface roughness increases, the number of contact point on the active materials will be higher when compared to a flat layer having a single large contact points(32). Therefore, creating micro roughness on the surface of the triboelectric layer is a key factor in fabricating a contact separation device. Various techniques on creating surface roughness on the films are explored and reported widely in a cost-effective way.

The present manuscript demonstrates an integrated energy harvester combined with both triboelectric and piezoelectric mechanisms in a single unit as a piezoelectric composite film-based hybrid nanogenerator (PCF-HG). The active layer is a piezoelectric composite film made of a dual perovskite system $(1-x)$ $K_{0.5}Na_{0.5}NbO_3$- x $BaTiO_3$ (designated as KNN- x BTO) at x = 0, 0.02, 0.04, 0.06 and 0.08 with a

제주대학교 중앙도서관
JEJU NATIONAL UNIVERSITY LIBRARY

Polydimethylsiloxane (PDMS) polymer matrix. The device is made at a contact and separation working mode with the composite film as a triboelectric layer and ITO as another triboelectric layer. The electrical output generated from the PCF-HG device majorly relies on the weight percentage of particles into the polymer matrix and electrical poling of the composite film. The electrical response with respect to individual components and the combined hybrid system is studied individually and the electrical responses with respect to surface roughness have also been studied in this work. The single working mechanism with the combined effects have been explored and schematically given. Further the capabilities of PCF-HG device in powering low powered electronic devices have been demonstrated. This work suggests that the influence of surface roughness is greatly contributes in enhancing the electrical output of the contact separation-based energy harvesting devices as well as the integration of both the TENG and PENG components in a single system.

6.2 Experimental details

6.2.1 Synthesis of nanoparticles and device fabrication

The nanoparticles were synthesized by grinding the commercially purchased potassium carbonate (K_2CO_3), sodium carbonate (Na_2CO_3), niobium pentoxide (Nb_2O_5), barium carbonate (Ba_2CO_3) and titanium dioxide (TiO_2) using an agate mortar and pestle formulated with the stoichiometric of (1-x) KNN-x BTO through SSR method. All precursors were purchased from Daejung chemicals and metals co., ltd, Korea. The pure KNN nanoparticles and (1-x) KNN- x BTO nanoparticles were synthesized with the firing temperature of 850 ℃ and 1200 ℃ respectively at a heating rate of 5℃/ min for 2 h. The obtained products were washed again thoroughly and

dried overnight. The dried products were grounded and sintered again for the proper densification of nanoparticles in order to get high crystalline phase.

The nanoparticles (5 wt %, 10 wt %, 15 wt %, 20 wt % and 25 wt %) were blended into a PDMS (monomer and cross linker 10:1) and stirred for 20 min to obtain a homogeneous solution. The film fabrication was done based on our previously reported protocol(33). The composite solution is then poured into a surface modified petri dish, distributed evenly by spin coating and placed in a hot air oven at 70 ℃ for 30 min. Similarly, the solution is poured into a sandpaper, spin coated and placed in an oven at 70 ℃ for 30 min. The cured film is then peeled off from the petri dish and sandpaper individually and used as an active layer for the hybrid nanogenerator device. The composite film is then cut into a required dimension (4 × 4 cm) and attached into a ITO/PET sheet to form a negative triboelectric layer, Cu wires are attached on the ITO to make electrical contacts. Another ITO/PET sheet was used as a positive triboelectric layer and made as a contact separation based piezoelectric-triboelectric hybrid nanogenerator device.

6.2.2 Characterization and electrical measurements

The surface morphology and elemental mapping analysis were performed by a field emission scanning electron microscope (FE-SEM) TESCAN, MIRA. The Raman analysis was performed by using a Raman spectroscopy LabRAM, Japan with the excitation wave length of 514 nm. The phase structure was analyzed by x-ray diffractometer (XRD, Rigaku, Japan with λ = 1.5406 A with Cu-Kα radiation under room temperature with the operating electrical supply of 40 kV and 40 mA). The polarization vs voltage response was recorded by a P-E loop tester precision LC II 1o

제주대학교 중앙도서관
JEJU NATIONAL UNIVERSITY LIBRARY

kV-SC (RADIANT Technologies) and the electrical measurements of the hybrid nanogenerator was measured using an electrometer (Keithley-6514).

6.3 Results and discussions

The detailed schematic of synthesis of (1-x) KNN- x BTO nanoparticles and the composite film fabrication are illustrated in Figure 6.1. Initially the precursor powders were taken in a formulated stoichiometric ratio, homogenize and calcined at required temperature to obtain a pure KNN and KNN-x BTO nanoparticles as shown in Figure 6.1a. The synthesized particles at desired wt % were mixed in to a 10:1 ration of PDMS monomer and its hardener and stirred carefully for a period of 20 min to get a fully homogenized white colored PDMS/KNN- x BTO solution as shown in Figure 1b. In order to fabricate micro-roughness created composite films, a soft lithographic technique is employed where the blended PDMS solutions is poured into a rough mold and replicate its rough pattern on to the surface of the polymer. Figure 1c shows the creation of micro-roughness using an acetone treated plastic petri dish as a mold. The plastic petri dishes were made of Acrylonitrile butadiene styrene (ABS) polymer and are sensitive to ketones, acetone and esters. Here, acetone is used as an etchant in the surface modification process by dipping the ABS petri dish in to a beaker full of acetone and treated for 120 s. The petri dish is then washed and dried in oven carefully to get the irregular rough template petri dish. The mixed PDMS/KNN-x BTO solution is then poured into the template petri dish and spin coated to spread evenly. The petri dish is then placed into the hot air oven at 60 °C for 1 hr. On the other hand, commercially available sandpaper with the rough structure template is used for creating micro roughness composite film as shown in Figure 6.1d. The sandpaper is

cut into a required dimension and attached on an acrylic board and the polymer solution is powered into it and spin coated. The sandpaper is then dried at 60 °C for 1 hr. After curing, the film is peeled from the sandpaper as well as from the petri dish.
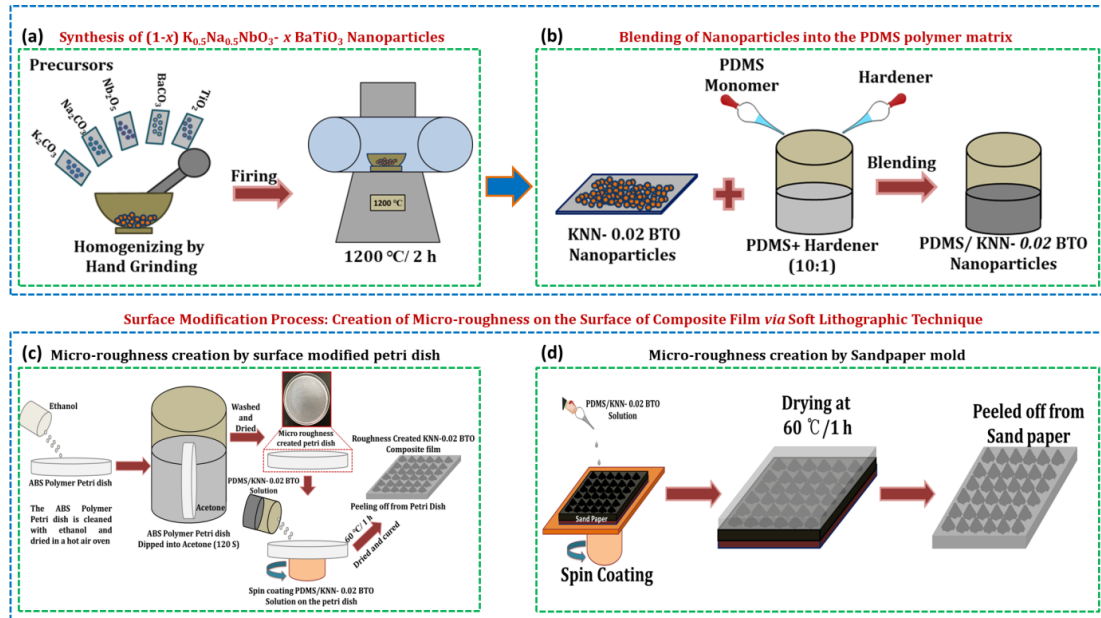
Figure 6.1 Synthesis of nanoparticles and composite film fabrication (a) synthesis of $(1-x)$ $K_{0.5}Na_{0.5}NbO_3$- x $BaTiO_3$ nanoparticles by a solid state reaction technique (b) blending of nanoparticles into the PDMS polymer matrix (c) micro-roughness creation by surface modified petri dish using acetone treatment and (d) micro-roughness creation by sandpaper method using soft-lithographic technique.

The phase purity of KNN and KNN-x BTO nanoparticles was evaluated by X-ray Diffractometer and Raman spectroscopic techniques. Pure KNN nanoparticles exhibits orthorhombic crystalline phase structure, which is confirmed by the reference pattern from ICSD No. 01-073-6542. There is a peak splitting at 45⁰, which corresponds to the planes (040) and (004) and the space group number *pmm*2/25 confirms the orthorhombic phase of KNN as shown in Figure 6.2a. The orthorhombic phase of the KNN nanoparticles were stable until the BTO content reached $x = 0.02$,

which indicates that there is no phase change. When the BTO content reaches to $x = 0.04$, the peak at 45⁰ tends to merge as a less intensified single broad peak, indicating its transformation from orthorhombic to tetragonal. The phenomenon is observed in the further doping concentrations of x as, $x = 0.06$ and $x = 0.08$. Similarly, the atomic vibrations of the system were analyzed using Raman spectroscopic patterns which are shown in Figure 6.2b. The KNN and KNN-x BTO nanoparticles with its orthorhombic crystal structure has six modes positioned at $v1$, $v2$, $v3$, $v5$, $v6$ and $v1 + v5$ with the Raman shift values at 621 cm^{-1}, 568 cm^{-1}, 649 cm^{-1}, 267 cm^{-1}, 200 cm^{-1} and 869 cm^{-1}. These Raman active modes are directly related to the vibrations of NbO_6 polyhedron in the entire KNN lattice. Figure 6.2c shows the polarization vs electric field analysis of the KNN-0.02 BTO nanoparticles with the obtained polarization of 25 $\mu C/cm^2$ at 2000 V cm^{-1}. The micro roughness created surface morphology of the composite film made by the acetone treated petri dish and sandpaper template films are shown in Figure 6.2d and e. The composite films made through petri dish template shows small and random roughness on its surface, whereas the composite film fabricated with sandpaper template shows high and dense roughness. Figure 6.2f shows the cross section of the composite film in which the inset shows the roughness peak height. The pure KNN nanoparticles shows a cubic morphology and when the x value increases the morphology slightly turns from cubic to a distorted cubic morphology. This also shows the influence of doping the BTO nanoparticles into the KNN nanoparticles. Figure 6.2g shows the digital photographic image of the fabricated PCF-HG device and its corresponding layer-by-layer schematic is shown in Figure 6.2h. Figure 6.2i to l show the digital image of plain composite film with its flexibility (Stretchable, role able and bendable) nature.
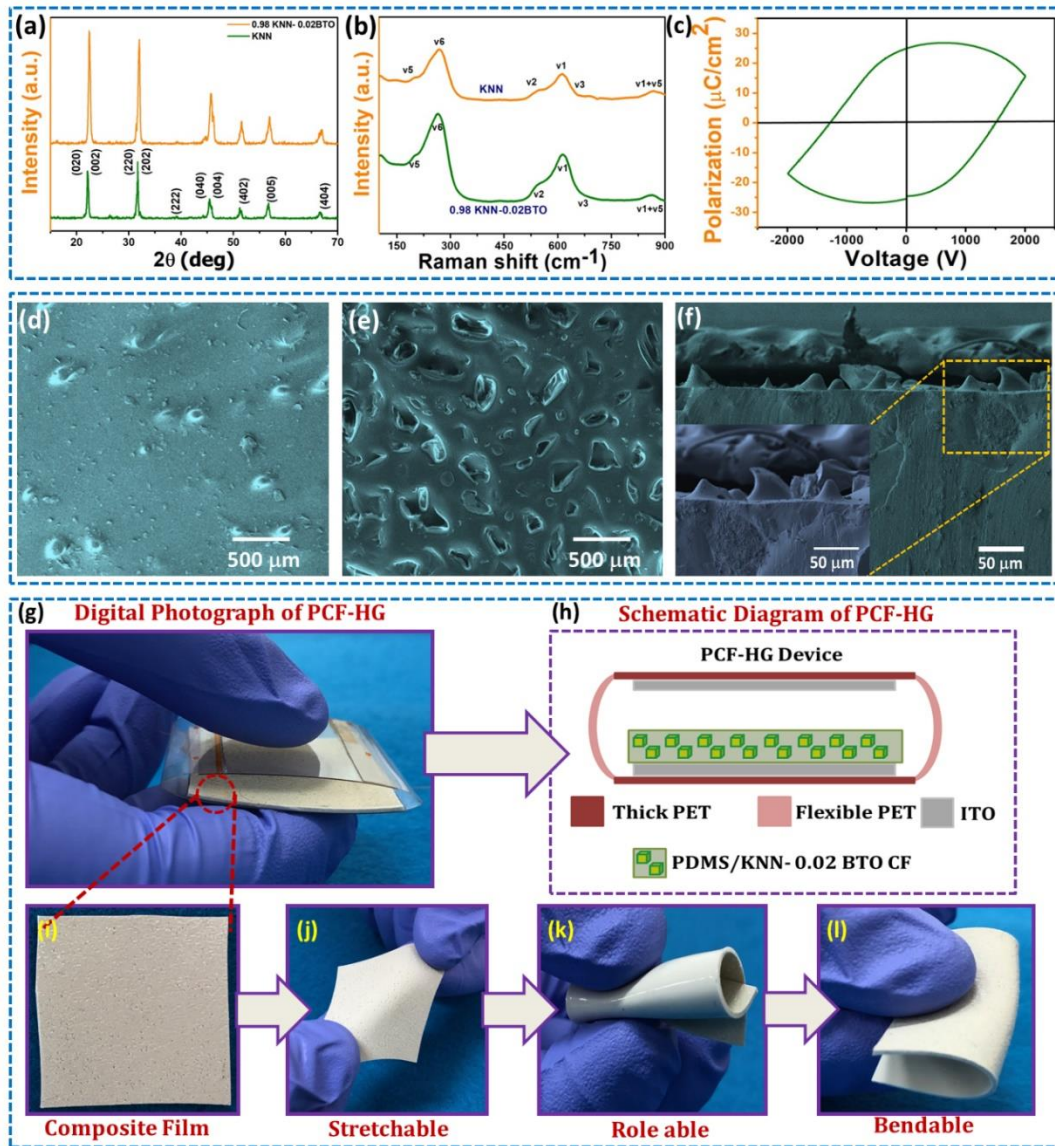
Figure 6.2 Structural analysis, surface morphology of KNN and (1-*x*) K$_{0.5}$Na$_{0.5}$NbO$_3$- *x* BaTiO$_3$ and schematic diagram of PCF-HG device (a) XRD pattern of the synthesized nanoparticles (b) Raman spectroscopy analysis of KNN and (1-*x*) K$_{0.5}$Na$_{0.5}$NbO$_3$- *x* BaTiO$_3$ nanoparticles (c) P-E loop analysis of KNN- 0.02 BTO nanoparticles (d) and (e) surface morphology of micro roughness made by acetone treated petri dish and sandpaper template of the composite films (f) cross section of composite film showing the rough surface and the inset shows the height of the rough surface (g) digital photographic image of the PCF-HG device (h) schematic diagram showing various layers of the PCF-HG device and (i to l) shows the composite film and its flexible nature (stretching, bending and rolling).

The working mechanism of PCF-HG device is schematically shown in Figure 6.3a. In the initial state (during pressing), the electrons transfer from ITO to the

composite film creating a large potential difference (as shown in step i). At the same time an opposite charge was induced on the other side of the composite film making the current flow between the electrodes. When the device is pressed fully (step ii) the compression force acts on the composite film leading to the generation of piezoelectric polarization. When the compressive force gets remove from the device (step iii) the piezoelectric polarization becomes zero leading to the reversal of the current signal. In the final stage (step iv), the composite film gets separated from the top electrode and induce the tribo charge to flow back leading to the development of a negative peak. Figure 6.3b and c shows the voltage and current response of the PCF-HG device made with different surface roughness created composite films. Among the other surface roughness devices, sandpaper template device shows high peak - to - peak electrical response at $\approx$ 610 V/ 13.7 μA which is twofold higher when compared to plain composite film-based PCF-HG device ($\approx$ 305 V/ 6.9 μA). This is due to the highly dense and uniform surface roughness created due to the sandpaper template, and eventually increases more contact points during the contact and separation motions. This directly reflects in the generation of electrical output. The petri dish template composite film has non uniform and random roughness on its surface. This makes less contact points during the contact and separation process, which tends to the development of less electrical output compared to the sandpaper replicated film ($\approx$ 450 V and 9 μA). Before measuring the electrical response of the PCF-HG device, the composite films are electrically poled at different external power supply from 1 kV, 3 kV and 5 kV for a period of 1 h. The composite film poled at 3 kV shows higher electrical response compared to the other two. This is due to the film poled at 1 kV does not have sufficient strength to orient the maximum dipoles and similarly, the 5

kV poled film depolarizes due to higher applied electric potential. In order to find the electrical response from device, a switching polarity test is required for its confirmation.
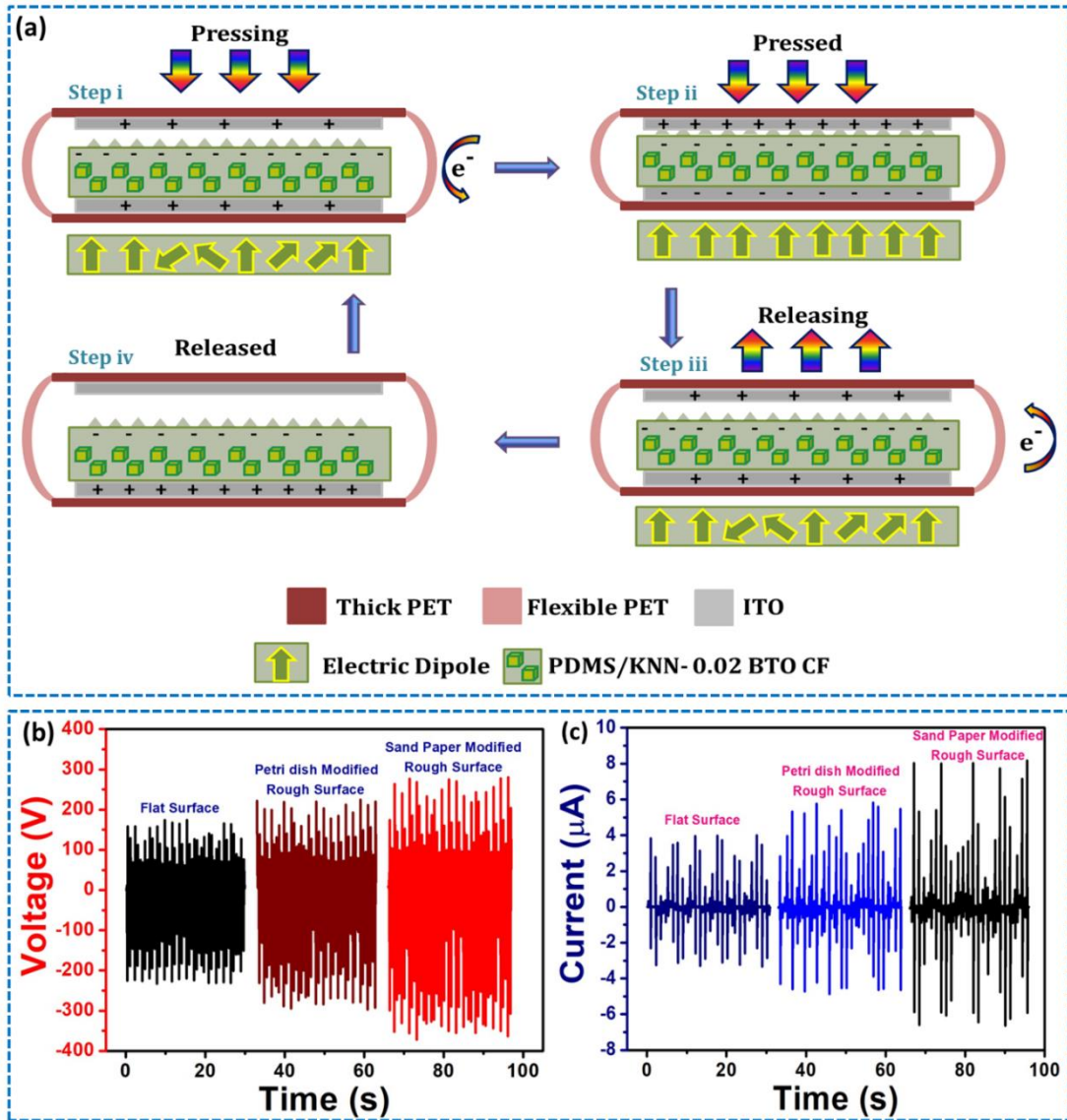
Figure 6.3 Working mechanism of PCF-HG device and the electrical response with different surface roughness (a) working mechanism of PCF-HG device with its step by step operation showing the triboelectric charges and piezo potential with the dipole orientations (b) and (c) voltage and current response of the composite films with flat and rough surfaces.
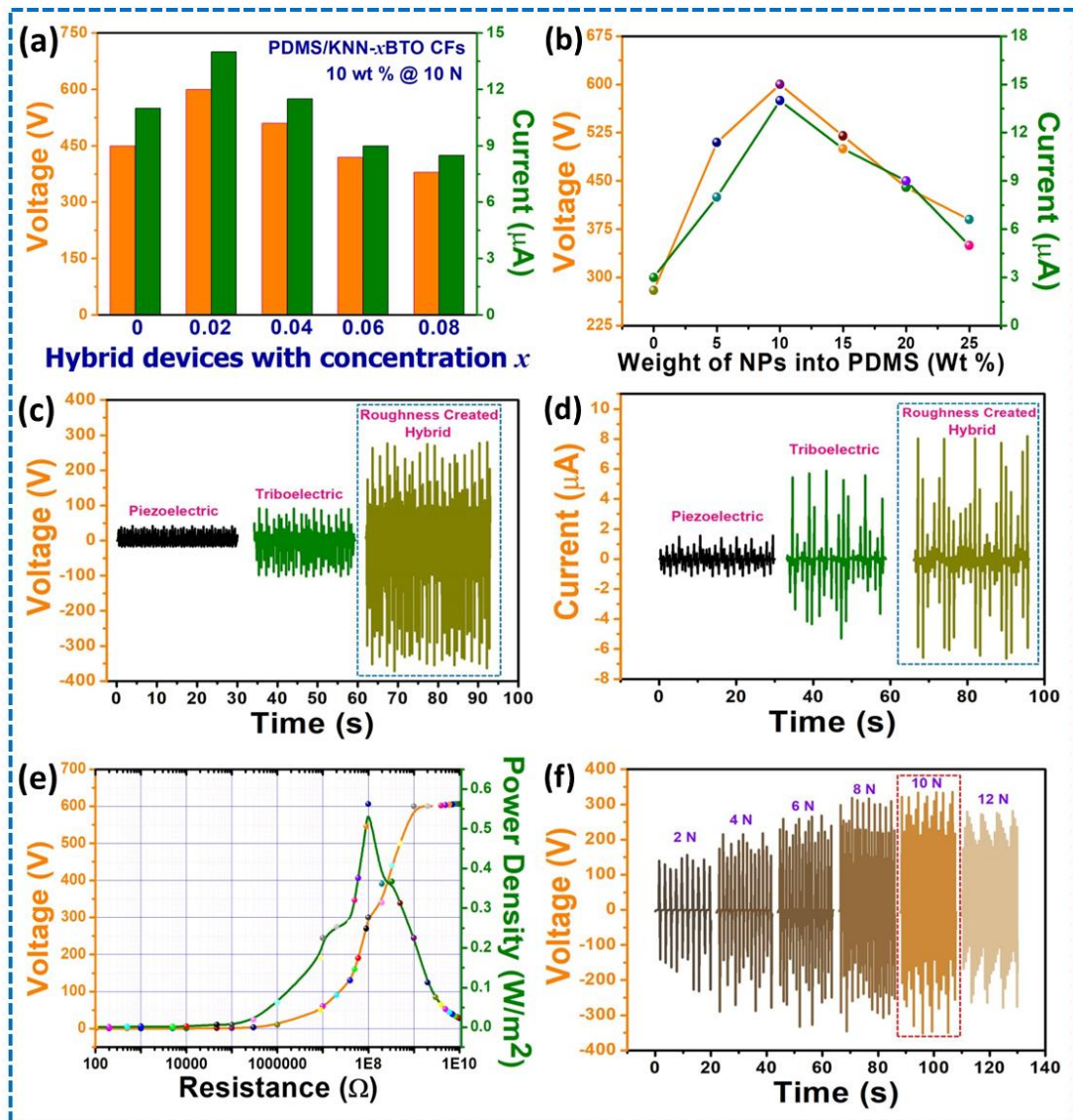
Figure 6.4 Electrical response of PCF-HG device (a) electrical response of PCF-HG device made with various concentrations of x (b) Electrical response of PCF-HG device made of composite films with different wt % of nanoparticles into PDMS matrix (c) and (d) voltage and current response of individual components such as PENG and TENG in comparison with hybrid device (e) load resistance vs power density analysis of PCF-HG device showing the power density of 0.55 W/m^2 at 100 MΩ resistance and (f) force analysis of PCF-HG device showing the maximum voltage at 10 N force.

Figure 6.4a shows the electrical response of the composite film made with different doping concentrations of KNN- x BTO (x = 0, 0.02, 0.04, 0.06 and 0.08). The

polymer to particle weight percentage is fixed as 10 wt % and the force at 10 N. The device made of $x = 0.02$ shows high electrical response compared to the other concentration. This phenomenon is directly connected with the polarization response obtained from the P-E loop analysis, in which the $x = 0.02$ concentration shows higher polarization compared with other concentrations of x. Figure 6.4b shows the electrical output response of the PCF-HG device upon the various weight percentage of nanoparticles into the PDMS matrix. The electrical output is high in the case of 10 wt % particles into the PDMS polymer. When the concentration of nanoparticles increases, the electrical response decreases. This is due to the agglomeration of particles into the polymer forms a dense layer of particles inside the composite film, leading to the improper dipole orientation under the applied mechanical force. The poor dipole orientation gets reflected directly in the electrical response behavior showing the reduced electrical response. When the weight ratio of nanoparticles in the film is 5 wt %, the nanoparticles are dispersed randomly, cresting the generation of less electrical output. Figure 6.4c and d shows the electrical response (voltage and current) comparison of piezoelectric, triboelectric and hybrid nanogenerators observed ≈ 58 V/ 1 μA, ≈ 195 V/ 6 μA and ≈ 610 V/ 13.7 μA respectively. The results clearly indicate that the hybrid device generates higher electrical output compared to the individual components. The high potential is generated due to the combination of both triboelectric and piezoelectric effects in a single working structure. Figure 6.4e shows the impedance matching of the hybrid device at the load resistance of 100 MΩ, with the maximum power density ≈ 0.55 W/m^2. Further, a force analysis had been performed to identify the optimum force in which the PCF-HG device generates maximum electric potential. The device shows maximum output at 10 N forces and at

153

12 N the electrical response starts to decrease as shown in Figure 6.4f, which is due to the depolarization in composite film and improper charge transfer during the contact and separation process.
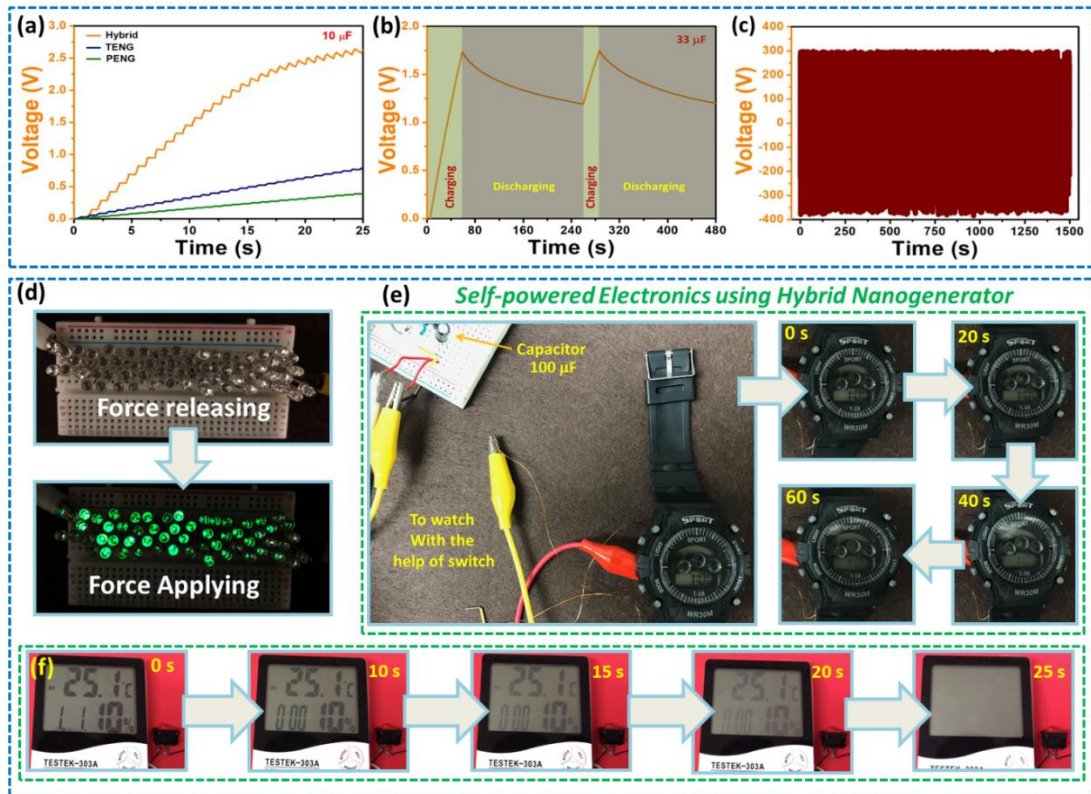
Figure 6.5 Capacitor charging analysis and real-time application of self-powered electronics (a) commercial capacitor charging using individual components such as TENG, PENG and hybrid combinations (b) cyclic stability test using a commercial 33 μF capacitor (c) stability test of PCF-HG device showing the stable electrical response for a period of 1500 s (d) 60 green LED lit up using PCF-HG device under the compressive force (e) and (f) demonstration of self-powered electronics using PCF-HG device by powering a wrist watch and a temperature sensor.

To validate the electrical signals generated form the PCF-HG device, various analysis such as capacitor charging, cyclic stability of capacitor charging-discharging; LED lit up and powering low power electronic devices had been performed. The

capacitor charging analysis was performed with TENG, PENG and hybrid nanogenerator devices by charging a commercial capacitor of 10 µF for a period of 25 s as shown in Figure 6.5a. The hybrid devices charge the capacitor to the maximum of 2.5 V in 25 s, the TENG and PENG device charges to 0.7 V and 0.35 V respectively. The faster and higher charging behavior by the PCF-HG device is due to the development of high electrical output generated from the hybrid device. The cyclic stability of a 33 µF capacitor with its charging and discharging characteristics is shown in Figure 6.5b. One other important test for any energy harvesting device is its stability analysis. Figure 6.5c shows the stability test of PCF-HG device which has the constant response for the entire period of 1500 s, proves that the device is stable for a long period of time. Figure 6.5d shows the LED lit up demonstration using PCF-HG device which potentially powers 60 green LEDs brightly upon applying the external force. Figure 6.5e and f shows the application demonstrating self-powered electronics by powering a wrist watch and a temperature sensor using a commercial capacitor of 100 µF. The capacitor is charged using PCF-HG device and connected to the wrist watch and temperature sensor device using a ON and OFF switch. When the capacitor is charged the switch is closed and allowed the device to work in the energy stored by the capacitor. The wrist watch glows for 60s and the temperature sensor device works for 25 s, the time of powering depends on the power rating required to drive the devices. The above results proved that PCF-HG device is a promising device for energy harvesting, can be used as an active sensor, and driving low power electronic devices.

6.4 Conclusions

In summary, a high-performance hybrid nanogenerator (PCF-HG) had been fabricated using PDMS/ (1-x) KNN- x BTO composite films which work under contact and separation mode. The hybrid nanogenerator is made of combining both triboelectric and piezoelectric effects in a single structure. The electrical output of the device was studied and optimized upon various concentrations of BTO doping and the weight ration of nanoparticles into the composite films. The device made of x = 0.02 with the PDMS to nanoparticles weight ratio of 10 wt % generates a maximum electrical output of ≈ 610 V/ 13.7 µA. Also, the electrical responses of the hybrid device as well as the individual components have been systematically studied. The electrical performance of the PCF-HG device was compared with the various roughness created composite films to understand the influence of surface roughness in enhancing the electrical output. The device shows a maximum power density of ≈ 0.55 W/m^2 at 100 MΩ load resistance showing higher response than the individual components. Further, the device exhibited its long-term stability for a period of 1500 s continuously and showed its capability in powering 60 green LEDs, wrist watch and a temperature sensor by using a bridge rectifier and commercial capacitor.

6.5 References

1.   Chen J, Guo H, Zheng J, Huang Y, Liu G, Hu C, et al. Self-Powered Triboelectric Micro Liquid/Gas Flow Sensor for Microfluidics. ACS Nano. 2016;10(8):8104-12.

2.   Tang Q, Yeh M-H, Liu G, Li S, Chen J, Bai Y, et al. Whirligig-inspired triboelectric nanogenerator with ultrahigh specific output as reliable portable instant power supply for personal health monitoring devices. Nano Energy. 2018;47:74-80.

3.   Zhang X-S, Han M-D, Wang R-X, Zhu F-Y, Li Z-H, Wang W, et al. Frequency-Multiplication High-Output Triboelectric Nanogenerator for Sustainably Powering Biomedical Microsystems. Nano Letters. 2013;13(3):1168-72.

4.   Li Z, Feng H, Zheng Q, Li H, Zhao C, Ouyang H, et al. Photothermally tunable biodegradation of implantable triboelectric nanogenerators for tissue repairing. Nano Energy. 2018;54:390-9.

5.   Maria Joseph Raj NP, Alluri NR, Vivekananthan V, Chandrasekhar A, Khandelwal G, Kim S-J. Sustainable yarn type-piezoelectric energy harvester as an eco-friendly, cost-effective battery-free breath sensor. Applied Energy. 2018;228:1767-76.

6.   Alluri NR, Vivekananthan V, Chandrasekhar A, Kim S-J. Adaptable piezoelectric hemispherical composite strips using a scalable groove technique for a self-powered muscle monitoring system. Nanoscale. 2018;10(3):907-13.

7.   Chen J, Wang ZL. Reviving Vibration Energy Harvesting and Self-Powered Sensing by a Triboelectric Nanogenerator. Joule. 2017;1(3):480-521.

8.   Kim W, Choi D, Kwon J-Y, Choi D. A self-powered triboelectric microfluidic system for liquid sensing. Journal of Materials Chemistry A. 2018;6(29):14069-76.

9.   Fan X, Chen J, Yang J, Bai P, Li Z, Wang ZL. Ultrathin, Rollable, Paper-Based Triboelectric Nanogenerator for Acoustic Energy Harvesting and Self-Powered Sound Recording. ACS Nano. 2015;9(4):4236-43.

10.   Wang ZL, Song J. Piezoelectric Nanogenerators Based on Zinc Oxide Nanowire Arrays. Science. 2006;312(5771):242-6.

11.   Vivekananthan V, Alluri NR, Chandrasekhar A, Purusothaman Y, Gupta A, Kim S-J. Zero-power consuming intruder identification system by enhanced piezoelectricity of K0.5Na0.5NbO3 using substitutional doping of BTO NPs. Journal of Materials Chemistry C. 2019.

12.   Fan F-R, Tian Z-Q, Lin Wang Z. Flexible triboelectric generator. Nano Energy. 2012;1(2):328-34.

13.   Lee S, Lee Y, Kim D, Yang Y, Lin L, Lin Z-H, et al. Triboelectric nanogenerator for harvesting pendulum oscillation energy. Nano Energy. 2013;2(6):1113-20.

14.   Chandrasekhar A, Alluri NR, Vivekananthan V, Park JH, Kim S-J. Sustainable Biomechanical Energy Scavenger toward Self-Reliant Kids' Interactive Battery-Free Smart Puzzle. ACS Sustainable Chemistry & Engineering. 2017;5(8):7310-6.

15.   Suo G, Yu Y, Zhang Z, Wang S, Zhao P, Li J, et al. Piezoelectric and Triboelectric Dual Effects in Mechanical-Energy Harvesting Using BaTiO3/Polydimethylsiloxane Composite Film. ACS Applied Materials & Interfaces. 2016;8(50):34335-41.

16.   Liu Z, Ma Y, Ouyang H, Shi B, Li N, Jiang D, et al. Transcatheter Self-Powered Ultrasensitive Endocardial Pressure Sensor. Advanced Functional Materials. 2019;29(3):1807560.

17.   Proto A, Penhaker M, Conforto S, Schmid M. Nanogenerators for Human Body Energy Harvesting. Trends in Biotechnology. 2017;35(7):610-24.

18.   Lee S, Bae S-H, Lin L, Yang Y, Park C, Kim S-W, et al. Super-Flexible Nanogenerator for Energy Harvesting from Gentle Wind and as an Active Deformation Sensor. Advanced Functional Materials. 2013;23(19):2445-9.

19.   Liang X, Jiang T, Liu G, Xiao T, Xu L, Li W, et al. Triboelectric Nanogenerator Networks Integrated with Power Management Module for Water Wave Energy Harvesting. Advanced Functional Materials.0(0):1807241.

20.   Wu B, Chen W, Zhang C. On free vibration of piezoelectric nanospheres with surface effect. Mechanics of Advanced Materials and Structures. 2017:1-14.

21.   Wang Z, Zhang Y, Yang S, Hu Y, Wang S, Gu H, et al. (K,Na)NbO3 Nanofiber-based Self-Powered Sensors for Accurate Detection of Dynamic Strain. ACS Applied Materials & Interfaces. 2015;7(8):4921-7.

22.   Purusothaman Y, Alluri NR, Chandrasekhar A, Vivekananthan V, Kim SJ. Regulation of Charge Carrier Dynamics in ZnO Microarchitecture-Based UV/Visible Photodetector via Photonic-Strain Induced Effects. Small. 2018;14(11):1703044.

23.   Vivekananthan V, Chandrasekhar A, Alluri NR, Purusothaman Y, Joong Kim W, Kang C-N, et al. A flexible piezoelectric composite nanogenerator based on doping enhanced lead-free nanoparticles. Materials Letters. 2019;249:73-6.

24.   Wen Z, Yeh MH, Guo H, Wang J, Zi Y, Xu W, et al. Self-powered textile for wearable electronics by hybridizing fiber-shaped nanogenerators, solar cells, and supercapacitors. Sci Adv. 2016;2(10):e1600097.

25.   Yang H, Wang M, Deng M, Guo H, Zhang W, Yang H, et al. A full-packaged rolling triboelectric-electromagnetic hybrid nanogenerator for energy harvesting and building up self-powered wireless systems. Nano Energy. 2019;56:300-6.

26.   Vivekananthan V, Chandrasekhar A, Alluri NR, Purusothaman Y, Khandelwal G, Pandey R, et al. Fe2O3 magnetic particles derived triboelectric-electromagnetic hybrid generator for zero-power consuming seismic detection. Nano Energy. 2019;64:103926.

27.   Alluri NR, Chandrasekhar A, Kim S-J. Exalted Electric Output via Piezoelectric–Triboelectric Coupling/Sustainable Butterfly Wing Structure Type Multiunit Hybrid Nanogenerator. ACS Sustainable Chemistry & Engineering. 2018;6(2):1919-33.

28. Dudem B, Bharat LK, Patnam H, Mule AR, Yu JS. Enhancing the output performance of hybrid nanogenerators based on Al-doped BaTiO3 composite films: a self-powered utility system for portable electronics. Journal of Materials Chemistry A. 2018;6(33):16101-10.

29. Qiu Y, Zhang H, Hu L, Yang D, Wang L, Wang B, et al. Flexible piezoelectric nanogenerators based on ZnO nanorods grown on common paper substrates. Nanoscale. 2012;4(20):6568-73.

30. Park K-I, Son JH, Hwang G-T, Jeong CK, Ryu J, Koo M, et al. Highly-Efficient, Flexible Piezoelectric PZT Thin Film Nanogenerator on Plastic Substrates. Advanced Materials. 2014;26(16):2514-20.

31. Saadatnia Z, Esmailzadeh E, Naguib HE. High Performance Triboelectric Nanogenerator by Hot Embossing on Self-Assembled Micro-Particles. Advanced Engineering Materials. 2019;21(1):1700957.

32. Chandrasekhar A, Vivekananthan V, Khandelwal G, Kim SJ. A fully packed water-proof, humidity resistant triboelectric nanogenerator for transmitting Morse code. Nano Energy. 2019;60:850-6.

33. Chandrasekhar A, Alluri NR, Vivekananthan V, Purusothaman Y, Kim S-J. A sustainable freestanding biomechanical energy harvesting smart backpack as a portable-wearable power source. Journal of Materials Chemistry C. 2017;5(6):1488-93.

CHAPTER 7

7.1 A Sliding mode Contact Electrification based Triboelectric-Electromagnetic Hybrid Generator for Small-Scale Biomechanical Energy Harvesting

Highlights

➢ The present work describes the hybridization of two different energy harvesters works simultaneously in a single package. By applying simultaneous mechanical force, two components such as triboelectric nanogenerator (TENG) and electromagnetic generator (EMG) independently produce power.

➢ The hybrid device was made with a polymeric cylinder composed of Kapton in the inner wall; a copper coil wound outside the cylinder and neodymium magnet and small bits of paper housed inside it.

➢ The paper flakes having the dimension of 5 mm × 5 mm, which are triboelectric positive slides over the negative triboelectric layer Kapton.

➢ The triboelectric component generates the maximum output with the voltage of ≈ 20 V and the current of 300 nA. The magnet inside the cylinder moves simultaneously along with the paper made the production of electric flux in the coil. The alternating magnetic flux induces the current in the outer coil as per the Lenz's law.

➢ The maximum output generated from the EMG component with the obtained voltage of 2 V and the maximum current of 10 mA. Further, to analyze the actual working behavior of the device, commercial capacitor charging behavior was analyzed.

7.1.1 Introduction

A vast amount of vibration energy had been produced in the environment from our day to life either naturally or by human-made (1). This vibration energy can be found in the form of vehicle motions(2), human motions(3), ocean waves(4), wind(5), and heavy industries(6). After the invention of nanogenerators, it has been reported that the waste mechanical energy can be scavenged and eventually been used for powering up small electronic devices and can also be used for portable and wearable applications (7, 8). By using the nanogenerators, the vibration energy can be scavenged using piezoelectric nanogenerator (PENG)(9), triboelectric nanogenerator (TENG)(10), and electromagnetic generator (EMG)(11). Among these effects, TENG has shown enormous advantages such as simple fabrication, low cost, and lightweight(12). Other than harvesting vibration energy TENGs can be used to harvest most of the forms of mechanical energy such as wind(13), ocean(14), rotational(15), tidal(16) and acoustic(17). On the other hand, TENG itself cannot produce high current to use for various real-time applications. To improve the efficiency of the TENG device, a hybrid approach has been utilized with the combination of two different energy harvesting modes in a single package. This type of hybrid nanogenerators can be used for boosting the electrical output performance of the nanogenerator and can also be able to improve the efficiency of the energy harvester. Among the various hybrid energy harvesters, TENG and EMG hybrid combination had gained huge attention because of its energy harvesting performance under the simultaneous mechanical motions(18, 19). TENG and EMG can work efficiently as a hybrid generator under sliding, contact-separation and rotation modes.

163

Very recently many researchers are working on hybrid generators for scavenging vibrational energy for various self-powered applications. J. He et al. had reported a hybrid generator composed of TENG, PENG, and EMG in a single unit for self-powered wireless monitoring system(20). Similarly, H. Shao et al. fabricated a hybrid generator device with TENG and EMG components for scavenging water wave energy with the sea wave oscillation and eventually been used to operate an electronic thermometer(21). In either case, the device uses a complex construction and uses expensive triboelectric materials such as copper, carbon nanotubes, polyethylene terephthalate (PET). However, the device used in the present manuscript is used as the triboelectric material which is very cheap and simple in overall construction of the device. Since it is small cylindrical in shape it can easily harvest vibrational motions upon any kind of mechanical motions. The triboelectric components work on sliding mode with paper as triboelectric material which cannot create damage on the Kapton layer due to friction like the traditional sliding mode triboelectric nanogenerator. The device the have a smaller dimension which has the dimension equal to C size battery and houses both triboelectric and electromagnetic generator. The device is completely eco-friendly without any harmful effects

The present work describes the TENG-EMG hybrid generator which works simultaneously upon the same sliding motions. The device was made of a polyethylene terephthalate (PET) cylinder housing composed of kapton film with gold-coated electrodes placed at the inner side and made as a negative triboelectric layer and paper bits as a positive triboelectric layer. The triboelectric series chart showing various triboelectric materials with their respective charges in Figure S1. The outer side of the PET was wound with a copper coil and magnet is placed inside to generate EMG output.

The TENG component generates more voltage and less current, whereas the EMG component generates low voltage and high current. By hybridizing both the harvesters using proper load matching resistance and rectification circuit the output power had been boosted and eventually been used for real-time demonstration such as charging the commercial capacitor and lighting up light-emitting diodes (LEDs). Further, the hybrid device had been used for scavenging small-scale biomechanical energy by placing the device on the backpack and been generated electrical output under the walking, running and bending motions of the human body. This type of hybrid energy harvester with enhanced output power can be used successively for self-powered sensors/systems and can be used for micro or nano-electromechanical systems (MEMS/NEMS) based applications

7.1.2 Device fabrication and measurements

A cylindrical housing made of PET had been used as the outer layer for the hybrid device (length is 50 mm and diameter is 20 mm). A Kapton film was cut according to the size of the PET and coated with aluminum (Al) at the backside as the electrode material. The Kapton layer was kept as the inner wall and also acts as the negative triboelectric layer. A copper coil of 500 turns has been wounded outside the cylinder for the EMG component. Further neodymium magnet (1/2" diameter and 1/4" thick) and small bits of paper had placed inside the cylinder, where the paper acts as positive triboelectric material and magnet for the production of electromagnetic induction.

The electrical measurements were carried out with the help of an electrometer (Keithley 6514), and the linear vibration to the device for the measuring the electrical output was given using a linear motor (Lin Mot, Inc, USA). All measurements were

carried out in room temperature inside a homemade Faraday cage for avoiding any external interference.

7.1.4 Results and discussion

Figure 7.1.1a shows the step by step schematic of the fabrication of the TENG-EMG hybrid generator device. The cylindrical housing made of PET with a dimension of L = 50 mm and Φ = 20 mm. Kapton film with aluminum electrode coating was placed as the inner wall of the PET cylinder and eventually been used as a negative triboelectric layer. The outer wall of the cylinder was wounded by a copper coil with a maximum of 500 turns towards the fabrication of EMG component. Small square-shaped papers were cut and placed inside the cylinder, which acts as a positive triboelectric material and a lightweight neodymium magnet as shown in Figure 7.1.1c is placed inside for the production of electromagnetic induction through the coil. This type of arrangement in the device can make the simultaneous generation of electric power from both EMG and TENG independently upon the same mechanical vibration. Figure 7.1.1b shows the comparison of the use of the TENG-EMG hybrid device over the usage of battery. It is well known that the battery has certain drawbacks such as limited lifetime and requires periodical replacement. Rechargeable batteries require external power for recharging it for its continuous usage. With the time passing the battery performance can be affected due to its aging effect. The safety about the battery is still a problem because chemical energy has been converted into electrical energy and it is not eco-friendly. These drawbacks can be overcome easily by using the TENG-EMG hybrid device. The only drawback which these types of devices face is that it requires an external power management circuit to deliver the stable electrical output

for using it into any real-time applications. Figure 7.1.1d shows the cross-section of the device fabricated, showing the paper flakes and magnet. The Kapton film used here is a micro-roughness created film using a plasma etching process. The micro-roughness enhances the number of contact point s on the layers leading to the development of high electrical output. The roughness profile was measured using a field emission scanning electron microscope (FE-SEM) and is shown in Figure 7.1.1e.
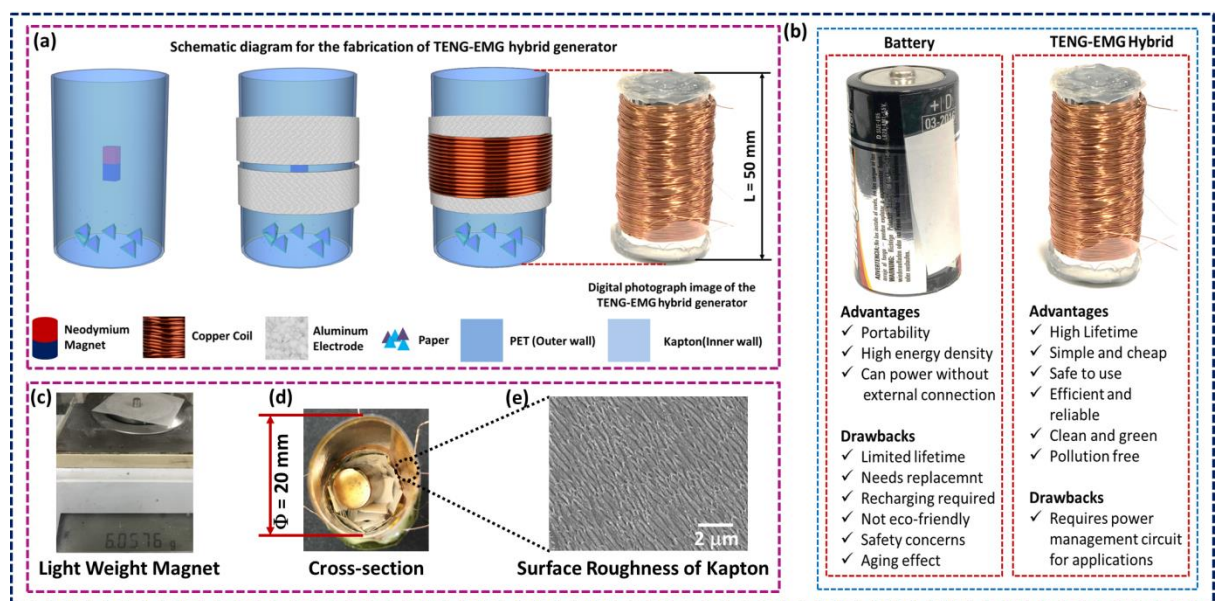
Figure 7.1.1 (a) Schematic diagram of the fabrication of TENG-EMG hybrid device (b) Comparison of the performance of TENG-EMG hybrid device and commercial battery with their advantages and disadvantages (c) Digital photograph image of the magnet used and its weight (d) cross-section of the device showing the magnet and paper flakes with dimension and (e) FE-SEM image showing the surface roughness created on Kapton film using plasma etching process.

Figure 7.1.2 describes the working mechanism of both triboelectric nanogenerator and electromagnetic generator upon the sliding mode. Figure 7.1.2a shows the working mechanism of sliding mode TENG, in which the paper slides on the kapton film. Under linear vibration applied on the device, the papers inside the

devices act as a positive triboelectric layer that moves over the negative kapton surface, leads to the generation of electric potential. This makes the electron to flow from one electrode to the other through an external load resistance as shown in Figure 7.1.2a (ii). Figure 7.1.2a (iii) shows the papers were back to the normal position and makes to complete one half-cycle of the TENG component with no flow of electrons. Next, with the second half cycle, the paper moves on the opposite direction make the electrons to flow in the reverse direction as shown in figure 7.1.2b (iv). Figure (c) and (d) shows the triboelectric output voltage and current with the maximum electrical output of open-circuit voltage of 20 V and short circuit current of 300 nA peak to peak. Similarly, the working mechanism of EMG was shown in Figure 7.1.2b (i to iv). When a linear vibration is applied to the device, the magnet inside the cylinder moves across the coil leads to the production of magnetic flux around the coil which pushes electrons in the copper wire. The electrons mobility is directly responsible for the electric charge flow which was determined through Lenz's law. The generated output voltage and current from the EMG component can be calculated using Faraday's law. Figure 7.1.2 (e) and (f) shows the electrical output of the EMG with the maximum peak to peak voltage $\approx$ 2 V and a current of 10 mA at an operating frequency of 2 Hz. Figure 7.1.3 (a) and (b) shows the force analysis of the triboelectric component. The voltage and current response have been analyzed by applying the linear acceleration ranging 1 m/s^2, 3 m/s^2, 5 m/s^2 and 7 m/s^2. The output gets stabilized once the acceleration reaches 5 m/s^2, with the further increase in the acceleration to 7 m/s^2 the output response gets stabilized.
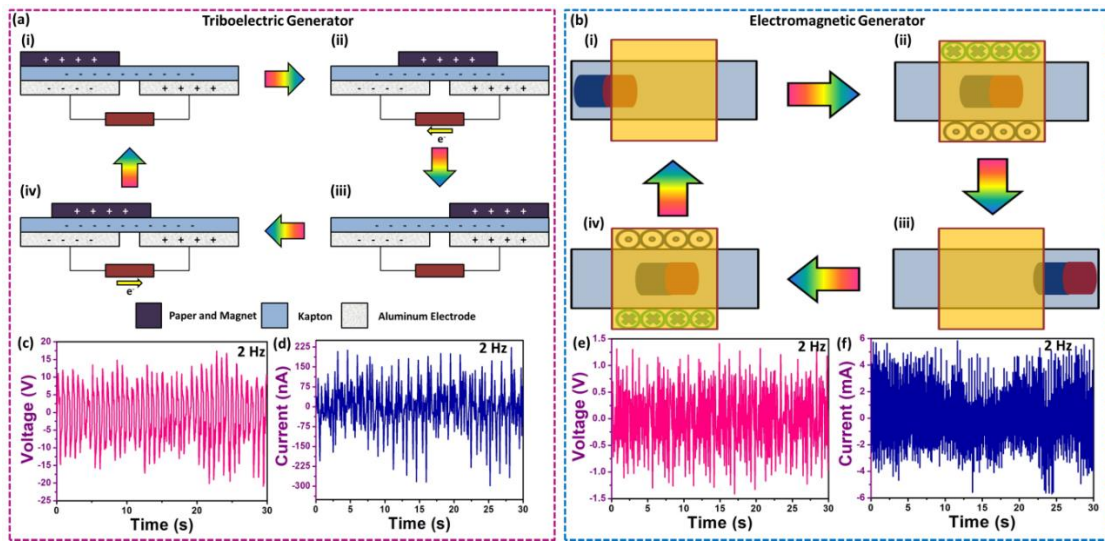
Figure 7.1.2 (a) working mechanism of the triboelectric generator under sliding motion (b) Working mechanism of the electromagnetic generator (c) and (d) voltage and current output of TENG component (e) and (f) voltage and current output of EMG component.
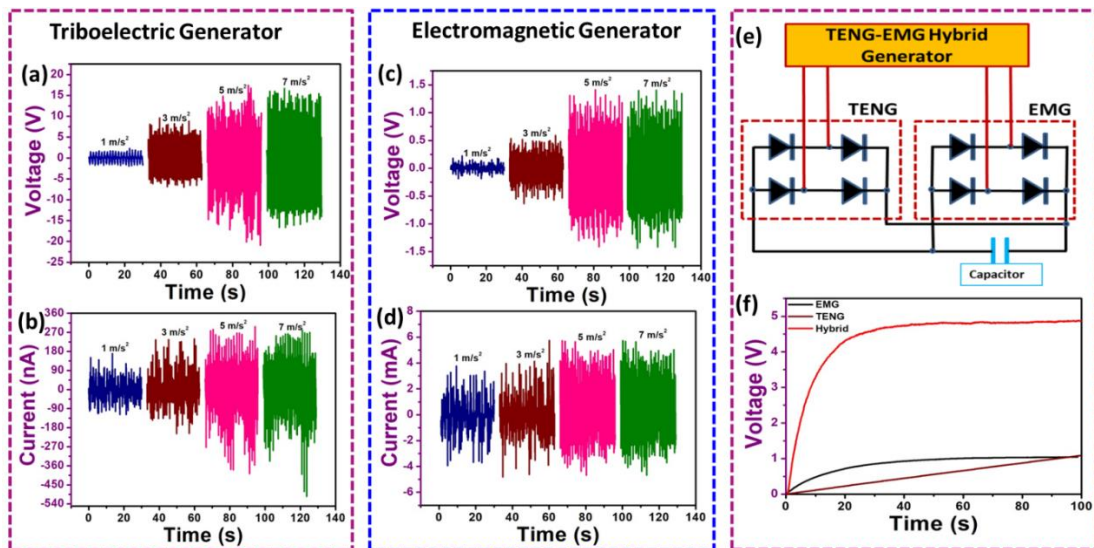
Figure 7.1.3 (a) and (b) Force analysis of TENG component with different acceleration ranging from ranging 1 m/s^2, 3 m/s^2, 5 m/s^2 and 7 m/s^2 (c) Load resistance analysis of TENG component (d) and (e) Force analysis of EMG component under various acceleration from ranging 1 m/s^2, 3 m/s^2, 5 m/s^2 and 7 m/s^2 (f) Load resistance analysis of EMG component (g) circuit connection diagram used for charging commercial capacitor (h) Capacitor charging characteristics by TENG, EMG and hybrid combination.

This is due to the volume of the cylinder used as well the quantity of the paper used. From this, the maximum acceleration used was confirmed to be 5 m/s^2, and the output voltage generated was 20 V and the maximum current of 300 nA. On the other hand, the force analysis was performed for the EMG component with the same acceleration used for the TENG component as shown in Figure 7.1.3c and d. Similar to the TENG component the output of EMG component also saturates at 5 m/s^2 acceleration, showing the maximum output voltage of 2 V and a current of 10 mA. Figure 3e shows the circuit diagram used for charging the commercial capacitor of 2.2 μF under TENG, EMG, and hybrid configurations. The charging characteristics of a commercial capacitor using the hybrid connection charges rapidly when compared to individual TENG and EMG components. This behavior is due to the higher output under hybrid connection, whereas in the individual TENG the voltage is higher and current is too low to trigger the charging phenomenon. The same behavior in charging occurs for the individual EMG, where the voltage is less to induce the charging as shown in Figure 7.1.3f. The load matching analysis was performed by using different load resistance, and the TENG component shows the instantaneous peak power of 1 μW and the power density 1.2 mW/m^2 at a load resistance of 500 MΩ. The EMG component shows the peak power of 4 mW at 5 kΩ load resistance as shown in Figure 7.1.4a and c. The voltage response of both TENG and EMG device was concerning change in frequency is shown in Figure 7.1.4b and 7.1.4d.
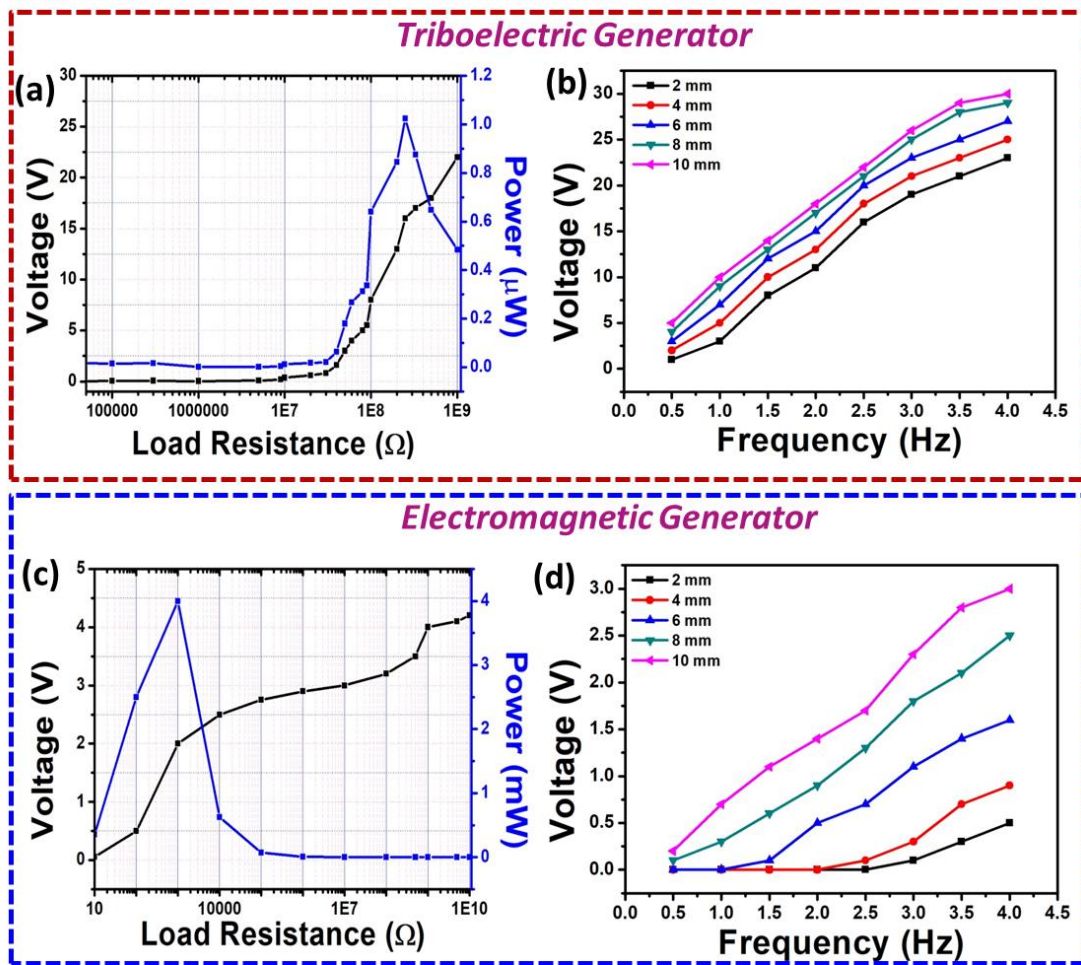
Figure 7.1.4 (a) Load resistance analysis of the TENG component and its instantaneous power value (b) voltage measurement of the TENG component with respect to different frequency (c) load resistance and power analysis of the EMG component (d) voltage measurement of EMG component with respect to the different operating frequency.

The device was mounted on an electro-dynamic shaker and measured its voltage response for different frequency. The displacement of the shaft is also a factor considered during measurement. So, the displacement is considered from 2 mm, 4 mm, 6 mm, 8 mm and 10 mm and the respected change in frequency response have also been measured. The durability of the fabricated device was shown in Figure 7.1.5 (a) and (b) for 2000 seconds by analyzing the voltage (TENG) and current (EMG). Figure

5c shows the demonstration of lighting up high power white LEDs with force ON and OFF to the device. Further 60 green LEDs were also lit up using the hybrid configuration which is shown in Figure 7.1.5. The hybrid device had been used for the real-time demonstration of small-scale bio-mechanical energy scavenging by placing the device on a backpack. Both the EMG and TENG output connections have been connected in series for the real-time human motion data response acquisition. Figure 7.1.5 e-g shows the device attached on the backpack and could scavenge the biomechanical energy through walking, running and bending motion of the human wearing the bag. The real-time electrical output of the hybrid device (TENG-EMG connected in series) on scavenging the biomechanical energy is shown in figure 7.1.5h. The higher output was obtained from the running motion which is due to the high acceleration applied to the device during a running motion. Similarly, the output is low during walking and bending. The change in output is directly related to the triboelectric component (i.e., paper) which moves according to the force applied on to the device. The phenomenon can be understood directly from the peak pattern in the electrical signal during the real-time analysis.
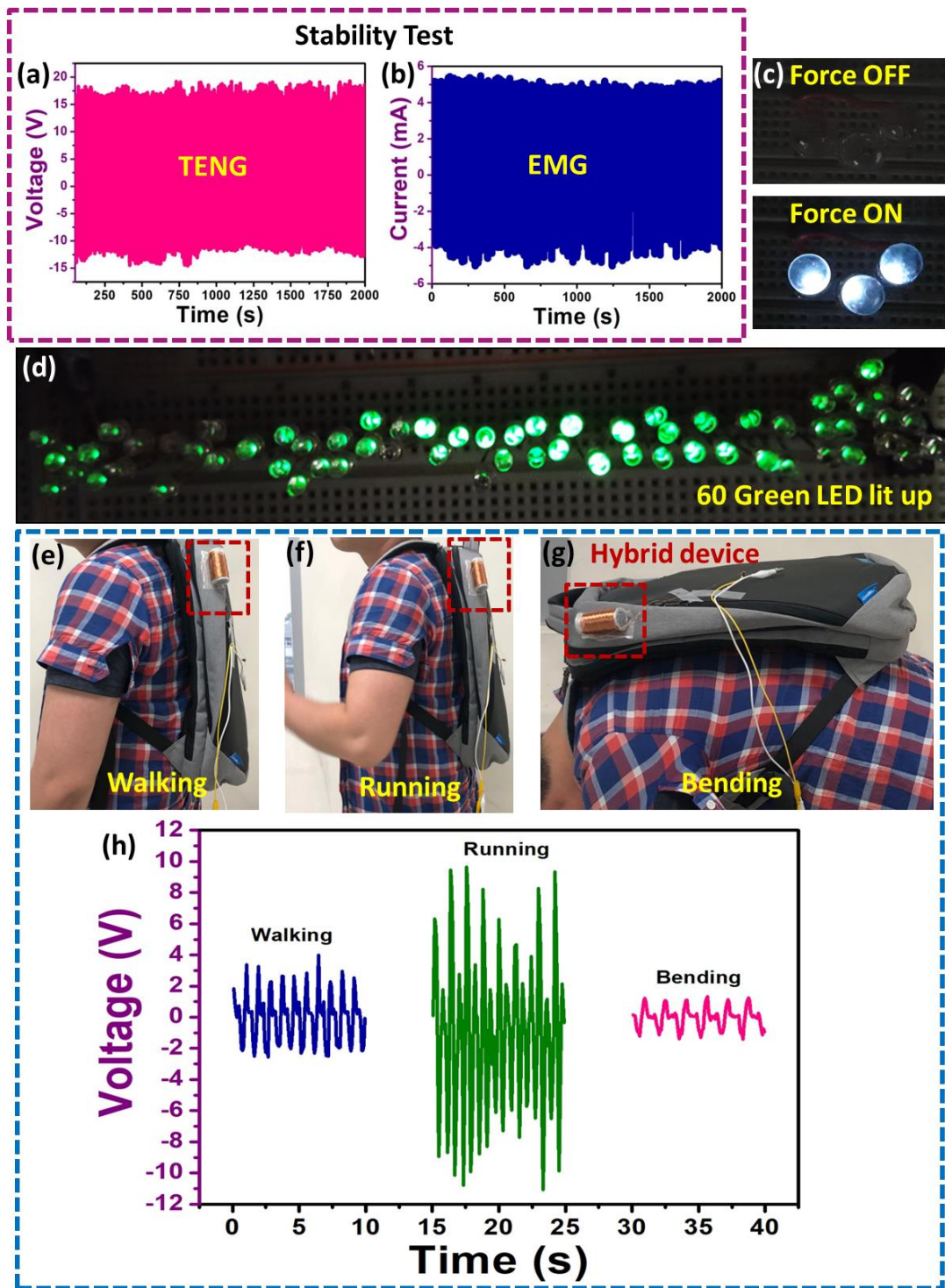
Figure 7.1.5 (a) and (b) Stability analysis of TENG and EMG component (c) High power White LEDs lit up under hybrid connection (d) 60 green LED lit up using hybrid device (e) to (g) real time biomechanical energy harvesting by attaching the device on a backpack and analysis of electrical output by walking, running and bending motions (h) electrical output generated under walking, running and bending.

Hence the above results clearly show that the TENG-EMG hybrid device is a promising candidate for scavenging small-scale biomechanical energy and can to charge the commercial capacitor and lighting up LEDs. With further development in this field can make a potential breakthrough in the field of MEMS & NEMS systems as well as self-powered sensors and systems.

7.1.5 Conclusions

In summary, a single package hybrid generator composed of TENG and EMG had reported via a cost-effective and easy fabrication method. The device works actively upon various accelerations and generates electrical output simultaneously from both TENG and EMG components upon the same motion. The working mechanism of the individual components have been discussed, and the electrical analysis had performed extensively under various accelerations, load matching analysis, capacitor charging, and LED lit up. The device generates a maximum electrical output of 20 V and 300 nA current at an acceleration of 5 m/s^2 with an instantaneous power density of 1 mW/m^3 for the TENG component. Similarly, the EMG component generates a maximum output with the voltage of 2 V and a current of 10 mA at 5 m/s^2 with an instantaneous power $\approx$ 4 mW for EMG and 1 μW for TENG components. Further, the hybrid device has been used for demonstrating the real-time application of small-scale biomechanical energy scavenging by attaching the device on the backpack and harvest energy from human walking, running and bending motions. From the above results, the hybrid energy harvesting technology using TENG and EMG paves the way for smart self-powered sensors and systems.

7.1.6 References

1.   Wang S, Wang X, Wang ZL, Yang Y. Efficient Scavenging of Solar and Wind Energies in a Smart City. ACS Nano. 2016;10(6):5696-700.

2.   Vivekananthan V, Alluri NR, Purusothaman Y, Chandrasekhar A, Kim S-J. A flexible, planar energy harvesting device for scavenging road side waste mechanical energy via the synergistic piezoelectric response of K0.5Na0.5NbO3-BaTiO3/PVDF composite films. Nanoscale. 2017;9(39):15122-30.

3.   Vivekananthan V, Alluri NR, Chandrasekhar A, Purusothaman Y, Gupta A, Kim S-J. Zero-power consuming intruder identification system by enhanced piezoelectricity of K0.5Na0.5NbO3 using substitutional doping of BTO NPs. Journal of Materials Chemistry C. 2019.

4.   Wen Z, Guo H, Zi Y, Yeh MH, Wang X, Deng J, et al. Harvesting Broad Frequency Band Blue Energy by a Triboelectric-Electromagnetic Hybrid Nanogenerator. ACS Nano. 2016;10(7):6526-34.

5.   Li DJ, Hong S, Gu S, Choi Y, Nakhmanson S, Heinonen O, et al. Polymer piezoelectric energy harvesters for low wind speed. Applied Physics Letters. 2014;104(1):012902.

6.   Lee S, Bae S-H, Lin L, Yang Y, Park C, Kim S-W, et al. Super-Flexible Nanogenerator for Energy Harvesting from Gentle Wind and as an Active Deformation Sensor. Advanced Functional Materials. 2013;23(19):2445-9.

7.   Hinchet R, Kim S-W. Wearable and Implantable Mechanical Energy Harvesters for Self-Powered Biomedical Systems. ACS Nano. 2015;9(8):7742-5.

8.   Vivekananthan V, Chandrasekhar A, Alluri NR, Purusothaman Y, Joong Kim W, Kang C-N, et al. A flexible piezoelectric composite nanogenerator based on doping enhanced lead-free nanoparticles. Materials Letters. 2019;249:73-6.

9.   Wang ZL, Song J. Piezoelectric Nanogenerators Based on Zinc Oxide Nanowire Arrays. Science. 2006;312(5771):242-6.

10.   Pan R, Xuan W, Chen J, Dong S, Jin H, Wang X, et al. Fully biodegradable triboelectric nanogenerators based on electrospun polylactic acid and nanostructured gelatin films. Nano Energy. 2018;45:193-202.

11.   Quan T, Wang X, Wang ZL, Yang Y. Hybridized Electromagnetic–Triboelectric Nanogenerator for a Self-Powered Electronic Watch. ACS Nano. 2015;9(12):12301-10.

12.   Chandrasekhar A, Alluri NR, Vivekananthan V, Park JH, Kim S-J. Sustainable Biomechanical Energy Scavenger toward Self-Reliant Kids' Interactive Battery-Free Smart Puzzle. ACS Sustainable Chemistry & Engineering. 2017;5(8):7310-6.

13.   Zhao Z, Pu X, Du C, Li L, Jiang C, Hu W, et al. Freestanding Flag-Type Triboelectric Nanogenerator for Harvesting High-Altitude Wind Energy from Arbitrary Directions. ACS Nano. 2016;10(2):1780-7.

14.   Yao Y, Jiang T, Zhang L, Chen X, Gao Z, Wang ZL. Charging System Optimization of Triboelectric Nanogenerator for Water Wave Energy Harvesting and Storage. ACS Appl Mater Interfaces. 2016;8(33):21398-406.

15.   Zhang B, Chen J, Jin L, Deng W, Zhang L, Zhang H, et al. Rotating-Disk-Based Hybridized Electromagnetic-Triboelectric Nanogenerator for Sustainably Powering Wireless Traffic Volume Sensors. ACS Nano. 2016;10(6):6241-7.

16.   Lei R, Zhai H, Nie J, Zhong W, Bai Y, Liang X, et al. Butterfly-Inspired Triboelectric Nanogenerators with Spring-Assisted Linkage Structure for Water Wave Energy Harvesting. Advanced Materials Technologies. 2019;4(3):1800514.

17.   Fan X, Chen J, Yang J, Bai P, Li Z, Wang ZL. Ultrathin, Rollable, Paper-Based Triboelectric Nanogenerator for Acoustic Energy Harvesting and Self-Powered Sound Recording. ACS Nano. 2015;9(4):4236-43.

18.   Quan T, Wang ZL, Yang Y. A Shared-Electrode-Based Hybridized Electromagnetic-Triboelectric Nanogenerator. ACS Appl Mater Interfaces. 2016;8(30):19573-8.

19.   Vivekananthan V, Chandrasekhar A, Alluri NR, Purusothaman Y, Khandelwal G, Pandey R, et al. Fe2O3 magnetic particles derived triboelectric-electromagnetic hybrid generator for zero-power consuming seismic detection. Nano Energy. 2019;64:103926.

20.   He J, Wen T, Qian S, Zhang Z, Tian Z, Zhu J, et al. Triboelectric-piezoelectric-electromagnetic hybrid nanogenerator for high-efficient vibration energy harvesting and self-powered wireless monitoring system. Nano Energy. 2018;43:326-39.

21.   Huiyun S, Ping C, Ruixuan C, Lingjie X, Na S, Qingqing S, et al. Triboelectric–Electromagnetic Hybrid Generator for Harvesting Blue Energy. Nano-Micro Letters. 2018;10(3):54.

7.3 Fe_2O_3 Magnetic Particles derived Triboelectric-Electromagnetic Hybrid Generator for Zero-Power Consuming Seismic Detection

Highlights

➢ A zero power consuming seismic vibration detector had been reported for the first time using TENG and EMG hybrid generator.

➢ The hybrid energy harvester generates electrical signal from TENG and EMG independently, upon the same particle motions.

➢ The device generates a maximum rectified output of 3 V/ 16 μA under hybrid combination upon vertical vibration.

➢ The intensity of seismic vibration enables the device to send the trigger signal to Arduino board and drives LED and buzzer.

Graphical Outline
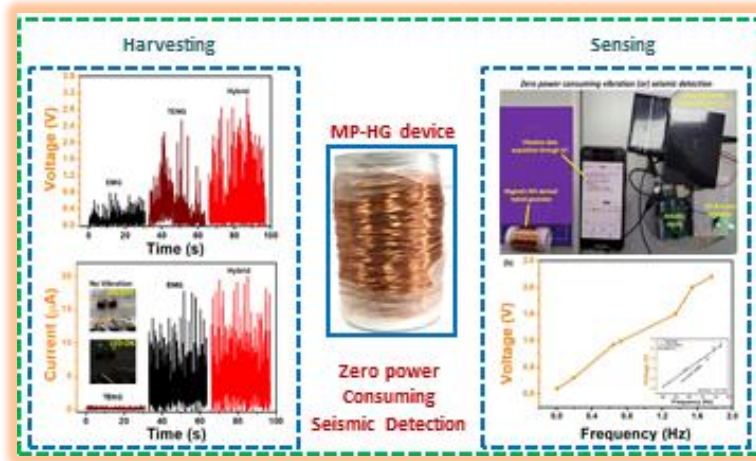
7.2.1 Introduction

The increase in population density becomes a threat to human society under natural and human-made seismic events. There have been many occurrences of seismic events in the past two decade leads to high causalities to humans as well as industries. World health organization (WHO) had reported that high occupancy, dense building concentration, lack of public awareness on earthquake risks, and absence of warning systems are the main factors of vulnerability on the seismic events. The epicenter of the 2004 deadliest earthquake at Sumatra (Indonesia) and the impact were felt in 14 countries at various magnitudes analyzed by the national science foundation (NSF) in 2005. The NSF stated that many states do not have vibration alert systems or earthquake or tsunami warning systems. There are even minor earthquakes occurring every day at various places in the world which cannot be predicted[1, 2]. Other than earthquakes, there are human-made seismic events that cause heavy vibrations such as nuclear explosive tests, industries, drilling on the ground, making an impact which can threaten human society. Concerning the safety of the society, a zero-power consuming warning system with good accuracy and uninterrupted operating capability is highly desired.

However, the existing seismic vibration sensing device uses an accelerometer which requires an external power supply to drive, and most of the devices use batteries as we know that batteries are not environmentally friendly and having few drawbacks such as large packaging size and risk of environmental pollution. Also, accelerometers have various disadvantages such as fixed sensitivity, prone to temperature, the high impedance, which eventually makes the accelerometers more vulnerable to noise,

제주대학교 중앙도서관
JEJU NATIONAL UNIVERSITY LIBRARY

requires more maintenance and operational expertise is needed. The existing seismic detector requires uninterrupted electric power and requires intense periodical maintenance for its safety. To work with this type of system, a highly skilled operator is required to handle. Other than the hardware issues, there are several other issues regarding the data collection, such as the data is expensive to acquire, and the logistics of the data acquisition are more intense. The data reduction and processing can be time-consuming, and it requires sophisticated computer hardware and expertise to analyze. This clearly shows that the detection system works solely upon the presence of an external power source, and the analysis will take an expensive process. Therefore, it is proved that the requirement of an active system which does not rely on battery and provides continuous operation all over the time is highly necessary. This could be able to replace the accelerometer with an active detector, i.e., Nanogenerator[3, 4] which senses the seismic vibration and triggers the alarming system.

The rapid advancement in the field of nanogenerators as a self-powered sensors[5] i.e. physical sensors[6] (pressure[7, 8], acoustic[9], flexion[10], force[11, 12]), optical[13] (photodetectors[14], switches[15]), chemical/biological[16] (glucose[17], pH[18], gas[19], biomarkers[20, 21]) and its basic prototypes were extensively investigated. Here the triboelectric (TENG)[22, 23], piezoelectric (PENG) nanogenerators and hybrid generators[24] (such as TENG and electromagnetic generator (EMG)[25]) were studied based on the nanostructures, device designs and output performance wise. Among that the hybrid generator made of TENG (voltage source, low operating frequency) and EMG (current source, high frequency) had attracted considerable interest due to easy construction, enabling TENG component in EMG structure itself (reducing device area), and extending the operating bandwidth of

182

device with same mechanical stimuli. There are a lot of reports which successfully demonstrates hybrid nanogenerators as a mechanical energy harvester in low-frequency and small amplitudes[26], as well as for various self-powered sensing applications such as knee rehabilitation assessment[27], pinwheel type wind energy harvesting[28], self-powered biomechanical energy harvester[29], water wave energy harvesting[30], portable power banks[31], traffic monitoring[32], security systems[33], and vibrational energy harvesting[34]. However, using the individual commercial magnetic parts (spherical beads, bar and horseshoe magnets) and multiple triboelectric layers (positive, negative) and additional packaging layers increases the weight of the hybrid device creating the harsh magnetic movements (high wear/tear on device components) which eventually reduces the overall life span of hybrid generator. Moreover using rigid magnetic bars in hybrid generator restricts the applicability in the field of micro/nanosensing levels in various industries, even though it produces the high instantaneous power density[35]. Minimizing the active layers or components in the hybrid device structure is still the greatest challenge in the field of the mechanically driven energy harvester. Also, the performance of nanogenerator affects drastically due to the temperature effects. This part is still challenging towards its commercialization[36].

To overcome the above issues, lower weight, reduced device layers based magnetic nanoparticle derived cylindrical hybrid generator (MP-HG) with full packed structure is proposed. Here, the magnetic particles act as a source for creating the magnetic flux in EMG, as well as develops the contact electrification (as a positive layer) in TENG during the simultaneous mechanical motions. The detailed electrical output responses of TENG, EMG, and MP-HG measured by the vertical and lateral

mechanical motions. Also investigated the filling ratio of magnetic particles (10, 20, 30, 40 and 50 %) in the cylindrical hybrid device (length (l) = 50 mm and diameter (ϕ) = 20 mm) structure and tested the output behavior in various humidity conditions (10 to 90 %RH). The 40% filling ratio of MP-HG generates ($\approx$ 3 V, 16 μA) and instantaneous power density are (0.4 mW/m^2) upon the vertical mechanical motion. Overall the weight of MP-HG device reduced and can also be protected from the humidity issues, which the conventional hybrid generator lags. Further, a real-time zero power consuming seismic detection was demonstrated using the MP-HG device placed on the compressor motor and audio speakers. The alarming unit was connected to an Arduino circuit which was powered using a solar cell. This arrangement made the entire unit as a self-powered system replacing the external battery source. The proposed system would be highly useful in places which are prone to natural calamities, high occupancy regions, a highly industrialized area where man-made seismic events can occur. The projected report paves the way for self-powered automated surveillance technologies.

7.2.2 Experimental details

The Iron oxide (Fe_2O_3) particles were synthesized by a simple co-precipitation method with the precursor solution as iron chloride hexahydrate ($FeCl_3 \cdot 6H_2O$) and ammonia solution (NH_4OH) as a precipitating agent. $FeCl_3 \cdot 6H_2O$ was dissolved in 100 ml deionized water using magnetic stirring for 30 min at 80 °C. Similarly, 50 mL aqueous solution of NH_4OH was added dropwise to the precursor solution under a pH value of 11. The mixture was stirred continuously for 3 h, and the precipitations were collected and washed using ethanol several times and dried in a hot air oven at 80 °C for 6 h.

The dried particles were then calcined at 600 °C for 4h to get the magnetic particles.

7.2.2.1 Characterization

Various sophisticated characterization techniques were employed to characterize as prepared particles. The crystalline phase of the particles were characterized using a X-Ray Diffractometer system (XRD) at Cu-Kα radiation (λ=1.5418Å) at Korea Basic Science Research Centre (KBSI) Daegu Centre, Raman spectroscopy analysis were performed using a LabRam Raman spectrometer (Horiba Jobin-Yvon, France), X-Ray Photoelectron Spectroscopy (XPS, ESCA-2000, VG Microtech Ltd.), at KBSI, Busan Centre. The magnetic property of the Fe2O3 material was analyzed using a superconducting quantum interference device (SQUID, MPMS3- Evercool), at Korea Advanced Institute of Science and Technology (KAIST). The surface morphology of particles was analyzed by a Field emission scanning electron microscopy (FE-SEM, TESCAN, MIRA 3) and Transmission electron microscopy (TEM, JEM-2011, JEOL) at KBSI. Busan Centre.

7.2.2.2 MPMP-HG-HG Device fabrication and Electrical measurement

A cylindrical structure (50 mm × 20 mm) was made of PET used as a housing material for the MP-HG device. A KAPTON film was cut as per the dimension of the PET cylinder and attached with Al electrodes on the back side. The KAPTON film is then rolled and placed inside the cylinder, and two Cu wires were connected to the Al electrodes to form a free-standing TENG. The cylinder was then filled with Fe_2O_3 particles having the magnetic field strength with a remnant magnetization of 7 emu/g and coercivity of 0.038 T and closed on either side of the cylinder. The copper coil is the wounded on the cylinder 1000 times on the outer side with the size of 30 AWG, 0.010". A NdFeB magnet (2230) was attached at the bottom of the device for polarizing

제주대학교 중앙도서관
JEJU NATIONAL UNIVERSITY LIBRARY

the magnetic particles. A linear vibration was given to the device vertically and laterally using a linear motor setup (Lin Mot, Inc, USA) and the electrical outputs were measured using an electrometer (Keithley 6514).

7.2.3 Results and discussion

The Phase and crystal structure of the synthesized Fe_2O_3 particles were analyzed by XRD technique, which is shown in Figure 7.2.1a. The peaks are well matched with the JCPDS card no. 85-0987. The particle exhibits high crystallinity without any impurities and having an expected rhombohedral (hexagonal) crystal structure. The planes (012), (104), (110), (113), (024), (116) and (018) appeared at the 2θ range 24.16°, 33.12°, 35.63°, 40.64°, 49.47°, 54.08° and 57.42° corresponds to pure iron oxide particles. The Fe_2O_3 particles are having a space group of R-3c with a lattice constant of $\alpha = \beta = \gamma = 55.4°$ and $a = b = c = 5.034$ Å. The Raman spectroscopy of pure Fe_2O_3 particles was recorded at room temperature using a 514 nm excitation wavelength is shown in Figure 7.2.1b. A_{1g} and E_g are the phonon modes that appeared in the Raman spectroscopy. The A_{1g} modes correspond to the peak at 221 cm^{-1} and 492 cm^{-1} whereas the peaks at 290 cm^{-1}, 608 cm^{-1} and minor peaks at 245 cm^{-1}, 299 $cm^{-1,}$ and 409 cm^{-1} are related to E_g modes. The analysis has proved the phase of the Fe2O3 material has formed well without any other impurities.

Figure 7.2.1c shows the magnetic hysteresis of the as-synthesized particles at room temperature. The measurement was carried out at a magnetic field sweep from -20000 to 20000 Oe. The loop shows a ferromagnetic behavior with the coercively of 361 Oe shown in the inset of Figure 7.2.1c. The remnant magnetization and the saturation magnetization are said to be 7 emu/g and 26 emu/g respectively. To identify the elemental composition of the synthesized Fe_2O_3 nanoparticle, XPS spectroscopy

was carried out in the range of 200 to 750 eV, as shown in Figure 7.2.1d. No reductant peaks were observed in the spectrum other than Fe 2p, C1s, and O1s. There were two peaks appear at 710.5 and 724.2 eV which corresponds to Fe $2p_{3/2}$ as shown in Figure 7.2.1e, as said to be the characteristic peaks of the Fe^{3+}. Also, no shoulder peaks were observed at smaller binding energies which would be expected the presence of Fe^{2+} ion at 708 eV. After that, a small additional peak at 718.7 eV is the satellite peak, which indicates the unavailability of Fe^{2+}. Figure 7.2.1f shows the crystalline structure of the prepared Fe_2O_3 particles. The device schematic of the MP-HG was shown in Figure 7.2.1g with different layers, and the digital photographic image shows its side view and top view. The detailed fabrication method was discussed in the device fabrication and electrical measurement section. The digital photograph of the prepared red colored iron oxide particles was shown in the inset of Figure 7.2.2a, and the main image shows the nanoparticle attracted under the magnet. This indicates that the particle is active under magnetic field, which further used for EMG device.
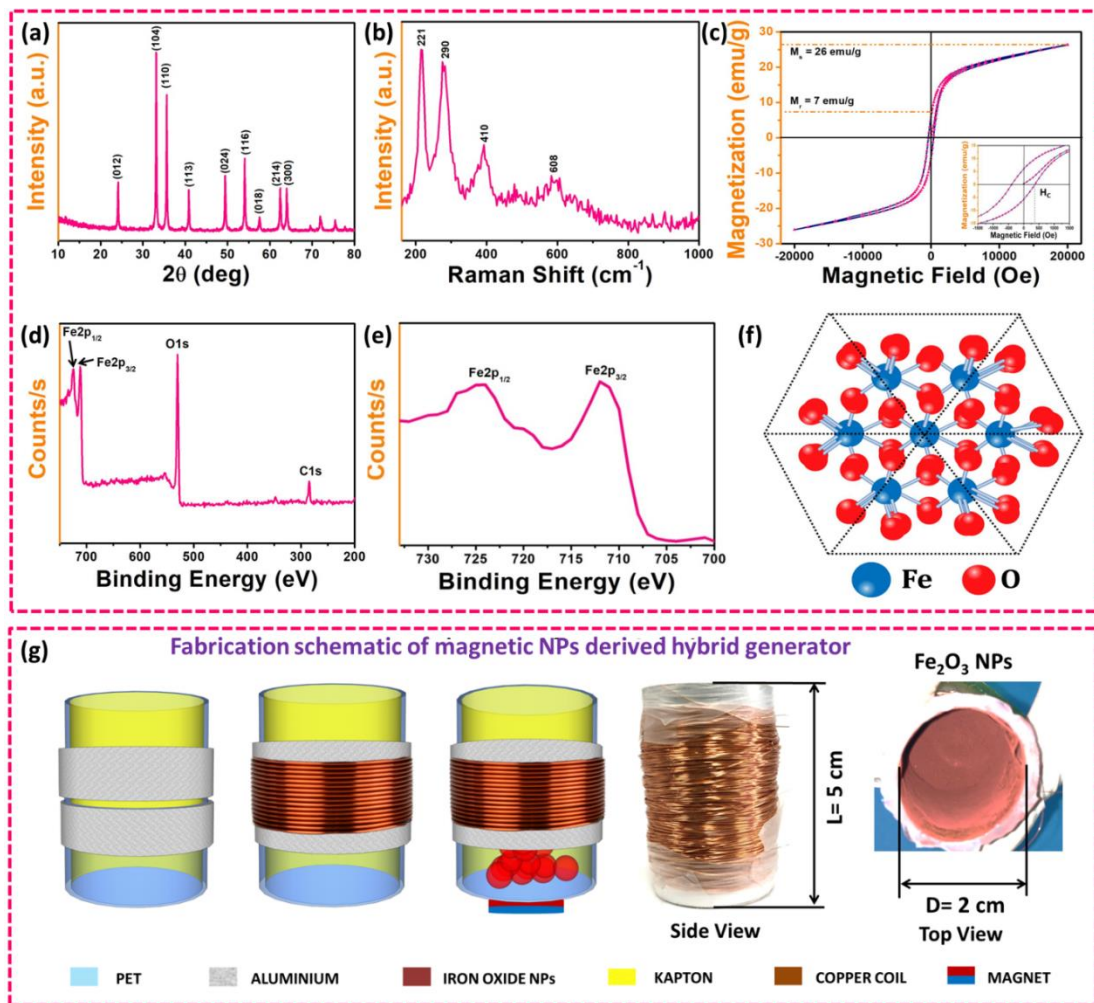
Figure 7.2.1 (a) and (b) XRD and Raman analysis of the synthesized Fe2O3 magnetic particles (c) Magnetic property measurement of the nanoparticle showing the remnant magnetization of 7 emu/g and a saturation magnetization of 26 emu/g. Inset shows the expanded region of coercivity (d) XPS analysis spectra showing C1s, O1s states (e) XPS spectra showing the major peaks $Fe2p_{1/2}$ and $Fe2p_{3/2}$ and (f) Crystal structure of Fe_2O_3 (g) Step - by - step fabrication and schematic diagram of the MP-HG hybrid generator and its digital photograph showing the side view and top opened view showing the particles inside.

Figure 7.2.2b shows the FE-SEM morphology of the iron oxide particles, where a large quantity of uniformly distributed particles was observed at a size of 500 nm. The TEM analysis of the particles, as shown in Figure 7.2.2c to f with the content of particle size, lattice fringes, and selected area electron diffraction (SAED) pattern. The

particles exhibit an elongated morphology with the size of ~ 150 nm, which is shown in Figure 7.2.2c and d.
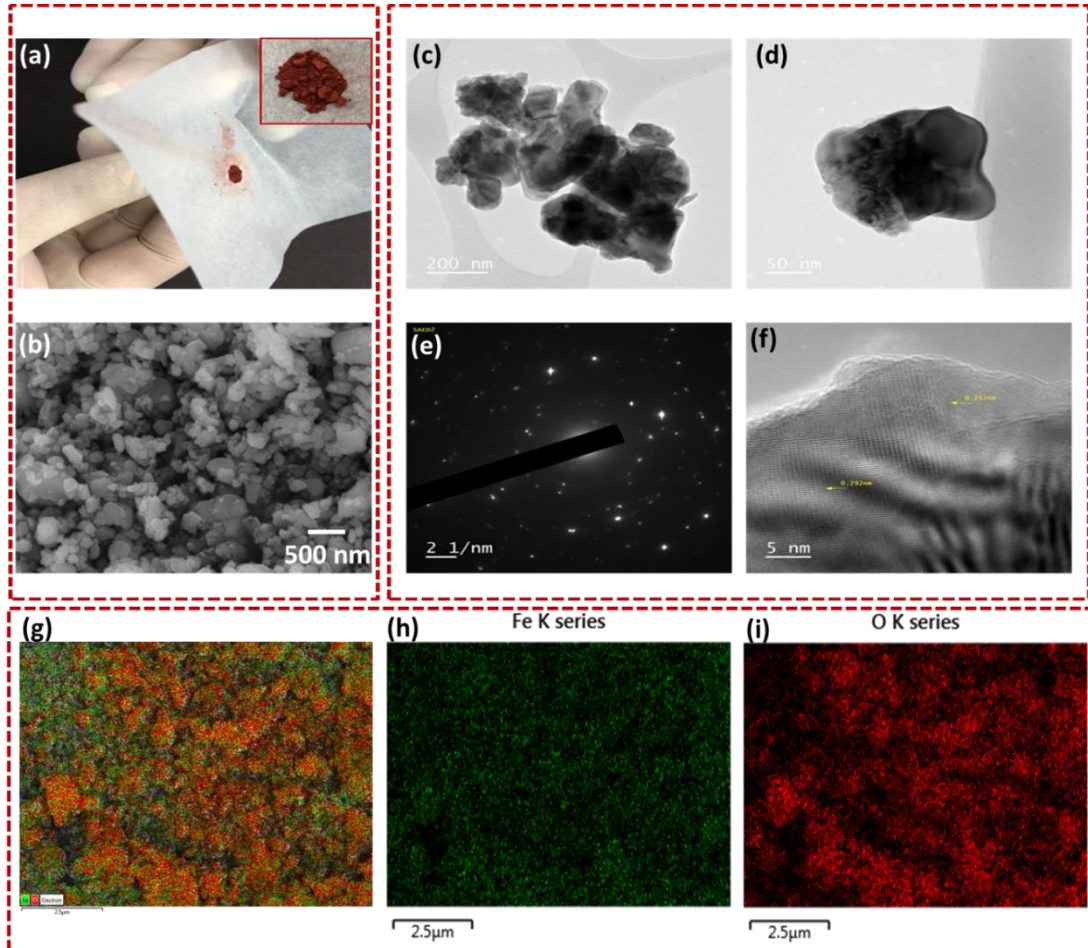
Figure 7.2.2 (a) Morphological analysis of Fe₂O₃ nanoparticles (a) Digital photographic image of the synthesized iron oxide nanoparticles showing its magnetic property by attracting it under magnets, and the inset shows the red colored magnetic nanoparticles (b) FE-SEM image of the synthesized particles at 500 nm magnifications. (c) Shows the TEM morphology of the particles at 200 nm (d) shows the TEM morphology of single particle at 50 nm (e) SAED diffraction pattern and (f) lattice fringes and two different interplanar distance of 0.25 nm and 0.29 nm, that are the characteristic planes of (012) and (116) respectively (g-i) Elemental analysis of the synthesized nanoparticles

Figure 7.2.2e shows the SAED diffraction pattern of the synthesized particles and Figure 7.2.2f shows the two different planes with the different interplanar distance of 0.25 nm and 0.29 nm, that are the characteristic planes of (012) and (116)

respectively. The elemental analysis of the Fe_2O_3 particles was shown in Figure 7.2.2g-i. The overall elemental compositions were given in Figure S2g, and the individual forms of Fe and O were shown in Figure 7.2.2 h and i with the Fe of 46.2 At % and O of 53.8 At %.
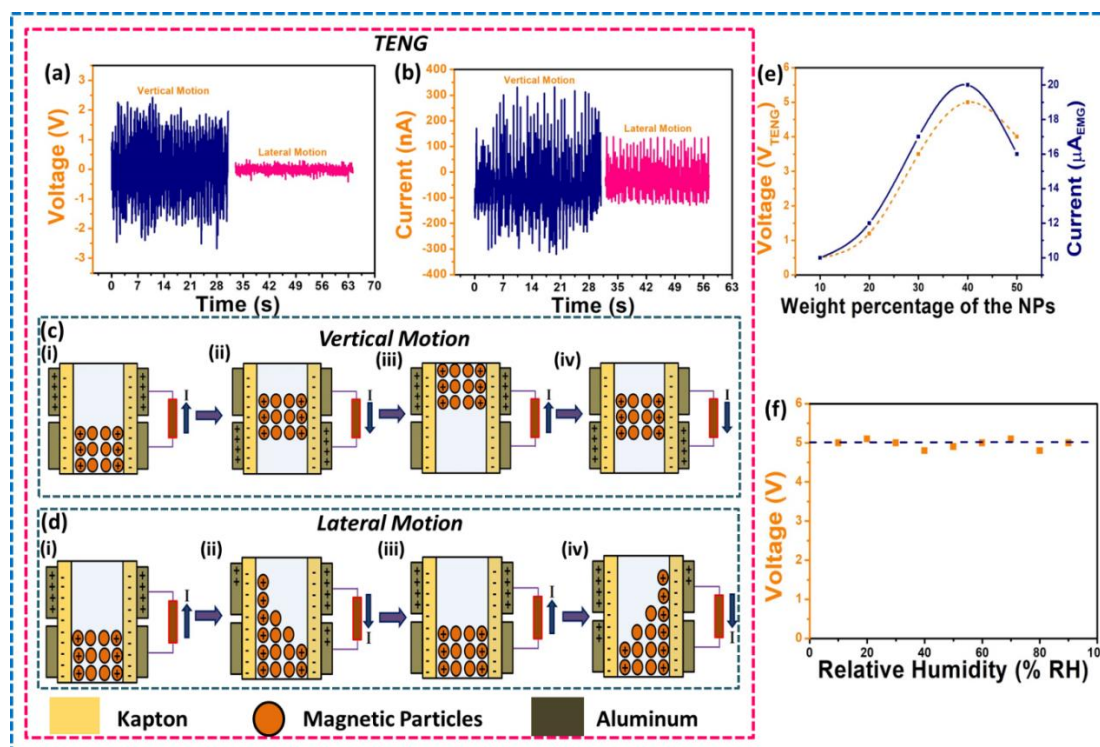
Figure 7.2.3 Working mechanism and electrical performance of TENG component (a) and (b) Voltage and current output of TENG component under vertical and lateral motion (c and d) Operating mechanism of free-standing TENG component under vertical and lateral motions (e) Weight ratio analysis of MP-HG device and its respected voltage (TENG) and current (EMG) and (f) Humidity test analysis of MP-HG device under various percentages of relative humidity (10-90 % RH).

The TENG component generates a maximum electrical output of ≈ 4 V peak to peak and ≈ 600 nA under vertical motion, whereas the same TENG component makes a maximum of ≈ 400 mV and ≈ 200 nA in a lateral motion as shown in figure 7.2.3a and b. Figure 7.2.3c and d show the working mechanism of the TENG component

under vertical and lateral motions. The TENG in the MP-HG device works on the free-standing mode of the triboelectrification process. The inner wall of the cylinder contains Kapton film which acts as the negative triboelectric layer and the powder inside the device acts as positive triboelectric material. When mechanical vibration was applied to the device, the motion of a particle on to the negative layer makes electrons from one electrode to another. Since the movement is unconstrained, the electrical output is less in Lateral motion when compared with the vertical motion. As per the freestanding mode of triboelectrification when the particles move on the top side, positive charges accumulate on the upper electrode, which in turn makes the electrons flow from the bottom electrode to the top electrode. In the same way, when the particle moves towards the bottom, the electrons flow from the top electrode to bottom. The voltage and current output of TENG was measured using an electrometer, which can be expressed via equations as follows

$$V_{TENG} = \frac{\sigma S}{C} \quad \text{----- (7.1)}$$

$$I_{TENG} = S\frac{dQ_{SC}}{dt} \text{ ----- (7.2)}$$

Where C is the capacitance between the electrodes, S is the contact area, σ is the surface charge density of the iron oxide particle.

Further, the electrical output of the MP-HG shows the maximum at 40 % of the particles filled inside the device. When the particle was filled to 50 % the TENG electrical output decreases, this is due to the distance between the electrode and particles decreases; it leads to the reduction of charge transfer.

191
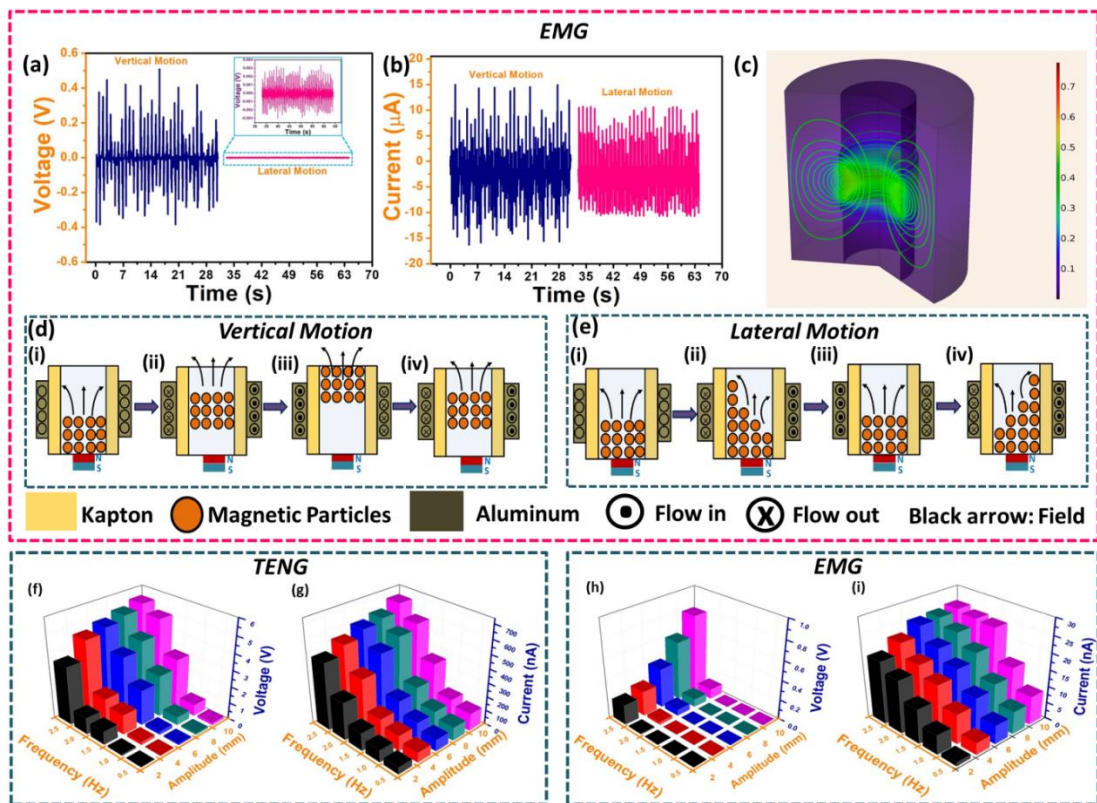
Figure 7.2.4 Working mechanism and electrical performance of EMG component (a) and (b) Voltage and current output of EMG component under vertical and lateral motion (c) 3D model diagram showing the magnetic flux density around the coil (d and e) working mechanism of EMG component under vertical and lateral motions (f and g) 3D bar diagram of voltage and current output of TENG component under different amplitude and vibration frequencies (h and i) 3D bar diagram of voltage and current output of EMG component under different amplitude and vibration frequencies.

Also, the contact area between the electrode and particles increases with the increase in the number of particles. Similarly, the EMG output also decreases when the container gets filled with 50 %. This is due to the restricted motion of particles inside the cylinder, which eventually confine the magnetic flux production through the coil, as shown in Figure 7.2.3e. Figure 2f shows the electrical output of the device under a humidity condition; this is to prove the stability of the device under external environments such as humidity. The device was placed under a homemade humidity

chamber and operated under various percentages of relative humidity. The device operates stably without much output variation until the humidity reaches 90 %. This result shows that the device performance had not been affected due to moisture as the device is completely packed and sealed.

Figure 7.2.4a and b show the electrical output performance of EMG under vertical and lateral vibrating motions. The EMG generates a maximum electrical output of $\approx$ 800 mV and $\approx$ 25 µA in vertical motions and $\approx$ 100 mV and $\approx$ 18 µA in Lateral motion. The lower electrical output is due to the restricted particle motion across the electrodes under lateral movement and controlled movement of particles across the coil wounded on the device. Figure 7.2.4c shows the 3D model of the simulated EMG component showing the generation of flux. The two dimensional schematic shows the movement of magnetic particles inside the tube wound by a coil with the varying time period at t = 0, 0.4, 0.8, 1.2, 1.6, and 2 s. When magnetic particles moved into the coil of wire, changing the magnetic field and magnetic flux through the coil, a voltage will be generated in the coil according to Faraday's law. Figure 3d and e describe the working mechanism of the EMG component under lateral and vertical vibrating motions. When the device vibrates in vertical and lateral directions, the magnetic particles tend to move across the coil leads to cut the lines of flux. The magnetic field then pushes the electrons in the copper wire. As it is well known that copper (Cu^{2+}) has 27 electrons, and the last two electrons in orbit are easily pushed on to the nearby atom. This movement of electrons is responsible for the electric charge flow as determined by Lenz's law. The magnetic field applied to the device would vary when the mechanical energy gets applied to the device. This is due to the fluid-like the behavior of the particle. Similarly, when the device oscillates in a lateral direction, the

193

particles can't move freely across the coil. The particles make the coil to produce fewer electrons due to the limited electric flux through the coil. To align the magnetic moment of the particles, a small magnet is placed at the bottom of the device; this, in turn, makes the particles to align along the applied external magnetic field. The electrical output voltage and current from the EMG component could be calculated using the Faraday's law as follows[37]

$$V_{EMG} = -N \frac{d\Phi_B}{dt} \text{ ----- (7.3)}$$

$$I_{EMG} = \frac{V_{OC}}{R} \text{ ----- (7.4)}$$

Where Φ_B the magnetic flux in each coil, N is the number of turns and B is the magnetic field. Further, to analyze the electrical performance of the EMG and TENG component under various operating frequency, the device was mounted on an electrodynamic shaker in a vertical oscillating motion. Various amplitudes and motion frequencies were applied to the device, and the corresponding electrical response have been measured, as shown in the Figure 3f to i. The 3D bar graphs exhibit the output performance of the device independently with TENG and EMG with the parameters of amplitude, frequency, and voltage/current. The electrical output increases with increase in frequency under various amplitude distance such as 2 mm, 4 mm, 6 mm and 10 mm. Further, the output voltage gets stabilized at 2.5 Hz frequency with the maximum peak-to-peak output of ~ 5 V/ ~ 600 nA for TENG component and ~ 0.8 V/ ~ 25 µA for EMG component.
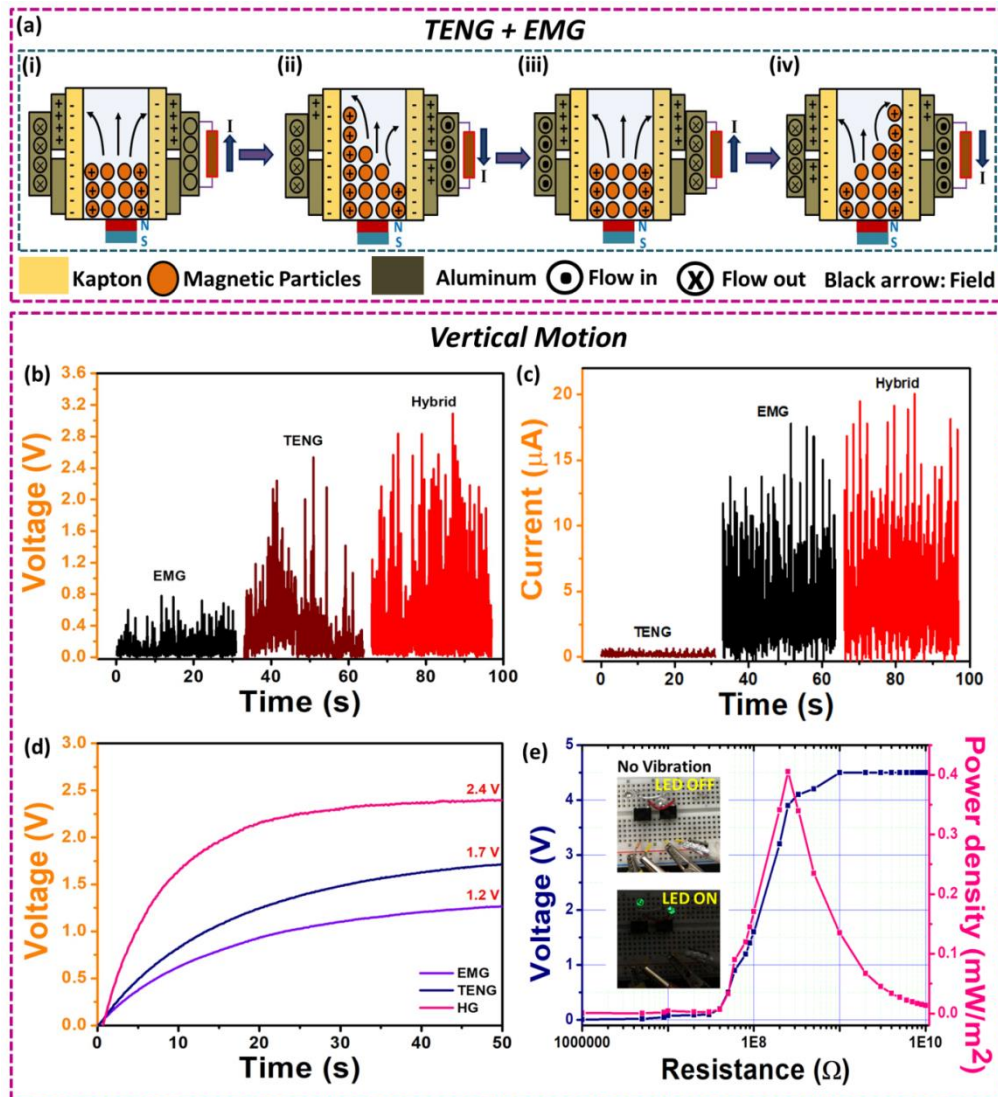
Figure 7.2.5 (a) Working mechanism of combined TENG and EMG component under both vertical and lateral motion (b and c) Rectified voltage and current output performance of voltage, current and hybrid combinations under vertical motions (d) Capacitor charging analysis using MP-HG device by individual TENG, EMG and hybrid combinations (e) Load resistance and power density analysis of the TENG device showing the maximum power density 0.4 mW/m^2 at 300 MΩ resistance.

Figure 7.2.5a shows the combined mechanism of TENG and EMG components, which works in combination on the above-discussed mechanisms. The rectified output voltage and current performance of the MP-HG device under vertical vibration mode with each component such as TENG, EMG, and Hybrid were shown in Figure 7.2.5b

and c. The generated output is maximum in the case of a hybrid combination. The measurement was performed with the help of a bridge rectifier circuit connected with TENG and EMG component of the hybrid device. The maximum voltage and current are $\approx$ 3 V/ 16 μA (rectified) for hybrid combination. Whereas, the output was $\approx$ 2.2 V/ 300 nA for TENG, $\approx$ 400 mV/ 14 μA for EMG as shown in Figure 7.2.5b and c. Further, to validate the hybrid output commercial capacitor charging and LED lit up has been performed using a bridge rectifier circuit. Figure S5a shows the circuit diagram using two bridge rectifiers connected separately on the EMG and TENG components of the MP-HG hybrid device for glowing the LED. Figure 7.2.5d shows the charging characteristics of a commercial capacitor of 1 μF under EMG, TENG, and hybrid electrical output. The capacitor charges a maximum of 1.2 V for 50 s using EMG, whereas for TENG and Hybrid the capacitor charges to 1.7 V and 2.4 V respectively. Overall, the capacitor charging is higher in the case of a hybrid connection. Another critical parameter for an energy harvesting device is the instantaneous peak power density. The device under TENG configuration exhibits a maximum power density $\approx$ 0.4 mW/m2 under a load resistance of 300 MΩ which is shown in Figure 7.2.5e. The load resistance analysis of TENG and EMG component individually, in which the maximum peak power of $\approx$ 0.06 μW was be obtained at 300 MΩ resistance from a TENG device, and $\approx$ 0.8 mW was be obtained at 90 Ω from an EMG device. Here both the devices followed the ohms law and showed an increment in the voltage with an increment in the external load resistance. In addition to this, two LEDs are connected and were lit up using the MP-HG device shown in the inset of Figure 7.2.5e. The LEDs were lit up under the hybrid connection but couldn't lit up in the TENG and EMG individually due to insufficient power from the individual component. The stability

test of TENG and EMG components were measured individually for a period of 1000 seconds each.
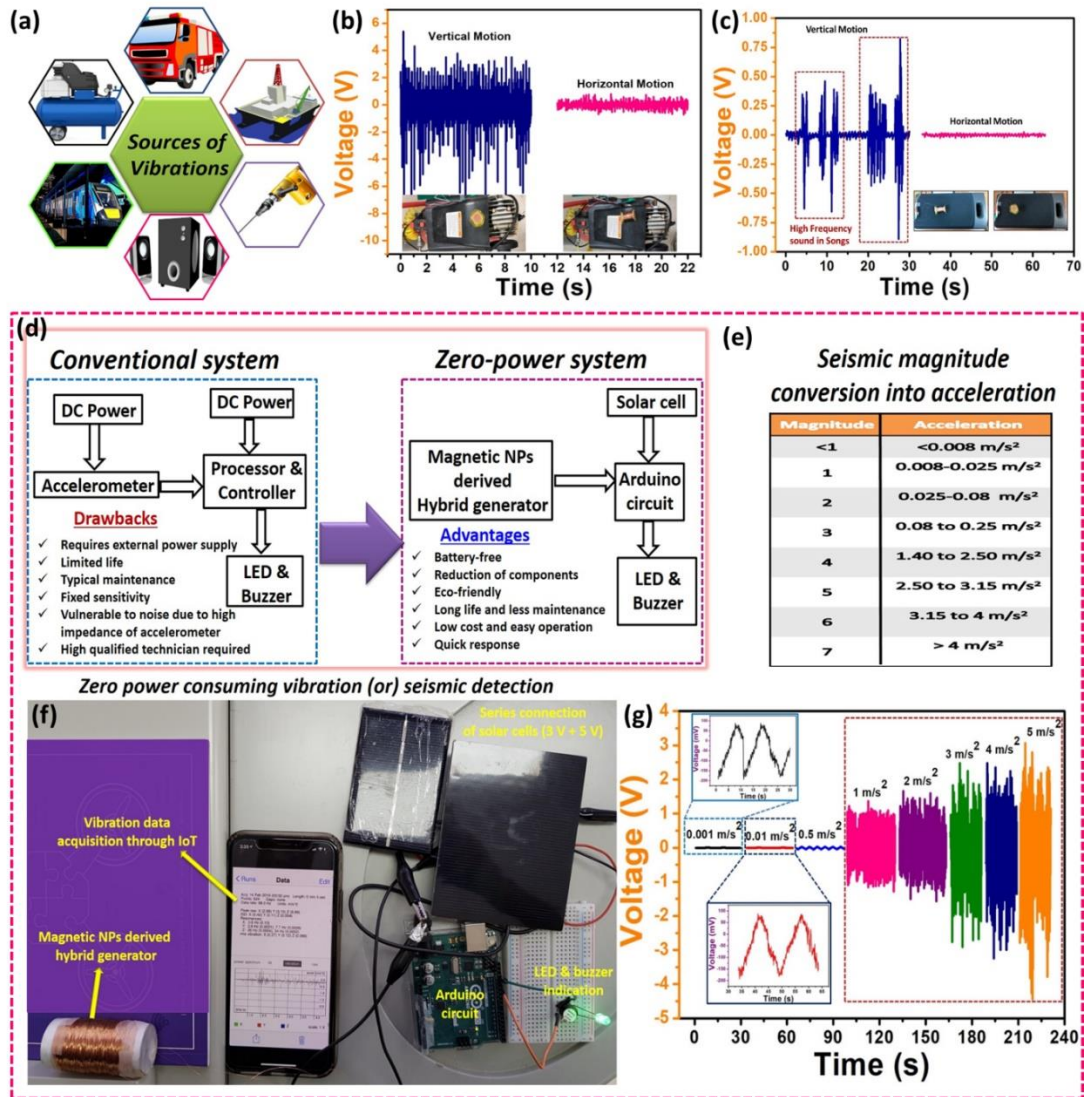
Figure 7.2.6 (a) Various sources of day-to-day vibrations (b and c) Testing of MP-HG device by placing it on a compressor motor and speaker in both vertical and Lateral directions (d) Comparison of schematics for both conventional and zero power consuming vibration or seismic detection with its drawbacks and advantages (e) Table showing the conversion of seismic magnitude into acceleration (f) Real-time demonstration of zero power consuming vibration or seismic detection using solar cells, Arduino, LED and buzzer. (g) The electrical signal output of MP-HG device and various accelerations.

To demonstrate the effectiveness of the nanoparticle-based hybrid device, a zero-power consuming or self-powered seismic detector has been demonstrated with the help of Arduino programming. The vibration had sensed using the MP-HG device, and the generated electrical signal was used as a trigger pulse to trigger the buzzer and LED under disaster conditions such as typhoon, the earthquake in buildings and bridges. Before proceeding with the real-time application of seismic detection, a test experiment had been performed by placing the device on various vibrating instruments in our laboratory, such as air compressor and audio speakers. Figure 7.2.6a shows the various sources of human-made vibrations generated in our day to day life. The MP-HG device was placed vertically and laterally on an air compressor (2 HP), and the electrical output had been recorded based on its vibration during its operation, which is shown in Figure 7.2.6b. The device generates a maximum of 6 V at an average upon the heavy vibration in vertical mode and 500 mV in Lateral mode. Similarly, a loud beat song was played in the speaker, and the device was kept on the speaker. Under vertical mode, the particle vibrates concerning the vibration produced on different acoustic frequencies, and there are no notable changes seen under lateral mode, which is shown in Figure 7.2.6c. The comparison of the conventional seismic detection system and the zero-power consuming seismic detector were shown in Figure 7.2.6d. This clearly shows that the proposed has more advantages than the conventional system. Further, the real-time analysis of zero power consuming seismic detection had been done by comparing the seismic vibration produced with magnitudes of the earthquake. The table shown in Figure 7.2.6e and Table S1 shows the magnitude of the earthquake and its converted acceleration. Figure 7.2.6d shows the comparison of conventional and zero power system on seismic detection and its advantages over the

existing conventional system. The Arduino circuit board was programmed to activate the LED and buzzer upon receiving the trigger signal form the MP-HG device. The MP-HG device sends the trigger signal to the Arduino board whenever the acceleration reaches $1m/s^2$. This due to the command signal is in the form of voltage, and the corresponding triggering voltage would be generated when the device reaches $1m/s^2$ and above. The corresponding voltage signal and the respected acceleration are shown in Figure 7.2.6g. When the vibration level is higher than $1 m/s^2$ [Magnitude above 3 (even felt by few people)], the electrical voltage generated from the device triggers the Arduino board, which activates the LED signaling and the buzzer sound. Figure 7.2.6f shows the real-time test setup for demonstrating the zero-power consuming seismic detectors. The self-powered system replaces the requirement of accelerometer, which requires an external battery and the usage of DC power source for the control unit with a solar cell. The MP-HG device performs the role of accelerometer without the requirement of any external power source. Here solar panel was used to power the Arduino, and the vibration was calculated with the help of IoT display. Hence, the proposed MP-HG device overcomes the drawbacks in the conventional TENG-EMG hybrid generator as well as used as a self-powered seismic detector without the requirement of battery source. The study signifies the usage of TENG-EMG hybrid generator as an energy harvesting unit as well as an active stand-alone sensor.

7.2.4 Conclusions

In summary, for the first time, a zero-power consuming/self-powered seismic detector using magnetic nanoparticle derived hybrid generator was designed, fabricated, and demonstrated successfully. The MP-HG device generates electrical energy from external vibrations under both lateral and vertical directions. The electrical analysis has been studied in detail on EMG, TENG, and hybrid configurations under vertical and lateral motions. The device undergoes various tests such as humidity analysis, weight ratio analysis, capacitor charging analysis, and LED lit up. The device had been used to demonstrate a novel concept of zero power consuming seismic detection by replacing the accelerometer present in the existing system, which has several drawbacks. However, the self-powered system does not require any external power supply or battery, and the Arduino circuit can be powered with the help of a solar cell. With the help of an Arduino system, the vibration could be sensed and alert the people in the buildings by blinking the LEDs and warning alarm. The proposed system would be highly useful in places which are prone to natural calamities, high occupancy regions, a highly industrialized area where man-made seismic events can occur. The projected report paves the way for the practical application of self-powered sensors in the future as a promising system for environmental monitoring.

7.2.5 References

1.   Nalbant, S. S.; Steacy, S.; Sieh, K.; Natawidjaja, D.; McCloskey, J., Earthquake risk on the Sunda trench. *Nature* **2005,** *435* (7043), 756-757.

2.   West, M.; Sánchez, J. J.; McNutt, S. R., Periodically Triggered Seismicity at Mount Wrangell, Alaska, After the Sumatra Earthquake. *Science* **2005,** *308* (5725), 1144-1146.

3.   Wang, Z. L.; Song, J., Piezoelectric Nanogenerators Based on Zinc Oxide Nanowire Arrays. *Science* **2006,** *312* (5771), 242-246.

4.   Fan, F.-R.; Lin, L.; Zhu, G.; Wu, W.; Zhang, R.; Wang, Z. L., Transparent Triboelectric Nanogenerators and Self-Powered Pressure Sensors Based on Micropatterned Plastic Films. *Nano Letters* **2012,** *12* (6), 3109-3114.

5.   Tang, Q.; Yeh, M.-H.; Liu, G.; Li, S.; Chen, J.; Bai, Y.; Feng, L.; Lai, M.; Ho, K.-C.; Guo, H.; Hu, C., Whirligig-inspired triboelectric nanogenerator with ultrahigh specific output as reliable portable instant power supply for personal health monitoring devices. *Nano Energy* **2018,** *47*, 74-80.

6.   Pu, X.; Guo, H.; Chen, J.; Wang, X.; Xi, Y.; Hu, C.; Wang, Z. L., Eye motion triggered self-powered mechnosensational communication system using triboelectric nanogenerator. *Science Advances* **2017,** *3* (7).

7.   Rasel, M. S.; Maharjan, P.; Salauddin, M.; Rahman, M. T.; Cho, H. O.; Kim, J. W.; Park, J. Y., An impedance tunable and highly efficient triboelectric nanogenerator for large-scale, ultra-sensitive pressure sensing applications. *Nano Energy* **2018,** *49*, 603-613.

8.   Liu, Z.; Ma, Y.; Ouyang, H.; Shi, B.; Li, N.; Jiang, D.; Xie, F.; Qu, D.; Zou, Y.; Huang, Y.; Li, H.; Zhao, C.; Tan, P.; Yu, M.; Fan, Y.; Zhang, H.; Wang, Z. L.; Li, Z., Transcatheter Self-Powered Ultrasensitive Endocardial Pressure Sensor. *Advanced Functional Materials* **2019,** *29* (3), 1807560.

9.   Fan, X.; Chen, J.; Yang, J.; Bai, P.; Li, Z.; Wang, Z. L., Ultrathin, Rollable, Paper-Based Triboelectric Nanogenerator for Acoustic Energy Harvesting and Self-Powered Sound Recording. *ACS Nano* **2015,** *9* (4), 4236-4243.

10.   Yang, Y.; Zhang, H.; Lin, Z.-H.; Zhou, Y. S.; Jing, Q.; Su, Y.; Yang, J.; Chen, J.; Hu, C.; Wang, Z. L., Human Skin Based Triboelectric Nanogenerators for Harvesting Biomechanical Energy and as Self-Powered Active Tactile Sensor System. *ACS Nano* **2013,** *7* (10), 9213-9222.

11.   Guo, H.; Chen, J.; Tian, L.; Leng, Q.; Xi, Y.; Hu, C., Airflow-Induced Triboelectric Nanogenerator as a Self-Powered Sensor for Detecting Humidity and Airflow Rate. *ACS Applied Materials & Interfaces* **2014,** *6* (19), 17184-17189.

12.   Chen, J.; Zhu, G.; Yang, W.; Jing, Q.; Bai, P.; Yang, Y.; Hou, T.-C.; Wang, Z. L., Harmonic-Resonator-Based Triboelectric Nanogenerator as a Sustainable Power Source and a Self-Powered Active Vibration Sensor. *Advanced Materials* **2013,** *25* (42), 6094-6099.

13.   Wang, X.; Peng, D.; Huang, B.; Pan, C.; Wang, Z. L., Piezophotonic effect based on mechanoluminescent materials for advanced flexible optoelectronic applications. *Nano Energy* **2019,** *55*, 389-400.

14.   Purusothaman, Y.; Alluri, N. R.; Chandrasekhar, A.; Vivekananthan, V.; Kim, S. J., Regulation of Charge Carrier Dynamics in ZnO Microarchitecture-Based UV/Visible Photodetector via Photonic-Strain Induced Effects. *Small* **2018,** *14* (11), 1703044.

15.   Yang, X.; Hu, G.; Gao, G.; Chen, X.; Sun, J.; Wan, B.; Zhang, Q.; Qin, S.; Zhang, W.; Pan, C.; Sun, Q.; Wang, Z. L., Coupled Ion-Gel Channel-Width Gating and Piezotronic Interface Gating in ZnO Nanowire Devices. *Advanced Functional Materials 0* (0), 1807837.

16.   Zhao, C.; Feng, H.; Zhang, L.; Li, Z.; Zou, Y.; Tan, P.; Ouyang, H.; Jiang, D.; Yu, M.; Wang, C.; Li, H.; Xu, L.; Wei, W.; Li, Z., Highly Efficient In Vivo Cancer Therapy by an Implantable Magnet Triboelectric Nanogenerator. *Advanced Functional Materials 0* (0), 1808640.

17.   Selvarajan, S.; Alluri, N. R.; Chandrasekhar, A.; Kim, S.-J., BaTiO3 nanoparticles as biomaterial film for self-powered glucose sensor application. *Sensors and Actuators B: Chemical* **2016,** *234*, 395-403.

18.   Alluri, N. R.; Selvarajan, S.; Chandrasekhar, A.; Balasubramaniam, S.; Jeong, J. H.; Kim, S.-J., Self powered pH sensor using piezoelectric composite worm structures derived by ionotropic gelation approach. *Sensors and Actuators B: Chemical* **2016,** *237*, 534-544.

19.   Vivekananthan, V.; Alluri, N. R.; Purusothaman, Y.; Chandrasekhar, A.; Selvarajan, S.; Kim, S.-J., Biocompatible Collagen Nanofibrils: An Approach for Sustainable Energy Harvesting and Battery-Free Humidity Sensor Applications. *ACS Applied Materials & Interfaces* **2018,** *10* (22), 18650-18656.

20.   Guan, H.; Zhong, T.; He, H.; Zhao, T.; Xing, L.; Zhang, Y.; Xue, X., A self-powered wearable sweat-evaporation-biosensing analyzer for building sports big data. *Nano Energy* **2019,** *59,* 754-761.

21.   Han, W.; He, H.; Zhang, L.; Dong, C.; Zeng, H.; Dai, Y.; Xing, L.; Zhang, Y.; Xue, X., A Self-Powered Wearable Noninvasive Electronic-Skin for Perspiration Analysis Based on Piezo-Biosensing Unit Matrix of Enzyme/ZnO Nanoarrays. *ACS Applied Materials & Interfaces* **2017,** *9* (35), 29526-29537.

22.   Pu, X.; Guo, H.; Tang, Q.; Chen, J.; Feng, L.; Liu, G.; Wang, X.; Xi, Y.; Hu, C.; Wang, Z. L., Rotation sensing and gesture control of a robot joint via triboelectric quantization sensor. *Nano Energy* **2018,** *54,* 453-460.

23.   Fan, F.-R.; Tian, Z.-Q.; Lin Wang, Z., Flexible triboelectric generator. *Nano Energy* **2012,** *1* (2), 328-334.

24.   Yang, H.; Wang, M.; Deng, M.; Guo, H.; Zhang, W.; Yang, H.; Xi, Y.; Li, X.; Hu, C.; Wang, Z., A full-packaged rolling triboelectric-electromagnetic hybrid nanogenerator for energy harvesting and building up self-powered wireless systems. *Nano Energy* **2019,** *56,* 300-306.

25.   Seol, M.-L.; Han, J.-W.; Park, S.-J.; Jeon, S.-B.; Choi, Y.-K., Hybrid energy harvester with simultaneous triboelectric and electromagnetic generation from an embedded floating oscillator in a single package. *Nano Energy* **2016,** *23*, 50-59.

26.   Zhao, J.; Zhen, G.; Liu, G.; Bu, T.; Liu, W.; Fu, X.; Zhang, P.; Zhang, C.; Wang, Z. L., Remarkable merits of triboelectric nanogenerator than electromagnetic generator for harvesting small-amplitude mechanical energy. *Nano Energy* **2019,** *61*, 111-118.

27.   Askari, H.; Asadi, E.; Saadatnia, Z.; Khajepour, A.; Khamesee, M. B.; Zu, J., A flexible tube-based triboelectric–electromagnetic sensor for knee rehabilitation assessment. *Sensors and Actuators A: Physical* **2018,** *279*, 694-704.

28.   Guo, Y.; Chen, Y.; Ma, J.; Zhu, H.; Cao, X.; Wang, N.; Wang, Z. L., Harvesting wind energy: A hybridized design of pinwheel by coupling triboelectrification and electromagnetic induction effects. *Nano Energy* **2019,** *60*, 641-648.

29.   Askari, H.; Saadatnia, Z.; Asadi, E.; Khajepour, A.; Khamesee, M. B.; Zu, J., A flexible hybridized electromagnetic-triboelectric multi-purpose self-powered sensor. *Nano Energy* **2018,** *45*, 319-329.

30.   Saadatnia, Z.; Asadi, E.; Askari, H.; Zu, J.; Esmailzadeh, E., Modeling and performance analysis of duck-shaped triboelectric and electromagnetic generators for water wave energy harvesting. *International Journal of Energy Research* **2017,** *41* (14), 2392-2404.

31.   Liu, L.; Tang, W.; Chen, B.; Deng, C.; Zhong, W.; Cao, X.; Wang, Z. L., A Self-Powered Portable Power Bank Based on a Hybridized Nanogenerator. *Advanced Materials Technologies* **2018,** *3* (3), 1700209.

32.   Askari, H.; Asadi, E.; Saadatnia, Z.; Khajepour, A.; Khamesee, M. B.; Zu, J., A hybridized electromagnetic-triboelectric self-powered sensor for traffic monitoring: concept, modelling, and optimization. *Nano Energy* **2017,** *32*, 105-116.

33.   Wang, W.; Xu, J.; Zheng, H.; Chen, F.; Jenkins, K.; Wu, Y.; Wang, H.; Zhang, W.; Yang, R., A spring-assisted hybrid triboelectric–electromagnetic nanogenerator for harvesting low-frequency vibration energy and creating a self-powered security system. *Nanoscale* **2018,** *10* (30), 14747-14754.

34.   Quan, T.; Wu, Y.; Yang, Y., Hybrid electromagnetic–triboelectric nanogenerator for harvesting vibration energy. *Nano Research* **2015,** *8* (10), 3272-3280.

35.   Seol, M.-L.; Jeon, S.-B.; Han, J.-W.; Choi, Y.-K., Ferrofluid-based triboelectric-electromagnetic hybrid generator for sensitive and sustainable vibration energy harvesting. *Nano Energy* **2017,** *31*, 233-238.

36.   Lu, C. X.; Han, C. B.; Gu, G. Q.; Chen, J.; Yang, Z. W.; Jiang, T.; He, C.; Wang, Z. L., Temperature Effect on Performance of Triboelectric Nanogenerator. *Advanced Engineering Materials* **2017,** *19* (12), 1700275.

37.   Kim, D.; Jin, I. K.; Choi, Y.-K., Ferromagnetic nanoparticle-embedded hybrid nanogenerator for harvesting omnidirectional vibration energy. *Nanoscale* **2018,** *10* (26), 12276-12283.

CHAPTER VIII

Summary and Future Prospective

8.1 Summary

This chapter summarizes the overall thesis and suggests the extension of this thesis into a future extension. The thesis majorly concentrates on the development of hybrid generator and utilizing it for self-powered sensors. The hybrid generators were made of TENG-PENG and TENG-EMG combinations housed into a single device. Prior to the development of hybrid generator, individual TENG and PENG devices were fabricated and studied in detail with its electrical output response and directly been utilizing as a self-powered sensor for sensing or detecting various physical and chemical quantities. The PNG device was made of piezoelectric nanomaterials such as KNN, BTO and KNN-BTO materials prepared by SSR method. The nanomaterials were blended it polymers such as PDMS and PVDF for the fabrication of composite films. Further combination of electrodes such as Al/CF/Al, ITO/CF/ITO, and ITO/CF/Al were employed for the fabrication of PNG devices. In a similar fashion a bio-polymer, collagen has been investigated for its piezoelectric property and used as an energy harvester as well as a battery-free humidity sensor. The TENG device has also been investigated and used as a water-resistant device with Nickel as positive layer and silicone elastomer as negative layer. The EMG device was developed with conventional magnet and Cu coil as well as for the first time using magnetic particles instead of magnets and activates both TENG and EMG components of the hybrid device and used for seismic detection. The thesis finally shows that the developed energy harvesters have the potential to replace battery and been used as zero-power

207

consuming sensor systems in the near future and commercialize to use in day-to-day life.

➢ The thesis started with providing a broad knowledge on the development of various energy harvesters and combining them to make a hybrid generator for its application in zero-power consuming/self-powered sensors. The thesis shows that (i) the sensors were fabricated and analyzed its performance and the nanogenerators acts as a power source (ii) The nanogenerator itself acts as the sensor device with its electrical response upon its interaction with various physical and chemical quantities. The types of energy harvesters and their capability to use as self-powered sensors are discussed (Chapter I)

➢ Followed by the overview and background of this research, the material requirement, synthesis techniques and device fabrication methods have been discussed in detail. Along with that, the characterization instruments required and their specifications, electrical characterization techniques and parameters required are also discussed (Chapter II)

➢ Collagen, a bio polymer material had been investigated for its energy harvesting performance and been utilized for a humidity sensing application is discussed briefly with its energy harvesting and sensing performances. The collagen material was coated on to a cotton substrate and freeze dried, followed by attaching electrodes on either side's to make as a collagen PNG device. The device shows an energy harvesting response of 45 V/250 nA upon 5 N and a sensing response of with an excellent sensitivity of 0.1287 μA/ % RH and a correlation coefficient of 0.99554 (Chapter III)

➢ Next, a ceramic based dual perovskite solid system made of doping BTO into the KNN lattice was investigated for piezoelectric nanogenerator. The piezoelectric property of the KNN material was enhanced by doping another piezoelectric perovskite material BTO. The synthesized KNN-BTO material is then used to make flexible, planar composite piezoelectric nanogenerators (C-PNGs) to harness waste mechanical energy using the cost-effective CFs prepared by probe-sonication technique. The CFs were made up of highly crystalline, randomly oriented lead free piezoelectric nanoparticles KNN- x BTO where x=0.02, 0.04, 0.06, 0.08, and blended it in polymers such as PDMS and PVDF for the fabrication of composite films. Further combination of electrodes such as Al/CF/Al, ITO/CF/ITO, and ITO/CF/Al were employed for the fabrication of PNG devices and utilized for applications such as waste mechanical energy harvesting, intruder identification system and self-powered sleep monitoring systems and framed as 4.1, 4.2 and 4.3 in (Chapter IV)

➢ On the other hand, the energy harvesting performance of TENG device has been analyzed by using Ni electrode as positive layer and silicone elastomer as negative triboelectric layer. This device overcomes the humidity issues by the introduction of an impervious TENG concept, where we restrict the effect of humidity which is the main reason for affecting the device performance. The device is extremely light weight and generates a maximum power density ~17 mW/m^2. Also, it is highly reliable and stable for a long period. The electrical output of TENG device was tested under various percentages of relative humidity from 10% R-H to 99% R-H. Under both humid and dry conditions, the electrical output is stable without any interruptions. Further,

the device was used to demonstrate a real-time application of scavenging bio-mechanical energy and also been used for zero power consuming/ self-powered pressure sensing applications (Chapter V)

➤ After investigating the energy harvesting performance of individual TENG and PENG components, the performance of hybrid device made of utilizing both triboelectric and piezoelectric mechanisms in a single device. The electrical output of the device was studied and optimized upon various concentrations of BTO doping and the weight ration of nanoparticles into the composite films. The device made of x = 0.02 with the PDMS to nanoparticles weight ratio of 10 wt % generates a maximum electrical output of $\approx$ 610 V/ 13.7 µA. Also, the electrical responses of the hybrid device as well as the individual components have been systematically studied. The device shows a maximum power density of $\approx$ 0.55 W/m^2 at 100 MΩ load resistance showing higher response than the individual components. Further, the device exhibited its long-term stability for a period of 1500 s continuously and showed its capability in powering 60 green LEDs, wrist watch and a temperature sensor by using a bridge rectifier and commercial capacitor (Chapter VI)

➤ a single package hybrid generator composed of TENG and EMG had reported via a cost-effective and easy fabrication method. The device works actively upon various accelerations and generates electrical output simultaneously from both TENG and EMG components upon the same motion. The device generates a maximum electrical output of 20 V and 300 nA current at an acceleration of 5 m/s^2 with an instantaneous power density of 1 mW/m^3 for the TENG component. Similarly, the EMG component generates a maximum

output with the voltage of 2 V and a current of 10 mA at 5 m/s^2 with an instantaneous power ≈ 4 mW for EMG and 1 μW for TENG components. In a similar fashion, a magnetic nanoparticle derived hybrid generator was designed, fabricated, and demonstrated successfully. The MP-HG device generates electrical energy from external vibrations under both lateral and vertical directions. The electrical analysis has been studied in detail on EMG, TENG, and hybrid configurations under vertical and lateral motions. The device undergoes various tests such as humidity analysis, weight ratio analysis, capacitor charging analysis, and LED lit up. The device had been used to demonstrate a novel concept of zero power consuming seismic detection by replacing the accelerometer present in the existing system, which has several drawbacks (Chapter VII)

Finally, the thesis gives a complete overview of development of energy harvesters such as TENG, PENG, EMG and the hybrid systems and successfully been utilized for various self-powered sensing applications. This approach leads to the replacement of batteries in electronic systems and work as a promising power source for future electronic devices.

8.2 Suggestions for future improvement

The future direction of this thesis will focus on developing miniaturized energy harvesters and will explore the possibilities to solve the energy demands, leading to the development of zero-power consuming sensors. The future aspects need to consider the following points.

➢ Over the past decades, the work on energy harvesters for self-powered sensing has not been commercialized well. There is less than 5 products were in commercialization stage or commercialized. To make this technology towards a product level, high adaptability in device is required. One prospective is to investigate a promising material which can boost the performance of energy harvesting.

➢ Development of highly stretchable material and can be used as a wearable device. There is a high demand in the field of wearable electronic devices having multipurpose functionalities. This approach moves towards a development of e-skin based devices with inbuilt energy harvesters and sensors in a single package.

➢ The successful development of this device leads to the possibility of use in various fields such as robotics, bio-medical, health care and wearable electronics.

Appendix: List of Publications

1. **Vivekananthan, V**., Alluri, N.R., Chandrasekhar, A., Purusothaman, Y., Gupta, A. and Kim, S.J., 2019. Zero-power consuming intruder identification system by enhanced piezoelectricity of K 0.5 Na 0.5 NbO 3 using substitutional doping of BTO NPs. *Journal of Materials Chemistry C,7,* pp, *7563-7571*

2. **Vivekananthan V**, Chandrasekhar A, Alluri NR, Purusothaman Y, Khandelwal G, Pandey R, Kim SJ. Fe2O3 magnetic particles derived triboelectric-electromagnetic hybrid generator for zero-power consuming seismic detection. **Nano Energy**. 2019 Oct 1;64:103926.

3. **Vivekananthan, V**., Chandrasekhar, A., Alluri, N.R., Purusothaman, Y., Kim, W.J., Kang, C.N. and Kim, S.J., 2019. A flexible piezoelectric composite nanogenerator based on doping enhanced lead-free nanoparticles. *Materials Letters*, *249*, pp.73-76.

4. Purusothaman Y, Alluri NR, Chandrasekhar A, **Vivekananthan V**, Kim SJ. Piezophototronic gated optofluidic logic computations empowering intrinsic reconfigurable switches. **Nature communications.** 2019 Sep 26;10(1):1-9.

5. Chandrasekhar, A., **Vivekananthan, V**., Khandelwal, G. and Kim, S.J., 2019. A fully packed water-proof, humidity resistant triboelectric nanogenerator for transmitting Morse code. *Nano Energy*, *60*, pp.850-856.

6. **Vivekananthan V**, Kim WJ, Alluri NR, Purusothaman Y, Abisegapriyan KS, Kim SJ. A sliding mode contact electrification based triboelectric-electromagnetic hybrid generator for small-scale biomechanical energy harvesting. **Micro and Nano Systems Letters.** 2019 Oct 5;7(1):NA

7. Chandrasekhar A, **Vivekananthan V**, Khandelwal G, Kim SJ. Sustainable Human-Machine Interactive Triboelectric Nanogenerator toward a Smart Computer Mouse. **ACS Sustainable Chemistry & Engineering.** 2019 Feb 28;7(7):7177-82.

8. **Vivekananthan, V**., Alluri, N.R., Purusothaman, Y., Chandrasekhar, A., Selvarajan, S. and Kim, S.J., 2018. Biocompatible Collagen Nanofibrils: An Approach for Sustainable Energy Harvesting and Battery-Free Humidity Sensor Applications. *ACS applied materials & interfaces*, *10*(22), pp.18650-18656.

9. **Vivekananthan, V**., Alluri, N.R., Purusothaman, Y., Chandrasekhar, A. and Kim, S.J., 2017. A flexible, planar energy harvesting device for scavenging road side waste mechanical energy via the synergistic piezoelectric response of K 0.5 Na 0.5 NbO 3-BaTiO 3/PVDF composite films. *Nanoscale*, *9*(39), pp.15122-15130.

10. Alluri NR, **Vivekananthan V**, Chandrasekhar A, Kim SJ. Adaptable piezoelectric hemispherical composite strips using a scalable groove technique for a self-powered muscle monitoring system. **Nanoscale**. 2018 Jan 18;10(3):907-13.

11. Purusothaman, Y., Alluri, N.R., Chandrasekhar, A., **Vivekananthan, V**. and Kim, S.J., 2018. Regulation of Charge Carrier Dynamics in ZnO Microarchitecture-Based UV/Visible Photodetector via Photonic-Strain Induced Effects. *Small*, *14*(11), p.1703044.

12. Raj NP, Alluri NR, **Vivekananthan V**, Chandrasekhar A, Khandelwal G, Kim SJ. Sustainable yarn type-piezoelectric energy harvester as an eco-friendly, cost-effective battery-free breath sensor. **Applied energy**. 2018 Oct 15;228:1767-76.

13. Purusothaman Y, Alluri NR, Chandrasekhar A, **Vivekananthan V**, Kim SJ. Direct In Situ Hybridized Interfacial Quantification to Stimulate Highly Flexile Self-Powered Photodetector. **The Journal of Physical Chemistry C**. 2018 May 21;122(23):12177-84.

14. Chandrasekhar A, Khandelwal G, Alluri NR, **Vivekananthan V**, Kim SJ. Battery-free electronic smart toys: a step toward the commercialization of sustainable triboelectric nanogenerators. **ACS Sustainable Chemistry & Engineering**. 2018 Apr 4;6(5):6110-6.

15. Khandelwal G, Chandrasekhar A, Alluri NR, **Vivekananthan V**, Raj NP, Kim SJ. Trash to energy: A facile, robust and cheap approach for mitigating environment pollutant using household triboelectric nanogenerator. **Applied energy**. 2018 Jun 1;219:338-49.

16. Chandrasekhar A, Alluri NR, **Vivekananthan V**, Park JH, Kim SJ. Sustainable Biomechanical Energy Scavenger toward Self-Reliant Kids' Interactive Battery-Free Smart Puzzle. **ACS Sustainable Chemistry & Engineering**. 2017 Jul 12;5(8):7310-6.

17. Alluri NR, Chandrasekhar A, **Vivekananthan V**, Purusothaman Y, Selvarajan S, Jeong JH, Kim SJ. Scavenging biomechanical energy using high-performance, flexible BaTiO3 nanocube/PDMS composite films. **ACS Sustainable Chemistry & Engineering**. 2017 Apr 24;5(6):4730-8.

18. Chandrasekhar A, Alluri NR, **Vivekananthan V**, Purusothaman Y, Kim SJ. A sustainable freestanding biomechanical energy harvesting smart backpack as a portable-wearable power source. **Journal of Materials Chemistry C**. 2017;5(6):1488-93.

Appendix: List of conferences

1. **Vivekananthan Venkateswaran**, Nagamalleswara Rao Alluri, Yuvasree Purusothaman, Nirmal Prashanth Maria Joseph Raj, Woo Joong Kim, Sang-Jae Kim "A Water Resistant Triboelectric Nanogenerator as a Bio-mechanical Energy Harvester and a Self-powered Pressure Sensor" ICMR 2019, Nov. 27, 2019

2. Nagamalleswara Rao Alluri, Yuvasree Purusothaman, Nirmal Prashanth Maria Joseph Raj, **Vivekananthan Venkateswaran**, Sang-Jae Kim "Reliability of PVDF/1D Se Mcro-rod Based Composite Films for Energy Harvesters" ICMR 2019, Nov. 27, 2019

3. Woo Joong Kim, **Venkateswaran Vivekananthan**, Gaurav Khandelwal, Arunkumar Chandrasekar, Sang-Jae Kim "Triboelectric-Electromagnetic Hybrid Generator for Wind Energy Harvesting" ICMR 2019, Nov. 27, 2019

4. **Venkateswanran Vivekananthan**, Nagamalleswara Rao Alluri, Yuvasree Purusothaman, Woo Joong Kim, Sang-Jae Kim "A High Output Triboelectric and Piezoelectric Hybrid Nanogenerator Based on K0.5Na0.5NbO3 Nanoparticles into PDMS Composite Films" KSME 2019, Nov. 15, 2019

5. Woo Joong Kim, **Venkateswaran Vivekananthan**, Gaurav Khandelwal, Sang-Jae Kim "Highly Reliable Flutter Driven Triboelectric-electromagnetic Hybrid Generator for Efficient Wind Energy Harvesting" KSME 2019, Nov. 15, 2019

6. **Vivekananthan Venkateswaran**, Nagamalleswara Rao Alluri, Yuvasree Purusothaman, Arunkumar Chandrasekhar, Sang-Jae Kim "Enhancement of Electrical Output in Triboelectric-Piezoelectric Hybrid Nanogenerator Using $CaTiO_3$ Doped $K_{0.5}Na_{0.5}NbO_3$ and Activated Carbon Filler" ICAE 2019, Nov. 7, 2019

7. Yuvasree Purusothaman, Nagamalleswara Rao Alluri, **Vivekananthan Venkateswaran**, Sang-Jae Kim "Intrinsic Reconfigurable Piezo-phototronic Gated Optofluidic Switching Devices" ICAE 2019, Nov. 5, 2019

8. Nagamalleswara Rao Alluri, Nirmal Prashanth Maria Joseph Raj, **Vivekananthan Venkateswaran**, Yuvasree Purusothaman, Sang-Jae Kim "Multifunctional Piezoelectric Materials for Nanogenerators and Battery-Free Sensors" ICAE 2019, Nov. 5, 2019

9. **Vivekananthan Venkateswaran**, Nagamalleswara Rao Alluri, Yuvasree Purusothaman, Sang-Jae Kim "A Flexible Piezoelectric Nanogenerators based on Lead-free $K_{0.5}Na_{0.5}NbO_3$-$BaTiO_3$ Nanoparticles for Self-powered Sensors" MCARE 2019, Aug. 22, 2019

10. Yuvasree Purusothaman, Nagamalleswara Rao Alluri, **Vivekananthan Venkateswaran**, Sang-Jae Kim "Intrinsic Reconfigurable OR↔AND Switches based on Piezo-phototronic Gated Optofluidic Channels" MCARE 2019, Aug. 21, 2019

11. **Vivekananthan Venkateswaran**, Nagamalleswara Rao Alluri, Yuvasree Purusothaman, Sang-Jae Kim "Dual Arc Shaped Hybrid Nanogenerator based on CaTiO3 Doped K0.5Na0.5NbO3 Piezoelectric Composite films" 2019 KIEEME summer, Jun. 20, 2019

12. **Vivekananthan Venkateswaran**, Nagamalleswara Rao Alluri, Yuvasree Purusothaman, Woo Joong Kim, Sang-Jae Kim "Fabrication of Self-Powered Sensors using Doped Piezoelectric Nanogenerators" KSDT 2019, May. 9, 2019

13. **Venkateswaran Vivekananthan**, Arunkumar Chandrasekhar, Nagamalleswara Rao Alluri, Yuvasree Purusothaman, Woo Joong Kim, Sang-Jae Kim "Development of a hybrid energy harvester based on ferromagnetic Fe_2O_3 nanoparticles" 21th KMEMS, Apr. 6, 2019

14. Woo Joong Kim, **Venkateswaran Vivekananthan**, Gaurav Khandelwal, Arunkumar Chandrasekhar, Sang-Jae Kim "A combined Triboelectric-Electromagnetic cylindrical hybrid nanogenerator for water wave energy scavenging" 21th KMEMS, Apr. 6, 2019

15. Nagamalleswara Rao Alluri, Nirmal Prashanth Maria Joseph Raj, **Vivekananthan Venkateswaran**, Sang-Jae Kim "자가 구동 시스템을 위한 지속 가능한 마이크로 압전 와이어/스트립 기반 전원 공급 장치" KSME 2019, Feb. 27, 2019

16. **Vivekananthan Venkateswaran**, Nagamalleswara Rao Alluri, Yuvasree Purusothaman, Nirmal Prashanth Maria Joseph Raj, Arunkumar Chandrasekhar, Sang-Jae Kim "압전복합체 박막을 이용한 고신뢰성 자가구동 침입자 식별 시스템" KSME 2019, Feb. 27, 2019

17. Woo Joong Kim, **Venkateswaran Vivekananthan**, Gaurav Khandelwal, Arunkumar Chandrasekhar, Sang-Jae Kim "블루에너지 수확을 위한 원기둥형 마찰전기-전자기 하이브리드 발전기의 작동신뢰성" KSME 2019, Feb. 27, 2019

18. **Vivekananthan Venkateswaran**, Arunkumar Chandrasekhar, Nagamalleswara Rao Alluri, Yuvasree Purusothaman, Sang-Jae Kim "High-performance Piezoelectric Nanogenerators based on Lead-free $K_{0.5}Na_{0.5}NbO_3$-$BaTiO_3$ Nanoparticles as an Energy Harvester and Self-powered Sensor" ANEH 2019, Feb. 4, 2019

19. Arunkumar Chandrasekhar, Gaurav Khandelwal, **Vivekananthan Venkateswaran**, Woo Joong Kim, Sang-Jae Kim "Triboelectric Nanogenerator as Smart Gadgets and Its Self-Powered Applications" ENGE 2018, Nov. 14, 2018

20. **Vivekananthan Venkateswaran**, Nagamalleswara Rao Alluri, Arunkumar Chandrasekhar, Yuvasree Purusothaman, Sang-Jae Kim "Enhanced Piezoelectricity in $K_{0.5}Na_{0.5}NbO_3$ and Its Application towards a Self-powered Burglar Alarming System" ENGE 2018, Nov. 13, 2018

21. Yuvasree Purusothaman, Nagamalleswara Rao Alluri, Arunkumar Chandrasekhar, **Vivekananthan Venkateswaran**, Sang-Jae Kim "$A^V B^{VI} C^{VII}$ Ternary Chalcohalides for the Development of Efficient Multifunctional Energy Harvester" ENGE 2018, Nov. 13, 2018

22. Arunkumar Chandrasekhar, Gaurav Khandelwal, **Vivekananthan Venkateswaran**, Sang-Jae Kim "Development of Battery-free Electronic Smart Toys" The 23rd Annual Joint Workshop, Oct. 15, 2018

23. Nagamalleswara Rao Alluri, Yuvasree Purusothaman, **Vivekananthan Venkateswaran**, Nirmal Prashanth Maria Joseph Raj, Kausalya Ganeshan, Sang-Jae Kim "Alternative Clean Energy Source for Driving Low Power Electronics: Piezoelectric Nanogenerators and Self-Powered Systems" The 23rd Annual Joint Workshop, Oct. 15, 2018

24. Yuvasree Purusothaman, Nagamalleswara Rao Alluri, Arunkumar Chandrasekhar, **Vivekananthan Venkateswaran**, Sang-Jae Kim "Multifunctional Energy Scavenger Based on Antimony Sulfoiodide (SbSI):Mechanical-Light Triggered Piezoelectric Nanogenerator" E-MRS 2018 Fall meeting, Sep. 18, 2018

25. Arunkumar Chandrasekhar, Gaurav Khandelwal, **Vivekananthan Venkateswaran**, Sang-Jae Kim "Development of Battery-free Electronic Smart Toys using Triboelectric Nanogenerator" 2018 KPS, Aug. 6, 2018

26. Yuvasree Purusothaman, Nagamalleswara Rao Alluri, Arunkumar Chandrasekhar, **Vivekananthan Venkateswaran**, Sang-Jae Kim "Self-Powered Photodetector Endorsed by Piezo-Phototronic Effect" 2018 KPS, Aug. 6, 2018

27. **Vivekananthan Venkateswaran**, Nagamalleswara Rao Alluri, Yuvasree Purusothaman, Arunkumar Chandrasekhar, Sang-Jae Kim "A dual function piezoelectric nanogenerator device based on bio-polymer" ISPSA 2018, Jul. 2, 2018

28. **Vivekananthan Venkateswaran**, Nagamalleswara Rao Alluri, Yuvasree Purusothaman, Arunkumar Chandrasekhar, Sang-Jae Kim "Bio-polymer based piezoelectric nanogenerator as a cost-effective self-powered humidity sensor" NGPT 2018, May. 11, 2018

29. Nagamalleswara Rao Alluri, **Vivekananthan Venkateswaran**, Arunkumar Chandrasekhar, Sang-Jae Kim "Groove Technique derived Adaptable Piezoelectric Hemispherical Composite Strips for Self-powered Muscle Monitoring System" NGPT 2018, May. 11, 2018

30. Arunkumar Chandrasekhar, Nagamalleswara Rao Alluri, **Vivekananthan Venkateswaran**, Gaurav Khandelwal, Sang-Jae Kim "Triboelectric Nanogenerators for Powering Portable/Wearable Devices and Its Self-Powered Systems Applications" NGPT 2018, May. 9, 2018

31. Yuvasree Purusothaman, Nagamalleswara Rao Alluri, Arunkumar Chandrasekhar, **Vivekananthan Venkateswaran**, Sang-Jae Kim "An Effectual Approach for Self-powered Photo Detection Endowed by Piezoelectric Potentials" NGPT 2018, May. 9, 2018

32. Arunkumar Chandrasekhar, Gaurav Khandelwal, **Vivekananthan Venkateswaran**, Nagamalleswara Rao Alluri, Sang-Jae Kim "Development of Smart Toys using Triboelectric Nanogenerator" 20th KMEMS, Apr. 6, 2018

33. Yuvasree Purusothaman, Nagamalleswara Rao Alluri, Arunkumar Chandrasekhar, **Vivekananthan Venkateswaran**, Sang-Jae Kim "Development of novel SbSI driven piezoelectric nanogenerator" 20th KMEMS, Apr. 6, 2018

34. **Vivekananthan Venkateswaran**, Nagamalleswara Rao Alluri, Arunkumar Chandrasekhar, Yuvasree Purusothaman, Gaurav Khandelwal, Maria Joseph Raj Nirmal Prashanth, Kausalya Ganesan, Chan-Nam Kang, Sang-Jae Kim "Bio-polymer based Piezoelectric Self-powered Humidity Sensor" 20th KMEMS, Apr. 5, 2018

35. **Vivekananthan Venkateswaran**, Nagamalleswara Rao Alluri, Yuvasree Purusothaman, Arunkumar Chandrasekhar, Maria Joseph Raj Nirmal Prashanth, Gaurav Khandelwal, Kausalya Ganesan, Chan-Nam Kang, Sang-Jae Kim "압전 나노발전기를 이용한 노변 폐기계에너지 수확" KSME 2018, Feb. 23, 2018

36. Arunkumar Chandrasekhar, Gaurav Khandelwal, **Vivekananthan Venkateswaran**, Nagamalleswara Rao Alluri, Sang-Jae Kim "생체에너지 수확을 위한 상호교감형 스마트 테이블" KSME 2018, Feb. 23, 2018

37. Yuvasree Purusothaman, Nagamalleswara Rao Alluri, Arunkumar Chandrasekhar, **Vivekananthan Venkateswaran**, Jong Hwan Lim, Kyung-ho Cho, Sang-Jae Kim "압전-광전자 효과를 이용한 ZnO 미세구조 기반 UV/Vis 광검출기" KSME 2018, Feb. 23, 2018

38. Gaurav Khandelwal, Arunkumar Chandrasekhar, Nagamalleswara Rao Alluri, **Vivekananthan Venkateswaran**, Nirmal Prashanth Maria Joseph Raj, Sang-Jae Kim "Ionic Conductor: Imparting Stretchability, Transparency and high Electrical Performance to Triboelectric Nanogenerator for Energy Harvesting Applications" ICAMD 2017, Dec. 8, 2017

39. **Vivekananthan Venkateswaran**, Nagamalleswara Rao Alluri, Yuvasree Purusothaman, Arunkumar Chandrasekhar, Sang-Jae Kim "Flexible, Planar

Piezoelectric Composite Films: A Solution to Harness Waste Mechanical energy" ICAMD 2017, Dec. 7, 2017

40. Nirmal Prashanth Maria Joseph Raj, Nagamalleswara Rao Alluri, Gaurav Khandelwal, **Vivekananthan Venkateswaran**, Arunkumar Chandrasekhar, Sang-Jae Kim "Harnessing Waste Biomechanical Energy using Bismuth Titanate Nanoparticles/PDMS Composite Thin Films" ICAMD 2017, Dec. 7, 2017

41. Nagamalleswara Rao Alluri, **Vivekananthan Venkateswaran**, Arunkumar Chandrasekhar, Sang-Jae Kim "Enhanced output performance of piezoelectric BaTiO3 Nanocubes/PDMS composite film" ICAMD 2017, Dec. 6, 2017

42. Arunkumar Chandrasekhar, Nagamalleswara Rao Alluri, **Vivekananthan Venkateswaran**, Gaurav Khandelwal, Sang-Jae Kim "Smart Puzzle Toy: A Step towards the Commercialization of Triboelectric Nanogenerator" ICAMD 2017, Dec. 6, 2017

43. Yuvasree Purusothaman, Nagamalleswara Rao Alluri, Arunkumar Chandrasekhar, **Vivekananthan Venkateswaran**, Sang-Jae Kim "Synergistic Effect on Self-Integration of PVDF/ZnO Nanorods for Enhanced Photodetector Performance" ICAMD 2017, Dec. 6, 2017

44. Arunkumar Chandrasekhar, Nagamalleswara Rao Alluri, **Vivekananthan Venkateswaran**, Sang-Jae Kim "Portable-Wearable Triboelectric Nanogenerators for Self-Powered Systems" ICAE 2017, Nov. 24, 2017

45. Yuvasree Purusothaman, Nagamalleswara Rao Alluri, Arunkumar Chandrasekhar, **Vivekananthan Venkateswaran**, Sang-Jae Kim "Significance of ZnO Micro-Architectures in Photosensing Performance Modulated by PiezoPhototronic Effect" ICAE 2017, Nov. 23, 2017

46. Nirmal Prashanth Maria Joseph Raj, Nagamalleswara Rao Alluri, **Vivekananthan Venkateswaran**, Arunkumar Chandrasekhar, Sang-Jae Kim "Facial, Cost-effective Approach for Piezoelectric Bi4Ti3O12 Films for Energy Conversion Applications" ICAE 2017, Nov. 22, 2017

47. **Vivekananthan Venkateswaran**, Nagamalleswara Rao Alluri, Yuvasree Purusothaman, Arunkumar Chandrasekhar, Sang-Jae Kim "Structural and Piezoelectric Analysis of Flexible (1-x)KNN-xBTO/PVDF Composite Films for Energy Harvesting Applications" ICAE 2017, Nov. 21, 2017

48. Gaurav Khandelwal, Arunkumar Chandrasekhar, Nagamalleswara Rao Alluri, **Vivekananthan Venkateswaran**, Sang-Jae Kim "Triboelectric Nanogenerator: An Approach Towards Utilization of Waste Material for Scavenging Biomechanical Energy" ICAE 2017, Nov. 21, 2017

49. **Vivekananthan Venkateswaran**, Nagamalleswara Rao Alluri, Arunkumar Chandrasekhar, Yuvasree Purusothaman, Sang-Jae Kim "Structural and piezoelectric analysis of flexible (1-x)KNN-xBTO/PVDF composite films for energy harvesting applications" JSST 2017, May. 25, 2017

50. Arunkumar Chandrasekhar, Nagamalleswara Rao Alluri, **Vivekananthan Venkateswaran**, Yuvasree Purusothaman, Sang-Jae Kim "Freestanding Triboelectric Nanogenerator as Smart Back Pack" MCARE 2017, Feb. 22, 2017

Appendix: List of awards

1. **Vivekananthan Venkateswaran**, Nagamalleswara Rao Alluri, Yuvasree Purusothaman, Nirmal Prashanth Maria Joseph Raj, Woo Joong Kim, Sang-Jae Kim "A Water Resistant Triboelectric Nanogenerator as a Bio-mechanical Energy Harvester and a Self-powered Pressure Sensor" ICMR 2019, Nov. 27, 2019 **– Best poster award**

2. **Vivekananthan Venkateswaran**, Nagamalleswara Rao Alluri, Yuvasree Purusothaman, Arunkumar Chandrasekhar, Sang-Jae Kim "Enhancement of Electrical Output in Triboelectric-Piezoelectric Hybrid Nanogenerator Using $CaTiO_3$ Doped $K_{0.5}Na_{0.5}NbO_3$ and Activated Carbon Filler" ICAE 2019, Nov. 7, 2019 **– Best poster award**

3. **Vivekananthan Venkateswaran**, Nagamalleswara Rao Alluri, Yuvasree Purusothaman, Sang-Jae Kim "A Flexible Piezoelectric Nanogenerators based on Lead-free $K_{0.5}Na_{0.5}NbO_3$-$BaTiO_3$ Nanoparticles for Self-powered Sensors" MCARE 2019, Aug. 22, 2019 **– Best poster award**

4. **Vivekananthan Venkateswaran**, Nagamalleswara Rao Alluri, Yuvasree Purusothaman, Woo Joong Kim, Sang-Jae Kim "Fabrication of Self-Powered Sensors using Doped Piezoelectric Nanogenerators" KSDT 2019, May. 9, 2019 **– Best poster award**

5. **Vivekananthan Venkateswaran**, Nagamalleswara Rao Alluri, Yuvasree Purusothaman, Nirmal Prashanth Maria Joseph Raj, Arunkumar Chandrasekhar, Sang-Jae Kim "압전복합체 박막을 이용한 고신뢰성 자가구동 침입자 식별 시스템" KSME 2019, Feb. 27, 2019 **– Best oral award**

6. **Vivekananthan Venkateswaran**, Nagamalleswara Rao Alluri, Arunkumar Chandrasekhar, Yuvasree Purusothaman, Sang-Jae Kim "Enhanced Piezoelectricity in $K_{0.5}Na_{0.5}NbO_3$ and Its Application towards a Self-powered Burglar Alarming System" ENGE 2018, Nov. 13, 2018 **– Best poster award**

7. **Vivekananthan Venkateswaran**, Nagamalleswara Rao Alluri, Arunkumar Chandrasekhar, Yuvasree Purusothaman, Sang-Jae Kim "Structural and piezoelectric analysis of flexible (1-x)KNN-xBTO/PVDF composite films for energy harvesting applications" JSST 2017, May. 25, 2017 – **Best oral award**

Appendix: Journal cover page

1. **Published as journal cover page: Vivekananthan, V**., Alluri, N.R., Chandrasekhar, A., Purusothaman, Y., Gupta, A. and Kim, S.J., 2019. Zero-power consuming intruder identification system by enhanced piezoelectricity of K 0.5 Na 0.5 NbO 3 using substitutional doping of BTO NPs. *Journal of Materials Chemistry C,7,* pp*, 7563-7571*
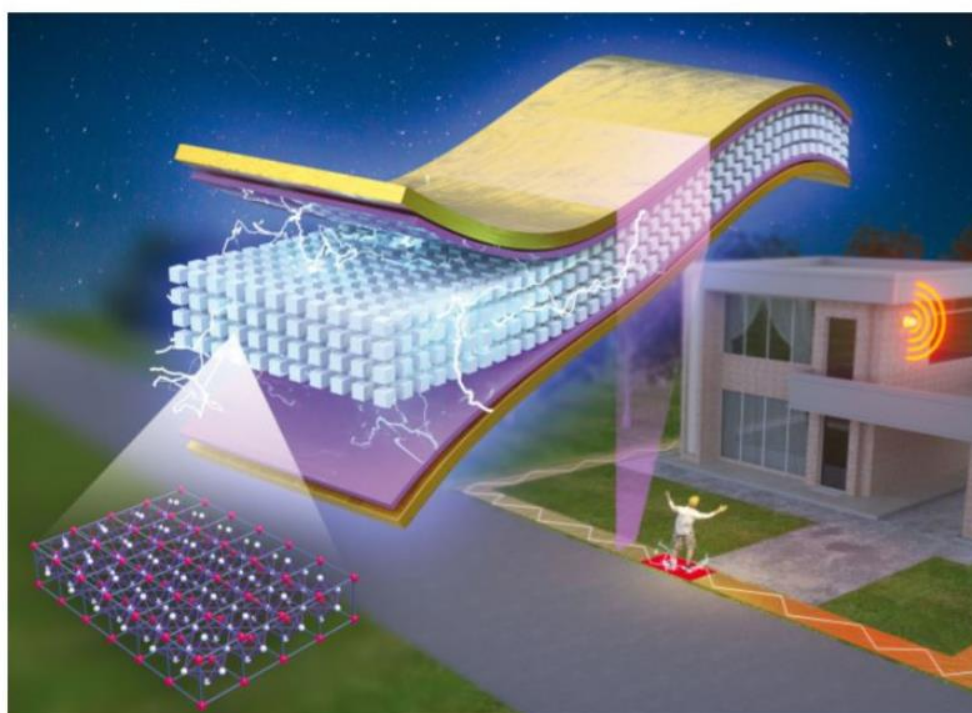

Featuring research work by V. Vivekananthan at Prof. Sang-Jae Kim's Nanomaterials and Systems Laboratory in the Department of Mechatronics Engineering at the Jeju National University, Jeju-do, South Korea.

Zero-power consuming intruder identification system by enhanced piezoelectricity of $K_{0.5}Na_{0.5}NbO_3$ using substitutional doping of BTO NPs

A zero-power consuming self-powered intruder system was reported for the first time using a flexible piezoelectric composite film nanogenerator made up of Polydimethylsiloxane and a solid state reaction based dual perovskite system, i.e. $(1 - x)K_{0.5}Na_{0.5}NbO_3 - _xBaTiO_3$. The device made of piezoelectric composite films was used to demonstrate the real-time application of a self-powered intruder system, which can produce a warning alarm/LED glow and display a message on a computer screen upon any intrusion on the device.

As featured in:
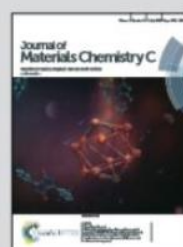
See Sang-Jae Kim et al., J. Mater. Chem. C, 2019, 7, 7563.

ROYAL SOCIETY OF CHEMISTRY | Celebrating IYPT 2019

rsc.li/materials-c

Registered charity number: 207890

Declaration

I, **Venkateswaran Vivekananthan**, hereby declare that the thesis entitled **"Development of Flexible Composite Film based Hybrid Energy Harvesters for Self-Powered Sensors"**, submitted to the Jeju National University, in partial fulfilment of the requirements for the award of the **Degree of Doctor of Philosophy in Department of Mechatronics Engineering** is a record of original and independent research work done and published by me during the period September 2016 to February 2020 under the supervision and guidance of **Prof. Sang Jae Kim,** Department of Mechatronics Engineering and the co-supervision from **Prof. Chang Nam Kang**, Department of Mechanical Engineering, Jeju National University. This thesis solely based on our publication in reputed journals, and it has not been formed on the basis from the award of any other Degree / Diploma / Associateship / Fellowship to any candidate of any university.

Venkateswaran Vivekananthan